

RESEARCH & REVIEWS IN SCIENCE AND MATHEMATICS

October 2022

EDITORS

Doç. Dr. Neslihan İYİT
Prof. Dr. Hasan Hüseyin DOĞAN
Prof. Dr. Hasan AKGÜL

gece
kitaplığı

İmtiyaz Sahibi / Publisher • Yaşar Hız
Genel Yayın Yönetmeni / Editor in Chief • Eda Altunel
Kapak & İç Tasarım / Cover & Interior Design • Gece Kitaplığı
Editörler / Editors • Doç. Dr. Neslihan İYİT
Prof. Dr. Hasan Hüseyin DOĞAN
Prof. Dr. Hasan AKGÜL
Birinci Basım / First Edition • © Ekim 2022
ISBN • 978-625-430-441-5

© copyright

Bu kitabın yayın hakkı Gece Kitaplığı'na aittir.

Kaynak gösterilmeden alıntı yapılamaz, izin
almadan hiçbir yolla çoğaltılamaz.

The right to publish this book belongs to Gece Kitaplığı.
Citation can not be shown without the source, reproduced in any way
without permission.

Gece Kitaplığı / Gece Publishing

Türkiye Adres / Turkey Address: Kızılay Mah. Fevzi Çakmak 1. Sokak
Ümit Apt. No: 22/A Çankaya / Ankara / TR
Telefon / Phone: +90 312 384 80 40
web: www.gecekitapligi.com
e-mail: gecekitapligi@gmail.com



Baskı & Cilt / Printing & Volume

Sertifika / Certificate No: 47083

Research & Reviews in Science and Mathematics

October 2022

EDITORS

DOÇ. DR. NESLİHAN İYİT

PROF. DR. HASAN HÜSEYİN DOĞAN

PROF. DR. HASAN AKGÜL

CONTENTS

Chapter 1

WRAPPED TWO-SIDED LINDLEY DISTRIBUTION

Cenker BİÇER, Abdullah YILMAZ 1

Chapter 2

EVALUATION OF MULTIPLE GROUP OUTLIERS FOR LOGISTIC REGRESSION MODELS

Burcin COSKUN, Ozlem ALPU 15

Chapter 3

UNIT ISHITA DISTRIBUTION WITH INFERENCE

Hayrinisa DEMİRCİ BİÇER, Cenker BİÇER 39

Chapter 4

TERNARY METAL COMPLEXES CONTAINING N,N-DONOR ATOMS AND SCHIFF BASES DERIVED FROM AMINO ACIDS

Duygu İNCİ ÖZBAĞCI, Rahmiye AYDIN 53

Chapter 5

PLUTO

E. Nihal ERCAN 71

Chapter 6

A STUDY ON EXTENSION OF MADDOX'S SPACE AND ITS CERTAIN MATRIX TRANSFORMATIONS

Fadime GÖKÇE 89

Chapter 7

AFLATOXIN B1 DETOXIFICATION FROM APPLE JUICE WITH A COMMERCIAL ACTIVATED CARBON ADSORBENT

Hacer Sibel KARAPINAR 109

Chapter 8

EFFECT OF CARVEDILOL APPLICATION ON ATOPIC DERMATITIS-LIKE SKIN LESIONS IN MICE

Kaan KALTALIOGLU 121

Chapter 9

ESTIMATION OF BASIC ASTROPHYSICAL PARAMETERS AND ORBITAL PERIOD ANALYSIS OF SEMI-DETACHED BINARY VX LAC

Muhammed Faruk YILDIRIM 135

Chapter 10

λ -STATISTICAL CONVERGENCE OF FRACTIONAL DIFFERENCE SEQUENCES ON NEUTROSOPHIC NORMED SPACES

Nazmiye GONUL BILGIN, Gurel BOZMA 151

Chapter 11

HARMONIC AND HYPERHARMONIC PADOVAN NUMBERS

Orhan DIŞKAYA, Hamza MENKEN 167

Chapter 12

REMOVAL OF MALACHITE GREEN FROM WASTEWATER

Oya AYDIN URUCU, Emrah ÇAKMAKÇI 179

Chapter 13

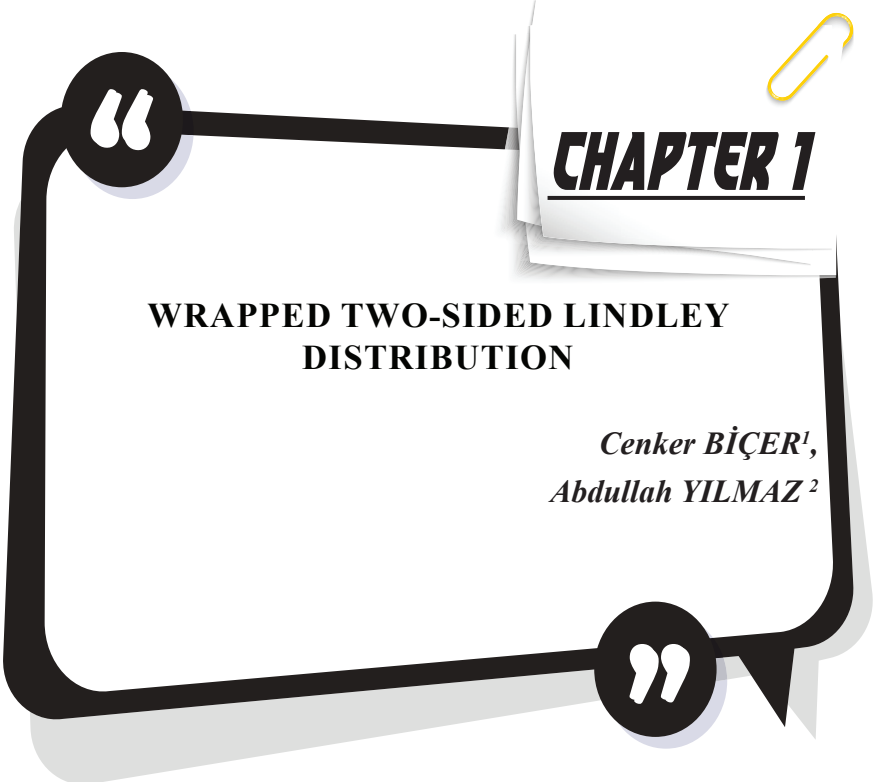
AN OVERVIEW OF PRISMATIC EYEGLASSES

Tuba ÖZDEMİR ÖGE, Mecit ÖGE 191

Chapter 14

CAUSALITY ANALYSIS IN STATISTICAL AND ECONOMETRIC MODELS: INVESTIGATING CAUSALITY RELATIONSHIP BETWEEN TURKEY'S PRIMARY ENERGY USE AND GROSS DOMESTIC PRODUCT BY GRANGER CAUSALITY TEST

Neslihan İYİT, Harun YONAR, Aynur YONAR 201



CHAPTER 1

WRAPPED TWO-SIDED LINDLEY DISTRIBUTION

*Cenker BİÇER¹,
Abdullah YILMAZ²*

1 Assoc.Prof.Dr., Kırıkkale Unv, Dep. of Statistics. ORCID: 0000-0003-2222-3208, cbicer@kku.edu.tr.

2 Asst.Prof.Dr., Kırıkkale Unv., Dep. of Actuarial Sciences. ORCID: 0000-0002-1196-9541, a.yilmaz@kku.edu.tr.

INTRODUCTION

Data is the most basic way of understanding and describing the events happening around our nature. Due to technological developments, we have access to much more data today. Statistical models provide us great convenience in the processing and modeling of these data. Optimal modeling of the data in terms of statistics is possible by using the most appropriate model for the data. There are different types of observations in our nature, such as linear or circular. In determining the most appropriate statistical model for the data, first of all, the type of data should be revealed. There are many distribution models in the vast literature of statistics for modeling linear data. However, although new breakthroughs have been made in recent years for derivating circular probability models, new developments are still needed. This type of data is encountered in a wide range of science such as meteorology, astronomy, medicine, biology, geology, physics, and sociology.

There are several methods in the literature that can be used to generate a circular distribution based on a distribution family in linear structure. The wrapping method is one of these approaches, and the models derived from this method are effectively used in modeling of circular data. We can exemplify some circular models derived so far based on the wrapping method as follows. Pewsey (Pewsey, 2000) obtained the probability density function of the wrapped skew-normal distribution by using the skew normal distribution given by Azzalini (Azzalini, 1985). Jammalamadaka and Kozubowski examined some stochastic properties of the circular distributions obtained by the wrapping Exponential, Laplace (Jammalamadaka & Kozubowski, 2004), and asymmetric Laplace (Jammalamadaka & Kozubowski, 2003) distributions. Pewsey obtained a new distribution by reparameterizing the wrapped-skewed normal distribution and worked on maximum likelihood estimations and simulation of this distribution (Pewsey, 2006). Lee focused on regression and correlation for such data in his study, which he published as a review for circular models (Lee, 2010). Jones and Pewsey (Jones & Pewsey, 2012) studied on a unimodal and symmetric circular probability density function, which includes smooth, von-Mises, cardioid, and wrapped-Cauchy distributions. In addition, Sanchez and Scarpa (Hernández-Sánchez & Scarpa, 2012) successfully modeled local wind data using the flexible generalized skewed normal (FGSN) distribution defined by Ma and Genton (Ma & Genton, 2004), using the circular distribution they named wrapped-FSGN. Yılmaz and Biçer (Yılmaz, & Biçer, 2018) introduce transmuted wrapped exponential distribution as new circular model and studied its properties. The aim of this work is to introduce a new flexible circular distribution based on two-sided Lindley distribution by employing the wrapping methodology, which is called

wrapped two-sided Lindley distribution (W2SLD).

The remainder of this article is organized as follows: Section 2 introduces the pdf and cdf of W2SLD. Some statistically important characteristics of W2SLD are investigated in Section 3, such as characteristic function, survival function, and the hazard function. Section 4 covers the solution to the estimation problem of W2SLD parameters by employing the maximum likelihood and least squares methodologies. A comprehensive Monte-Carlo simulation study is provided in Section 5 to compare the estimators obtained in this study according to bias and mean squared error criteria. Section 6 exemplifies real data modeling with W2SLD. Section 7 concludes the study.

WRAPPED TWO-SIDED LINDLEY DISTRIBUTION

Let X is a Two-Sided Lindley random variable with parameters α and β . then the pdf of the X is

$$f_X(x; \alpha, \beta) = \begin{cases} \frac{\alpha^2(x+1)e^{-\alpha x}}{2(\alpha+1)} & , x > 0 \\ \frac{\beta^2(1-x)e^{\beta x}}{2(\beta+1)} & , x \leq 0 \end{cases} ,$$

and the corresponding cdf is

$$F_X(x, \alpha, \beta) = \begin{cases} \frac{1}{2(\alpha + 1)} (\alpha - \alpha x + 1) \exp(\alpha x), & x < 0 \\ \frac{1}{2} + \frac{1}{2} \left(1 - \frac{\beta + 1 + \beta x}{\beta + 1} \exp(-\beta x) \right), & x > 0 \end{cases} ,$$

where α and β are the positive valued shape parameters of the distribution. The parameters α and β regularize both tail probabilities and skewness of the two-sided Lindley distribution. Some specific features of the distribution have been investigated by Altun (Altun, 2019).

Now we define a random variable by transformation

$$\Theta = X(mod 2\pi).$$

Thus, considering the transformation given by the equation (2) the W2SLD is given the following proposition.

Proposition 1. Let Θ a random variable have W2SLD. Then the pdf of Θ is $f_\Theta(\theta; \alpha, \beta) = \sum_{r=-\infty}^{\infty} f_X(\theta + 2\pi r; \alpha, \beta)$, or clearly

$$f_{\Theta}(\theta; \alpha, \beta) = \frac{e^{-\alpha\theta}}{2\Lambda_{\alpha}\Lambda_{\beta}} \left[e^{2\pi\alpha} \alpha^2 \Lambda_{\beta} (e^{2\pi\alpha}(\theta + 1) - \theta + 2\pi - 1) + \beta^2 \Lambda_{\alpha} (e^{2\pi\beta}(-\theta + 2\pi + 1) + \theta - 1) e^{\theta(\alpha+\beta)} \right],$$

where $\Lambda_{\alpha} = (e^{2\pi\alpha} - 1)^2(\alpha + 1)$ and $\Lambda_{\beta} = (e^{2\pi\beta} - 1)^2(\beta + 1)$. Also, the CDF of Θ is

$$F_{\Theta}(\theta; \alpha, \beta) = \frac{e^{\alpha(2\pi-\theta)} \left((\alpha + 1)e^{\alpha(\theta+2\pi)} + ((2\pi - 1)\alpha - 1)e^{\alpha\theta} \right)}{2\Lambda_{\alpha}} + \frac{\left(e^{\beta\theta}(\beta(\theta - 1) - 1) + \beta - e^{2\pi\beta}(2\pi\beta + \beta + 1) \right) + e^{\beta(\theta+2\pi)}(-\beta\theta + 2\pi\beta + \beta + 1) + 1}{2\Lambda_{\beta}}.$$

We present Figure 1 to show possible behaviours of the pdf of W2SLD for different values of the parameters.

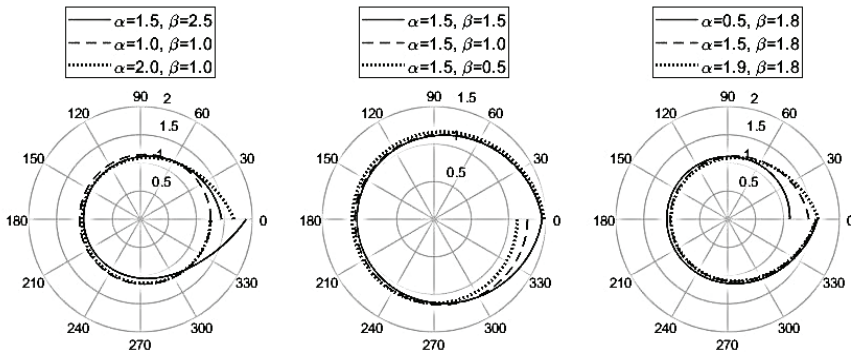


Figure 1. Pdf of the W2SLD for different values of the parameters α and β .

Figure 1 lucidly shows the W2SLD is a unimodal circular distribution. In addition, for different values of the parameters α and β , the distribution has clockwise or anti-clockwise skewness. If $\alpha = \beta$ the distribution concentrates around zero.

SOME CHARACTERISTICS OF W2SLD

This section of the study investigates the basic statistical features of the W2SLD such as survival function, hazard function, and characteristic function.

Survival and Hazard Function

Let Θ be a random variable distributed W2SLD with parameters α and β . The survival function $S(\cdot)$ of W2SLD is obtained, following the formal definition of the survival function, as

$$\begin{aligned}
 S(\theta; \alpha, \beta) &= 1 - F_{\Theta}(\theta; \alpha, \beta) \\
 &= \frac{-2e^{2\pi\alpha} - 3e^{4\pi\alpha} + 1}{8(e^{2\pi\alpha} - 1)^2} + \frac{4e^{2\pi\alpha - \alpha\theta}}{8\Lambda_{\alpha}} \left(\begin{array}{l} (-2\pi\alpha + \alpha + 1)e^{\alpha\theta} \\ + \alpha(-\theta + 2\pi - 1) \\ + e^{2\pi\alpha}(\alpha\theta + \alpha + 1) - 1 \end{array} \right) \\
 &\quad + \frac{1}{8\Lambda_{\beta}} \left(\begin{array}{l} (7e^{4\pi\beta} + 3) + e^{\beta\theta}(4 - 4\beta(\theta - 1)) \\ - 4\beta e^{\beta(\theta + 2\pi)} \left(-\theta + 2\pi + 1 + \frac{1}{\beta} \right) \\ + 2e^{2\pi\beta}((4\pi - 5)\beta - 5) \end{array} \right)
 \end{aligned}$$

Hence, we follow the general definition of the hazard function, see (Tuncel, 2017), $H(\cdot)$ hazard function of the W2SLD is immediately obtained as

$$\begin{aligned}
 H(\theta; \alpha, \beta) &= \frac{f_{\Theta}(\theta; \alpha, \beta)}{S(\theta; \alpha, \beta)} \\
 &= \frac{e^{-\alpha\theta} \left(\Lambda_{\alpha}\beta^2(e^{2\pi\beta}(-\theta + 2\pi + 1) + \theta - 1)e^{\theta(\alpha+\beta)} + e^{2\pi\alpha}\alpha^2\Lambda_{\beta}(e^{2\pi\alpha}(\theta + 1) - \theta + 2\pi - 1) \right)}{\left[\begin{array}{l} \Lambda_{\alpha} \left(\begin{array}{l} e^{\beta\theta}(-\beta\theta + \beta + 1) - e^{\beta(\theta+2\pi)}(-\beta\theta + 2\pi\beta + \beta + 1) \\ -\beta + e^{2\pi\beta}(2\pi\beta + \beta + 1) - 1 \end{array} \right) \\ + \Lambda_{\beta} \left(2\Lambda_{\alpha} - e^{2\pi\alpha - \alpha\theta} \left(\begin{array}{l} (\alpha + 1)e^{\alpha(\theta+2\pi)} + ((2\pi - 1)\alpha - 1)e^{\alpha\theta} \\ + \alpha(\theta - 2\pi + 1) - e^{2\pi\alpha}(\alpha\theta + \alpha + 1) + 1 \end{array} \right) \right) \end{array} \right]}
 \end{aligned}$$

Characteristic Function

The characteristic function $\varphi_{\Theta}(p)$ of the W2SLD is given by

$$\begin{aligned}
 \varphi_{\Theta}(p) &= E(e^{ip\Theta}) \\
 &= \frac{(p + i\alpha)^{-2}}{2\Lambda_{\alpha}\alpha^{-2}} \left(\begin{array}{l} e^{2\pi(\alpha+ip)}(2\pi\alpha - e^{2\pi(\alpha-ip)} - 2ip\pi + 1) \\ + e^{2ip\pi}(-2\pi\alpha + e^{2\pi(\alpha-ip)} + 2ip\pi - 1) \end{array} \right)
 \end{aligned}$$

$$\begin{aligned}
& + \frac{(p+i\alpha)^{-1}}{2\Lambda_\alpha\alpha^{-2}} \begin{pmatrix} -e^{2\pi\alpha} + e^{2i\pi p} + e^{2\pi\alpha}(e^{2\pi\alpha} - e^{2i\pi p}) \\ + 2\pi(e^{2\pi\alpha} - e^{2i\pi p}) \end{pmatrix} \\
& + \frac{(\beta+ip)^{-2}}{2\Lambda_\beta\beta^{-2}} \begin{pmatrix} (1 + e^{2\pi(\beta+ip)})(2\pi\beta + 2i\pi p - 1) \\ -e^{2\pi\beta}(1 + e^{2\pi(\beta+ip)})(2\pi\beta + 2i\pi p - 1) \end{pmatrix} \\
& + \frac{(\beta+ip)^{-1}}{2\Lambda_\beta\beta^{-2}} \begin{pmatrix} e^{2\pi\beta}(-1 + e^{2\pi(\beta+ip)}) + 1 - e^{2\pi(\beta+ip)} \\ + 2\pi e^{2\pi\beta}(-1 + e^{2\pi(\beta+ip)}) \end{pmatrix}.
\end{aligned}$$

One can also write p th trigonometric moments in terms of α_p and β_p

$$\varphi_p = \varphi_\Theta(p) = \alpha_p + i\beta_p, \quad p = 0, \pm 1, \pm 2, \dots$$

where α_p is p th cosine moment and defined as $\alpha_p = E(\cos p\Theta)$, β_p is p th sine moment and defined as $\beta_p = E(\sin p\Theta)$. The resultant vector length and direction for the p .cosine and sine moments of a circular distribution are calculated by,

$$\rho_p = \sqrt{\alpha_p^2 + \beta_p^2}, \quad \mu_p = \arctan^* \left(\frac{\alpha_p}{\beta_p} \right)$$

respectively, where $\arctan^*(.)$ is a quadrant-inverse tangent function. The first trigonometric moment can be expressed as $\varphi_1 = \rho_1 e^{i\mu_1}$ and has a special meaning. The values of ρ_1 and μ_1 are called the *angular concentration* and the *mean direction*, respectively. The mean direction vector gives information about the mean of the circular distribution, as an analogy of the mean in linear models. The length of this vector is a measure of the spread of the distribution around the mean. This is equivalent variance or standard deviation in circular models. Figure 2 presents contour plots of mean direction and angular concentration for values of parameter in range (1,5).

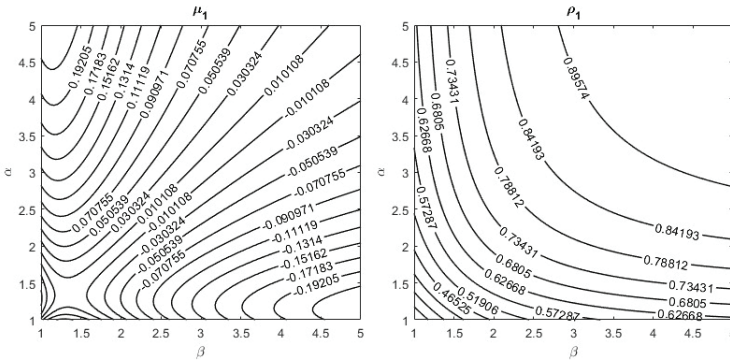


Figure 2. Contour plots of mean direction and angular concentration.

As can be seen from Figure 2, when the parameter values are changed, the value of the mean direction remains the same and its sign changes. The angular concentration increases as the parameter values increase.

INFERENCE

This section covers solution of inference problem of W2SL parameters by two different points of view, Maximum likelihood and least square estimation methods.

Maximum Likelihood Estimation

Let $\theta_1, \theta_2, \dots, \theta_n$ be a random sample drawn W2SLD with parameters α and β . The logarithmic likelihood function for the random variables $\theta_i, i = 1, 2, \dots, n$ can be immediately written as

$$L(\alpha, \beta; \theta_1, \theta_2, \dots, \theta_n) = \sum_{i=1}^n \log \left(\frac{e^{2\pi\alpha - \alpha\theta_i} \alpha^2 (e^{2\pi\alpha(\theta_{i+1} - \theta_i + 2\pi - 1)}}{2\Lambda_\alpha} + \frac{e^{\beta\theta_i} \beta^2 (e^{2\pi\beta(-\theta_i + 2\pi + 1) + \theta_i - 1)}}{2\Lambda_\beta} \right).$$

To obtain the maximum likelihood estimators of the α and β parameters, we first derive the logarithmic likelihood function given by the equation (3) according to the parameters. Thus, we have the following score functions.

$$\frac{\partial}{\partial \alpha} L(\alpha, \beta; \theta_1, \theta_2, \dots, \theta_n) = 0,$$

$$\frac{\partial}{\partial \beta} L(\alpha, \beta; \theta_1, \theta_2, \dots, \theta_n) = 0.$$

The maximum likelihood estimators of the α and β parameters can be obtained by solving the nonlinear system of equations constructed by

equation (4) and equation (5). Unfortunately, this system of equations cannot be solved analytically. However, the maximum likelihood estimates of the parameters can be easily obtained from the numerical solution of the system of equations given by the equations (4) and (5) using a numerical method such as Newton's method.

Least-Squares and Weighted Least Squares Estimation

In this sub section we investigate the least- square estimators of the W2SLD parameters based on approximation given by the study of Swain (Swain *et al.*, 1988). Let $\theta_1, \theta_2, \dots, \theta_n$ be a random sample drawn W2SLD with parameters α and β and $\theta_1 \leq \dots \leq \theta_n$ shows an order of it. Thus, following the notation of the, the least-square estimators of W2SLD parameters are obtained by minimizing utility function

$$Q = \sum_{j=1}^n \left(\frac{1}{2\Lambda_\alpha} [(\alpha + 1)e^{4\pi\alpha} + e^{2\pi\alpha}((2\pi - 1)\alpha - 1) + e^{2\pi\alpha - \alpha\theta_j}(\alpha(\theta_j - 2\pi + 1) + 1) - e^{4\pi\alpha - \alpha\theta_j}(\alpha + \alpha\theta_j + 1)] + \frac{1}{2\Lambda_\beta} [(\beta + 1) - e^{2\pi\beta}(2\pi\beta + \beta + 1) + e^{\beta\theta_j}(\beta(\theta_j - 1) - 1) + e^{\beta(\theta_j + 2\pi)}(2\pi\beta + \beta + \beta(-\theta_j) + 1)] - \frac{j}{n+1} \right)^2,$$

with respect to parameters α and β , where $j/(n + 1)$ is the value of the empirical distribution function for j^{th} observation. The solution of the utility function Q can be obtained numerically. A lower biased form of the least-squares estimator is known as weighted least-squares. The weighted least-squares estimators of the W2LSD parameters are obtained by minimizing

$$Q_1 = \sum_{j=1}^n \frac{(n + 1)^2(n + 2)}{j(n - j + 1)} \left(\frac{1}{2\Lambda_\alpha} [(\alpha + 1)e^{4\pi\alpha} + e^{2\pi\alpha}((2\pi - 1)\alpha - 1) + e^{2\pi\alpha - \alpha\theta_j}(\alpha(\theta_j - 2\pi + 1) + 1) - e^{4\pi\alpha - \alpha\theta_j}(\alpha + \alpha\theta_j + 1)] + \frac{1}{2\Lambda_\beta} [(\beta + 1) - e^{2\pi\beta}(2\pi\beta + \beta + 1) + e^{\beta\theta_j}(\beta(\theta_j - 1) - 1) + e^{\beta(\theta_j + 2\pi)}(2\pi\beta + \beta + \beta(-\theta_j) + 1)] - \frac{j}{n + 1} \right)^2$$

with respect to α and β .

SIMULATION STUDY

This part of the study covers some simulation studies comparing the estimation performances of ML, LS and WLS estimators of W2SLD parameters according to bias and mean squared error (MSE) criteria. In Monte-Carlo simulations based on 1000 iterations, parameter values are set as $(\alpha, \beta) = (5,3)$ and $(\alpha, \beta) = (2,7)$. In addition to comparing the estimation performances of the estimators, it is also aimed to demonstrate the large sample properties of the estimators. For this, the sample size has been set as $n = 30,50,100$ and 1000 and the simulations are repeated for each sample size. The results obtained from the simulation study are tabulated in Table 1-2.

According to the results given in Tables 1-2, all of the ML, LS and WLS estimators showed very satisfactorily estimation performance according to used comparison criteria the Bias and MSE. All estimators have both lower Bias and lower MSE values as sample size n increases. Therefore, it can be said that the obtained estimators in the study are asymptotically consistent and unbiased. Also, as can be clearly seen from Tables 1-2, the MLE estimators outperformed the other estimators with lower Bias and MSE values in all cases.

*Table 1: Simulation results for W2SLD parameters
 $(\alpha, \beta) = (5,3)$*

Method	n	$\hat{\alpha}$	Bias $\hat{\alpha}$	MSE $\hat{\alpha}$	$\hat{\beta}$	Bias $\hat{\beta}$	MSE $\hat{\beta}$
ML	50	5.22110	0.73637	0.87920	3.06128	0.37717	0.22274
	100	5.04477	0.43503	0.29709	3.05026	0.27945	0.12324
	500	5.02929	0.21842	0.07142	2.98206	0.12338	0.02529
	1000	5.00863	0.16546	0.04476	3.0030	0.08362	0.01121
LS	50	5.37945	1.22891	2.47327	3.07793	0.62713	0.63710
	100	5.05430	0.71548	0.75450	3.08386	0.44023	0.33008
	500	4.98863	0.38735	0.23838	3.00863	0.16483	0.04788
	1000	4.99258	0.25740	0.10128	3.00961	0.14906	0.0373
WLS	50	5.41047	1.17297	2.47779	3.07745	0.62390	0.64869
	100	5.09795	0.64676	0.74897	3.10410	0.44395	0.34315
	500	4.99574	0.38348	0.24808	3.01457	0.17467	0.05044
	1000	4.99888	0.26280	0.10301	3.00901	0.15000	0.03790

Table 2: Simulation results for W2SLD parameters
 $(\alpha, \beta) = (2, 7)$.

Method	n	$\hat{\alpha}$	Bias $\hat{\alpha}$	MSE $\hat{\alpha}$	$\hat{\beta}$	Bias $\hat{\beta}$	MSE $\hat{\beta}$
ML	50	2.05809	0.25634	0.12295	7.36224	1.02371	1.73922
	100	1.99895	0.18257	0.05179	7.19795	0.6973	0.79941
	500	2.00370	0.08738	0.01211	7.02473	0.32482	0.16112
	1000	2.00276	0.06051	0.00560	7.02063	0.22922	0.07750
LS	50	2.16291	0.40151	0.31728	7.18124	1.66306	4.57383
	100	1.95953	0.40670	0.36572	7.34014	1.44127	5.00045
	500	2.01182	0.13339	0.02761	6.97537	0.53737	0.39721
	1000	1.99394	0.09609	0.01483	7.06190	0.39053	0.24670
WLS	50	2.19172	0.42853	0.37047	7.27440	1.72993	4.90817
	100	2.05589	0.32887	0.18029	7.15618	1.17870	2.17144
	500	2.01823	0.13835	0.02857	6.95116	0.55901	0.42588
	1000	1.99539	0.09862	0.01581	7.07235	0.40127	0.26323

REAL-DATA EXAMPLE

This section exemplifies modeling a real-life dataset with W2SLD. For this purpose, we consider the ant dataset, which is a circular dataset. Ant data set includes the directions chosen by 100 ants in response to evenly illuminated black targets placed, as shown (Fisher *et al.*, 1993). We obtain the ML, the LS, and the WLS estimations of the parameters α and β by using the Octave software (Eaton *et al.*, 2019).

Remark: When applying the fixing subroutines, the parameter ranges should be selected as wide as possible to bypass the local maximum.

For the ant data set, parameter estimates, negative log-likelihood value ($-L$), Akaike information criterion (AIC) and Bayesian information criterion (BIC) values are presented in Table 3. The values given in Table 3 show that the best data fit is achieved with the ML estimates.

Table 3: Parameter estimates, $-L$, AIC , and BIC values for the Ant data

Method	$\hat{\alpha}$	$\hat{\beta}$	$-L$	AIC	BIC
ML	3.5778	0.8496	126.048	256.095	261.305
LS	3.8361	0.8134	126.278	256.378	261.489
WLS	3.8031	0.8515	126.133	256.266	261.476

Plots of the fitted density with ML estimates are shown in Figure 3, where panel (a) displays the circular data plot, rose diagram, and fitted pdf of the W2SLD. with ML estimations. The dashed arrow shows the sample mean resultant vector with $m_1 = 3.14^\circ$ and resultant length $r_1 = 0.6101$, and the solid arrow shows the mean direction vector and the resultant length of the fitted W2SLD, $\mu_1 = 352.29^\circ$ and $\rho_1 = 0.5319$ respectively.

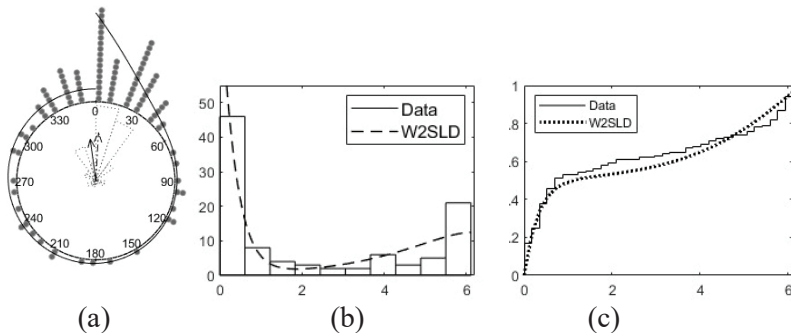


Figure 3. Plots for ant data set, (a)circular data plot, fitted pdf of W2SLD and rose diagram, (b) histogram and fitted pdf of W2SLD, and (c) empirical cdf and fitted cdf.

CONCLUSION

In this study, we have derived a new circular model called as W2SLD to model circular data. In the study, pdf and cdf of the derived distribution have been obtained in closed form and the formal behavior of its pdf in different values of the parameters has shown in Figure 1. In addition, statistically significant properties of the distribution have been investigated, such as the survival function, hazard function, characteristic function, and distribution of rank statistics. Also, several estimators based on maximum likelihood, least squares and weighted least squares methods for unknown parameters of the introduced distribution have been investigated. The performances of the estimators obtained in the study were also compared with a carried out series of Monte-Carlo simulation studies. In the light of the information obtained from the simulation study, it can be said that all obtained estimators of the W2SLD parameters are asymptotically consistent and unbiased. Moreover, MLE estimators have had lower bias and MSE values in all cases. Finally, the usability of the derived distribution has been exemplified by an application performed on a real-world dataset.

REFERENCES

1. Altun, E. (2019). Two-sided Lindley distribution with inference and applications. *Journal of the Indian Society for Probability and Statistics*, 20(2), 255-279.
2. Azzalini, A. (1985). A class of distributions which includes the normal ones. *Scandinavian journal of statistics*, 171-178.
3. Eaton, J. W., Bateman, D., Hauberg, S., & Wehbring, R. (2019). GNU Octave version 4.0. 0 manual: a high-level interactive language for numerical computations. 2015. URL <http://www.gnu.org/software/octave/doc/interpreter>, 8, 13.
4. Fisher, N. I., Lewis, T., & Embleton, B. J. (1993). *Statistical analysis of spherical data*. Cambridge university press.
5. Hernández-Sánchez, E., & Scarpa, B. (2012). A wrapped flexible generalized skew-normal model for a bimodal circular distribution of wind directions. *Chilean Journal of Statistics (ChJS)*, 3(2).
6. Jammalamadaka, S. R., & Kozubowski, T. J. (2003). A new family of circular models: The wrapped Laplace distributions. *Advances and applications in statistics*, 3(1), 77-103.
7. Jammalamadaka, S. R., & Kozubowski, T. J. (2004). New families of wrapped distributions for modeling skew circular data. *Communications in Statistics-Theory and Methods*, 33(9), 2059-2074.
8. Jones, M. C., & Pewsey, A. (2012). Inverse Batschelet distributions for circular data. *Biometrics*, 68(1), 183-193.
9. Lee, A. (2010). Circular data. *Wiley Interdisciplinary Reviews: Computational Statistics*, 2(4), 477-486.
10. Ma, Y., & Genton, M. G. (2004). Flexible class of skew-symmetric distributions. *Scandinavian Journal of Statistics*, 31(3), 459-468.
11. Pewsey, A. (2000). The wrapped skew-normal distribution on the circle. *Communications in Statistics-Theory and Methods*, 29(11), 2459-2472.
12. Pewsey, A. (2006). Modelling asymmetrically distributed circular data using the wrapped skew-normal distribution. *Environmental and*

Ecological Statistics, 13(3), 257-269.

13. Swain, J. J., Venkatraman, S., & Wilson, J. R. (1988). Least-squares estimation of distribution functions in Johnson's translation system. *Journal of Statistical Computation and Simulation*, 29(4), 271-297.
14. Tuncel, A. (2017). Residual lifetime of a system with a cold standby unit. *Istatistik Journal of The Turkish Statistical Association*, 10(1), 24-32.
15. Yilmaz, A., & Biçer, C. (2018). A new wrapped exponential distribution. *Mathematical Sciences*, 12(4), 285-293.



CHAPTER 2

EVALUATION OF MULTIPLE GROUP OUTLIERS FOR LOGISTIC REGRESSION MODELS*

*Burcin COSKUN¹,
Özlem ALPU²*

1 Res. Asst. Dr., Trakya University, Faculty of Education, Department of Measurement and Evaluation in Education, Edirne, Türkiye, burc_e@hotmail.com , ORCID: 0000-0002-6974-4353

2 Prof. Dr., Eskisehir Osmangazi University, Faculty of Science , Department of Statistics, Eskisehir, Türkiye. oalpu@ogu.edu.tr, ORCID: 0000-0002-2302-2953

* This work is derived from Ph.D. thesis with the number of 466568, and it was supported by Scientific Research Project of Eskisehir Osmangazi University (ESOGUBAP): [Grant Number 2015-903].

Introduction

Suspicious observation diagnostic measures are developed to identify the location of outlier or highly influential data points, measure the existence and intensity of the collinear relationships between the regression data, help to identify the variables in each, and determine the estimated coefficients that are most affected by the presence of suspicious observations (Belsley, Kuh & Welsch, 2008). The maximum likelihood estimation method, which is often used in logistic regression, is sensitive to suspicious observations (Pregibon, 1981; Salsas, Guillen & Alemany, 1999; Ahmad, Midi & Ramli, 2011; Norazan, Sanizah & Habshah, 2012).

An error in the identification of suspicious observations can cause serious distortions in the validity of the inferences that are obtained from the model. The identification and elimination of these observations is an important issue in modeling studies. In the regression analysis, suspicious observations are divided into three categories: outliers, influential observations, and high leverage points (Nurunnabi, Nasser & Imon, 2016). Outliers are observations that do not fit the homogeneous majority of the data in the proposed model (Rawlings, Pantula & Dickey, 1998). It is more difficult to identify the outliers in logistic regression compared to multiple linear regression (Cook & Weisberg, 1999).

Because the maximum likelihood estimation method is delicate to outliers in the regressor matrix and outliers in the dependent variable, in his most frequently cited and popular study, Pregibon (1981) developed some diagnostic measures that can be used to identify such observations and to determine the amount of the effect of these observations on the maximum likelihood fit. There are many other studies about the outlier diagnostic measures for the logistic regression model (Agresti, 2015; Ahmad, Ramli & Midi, 2012; Cordeiro, 2004; Hosmer & Lemeshow, 1980; Hosmer, Lemeshow & Sturdivant, 2013; Imon & Hadi, 2008; Jennings, 1986; Menard, 2002; Midi & Ariffin, 2013; Nurunnabi & Nasser, 2009; Pregibon, 1981, Salsas et al., 1999; Sarkar, Midi & Rana, 2011).

If the dataset contains multiple suspicious observations, diagnostic measures that are proposed based on removing a single observation from it may fail because of the masking or swamping effect. Masking occurs when a suspicious observation is hidden by another suspicious observation nearby. Swamping occurs when the observation is identified as a suspicious observation because of an observation group even if it is not the suspicious observation. This problematic situation led to the development of multiple outlier diagnostic measures based on the simultaneous elimination of the suspicious observation group from the

dataset. Based on this idea, Imon and Hadi (2008) proposed the generalized standardized Pearson residuals (GSPR) diagnostic measure, which is a modified version of the standardized Pearson residuals. In another study, Ahmad et al. (2011) proposed the multiple outlier diagnostic measure (DEVC), a generalization of deviance residuals based on the idea that Pearson residuals and deviance residuals fail in the presence of a high number of suspicious observations in the data.

In this study, classic outlier diagnostic measures and multiple outlier diagnostic measures from Ahmad et al. (2011) and Imon and Hadi (2008) were compared on a dataset, and a simulation study was conducted for these diagnostic measures. An overview of the logistic regression model is given in the first section of this study. The leverage matrix and outlier identification measures are discussed in the next section. In the third section, traditional outlier diagnostic measures on the Brown (1980) dataset or modified Brown datasets are compared with outlier diagnostic measures based on the simultaneous deletion of multiple group outliers from the dataset. Simulation studies for logistic regression models with single, two, and five regressors were carried out. These models had various sample sizes and contamination rates for multiple outlier diagnostic measures. The fifth section presents an interpretation of the findings.

1. Logistic Regression Model

The logit of the multiple logistic regression model when the conditional probability of the dependent variable takes the value 1 is $P(Y = 1|x) = \pi(x)$, with k regressor vector $\mathbf{x}' = (x_1, x_2, \dots, x_k)$ is given by Equation (1).

$$g(x) = \ln\left(\frac{\pi(x)}{1-\pi(x)}\right) = \beta_0 + \beta_1x_1 + \dots + \beta_kx_k \quad (1)$$

It is possible to obtain an equation where the parameters are linear using the logit transformation. Equation (2), therefore, is a representation of the logistic regression model.

$$\pi(X) = \frac{e^{\beta_0 + \beta_1X_1 + \dots + \beta_kX_k}}{1 + e^{\beta_0 + \beta_1X_1 + \dots + \beta_kX_k}} = \frac{e^{g(x)}}{1 + e^{g(x)}} \quad (2)$$

The matrix representation of the Equation (2) is expressed by the Equation (3),

$$g(X) = \mathbf{X}\boldsymbol{\beta}. \quad (3)$$

Given that $p=k+1$, X is the $n \times p$ -dimensional regressor matrix, and $\beta' = (\beta_0, \beta_1, \dots, \beta_k)$ is the regression parameter vector.

$$\varepsilon = \begin{cases} 1 - \pi(x), & y = 1 \\ -\pi(x), & y = 0 \end{cases} \quad (4)$$

The error term of the logistic regression model (Equation 4) has a binomial distribution (Nurunnabi, Imon & Nasser, 2010).

2. Leverage matrix and Outlier Diagnostic Measures

2.1. Leverage matrix

The leverage matrix is used to detect high leverage points in addition to developing suspicious observation diagnostic measures both in logistic regression and linear regression. In linear regression, the leverage matrix is expressed by the equation $H = X(X'X)^{-1}X'$. The difference between the \hat{y}_i predicted values corresponding to the observed y_i values is the i th residual value $e_i = y_i - \hat{y}_i$. The residual vector can also be expressed as, $e = y - X\hat{\beta} = y - Hy = (I - H)y$. Pregibon (1981) developed a linear regression-similarity approach to fit values that produces a leverage matrix for logistic regression employing the model of weighted least squares linear regression (Hosmer et al., 2013). Pregibon's (1981) leverage matrix is defined by Equation (5),

$$H = V^{1/2}X(X^TVX)^{-1}X^TV^{1/2}. \quad (5)$$

Here V is the diagonal matrix, X is the $n \times p$ dimensional regressor matrix. Another representation of the leverage matrix is,

$$h_{ii} = \hat{\pi}_i (1 - \hat{\pi}_i) x_i^T (X^TVX)^{-1} x_i = v_i \cdot b_i. \quad (6)$$

Here, h_{ii} represents the diagonal elements of the leverage matrix, $v_i = \hat{\pi}_i (1 - \hat{\pi}_i)$ is the variance for the logistic regression model, and b_i represents the weighted distance of x_i to the mean. The logistic regression leverage matrix's suggested threshold value is,

$$c^*p/n. \quad (7)$$

where k is the regressor number, $p=k+1$, and the value of c is a constant, like 2 or 3.

2.2. Diagnostic measures for single outlier in logistic regression

In linear regression, residuals can be calculated directly from the regression equation. In logistic regression analysis, there are several different residuals that correspond to different levels of analysis (probability, odds, and logit) that can be conceptualized. The purpose of the use of residual analysis in logistic regression is to identify observations where the model fits poorly or that show more than just the effect they share on parameter estimates (Menard, 2002). The residual sum of squares is the fundamental quantity in logistic regression, as it is in linear regression. The main principle of linear regression is that the error variance, $E(Y_i|x_i)$ is independent of the conditional mean. However, because the errors in logistic regression are binomially distributed, the conditional mean affects how much the error variance varies (Hosmer et al., 2013). In logistic regression, there are numerous approaches to measuring the difference between the observed and the predicted value. In logistic regression, when the i th variable's predicted value is expressed by Equation (8),

$$\hat{y}_i = \hat{\pi}_i = \frac{e^{\hat{g}(x_i)}}{1+e^{\hat{g}(x_i)}} \quad (8)$$

Here $\hat{g}(x_i)$ is the predicted logit.

The Pearson residuals, the deviation residuals, and the residuals used in linear regression are the three key measures of the disparity between the observed value and the predicted value in logistic regression. In assessing the model's fit, the residuals are crucial. The deviation and Pearson chi-square statistics are utilized to assess the generalized linear models' goodness of fit. They are the components of the Pearson residuals and deviation residuals, which are the two most well-known residual types in logistic regression (Cordeiro, 2004). Pearson residuals are raw residuals adjusted with the square root of the variance (Hilbe, 2009). Pearson residuals (PR) diagnostic measure is expressed as,

$$PR = r_{pi} = \frac{(y_i - \hat{\pi}_i)}{\sqrt{\hat{\pi}_i(1 - \hat{\pi}_i)}}. \quad (10)$$

The squared sum of the Pearson residuals is expressed as the Pearson chi-square statistics,

$$\chi^2 = \sum_{i=1}^n r_{pi}^2. \quad (11)$$

The deviation residuals (DR) are expressed by Equation (12).

$$DR = r_{Di} = \text{sgn}(y_i - \hat{\pi}_i) \left\{ 2 \left[y_i \ln \left(\frac{y_i}{\hat{\pi}_i} \right) + (1 - y_i) \ln \left(\frac{(1 - y_i)}{(1 - \hat{\pi}_i)} \right) \right] \right\}^{\frac{1}{2}} \quad (12)$$

$\text{sgn}(y_i - \hat{\pi}_i)$ in Equation (12) is a sign function that makes r_{Di} positive when $y_i \geq \hat{\pi}_i$ and negative when $y_i < \hat{\pi}_i$. If the r_{Di} value for the i th observation is higher than the ± 2 threshold value, an outlier is deemed to exist (Christensen, 1997). The deviation statistic (DEV) developed based on the deviation residuals is defined as,

$$DEV = \sum_{i=1}^n r_{Di}^2. \quad (13)$$

Assuming that the estimated regression model is accurate in every aspect, it is expected that the χ^2 and DEV statistics will have a chi-square distribution for $n - (k + 1)$ degrees of freedom (Hosmer et al., 2013). The deviance residuals are generally preferred to the Pearson residuals for evaluating the properties of the predicted regression model. The primary reason is that the deviance residuals show a similar distribution to the ordinal least squares residuals in linear regression (Hilbe, 2009).

The advantage and the disadvantage of these statistics is that they are used to summarize important information with a single number. Therefore, additional measures should be examined to determine if indeed the fit is maintained over the entire set of variable items before concluding that the model is adequate. This is accomplished through a set of measures referred to as regression diagnostics. Pregibon (1981) presented a theoretical study in which linear regression diagnostics were extended to logistic regression. It has concentrated on widening the use of logistic regression in evaluating fit (Hosmer et al., 2013). With Pregibon's linear regression-similarity approach, Pearson residuals can be interpreted as follows using the variance estimator of residuals $v_i = \pi(x)[1 - \pi(x)]$:

$$PR = r_{Pi} = \frac{(y_i - \hat{\pi}_i)}{\sqrt{v_i}}. \quad (14)$$

The standardized Pearson residuals (SPR) are obtained by dividing the Pearson residuals in Equation (14) by $\sqrt{1 - h_{ii}}$,

$$SPR = r_{SPi} = \frac{r_{Pi}}{\sqrt{1 - h_{ii}}}. \quad (15)$$

The variance value of the standardized Pearson residuals is 1. Although r_{SPi} is generally preferred to Pearson residuals in practice both residuals are similar (Scott, 1997). In comparison to Pearson and

deviance residuals, standardized Pearson residuals have the advantage of having approximately a $N(0,1)$ normal distribution as the sample size increases. If an observation's value is outside the range of ± 2 or ± 3 , there may not be a good fit (Agresti, 2015). The deviation residuals can also be standardized to have unit variance by dividing by $\sqrt{1 - h_{ii}}$. Standardized deviation residuals (SDR) can be expressed as,

$$SDR = r_{SDi} = \frac{r_{Di}}{\sqrt{1 - h_{ii}}} \tag{16}$$

2.3. Diagnostic Measures for Multiple Group Outliers in Logistic Regression

2.3.1. Generalized standardized Pearson residuals-GSPR

GSPR was proposed by Imon and Hadi (2008) as a diagnostic tool to identify multiple group outliers in logistic regression. The term "GSPR" stands for "generalized standardized Pearson residuals".

For the GSPR diagnostic measure, the remaining observation cluster in the analysis is indicated as R and the deleted observation cluster as D from the analysis when d observations are deleted from the n observation clusters before the model prediction. After removing d observation points from set D , R now contains $n-d$ observations. Assume that the matrices \mathbf{X} , \mathbf{Y} , and \mathbf{V} 's final d rows correspond to these observations. The matrices for \mathbf{X} , \mathbf{Y} , and \mathbf{V} are presented as,

$$\mathbf{X} = \begin{bmatrix} X_R \\ X_D \end{bmatrix} \quad \mathbf{Y} = \begin{bmatrix} Y_R \\ Y_D \end{bmatrix} \quad \mathbf{V} = \begin{bmatrix} V_R & 0 \\ 0 & V_D \end{bmatrix}. \tag{17}$$

When the coefficient vector estimated by removing a group of observations indicated by D is expressed as $\hat{\beta}_{(-D)}$, the logistic regression model's predicted values are computed by Equation (18).

$$\hat{\pi}_{i(-D)} = \frac{\exp(x_i' \hat{\beta}_{(-D)})}{1 + \exp(x_i' \hat{\beta}_{(-D)})} \quad i = 1, 2, \dots, n \tag{18}$$

Equations (19) and (20) are used to express the variances and leverage values depending on the removal of the outlier group from the set of data.

$$v_{i(-D)} = \hat{\pi}_{i(-D)}(1 - \hat{\pi}_{i(-D)}) \tag{19}$$

$$h_{ii(-D)} = \hat{\pi}_{i(-D)}(1 - \hat{\pi}_{i(-D)}) \mathbf{x}_i^T (\mathbf{X}_R^T \mathbf{V}_R \mathbf{X}_R)^{-1} \mathbf{x}_i \tag{20}$$

Based on the idea that in linear regression, internal residuals (for observations utilized in the regression model's estimation) and external residuals (for observations not used in the estimation of the regression model) cannot be measured on a similar scale, Hadi and Simonoff (1993) proposed the use of a new set of scaled residuals. Equation (21) represents the scaled residual group for the observation clusters indicated by R and D .

$$t_i^* = \begin{cases} \frac{y_i - x_i^T \hat{\beta}_{(-D)}}{\hat{\sigma}_R \sqrt{1 - x_i^T (X_R^T V_R X_R)^{-1} x_i}} & i \in R \\ \frac{y_i - x_i^T \hat{\beta}_{(-D)}}{\hat{\sigma}_R \sqrt{1 + x_i^T (X_R^T V_R X_R)^{-1} x_i}} & i \in D \end{cases} \quad (21)$$

Here, $\hat{\sigma}_R$ is the estimated value of σ calculated from the remaining observations in the dataset. Hadi and Simonoff's (1993) multiple outlier diagnostic measure (Equation 21) was defined as the GSPR (Equation 22) for logistic regression using the linear regression similarity approach.

$$r_{gspr}^{(-D)} = \begin{cases} \frac{y_i - \hat{\pi}_{i(-D)}}{\sqrt{v_{i(-D)}(1 - h_{ii(-D)})}} & i \in R \\ \frac{y_i - \hat{\pi}_{i(-D)}}{\sqrt{v_{i(-D)}(1 + h_{ii(-D)})}} & i \in D \end{cases} \quad (22)$$

An observation is an outlier if its $|GSPR|$ value is quite large (3 or more) (Imon ve Hadi, 2008). The selection of the observation set to be extracted from the dataset is the most crucial step in the calculation of the GSPR diagnostic measure (Imon and Hadi, 2008). For detecting multiple outliers, the initial set of elimination D of GSPR will be incorrect if the initial elimination set D does not contain all suspicious observations and some outliers remain in set R . For initial diagnosis, Imon and Hadi (2008) advised using robust diagnostics of LMS, LTS, BACON, or BOFOLS.

2.3.2. Deviation components-DEVC

DEVC is a multiple outlier diagnostic measure developed by Ahmad et al. (2011) to identify more than one outlier in logistic regression. The DEVC diagnostic measure was developed based on the components of the deviation residuals (Equation 12). Given that $Y_i =$

$\pi(x_i) + \varepsilon_i$, represents a logistic regression model for $i = 1, 2, \dots, n$, the probability value can be expressed as,

$$\pi(x_i) = \frac{\exp(x_i' \beta)}{1 + \exp(x_i' \beta)} \quad i = 1, 2, \dots, n. \tag{23}$$

Here β is a $(1 \times p)$ dimensional vector of coefficients for $p=k+1$ with k being the number of regressors, x is an $n \times p$ dimensional argument matrix and ε_i is an error vector with $(n \times 1)$ dimension. The functions of likelihood and log-likelihood for estimating the parameter β are represented by the Equation (24) and Equation (25).

$$L(\beta; y) = \prod_{i=1}^n \pi_i^{y_i} (1 - \pi_i)^{1-y_i} \tag{24}$$

$$l(\beta; y) = \log L(\beta; y) = \sum_{i=1}^n [y_i \log \pi_i + (1 - y_i) \log(1 - \pi_i)] \tag{25}$$

The deviation statistic (DEV) is used in logistic regression to assess how well the overall model fits the data. By squaring the deviation residuals, the equation for the DEV diagnostic measure is also represented as Equation (26).

$$DEV = \sum_{i=1}^n (r_{Di})^2 = \sum_{i=1}^n 2 \left[y_i \log \frac{y_i}{\hat{\pi}_i} + (1 - y_i) \log \left(\frac{1-y_i}{1-\hat{\pi}_i} \right) \right]. \tag{26}$$

Here $i=1, 2, \dots, n$ and $\hat{\pi}_i$, is the predictive values for the i th observation and r_{Di} is the deviance residuals. The deviation residual for the i th observation is also expressed as follows:

$$DR = r_{Di} = d(y_i, \hat{\pi}_i) = \pm \sqrt{-2 \log \left(\frac{y_i}{\hat{\pi}_i} \right) + (1 - y_i) \log \left(\frac{1-y_i}{1-\hat{\pi}_i} \right)} \tag{27}$$

This equation yields $r_{Di} = -\sqrt{-2|\log(1 - \hat{\pi}_i)|}$ for $y_i = 0$ and $r_{Di} = \sqrt{-2|\log \hat{\pi}_i|}$ for $y_i = 1$. If the absolute residual value of the observation is greater than 2, it is considered an outlier. DEVC diagnostic measure as a component of DR is expressed by Equation (28),

$$DEVC = dc_i = \begin{cases} 2 \log \left(\frac{1}{1-\hat{\pi}_i} \right), & y_i = 0 \\ 2 \log \left(\frac{1}{\hat{\pi}_i} \right), & y_i = 1 \end{cases} \tag{28}$$

DEVC is a practical measure that excludes negative values. The DEVC threshold value is determined as (Ahmad et al., 2011),

$$dc_i > \text{medyan}(dc_i) + 3MAD(dc_i). \tag{29}$$

3. Using Logistic Regression Diagnostic Measures on a Dataset

GSPR and DEVC diagnostic measures are compared with classical diagnostics based on the original Brown dataset or modified Brown dataset in this section.

A value of $y=0$ for the dependent variable LNI (lymph node involvement) in the original Brown (1980) dataset represents that the patient-experienced lymph node involvement (LNI), while a value of $y = 1$ represents that the patient did not experience LNI. The original dataset consisted of five regressors and included a single suspicious observation (observation 24) (Norazan et al., 2012). In this study, DEVC's performance was evaluated using the original Brown dataset, while GSPR's performance was evaluated using the modified Brown dataset. The datasets are shown in Tables 1 and 2.

Table 1. Original dataset by Brown (1980) with two regressors

Index	LNI	AP	AGE	Index	LNI	AP	AGE	Index	LNI	AP	AGE
1	0	0.48	66	20	0	0.98	56	39	0	0.76	53
2	0	0.56	68	21	0	0.52	67	40	0	0.95	67
3	0	0.5	66	22	0	0.75	63	41	0	0.66	53
4	0	0.52	56	23	1	0.99	59	42	1	0.84	65
5	0	0.5	58	24	0	1.87	64	43	1	0.81	50
6	0	0.49	60	25	1	1.36	61	44	1	0.76	60
7	0	0.46	65	26	1	0.82	56	45	1	0.7	45
8	0	0.62	60	27	0	0.4	64	46	1	0.78	56
9	1	0.56	50	28	0	0.5	61	47	1	0.7	46
10	0	0.55	49	29	0	0.5	64	48	1	0.67	67
11	0	0.62	61	30	0	0.4	63	49	1	0.82	63
12	0	0.71	58	31	0	0.55	52	50	1	0.67	57
13	0	0.65	51	32	0	0.59	66	51	1	0.72	51
14	1	0.67	67	33	1	0.48	58	52	1	0.89	64
15	0	0.47	67	34	1	0.51	57	53	1	1.26	68
16	0	0.49	51	35	1	0.49	65				
17	0	0.5	56	36	0	0.48	65				
18	0	0.78	60	37	0	0.63	59				
19	0	0.83	52	38	0	1.02	61				

Note: LNI: Lymph node involvement, AP: Acid phosphate level, AGE: Patient's age

The dataset in Table 2 is Brown's (1980) with two outliers added to the dataset. Values 24, 54, and 55 in the dataset are outliers.

Table 1. Modified Brown dataset of Imon and Hadi (2008)

Index	LNI	AP	Index	LNI	AP	Index	LNI	AP
1	0	48	20	0	98	39	0	76

2	0	56	21	0	52	40	0	95
3	0	50	22	0	75	41	0	66
4	0	52	23	1	99	42	1	84
5	0	50	24	0	187	43	1	81
6	0	49	25	1	136	44	1	76
7	0	46	26	1	82	45	1	70
8	0	62	27	0	40	46	1	78
9	1	56	28	0	50	47	1	70
10	0	55	29	0	50	48	1	67
11	0	62	30	0	40	49	1	82
12	0	71	31	0	55	50	1	67
13	0	65	32	0	59	51	1	72
14	1	67	33	1	48	52	1	89
15	0	47	34	1	51	53	1	126
16	0	49	35	1	49	54	0	200
17	0	50	36	0	48	55	0	220
18	0	78	37	0	63			
19	0	83	38	0	102			

Note: LNI: Lymph node involvement, AP: Acid phosphate level

3.1. Generalized standardized Pearson residuals -GSPR

On the modified Brown dataset (Table 2), the GSPR diagnostic measure was compared to the traditional diagnostic measures DR, PR, and SPR. Table 3 provides the comparison results.

Table 3. Comparison of GSPR with DR, PR, and SPR outlier diagnostics using Imon and Hadi's modified Brown dataset (2008)

Threshold	±2	±2	±2	3		±2	±2	±2	3
Index	DR	PR	SPR	GSPR	Index	DR	PR	SPR	GSPR
1	-0,92	-0,72	-0,73	-0,50	29	-0,92	-0,72	-0,73	-0,53
2	-0,93	-0,73	-0,74	-0,61	30	-0,91	-0,71	-0,72	-0,42
3	-0,92	-0,72	-0,73	-0,53	31	-0,93	-0,73	-0,74	-0,59
4	-0,92	-0,73	-0,74	-0,55	32	-0,93	-0,74	-0,74	-0,65
5	-0,92	-0,72	-0,73	-0,53	33	1,46	1,38	1,40	2,05
6	-0,92	-0,72	-0,73	-0,52	34	1,46	1,38	1,40	1,91
7	-0,91	-0,72	-0,73	-0,48	35	1,46	1,38	1,40	2,01
8	-0,93	-0,74	-0,75	-0,70	36	-0,92	-0,72	-0,73	-0,50
9	1,45	1,37	1,38	1,69	37	-0,94	-0,74	-0,75	-0,71
10	-0,93	-0,73	-0,74	-0,59	38	-0,99	-0,79	-0,80	-1,85
11	-0,93	-0,74	-0,75	-0,70	39	-0,95	-0,76	-0,76	-0,97
12	-0,95	-0,75	-0,76	-0,86	40	-0,98	-0,78	-0,79	-1,56
13	-0,94	-0,74	-0,75	-0,75	41	-0,94	-0,74	-0,75	-0,77
14	1,43	1,34	1,35	1,30	42	1,41	1,30	1,32	0,89
15	-0,92	-0,72	-0,73	-0,49	43	1,41	1,31	1,32	0,95
16	-0,92	-0,72	-0,73	-0,52	44	1,42	1,32	1,33	1,06
17	-0,92	-0,72	-0,73	-0,53	45	1,43	1,33	1,35	1,22
18	-0,95	-0,76	-0,77	-1,02	46	1,42	1,32	1,33	1,01
19	-0,96	-0,77	-0,77	-1,15	47	1,43	1,33	1,35	1,22
20	-0,98	-0,79	-0,80	-1,68	48	1,43	1,34	1,35	1,30

21	-0,92	-0,73	-0,74	-0,55	49	1,41	1,31	1,32	0,93
22	-0,95	-0,76	-0,76	-0,95	50	1,43	1,34	1,35	1,30
23	1,39	1,27	1,29	0,63	51	1,43	1,33	1,34	1,16
24	-1,10	-0,91	-1,02	-12,87	52	1,40	1,29	1,31	0,79
25	1,33	1,19	1,24	0,27	53	1,35	1,21	1,25	0,34
26	1,41	1,31	1,32	0,93	54	-1,12	-0,93	-1,07	-17,56
27	-0,91	-0,71	-0,72	-0,42	55	-1,15	-0,97	-1,16	-28,23
28	-0,92	-0,72	-0,73	-0,53					

When the GSPR values in Table 3 are examined, the absolute values of the 24th, 54th, and 55th observations are found to be greater than the threshold value of 3. Outliers for threshold value 2 could not be identified when the DR, PR, and SPR results were examined. These observations have been subjected to the masking effect. Figure 1 shows index graphs for the analyzed outlier diagnostic measures. A line on the graph represents the threshold value for each diagnostic measure.

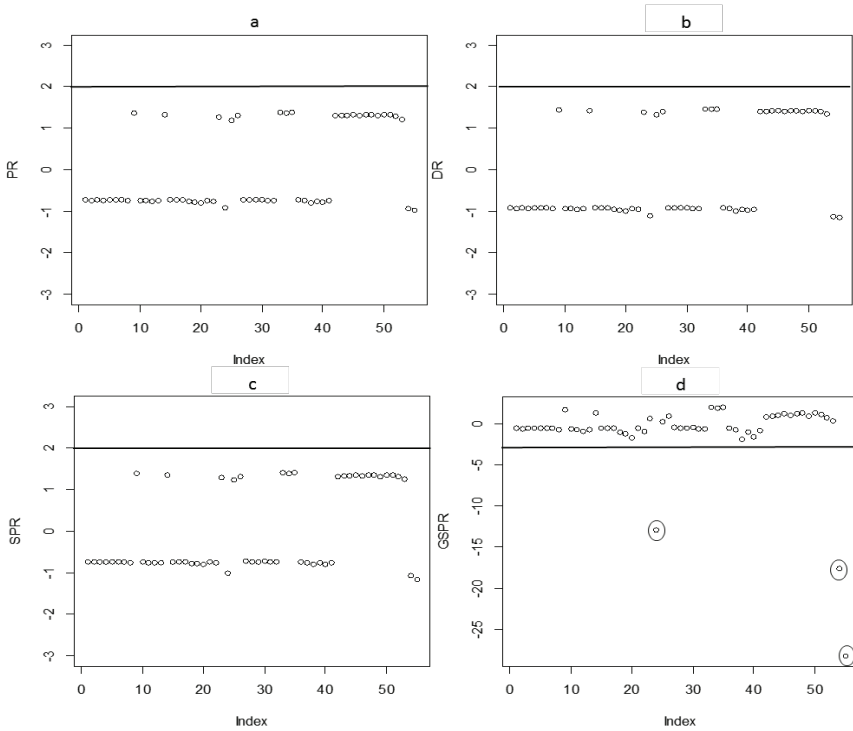


Figure 1. Index graphs for (a) PR, (b) DR, (c) SPR, and (d) GSPR diagnostic measures

3.2. Deviation components -DEVC

Based on the original Brown dataset, DEVC (Ahmad et al., 2011) performance was compared to PR, DR, SPR, and SDR diagnostic measures. Table 4 shows the results of the diagnostic measures.

Table 4. Outlier diagnostic measures DEVC and PR, DR, SPR, and SDR based on the original Brown (1980) dataset with two regressors

Threshold	±2	±2	±2	±2	3,11		±2	±2	±2	±2	3,11
Index	PR	DR	SPR	SDR	DEVC	Index	PR	DR	SPR	SDR	DEVC
1	-0,51	-0,67	-0,52	-0,69	0,45	29	-0,55	-0,72	-0,56	-0,74	0,52
2	-0,52	-0,69	-0,54	-0,71	0,48	30	-0,50	-0,67	-0,52	-0,69	0,45
3	-0,52	-0,69	-0,53	-0,70	0,47	31	-0,81	-1,00	-0,83	-1,03	1,00
4	-0,70	-0,89	-0,71	-0,91	0,80	32	-0,57	-0,75	-0,58	-0,77	0,56
5	-0,65	-0,84	-0,66	-0,85	0,70	33	1,58	1,58	1,61	1,61	2,50
6	-0,60	-0,79	-0,61	-0,80	0,62	34	1,49	1,53	1,51	1,55	2,33
7	-0,51	-0,68	-0,52	-0,69	0,46	35	1,90	1,75	1,95	1,79	3,06
8	-0,69	-0,89	-0,70	-0,90	0,79	36	-0,52	-0,69	-0,53	-0,71	0,48
9	1,16	1,30	1,20	1,35	1,70	37	-0,72	-0,92	-0,73	-0,93	0,84
10	-0,88	-1,07	-0,92	-1,12	1,15	38	-1,04	-1,21	-1,07	-1,25	1,46
11	-0,68	-0,87	-0,68	-0,88	0,75	39	-0,98	-1,16	-1,01	-1,19	1,35
12	-0,81	-1,00	-0,82	-1,01	1,01	40	-0,81	-1,01	-0,84	-1,05	1,01
13	-0,92	-1,11	-0,95	-1,14	1,24	41	-0,88	-1,07	-0,90	-1,10	1,15
14	1,66	1,63	1,70	1,67	2,65	42	1,31	1,41	1,34	1,45	2,00
15	-0,49	-0,65	-0,50	-0,67	0,42	43	0,89	1,08	0,92	1,12	1,16
16	-0,78	-0,97	-0,81	-1,01	0,95	44	1,24	1,36	1,25	1,38	1,86
17	-0,68	-0,88	-0,70	-0,89	0,77	45	0,87	1,06	0,93	1,13	1,12
18	-0,82	-1,02	-0,83	-1,03	1,04	46	1,08	1,25	1,10	1,26	1,55
19	-1,09	-1,25	-1,12	-1,29	1,57	47	0,89	1,08	0,95	1,15	1,17
20	-1,14	-1,29	-1,18	-1,33	1,67	48	1,66	1,63	1,70	1,67	2,65
21	-0,51	-0,68	-0,53	-0,70	0,47	49	1,26	1,38	1,29	1,41	1,91
22	-0,73	0,93	-0,74	-0,94	0,86	50	1,25	1,37	1,27	1,39	1,89
23	0,94	1,13	0,97	1,16	1,27	51	1,00	1,18	1,03	1,22	1,39
24	-2,36	-1,94	-2,80	-2,30	3,77	52	1,21	1,34	1,24	1,37	1,80
25	0,67	0,86	0,73	0,94	0,74	53	0,91	1,10	1,00	1,21	1,21
26	1,04	1,21	1,06	1,23	1,46						
27	-0,49	-0,66	-0,50	-0,67	0,43						
28	-0,59	-0,78	-0,60	-0,79	0,60						

The multiple outlier diagnostic measure DEVC correctly identified observation 24 in Table 4 with a threshold value of 3.11. The diagnostic measures PR, SPR, and SDR for the diagnosis of a single outlier (Agresti, 2015; Christensen, 1997) correctly diagnosed the outlier

(observation 24) in the dataset as well. The DR diagnostic measure failed to determine this observation for the ± 2 threshold value. Figure 2 depicts the index graphs for these diagnostic measures.

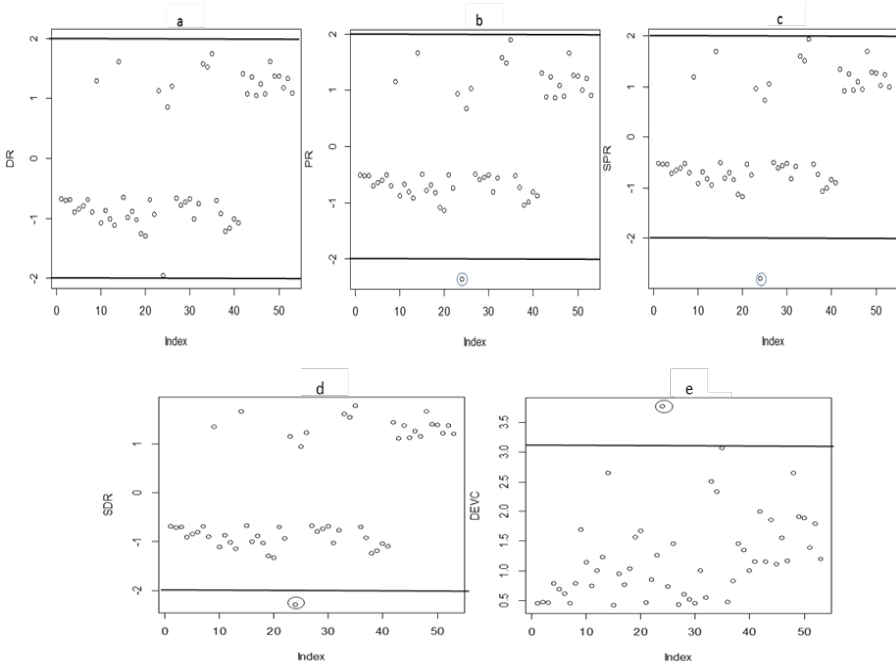


Figure 2. Index graphs for diagnostic measures (a) DR, (b) PR and (c) SPR (d) SDR and (e) DEVC

4. Simulation Study

4.1. Simulation scenario

Various sample sizes as $n=20, 30, 50, 100,$ and 1000 were used for simulation. Logistic regression models with single-, two-, and five-regressors were used in simulation studies. The regressors in the logistic regression model are derived from the normal distribution $N(0,1)$. The regression coefficients in the model are set to; $\beta_0 = 1$ and $\beta_1 = 2$ for a single-regressor model; $\beta_0 = 1, \beta_1 = 2,$ and $\beta_2 = 2$ for a two-regressor model; and $\beta_0 = 1, \beta_1 = 2, \beta_2 = 2, \beta_3 = 2, \beta_4 = 2,$ and $\beta_5 = 2$ for a five-regressor model. To satisfy the equation, the dependent variable values are derived by obtaining probability values from the equation $\pi(x) = \frac{e^{\beta_0 + \beta_1 x}}{1 + e^{\beta_0 + \beta_1 x}}$ (Norazan et al., 2012; Kordzakhia, Mishra ve Reiersolmoen, 2001).

$$y_i = \begin{cases} \beta_0 + \beta_1 x_1 + \dots + \beta_k x_k + \varepsilon_i < 0 & \text{ise } 0 \\ \beta_0 + \beta_1 x_1 + \dots + \beta_k x_k + \varepsilon_i \geq 0 & \text{ise } 1 \end{cases} \quad i = 1, 2, \dots, n$$

(30)

Contamination rates of 0,10, 0.20, and 0.30 were used to create contaminated sample sizes. Taking into account the contamination rates, it is assured that the set of contaminated values is generated at random in the samples. The contaminated regressor values were used as 4σ for mild outliers and 7σ for extreme outliers. The y values corresponding to the contaminated observations were changed to 1 and 0 in the simulation for the outlier (Nurunnabi et al., 2010). The correct diagnosis rate (CDR) was calculated the number of outliers correctly determined divided by the total number of outliers in the dataset. The swamping rate (SR) was calculated the number of observations incorrectly diagnosed as the outlier divided by the total number of non-outliers in the dataset. 1000 replications were used for each combination of sample size and contamination rate.

For the DEVC diagnostic measure, a different scenario has been prepared. The simulation scenario of Norazan et al. (2012) was used for the DEVC simulation. The regressors are derived from the normal distribution $x_i \sim N(0,1)$, and the errors are derived from the logistic distribution $\varepsilon_i \sim \Lambda(0,1)$. The dependent variable is derived by using Eq. (30).

The study of Ahmad et al. (2011) was used for the contamination rates and sample sizes of DEVC. The DEVC sample sizes were $n=40, 60, 80, 100,$ and $200,$ and the pollution rates were $0.05, 0.10,$ and $0.15.$ However, a contamination rate of 0.20 is also included in this simulation to examine how the results will behave at heavy contamination.

4.2. Simulation Results

4.2.1. GSPR results

A simulation study with a single regressor contaminated in each model was performed for the GSPR diagnostic measure for a logistic regression model with single, two, and five regressors. Table 5 shows the simulation results for datasets contaminated with extreme outliers for different sample sizes and combinations of contamination rates. Table 6 shows the simulation results in which the datasets were contaminated by mild outliers.

Table 5. Simulation results with an extreme outlier in the single-regressor for the GSPR diagnostic measure

n	CR (%)	Single regressor		Two regressors		Five regressors	
		CDR	SR	CDR	SR	CDR	SR
20	10	1,00	0,00	0,95	0,00	0,81	0,00
	20	0,99	0,00	0,94	0,00	0,75	0,00
	30	0,98	0,00	0,93	0,00	0,71	0,00
30	10	1,00	0,01	0,99	0,00	0,89	0,00
	20	1,00	0,01	0,98	0,00	0,87	0,00
	30	1,00	0,01	0,97	0,00	0,83	0,00
50	10	1,00	0,01	1,00	0,01	0,95	0,00
	20	1,00	0,01	1,00	0,01	0,95	0,00
	30	1,00	0,01	0,99	0,01	0,93	0,00
100	10	1,00	0,01	1,00	0,01	0,99	0,01
	20	1,00	0,01	1,00	0,01	0,98	0,00
	30	1,00	0,01	1,00	0,01	0,98	0,00
1000	10	1,00	0,01	1,00	0,02	1,00	0,01
	20	1,00	0,01	1,00	0,02	1,00	0,01
	30	1,00	0,01	1,00	0,02	1,00	0,01

Note: **CR**: Contamination rate; **CDR**: Correct diagnostic rate; **SR**: Swamping rate

According to Table 5, for the single-regressor model, the correct diagnosis rate of GSPR increases compared to small samples ($n=20$ and $n=30$) as the sample size increases. Meanwhile, as sample size increases, swamping rates increase, and swamping rates decrease in small samples as the contamination rate increases.

Comparing simulation results for models with single, two, and five regressors shows that the GSPR measure performed better on the single-regressor model. Furthermore, for $n = 20, 30, 50,$ and 100 , the swamping rate declines as the number of regressors increases.

Table 6. Simulation results with a mild outlier in the single-regressor for the GSPR diagnostic measure

n	CR (%)	Single regressor		Two regressors		Five regressors	
		CDR	SR	CDR	SR	CDR	SR
20	10	0,98	0,00	0,88	0,00	0,68	0,00
	20	0,97	0,00	0,86	0,00	0,64	0,00
	30	0,96	0,00	0,86	0,00	0,59	0,00
30	10	0,99	0,01	0,94	0,00	0,77	0,00
	20	0,99	0,01	0,93	0,00	0,74	0,00

	30	0,99	0,01	0,91	0,00	0,71	0,00
50	10	1,00	0,01	0,96	0,01	0,84	0,00
	20	1,00	0,01	0,96	0,01	0,83	0,00
	30	1,00	0,01	0,95	0,01	0,82	0,00
100	10	1,00	0,01	0,98	0,01	0,91	0,01
	20	1,00	0,01	0,98	0,01	0,89	0,00
	30	1,00	0,01	0,98	0,01	0,88	0,00
1000	10	1,00	0,01	0,99	0,02	0,93	0,01
	20	1,00	0,01	0,99	0,02	0,93	0,01
	30	1,00	0,01	0,99	0,02	0,93	0,01

Table 6 shows that the correct diagnosis rate of the GSPR and the rate of swamping increases as the sample size increases for the single regressor model in the presence of the mild outlier in the dataset. The swamping rate declines as the contamination rate increases for each combination of sample size and contamination rate.

When the simulation results of all models are compared, the single-regressor model outperforms both models in terms of the correct diagnosis rate of the GSPR. In all sample sizes, except for 500, the swamping rate of the GSPR declines as the number of regressors increases. For $n=1000$, the GSPR's swamping rate is highest in the two-regressors model.

Tables 5 and 6 show that GSPR's correct diagnostic rate is greater than the other measures when the dataset contains extreme outliers.

4.2.2. DEVC results

Unlike other simulation scenarios, the sample sizes and contamination rates for this diagnosis measure are derived from Ahmad et al. (2011). Table 7 provides simulation results for the DEVC measure in the presence of extreme outliers. The simulation results for the dataset with mild outliers are shown in Table 8.

Table 7 indicates that the DEVC measure performs best with small sample size and low contamination rate. Simulation results for the single-regressor model show that as the sample size increases, the rate of correct diagnosis of DEVC declines, while the rate of swamping increases.

The DEVC measure performs best when there are five regressors when the simulation results of the single regressor model and the other models are compared. Despite similarities between the swamping rates

for models with one and two regressors, the DEVC's swamping rate decreases as the number of regressors increases.

Table 7. Simulation results with an extreme outlier in the single-regressor for the DEVC diagnostic measure

n	CR (%)	Single regressor		Two regressors		Five regressors	
		CDR	SR	CDR	SR	CDR	SR
40	5	0,87	0,14	0,87	0,13	0,98	0,09
	10	0,60	0,14	0,61	0,14	0,78	0,08
	15	0,46	0,15	0,46	0,15	0,56	0,09
	20	0,36	0,16	0,37	0,16	0,41	0,09
60	5	0,80	0,15	0,81	0,15	0,94	0,11
	10	0,58	0,16	0,58	0,16	0,72	0,11
	15	0,46	0,17	0,45	0,17	0,53	0,11
	20	0,38	0,18	0,38	0,17	0,41	0,12
80	5	0,78	0,17	0,77	0,16	0,90	0,12
	10	0,57	0,17	0,57	0,17	0,68	0,13
	15	0,45	0,18	0,45	0,18	0,51	0,13
	20	0,39	0,19	0,39	0,19	0,41	0,14
100	5	0,76	0,17	0,76	0,17	0,88	0,14
	10	0,56	0,18	0,57	0,18	0,66	0,14
	15	0,46	0,19	0,46	0,19	0,51	0,15
	20	0,39	0,20	0,39	0,20	0,41	0,15
200	5	0,72	0,20	0,73	0,20	0,81	0,17
	10	0,56	0,22	0,56	0,22	0,61	0,18
	15	0,47	0,22	0,47	0,22	0,50	0,19
	20	0,42	0,23	0,41	0,23	0,42	0,20

Table 8. Simulation results with a mild outlier in the single-regressor for the DEVC measure

n	CR (%)	Single regressor		Two regressors		Five regressors	
		CDR	SR	CDR	SR	CDR	SR
40	5	0,90	0,21	0,91	0,21	0,97	0,16
	10	0,72	0,22	0,74	0,22	0,78	0,17
	15	0,61	0,23	0,62	0,23	0,63	0,19
	20	0,52	0,24	0,54	0,24	0,53	0,20
60	5	0,86	0,23	0,87	0,23	0,93	0,20
	10	0,72	0,24	0,71	0,25	0,76	0,22
	15	0,61	0,25	0,61	0,25	0,63	0,23
	20	0,53	0,26	0,54	0,26	0,55	0,24
80	5	0,86	0,25	0,87	0,25	0,90	0,22
	10	0,71	0,26	0,71	0,26	0,74	0,25

	15	0,61	0,26	0,61	0,27	0,62	0,25
	20	0,55	0,27	0,55	0,27	0,54	0,26
100	5	0,85	0,26	0,85	0,26	0,89	0,25
	10	0,71	0,27	0,71	0,27	0,73	0,26
	15	0,62	0,28	0,62	0,28	0,63	0,27
	20	0,55	0,27	0,54	0,28	0,55	0,27
200	5	0,84	0,29	0,85	0,29	0,86	0,29
	10	0,71	0,29	0,72	0,29	0,72	0,30
	15	0,62	0,29	0,63	0,29	0,63	0,30
	20	0,55	0,28	0,56	0,29	0,56	0,30

Table 8 shows that the DEVC measure performs better when there are mild outliers and more regressors. The rate of correct DEVC diagnosis declines as sample size and contamination rate for the single-regressor logistic regression model increase, while the rate of swamping increases. The performance of the DEVC measure improves as the number of regressors increases, and the swamping rate decreases in all sample sizes except $n = 200$, according to the simulation findings for the two- and five-regressor models. The DEVC measure is useful for small sample sizes and low contamination rates for models with one, two, and five regressors when comparing simulation results.

Comparing Tables 7 and 8 reveals in the presence of mild outliers in the data, the rate of correct diagnosis of the DEVC measure is greater.

5. Discussion

This study compared single and multiple outliers diagnostic measures to identify outliers in the logistic regression model. In addition, the performance of multiple outliers diagnostic measures was evaluated by the simulation study. The results of diagnostic measures whose performance is assessed by various simulation scenarios—wherein a single regressor is contaminated first and later all regressors are contaminated—are provided.

Using the modified Brown dataset of Imon and Hadi (2008), the performance of GSPR, a multiple outlier diagnostic measure for logistic regression, was compared with DR, PR, and SPR single outlier diagnostic measures. In contrast to the GSPR diagnostic measure, which successfully identified all outliers in the dataset, the DR, PR, and SPR diagnostic measures were found to mask outliers and hence failed to diagnose. Outliers in the GSPR are also more suited for graphical representation as compared to other diagnostic measures since they take larger values. Imon and Hadi (2008) obtained the same results in their study comparing GSPR with PR and SPR measures,

Using the original Brown dataset (1980) with two regressors, another multiple outlier diagnostic measure, DEVC (Ahmad et al., 2011),

was compared to the diagnostic measures PR, DR, SPR, and SDR developed for the identification of a single outlier. The diagnostic measures DEVC, PR, SPR, and SDR accurately identified the outlier in the dataset for the ± 2 threshold value. According to Agresti (2015), observations that are greater than the threshold values of ± 2 and ± 3 for traditional logistic regression diagnostic measures PR, DR, SPR, and SDR are outliers. Ahmad et al. (2011) found that DEVC performs better than other diagnostic measures when there are multiple outliers. Ahmad et al. (2011), in his study comparing DEVC and PR, DR, SPR, SDR diagnostic measures over different datasets for the threshold value of ± 3 , concluded that, unlike this study, traditional diagnostic measures were exposed to the masking effect and could not diagnose the outlier.

As sample size increases, the correct diagnosis rate and swamping rate of the multiple outlier diagnostic measure GSPR increase, according to simulation findings when the single regressor is contaminated. The rate of correct diagnosis and swamping of this diagnostic measure declines as the number of regressors increases. GSPR performs best when there are extreme outliers in the dataset and a single regressor model. According to the simulation findings, where all regressors were contaminated, it was observed that as the number of regressors increased, both in the case where the datasets were contaminated by mild and extreme outliers, the rate of correct diagnosis of GSPR increased and the swamping rate decreased. The GSPR diagnostic measure performs better in the presence of extreme outliers and in the five-regressor model where all the regressors were contaminated. According to Midi and Ariffin (2013), if the observations to be extracted from the dataset are correctly determined at the beginning of the analysis, the GSPR is the most effective measure recently developed for determining outliers in a logistic regression model.

The findings of the simulation study where the single regressor is contaminated show that the rate of correct diagnosis of DEVC, another measure of multiple outliers, decreases as the sample size and contamination rate increase, while the rate of swamping increases. As the number of regressors increases, the performance of the DEVC measure increases and the swamping rate declines. It can be said that the DEVC diagnostic measure is successful with a small sample size and low contamination rates. This diagnostic measure gives similar results for the simulation scenario in which all regressors are contaminated. Ahmad et al. (2011) compared DEVC with PR, DR, SPR, and SDR diagnostic measures in a simulation study for two regressor models. According to the results of their study, DEVC outperforms than other diagnostic measures in diagnosing all suspicious observations and multiple outliers. Unlike the results of Ahmad et al. (2011), Norazan et al. (2012) found

that RobDEVC and DEVC failed to identify all suspicious observations in a study comparing the diagnostic measure with a similar simulation scenario.

When GSPR and DEVC multiple outlier diagnostic measures are compared, the accuracy diagnosis rates of diagnostic measures increase as the number of regressors increases, and GSPR shows the best performance when regressors are contaminated by extreme outliers and DEVC when they are contaminated by mild outliers. The rate of correct diagnosis for both diagnostic tools increases as the number of regressors increase. The GSPR measure takes values close to 1 for both extreme and mild outliers except $n = 20$ sample size for this simulation scenario and outperforms than the DEVC. Its swamping rate was also found to be lower.

REFERENCES

- Agresti, A, 2015, *Foundations of Linear and Generalized Linear Models*, John Wiley & Sons.
- Ahmad, S, Ramli, N, M, Midi, H, 2010, Robust estimators in logistic regression: a comparative simulation study, *Journal of Modern Applied Statistical Methods*, 9, 2, 502-511.
- Ahmad, S, Midi, H, Ramli, N, M, 2011, Diagnostics for residual outliers using deviance component in binary logistic regression, *World Applied Sciences Journal*, 14, 8, 1125-1130.
- Ahmad, S, Ramli, N, M, Midi, H, 2012, Outlier detection in logistic regression and its application in medical data analysis, In *Humanities, Science and Engineering*, 503-507.
- Belsley D, A, Kuh E, Welsch R, E, 1980, *Regression Diagnostics: Identifying Influential Data and Sources of Collinearity*, New York: John Wiley & Sons.
- Brown, B, W, Jr, 1980, Prediction analysis for binary data, In: Miller, R, G, Jr, Efron, B, Brown, B, W, Jr, Moses, L, E, eds, *Biostatistics Casebook*, New York: Wiley.
- Christensen, R, 1997, *Log-Linear Models*, Springer Science & Business Media.
- Collet, D, 2003, *Modeling Binary Data*, Chapman & Hall.
- Cook, R, D, Weisberg, S, 1999, Graphs in statistical analyses: Is the medium the message? *The American Statistician* 53, 29–37.
- Cordeiro, G, M, 2004, On Pearson's residuals in generalized linear models, *Statistics and Probability Letters*, 66, 213-219.
- Hilbe, J, M, 2009, *Logistic Regression Models*, CRC Press.
- Hoaglin, D, C, Welsch, R, E, 1978, The hat matrix in regression and ANOVA, *The American Statistician*, 32, 1, 17-22.
- Hosmer, D, W, Lemeshow, S, 1980, Goodness of fit tests for the multiple logistic regression model, *Communications in statistics-Theory and Methods*, 9, 10, 1043-1069.
- Hosmer, D, W, Lemeshow, S, Sturdivant, R, X, 2013, *Applied Logistic Regression*, Third Edition, John Wiley & Sons.
- Imon, A, H, M, R, Hadi, A, S, 2008, Identification of multiple outliers in logistic regression, *Communications in Statistics-Theory and Methods*, 37, 11, 1697-1709.
- Jennings, D, E, 1986, Outliers and residual distributions in logistic regression, *Journal of the American Statistical Association*, 81, 396, 987-990.
- Kordzakhia, N, Mishra, G, D, Reiersølmoen, L, 2001, Robust estimation in the logistic regression model, *Journal of Statistical Planning and Inference*, 98, 1-2, 211-223.

- Long, S, J, 1997, Regression Models for Categorical and Limited Dependent Variables, Advanced Quantitative Techniques in The Social Sciences.
- Menard, S, 2002, Applied Logistic Regression Analysis, Second Edition, Sage Publications.
- Midi, H, Ariffin, S, B, 2013, Modified standardized Pearson residual for the identification of outliers in logistic regression model, Journal of Applied Sciences.
- Norazan, M, Sanizah, A, Habshah, M, 2012, Identifying bad leverage points in logistic regression model based on robust deviance components, 62-67.
- Nurunnabi, A, A, M, Nasser, M, 2009, Outlier diagnostics in logistic regression: a supervised learning technique, In Proceedings of International Conference on Machine Learning and Computing, 3, 90-95.
- Nurunnabi, A, A, M, Imon, A, H, M, R, Nasser, M, 2010, Identification of multiple influential observations in logistic regression, Journal of Applied Statistics, 37, 10, 1605-1624.
- Nurunnabi, A, A, M, Nasser, M, Imon, A, H, M, R, 2016, Identification and classification of multiple outliers, high leverage points and influential observations in linear regression, Journal of Applied Statistics, 43, 3, 509-525.
- Pregibon, D, 1981, Logistic regression diagnostics, The Annals of Statistics, 705-724.
- Rawlings, J, O, Pantula, S, G, Dickey D, A, 1998, Applied Regression Analysis; A Research Tool, Springer-Verlag, New York.
- Salsas, P, Guillen, M, Alemany, R, 1999, Perfect value and outlier detection in logistic binary choice models, Communications in Statistics-Theory and Methods, 28, 6, 1447-1460.
- Sarkar, S, K, Midi, H, Rana, M, 2011, Detection of outliers and influential observations in binary logistic regression: an empirical study, Journal of Applied Sciences, 11, 1, 26-35.



CHAPTER 3

UNIT ISHITA DISTRIBUTION WITH INFERENCE

*Hayrinisa DEMİRCİ BİÇER¹,
Cenker BİÇER²*

1 Assoc.Prof.Dr., Hayrinisa DEMİRCİ BİÇER, Kırıkkale Univ., Dep. of Statistics.
ORCID:0000-0002-1520-5004, hdbicer@kku.edu.tr

2 Assoc.Prof.Dr., Cenker BİÇER, Kırıkkale Univ., Dep. of Statistics. ORCID:
0000-0003-2222-3208, cbicer@kku.edu.tr.

INTRODUCTION

It is fair to say that it should be modeling the data compiled over the phenomena using the most appropriate or almost accurate models in order to draw correct conclusions from the analysis of the phenomena. The researchers have taken major attention to introducing more flexible probability distribution models by taking this fact into account. In general, the new distribution models introduced by adding extra parameters to the base distributions have a more flexible modeling performance than the base distributions. The support sets of most of these new distributions, which have been brought to the literature based on the base distribution transformation techniques, are the real line or the positive semi-real line. It is important to note, however, that the developments made in introducing probability distributions defined on the bounded interval hang behind those of distributions defined on the unbounded support sets.

Among the probability models represented on the bounded real line, the most popular distribution is the Beta distribution, which has a support set in the unit interval. For a long time, Beta distribution has been used as a model distribution in many branches of science from natural sciences to economics and engineering to health sciences since it has many beautiful features. Over time, a limited number of new distribution models have been proposed. These probability models are Topp-Leone model (Topp & Leone, 1955), the Kumaraswamy model (Kumaraswamy, 1980), unit gamma model (Grassia, 1977), log-Xgamma model (Altun & Hamedani, 2018), exponentiated Topp-Leone model (Pourdarvish et al., 2015), unit Lindley model (Mazucheli et al, 2019), log-Lindley model (Gómez-Déniz et al., 2014), unit Weibull model (Mazucheli et al., 2020), unit Burr - III model (Modi & Gill, 2020), unit inverse Gaussian model (Ghitany, et al., 2019), unit half normal model (Bakouch et al., 2021), and unit Teissier model (Krishna et al., 2022) by researchers who have studied the importance of introducing more flexible probability distribution models defined over the unit interval. In this context, the article derives a new and flexible probability model whose support set is the unit interval by considering the Ishita distribution as a base distribution.

We organize the remainder section of the paper as follows. The section "Unit Ishita Distribution" derives the UID. Basic properties of UID such as survival, hazard, reserved hazard, characteristic, and moment generating functions, and the distribution of its order statistics are investigated in section "Statistical Characteristics of the Unit Ishita Distribution". The "Inference" section investigates several estimators to estimate the UID's parameter. The section "Simulation Study" conducts comprehensive numerical studies to evaluate the performance of the

estimator obtained in the paper. The section "Conclusions" is concluded the work.

UNIT ISHTA DISTRIBUTION

Suppose X is a random variable from Ishita distribution with parameter $\theta > 0$. The probability density function (pdf) of X is given by

$$f(x, \theta) = \frac{\theta^3 e^{\theta(-x)}(\theta + x^2)}{\theta^3 + 2}, x > 0 \tag{1}$$

and the corresponding cumulative distribution function (cdf) is

$$F(x, \theta) = 1 - \frac{e^{-\theta x}(\theta^3 + \theta^2 x^2 + 2\theta x + 2)}{\theta^3 + 2}, \tag{2}$$

where θ is the shape parameter of the Ishita distribution. Ishita distribution was first introduced by the study of the Shanker (Shanker & Shukla, 2017). Fundamentally, the Ishita is a mixture probability model with two components, which are exponential(θ) and gamma(3 , θ) distributions. (Shanker & Shukla, 2017). Some specific statistical features of the distribution were also investigated by the authors. These features are figured in Table 1.

Table 1. Some statistical features of the Ishita distribution

Moment Generating Function $M_X(t)$	$\sum_{i=1}^n \frac{\theta^3 + (i + 1)(i + 2)}{\theta^3 + 2} \left(\frac{t}{\theta}\right)^i$
Expectation $E(X)$	$\frac{\theta^3 + 6}{\theta(\theta^3 + 2)}$
Variance $Var(X)$	$\frac{\theta^6 + 16\theta^3 + 12}{\theta^2(\theta^3 + 2)^2}$
Survival Function $S_X(x)$	$\frac{e^{-\theta x}(\theta^3 + \theta^2 x^2 + 2\theta x + 2)}{\theta^3 + 2}$
Hazard Function $H_X(x)$	$\frac{\theta^3(\theta + x^2)}{\theta^3 + \theta^2 x^2 + 2\theta x + 2}$

The pdf of the UID is derived from the conversion $Y = e^{-X}$ by considering the pdf of Ishita distribution given by the equation (1). We regularize its description by the Definition 1.

Definition 1. Suppose Y is a random variable from the UID with parameter θ . The pdf and the cdf of the UID are as follows:

$$f(y, \theta) = \frac{\theta^3 y^{\theta-1} (\theta + \ln^2(y))}{\theta^3 + 2}, 0 < y < 1 \tag{3}$$

and

$$F(y; \theta) = \frac{y^\theta (\theta^3 + \theta \ln(y) (\theta \ln(y) - 2) + 2)}{\theta^3 + 2}, 0 < y < 1 \tag{4}$$

respectively. We present the Figure 1 to illustrate the formal behavior of the pdf of the UID. As can be lucidly seen from Figure 1, UID is a possible probability distribution to model the left or right skewed data.

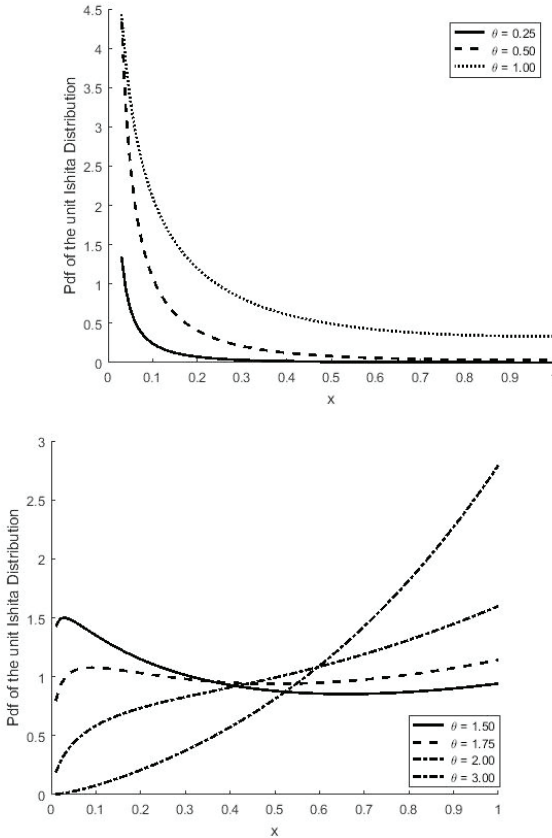


Figure 1. Pdf of the UID for different values of the parameter θ .

STATISTICAL CHARACTERISTICS OF UNIT ISTHITA DISTRIBUTION

This section of the study investigates some essential features of the UID, such as the survival, hazard rate, reserved hazard rate, characteristic,

and moment generating functions, and its first and second moments, variance, and the distribution of its order statistics.

Survival and Hazard Rate Functions

Let Y be a UID distributed random variable with parameters θ and $t \in (0,1)$. By these assumptions and considering the pdf (3) and the cdf (4), the survival function of the UID, say $S_Y(t; \theta)$, is given by

$$\begin{aligned}
 S_Y(t, \theta) &= 1 - F_Y(t, \theta) \\
 &= 1 - \frac{t^\theta(\theta^3 + \theta \ln(t)(\theta \ln(t) - 2) + 2)}{\theta^3 + 2}.
 \end{aligned}
 \tag{5}$$

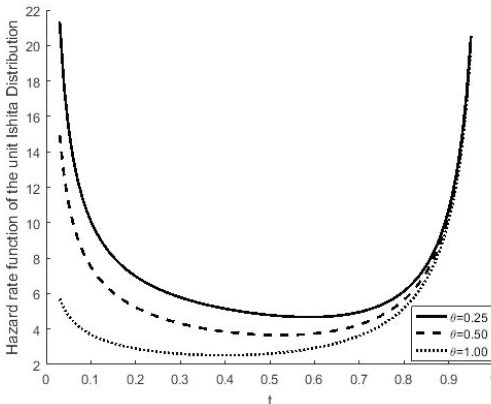
Following the general definition of the hazard rate function, the hazard rate and reserved hazard rate function of the UID are

$$H(t; \theta) = \frac{\theta^3 t^{\theta-1}(\theta + \ln^2(t))}{(\theta^3 + 2) \left(1 - \frac{x^\theta(\theta^3 + \theta \ln(t)(\theta \ln(t) - 2) + 2)}{\theta^3 + 2} \right)}
 \tag{6}$$

and

$$\xi(t; \theta) = \frac{\theta^3(\theta + \ln^2(t))}{t(\theta^3 + \theta \ln(t)(\theta \ln(t) - 2) + 2)},
 \tag{7}$$

respectively. Figure 2 illustrates the behavior the hazard rate function of the UID for different values of the parameter θ .



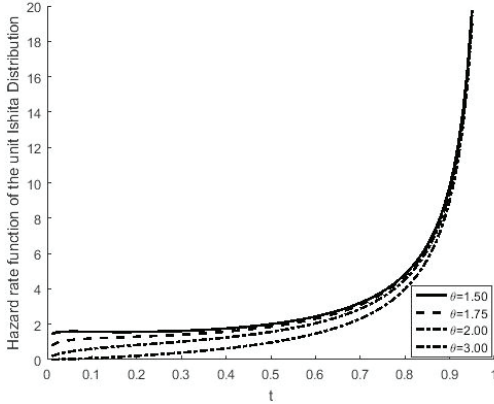


Figure 2. Hazard rate function of the UID for different values of the parameter θ

As can be seen from Figure 2, UID's hazard rate function is consistent with bathtub or increasing forms.

Characteristic Function

Following the definition of the characteristic function, the characteristic function of the UID is obtained as follows:

$$\phi_Y(t, \theta) = \int_{-\infty}^{\infty} e^{ity} f(y, \theta) dy$$

$$= \frac{{}_2F_3(\theta, \theta, \theta; \theta + 1, \theta + 1, \theta + 1; it) + \theta^4(-it)^{-\theta}(\Gamma(\theta) - \Gamma(\theta, -i \ 8))}{\theta^3 + 2}$$

where $\Gamma(\cdot)$ is the gamma function, $\Gamma(\cdot, \cdot)$ is the upper incomplete gamma function and ${}_aF_b(\cdot; \cdot; \cdot)$ is the hypergeometric function, see (Abramowitz et al., 1988) for advanced information on these functions.

Moment Generating Function and Moments

In this subsection, we obtain the moment generating function (MGF) and moments of the UID. The MGF of the UID can be immediately written as

$$\begin{aligned}
 &M_Y(t, \theta) \\
 &= \int_{-\infty}^{\infty} e^{ty} f(y, \theta) dy
 \end{aligned} \tag{9}$$

$$= \frac{(-t)^{-\theta} (2(-t)^\theta {}_3F_3(\theta, \theta, \theta; \theta + 1, \theta + 1, \theta + 1; t) + \theta^4 \Gamma(\theta))}{\theta^3 + 2} \tag{10}$$

where $\Gamma(\cdot)$ is the gamma function, $\Gamma(\cdot, \cdot)$ is the upper incomplete gamma function and ${}_aF_b(\cdot; \cdot; \cdot)$ is the hypergeometric function.

Suppose r is a non-negative integer than r^{th} raw moment of the UID is obtained as

$$\begin{aligned}
 \mu_r &= E(Y^r) = \int_{-\infty}^{\infty} y^r f(y, \theta) dy \\
 &= \int_0^1 y^r \frac{\theta^3 y^{\theta-1} (\theta + \ln^2(y))}{\theta^3 + 2} dy \\
 &= \frac{\theta^3 (\theta (\theta + r)^2 + 2)}{(\theta^3 + 2) (\theta + r)^3}
 \end{aligned} \tag{11}$$

By considering the equation (11), the first and secon moment of the UID can be written as

$$\mu_1 = E(Y) = \frac{\theta^3 (\theta (\theta + 1)^2 + 2)}{(\theta + 1)^3 (\theta^3 + 2)}$$

and

$$\mu_2 = E(Y^2) = \frac{\theta^3 (\theta (\theta + 2)^2 + 2)}{(\theta + 2)^3 (\theta^3 + 2)},$$

respectively. Thus the variance of the UID is obtained as follows:

$$\begin{aligned}
 Var(Y) &= E(Y^2) - (E(Y))^2 \\
 &= \mu_2 - \mu_1^2 \\
 &= \frac{\theta^3 (\theta (\theta + 2)^2 + 2)}{(\theta + 2)^3 (\theta^3 + 2)} - \frac{\theta^6 (\theta (\theta + 1)^2 + 2)^2}{(\theta + 1)^6 (\theta^3 + 2)^2}
 \end{aligned}$$

Order Statistics

Suppose Y_1, Y_2, \dots, Y_n is a sample from UID and $Y_{(1)} \cdots Y_{(n)}, (Y_{(1)} < \cdots < Y_{(n)})$ shows order statistics for this sample. With these notations, the pdf of the i^{th} order statistic is given by

$$\begin{aligned} f_{Y_{(i)}}(y) &= \frac{n!}{(i-1)!(n-i)!} F(y)^{i-1} f(y) (1-F(y))^{n-i} \\ &= \frac{n!}{(i-1)!(n-i)!} \frac{\theta^3 x^{\theta-1} (\theta + \ln^2(y))}{(\theta^3 + 2)} \\ &\quad \left(\frac{y^\theta (\theta^3 + \theta \ln(y) (\theta \ln(y) - 2) + 2)}{\theta^3 + 2} \right)^{i-1} \\ &\quad \times \left(1 - \frac{y^\theta (\theta^3 + \theta \ln(y) (\theta \ln(y) - 2) + 2)}{\theta^3 + 2} \right)^{n-i} \end{aligned} \quad (15)$$

By considering the equation (15), the pdf of the first and n^{th} order statistics are written as

$$f_{Y_{(1)}}(y) = \kappa \left(1 - \frac{y^\theta (\theta^3 + \theta \ln(y) (\theta \ln(y) - 2) + 2)}{\theta^3 + 2} \right)^{n-1}$$

and

$$f_{Y_{(n)}}(y) = \kappa \left(\frac{y^\theta (\theta^3 + \theta \ln(y) (\theta \ln(y) - 2) + 2)}{\theta^3 + 2} \right)^{n-1},$$

respectively, where $\kappa = \frac{n\theta^3 y^{\theta-1} (\theta + \ln^2(y))}{\theta^3 + 2}$.

INFERENCE

Maximum Likelihood Estimation

Let Y_1, Y_2, \dots, Y_n be random variables distributed UID with parameter θ and y_1, y_2, \dots, y_n shows a realization of the sample Y_1, Y_2, \dots, Y_n . Then the likelihood function $L(\theta, y_1, y_2, \dots, y_n)$ of UID based on y_1, y_2, \dots, y_n measurements written as

$$L(\theta, y_1, y_2, \dots, y_n) = \prod_{i=1}^n \frac{\theta^3 y_i^{\theta-1} (\theta + \ln^2(y_i))}{\theta^3 + 2}$$

and the log-likelihood function is written as

$$\ln L(\theta, y_1, y_2, \dots, y_n) = \sum_{i=1}^n \ln(\theta + \ln^2(y_i)) + (\theta - 1) \sum_{i=1}^n \ln(y_i) + n(3\ln(\theta) - \ln(\theta^3 + 2)). \tag{19}$$

Thus, by solving the score function given by equation (20), which derives the log-likelihood equation (19) with respect to θ and equates it to zero, we can obtain the maximum likelihood estimator of the θ parameter.

$$\frac{\delta \ln L(\theta, y_1, y_2, \dots, y_n)}{\delta \theta} = \sum_{i=1}^n \frac{1}{\theta + \ln^2(y_i)} + \sum_{i=1}^n \ln(y_i) + \left(\frac{3}{\theta} - \frac{3\theta^2}{\theta^3 + 2}\right)n = 0. \tag{20}$$

Unfortunately, the analytical solution of the score function (20) cannot be obtained by using elementary operations. However, by employing a numerical method such as Newton-Raphson or using software like Octave's (Eaton et al., 2019) "*fmincon*" function or "*mle*" function of R (Team, 2013), we can easily reach the maximum likelihood estimates of the parameter θ .

Least-Squares and Weighted Least-Squares Estimation

In this subsection, we investigate the least-squares estimator of the unknown θ parameter of the UID by following the notations of (Swain et al., 1988). Let $Y_{(1)}, Y_{(2)}, \dots, Y_{(n)}$ be an ordered random sample drawn from the UID with the θ parameter. Also, let a realization of $Y_{(1)}, Y_{(2)}, \dots, Y_{(n)}$ be represented as $y_{(1)}, y_{(2)}, \dots, y_{(n)}$. By these assumptions, least-squares estimator of the parameter θ is obtained by minimizing the objective function

$$Q_{LSE} = \sum_{i=j}^n \left(\frac{y_{(j)}^\theta (\theta^3 + \theta \ln(y_{(j)})) (\theta \ln(y_{(j)}) - 2) + 2}{\theta^3 + 2} - P_j \right)^2,$$

with respect to parameter θ , where $P_j = \frac{j}{n+1}$ is the value of the empirical distribution function for the j^{th} observation. Because of the fact that the objective function Q_{LSE} includes nonlinear functions, it is not possible to obtain an explicit form of the least-squares estimator. But, it can be easily solved using a numerical method.

By following similar steps, the weighted least-squares estimator of the parameter θ is obtained by minimizing

$$Q_{WLSE} = \sum_{j=1}^n \frac{(n+1)^2(n+2)}{j(n-j+1)} \left(\frac{y_{(j)}^\theta (\theta^3 + \theta \ln(y_{(j)})) (\theta \ln(y_{(j)}) - 2) + 2}{\theta^3 + 2} - P_j \right)^2,$$

with respect to θ . Here we propose using the "*fmincon*" function of the Octave (Octave manual) to minimize the objective functions Q_{LSE} and Q_{WLSE} .

Maximum Product Space Estimation

We suppose that let $Y_{(1)}, Y_{(2)}, \dots, Y_{(n)}$ is a random sample from the UID with parameter θ , and $y_{(1)}, y_{(2)}, \dots, y_{(n)}$ is a realization of it. By considering and following the notations of (Ranneby, 1984), the maximum product space estimator of the parameter θ is obtained by numerically maximizing the objective function

$$Q_{MPS} = \sum_{j=1}^{n+1} \ln[F(y_{(j)}, \theta) - F(y_{(j-1)}, \theta)]$$

$$Q_{MPS} = \sum_{j=1}^{n+1} \ln \left\{ \left[\frac{y_{(j)}^\theta (\theta^3 + \theta \ln(y_{(j)})) (\theta \ln(y_{(j)}) - 2) + 2}{\theta^3 + 2} - \left(\frac{y_{(j-1)}^\theta (\theta^3 + \theta \ln(y_{(j-1)})) (\theta \ln(y_{(j-1)}) - 2) + 2}{\theta^3 + 2} \right) \right] \right\}$$

with respect to parameter θ , where $F(\cdot, \theta)$ implies the cdf of the UID given by equation (4), $F(Y_{(0)}, \theta) \equiv 0$, and $F(Y_{(n+1)}, \theta) \equiv 1$. *fmincon* function of the Octave (Eaton et al., 2019) can be used to maximize the objective function Q_{MPS} .

SIMULATION STUDY

In this section, we investigate the performances of maximum likelihood, least-squares, weighted least-squares, and maximum product space estimators obtained in the previous section with numerical studies. In numerical studies, we use comparison criteria mean square error (MSE) and Bias given as

$$MSE = \frac{1}{m} \sum_{i=1}^n (\theta - \hat{\theta}_i)^2$$

and

$$Bias = \frac{1}{m} \sum_{i=1}^n \hat{\theta}_i - \theta,$$

respectively, where m is simulation repetition. In simulations repeated 1000 times, the value of the parameter θ is set as $(0.5,1.5,2.0)$. The results of the simulations carried out with different sample sizes of $n = 50,100,500$ and 1000 are presented in Tables 2-5.

According to the simulated results given in Tables 2-5, it can be said that the proposed MLE, LSE, WLSE, and MPSE estimators for parameter TTT exhibit good estimation performance. Given the results in Tables 2-5, we conclude that all estimators are asymptotically consistent and unbiased since all estimators have lower Bias and lower MSE values as sample size n increases. Moreover, we also concluded that the MLE estimator outperforms the other estimators with smaller MSE values.

Table 2: Simulated results for maximum likelihood estimation (MLE) in the different values of parameter θ , ($\theta = 0.5,1.5,2.0$)

		$\theta = 0.5$			$\theta = 1.5$			$\theta = 2.0$		
Method	n	$\hat{\theta}$	Bias $\hat{\theta}$	MSE $\hat{\theta}$	$\hat{\theta}$	Bias $\hat{\theta}$	MSE $\hat{\theta}$	$\hat{\theta}$	Bias $\hat{\theta}$	MSE $\hat{\theta}$
MLE	50	0.5046	0.0046	0.0020	1.5169	0.0169	0.0116	2.0118	0.0118	0.0294
	100	0.5044	0.0044	0.0011	1.5203	0.0203	0.0088	2.0100	0.0100	0.0125
	500	0.5033	0.0033	0.0007	1.5055	0.0055	0.0016	2.0025	0.0025	0.0031
	1000	0.5010	0.0010	0.0006	1.5030	0.0030	0.0006	2.0125	0.0125	0.0020

Table 3: Simulated results for least-squares estimation (LSE) in the different values of parameter θ , ($\theta = 0.5,1.5,2.0$)

		$\theta = 0.5$			$\theta = 1.5$			$\theta = 2.0$		
Method	n	$\hat{\theta}$	Bias $\hat{\theta}$	MSE $\hat{\theta}$	$\hat{\theta}$	Bias $\hat{\theta}$	MSE $\hat{\theta}$	$\hat{\theta}$	Bias $\hat{\theta}$	MSE $\hat{\theta}$
LSE	50	0.5184	0.0184	0.0017	1.5090	0.0090	0.0120	2.0015	0.0015	0.0380
	100	0.5152	0.0152	0.0008	1.5128	0.0128	0.0083	2.0064	0.0064	0.0156
	500	0.5230	0.0230	0.0007	1.5030	0.0030	0.0018	1.9948	0.0052	0.0033
	1000	0.5257	0.0257	0.0007	1.4989	0.0011	0.0006	2.0061	0.0061	0.0019

Table 4: Simulated results for weighted least-squares estimation (WLSE) in the different values of parameter θ , ($\theta = 0.5,1.5,2.0$)

		$\theta = 0.5$			$\theta = 1.5$			$\theta = 2.0$		
Method	n	$\hat{\theta}$	Bias $\hat{\theta}$	MSE $\hat{\theta}$	$\hat{\theta}$	Bias $\hat{\theta}$	MSE $\hat{\theta}$	$\hat{\theta}$	Bias $\hat{\theta}$	MSE $\hat{\theta}$
WLSE	50	0.5102	0.0102	0.0018	1.5115	0.0115	0.0126	2.0068	0.0068	0.0410
	100	0.5092	0.0092	0.0007	1.5134	0.0134	0.0082	2.0120	0.0120	0.0175
	500	0.5079	0.0079	0.0003	1.5032	0.0032	0.0018	1.9937	0.0063	0.0037
	1000	0.5087	0.0087	0.0001	1.4979	0.0021	0.0007	2.0043	0.0043	0.0020

Table 5: Simulated results for maximum product space estimation (MPSE) in the different values of parameter θ , ($\theta = 0.5, 1.5, 2.0$)

		$\theta = 0.5$			$\theta = 1.5$			$\theta = 2.0$		
Method	n	$\hat{\theta}$	Bias $\hat{\theta}$	MSE $\hat{\theta}$	$\hat{\theta}$	Bias $\hat{\theta}$	MSE $\hat{\theta}$	$\hat{\theta}$	Bias $\hat{\theta}$	MSE $\hat{\theta}$
MPSE	50	0.5200	0.0200	0.0154	1.5206	0.0206	0.0177	2.0315	0.0315	0.0339
	100	0.5194	0.0194	0.0066	1.5075	0.0075	0.0054	2.0286	0.0286	0.0144
	500	0.5034	0.0034	0.0013	1.5050	0.0050	0.0012	2.0100	0.0100	0.0025
	1000	0.5015	0.0015	0.0005	1.5068	0.0068	0.0008	2.0080	0.0080	0.0013

CONCLUSION

This study has focused on the introduction of a new probability distribution model called UID, which is capable of modeling data in a unit range. The pdf and cdf of the distribution that is the subject of the study were obtained by choosing the base distribution the Ishita distribution defined in the positive semi-real interval and using the e^{-y} transform. The pdf behavior of the UID is illustrated by given a figure. In addition, its features like moments and moment generating function, expectation, variance, and survival, hazard rate, reserved hazard rate functions, and order statistics' distribution are investigated in details. Four different estimator to estimate the unknown parameter θ are obtained by using the methodologies maximum likelihood, maximum product space, least-squares, and weighted least-squares. In addition, a numerical study is performed on different values of the θ parameter and estimation performances of the estimators obtained by the study are figured.

REFERENCES

1. Abramowitz, M., Stegun, I. A., & Romer, R. H. (1988). Handbook of mathematical functions with formulas, graphs, and mathematical tables.
2. Altun, E., & Hamedani, G. G. (2018). The log-xgamma distribution with inference and application. *Journal de la Société Française de Statistique*, 159(3), 40-55.
3. Bakouch, H. S., Nik, A. S., Asgharzadeh, A., & Salinas, H. S. (2021). A flexible probability model for proportion data: Unit-half-normal distribution. *Communications in Statistics: Case Studies, Data Analysis and Applications*, 7(2), 271-288.
4. Eaton, J. W., Bateman, D., Hauberg, S., & Wehbring, R. (2019). GNU Octave version 4.0. 0 manual: a high-level interactive language for numerical computations. 2015. URL <http://www.gnu.org/software/octave/doc/interpreter>, 8, 13.
5. Grassia, A. (1977). On a family of distributions with argument between 0 and 1 obtained by transformation of the gamma and derived compound distributions. *Australian Journal of Statistics*, 19(2), 108-114.
6. Ghitany, M. E., Mazucheli, J., Menezes, A. F. B., & Alqallaf, F. (2019). The unit-inverse Gaussian distribution: A new alternative to two-parameter distributions on the unit interval. *Communications in Statistics-Theory and Methods*, 48(14), 3423-3438.
7. Gómez-Déniz, E., Sordo, M. A., & Calderín-Ojeda, E. (2014). The Log-Lindley distribution as an alternative to the beta regression model with applications in insurance. *Insurance: Mathematics and Economics*, 54, 49-57.
8. Krishna, A., Maya, R., Chesneau, C., & Irshad, M. R. (2022). The Unit Teissier Distribution and Its Applications. *Mathematical and Computational Applications*, 27(1), 12.
9. Kumaraswamy, P. (1980). A generalized probability density function for double-bounded random processes. *Journal of hydrology*, 46(1-2), 79-88.
10. Mazucheli, J., Menezes, A. F. B., & Chakraborty, S. (2019). On the one parameter unit-Lindley distribution and its associated regression model for proportion data. *Journal of Applied Statistics*, 46(4), 700-714.
11. Mazucheli, J., Menezes, A. F. B., Fernandes, L. B., De Oliveira, R. P., & Ghitany, M. E. (2020). The unit-Weibull distribution as an alternative to the Kumaraswamy distribution for the modeling of quantiles conditional on covariates. *Journal of Applied Statistics*, 47(6), 954-974.

12. Modi, K., & Gill, V. (2020). Unit Burr-III distribution with application. *Journal of Statistics and Management Systems*, 23(3), 579-592.
13. Pourdarvish, A., Mirmostafae, S. M. T. K., & Naderi, K. (2015). The exponentiated Topp-Leone distribution: Properties and application. *Journal of Applied Environmental and Biological Sciences*, 5(7), 251-256.
14. Ranneby, B. (1984). The maximum spacing method. An estimation method related to the maximum likelihood method. *Scandinavian Journal of Statistics*, 93-112.
15. Swain, J. J., Venkatraman, S., & Wilson, J. R. (1988). Least-squares estimation of distribution functions in Johnson's translation system. *Journal of Statistical Computation and Simulation*, 29(4), 271-297.
16. Shanker, R., & Shukla, K. K. (2017). Ishita distribution and its applications. *Biometrics & Biostatistics International Journal*, 5(2), 1-9.
17. Team, R. C. (2013). R: A language and environment for statistical computing.
18. Topp, C. W., & Leone, F. C. (1955). A family of J-shaped frequency functions. *Journal of the American Statistical Association*, 50(269), 209-219.



CHAPTER 4

TERNARY METAL COMPLEXES CONTAINING N,N-DONOR ATOMS AND SCHIFF BASES DERIVED FROM AMINO ACIDS

*Assoc. Prof. Dr. Duygu İNCİ ÖZBAĞCI¹**,

Prof. Dr. Rahmiye AYDIN²

¹ Department of Chemistry, Faculty of Arts and Sciences, Bursa Uludag University, 16059 Bursa, Turkey, dyginci@uludag.edu.tr, ORCID: 0000-0002-0483-9642

² Department of Chemistry, Faculty of Arts and Sciences, Bursa Uludag University, 16059 Bursa, Turkey, rahmiye@uludag.edu.tr, ORCID: 0000-0003-4944-0181

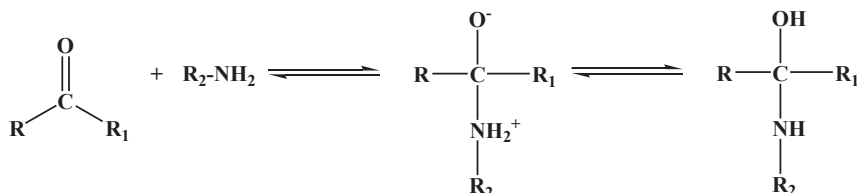
INTRODUCTION

Coordination chemistry is one of the most substantial and speedily developing branches of inorganic chemistry. Coordination compounds are very important in inorganic chemistry and have a wide research area due to their structure, abundance, colors, magnetic properties and chemical reactions. Today, coordination compounds are frequently encountered in industry, biological systems and various chemical processes (Zhang, 2017).

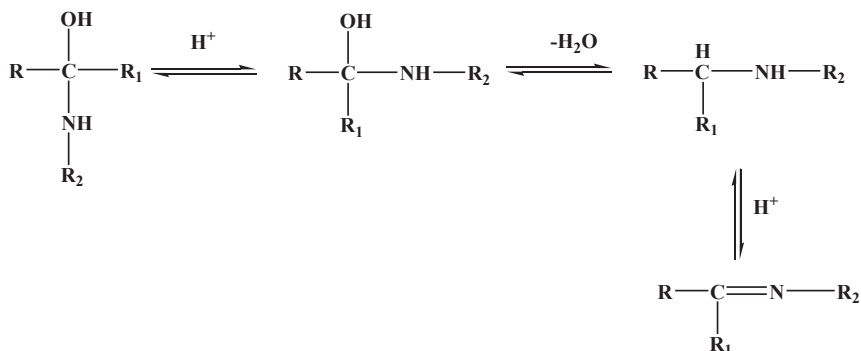
Schiff bases are the most used ligands in coordination chemistry. Schiff bases, which are formed by the condensation of primary amines with aldehydes, have been known as Schiff base compounds since they were first explored by the German chemist Hugo Schiff in 1864 (Schiff, 1864). Due to their very flexible and variable structural properties, many Schiff bases and their metal complexes have been investigated (Ebead *et al.*, 2016, İnci *et al.*, 2021). Schiff bases are also known as good nitrogen donor ligands. These ligands donate one or more electron pairs to the metal ion during the formation of the coordination compound. Schiff bases are from the ligand group frequently used in the field of coordination chemistry. Recently, some metal complexes have been used in the pharmaceutical industry, in the diagnosis of diseases and has started to gain importance in the treatment (Gasser, 2015). The determination of the effectiveness of the complexes of Schiff bases with transition metals in living organisms has led to an increase in studies on these compounds. The importance of coordination compounds in industry and biological systems today is increasing (Li *et al.* 2020, Bitu *et al.* 2020). Schiff bases are of interest in the scientific community because of their easy preparation, cheapness, accessibility, as well as many properties such as thermal resistance, liquid crystal property, conductivity and chelation, and their importance in our practical life is increasing day by day. This study highlights recently synthesized Schiff bases derived from amino acids containing *N,N*-donor atoms as well as their characterization methods.

Schiff bases

Schiff bases are compounds obtained from the condensation of aldehydes or ketones with primary amines. Because they contain C=N in their structure, they are called “imine” or “azomethine” compounds. Schiff bases are denoted by the formula $R_1C=NR$. R and R_1 are alkyl or aryl substituents (Park *et al.* 1998). As a result of the reaction of primary amines and carbonyl compounds such as aldehydes and ketones, it was determined that the Schiff base consists of two main steps.

First step:

In the first step, the carbonylamine is formed from the condensation of the carbonyl group with the primary amine. The first step usually occurs in acidic solutions. Therefore, imine formation is a reaction dependent on the pH of the medium. If the solution pH is too low, the amine concentration decreases to a negligible extent, in which case the normally fast addition step slows down and becomes the rate determining step in the reaction sequence (Mederos *et al.* 1999).

Second step:

In the second step, the OH⁻ group is separated as H₂O and the increase in the acid concentration in the medium increases the speed of the second step. In aqueous solutions, the condensation equilibrium of Schiff bases is prone to shift to hydrolysis, so condensations are carried out in environments where water can be removed by distillation. Imines formed from aromatic amines and aldehydes are more stable and more resistant to hydrolysis than those formed from aliphatic compounds (Malakyan *et al.* 2016).

Schiff bases can easily form complexes with electron donor atoms such as N, S, O. The type and number of these atoms have a great effect on the complex structure and diversity, but the resulting complex structure is not shaped only by donor atoms. Factors such as the metal salt with which the ligand reacts, the molar ratio of the reacting ligand

and the metal salt can also affect the structure of the complex. Depending on the type and number of donor atoms they contain Schiff bases can be defined as NO, N₂O₂, ONO, ONS, NS type ligand. Schiff bases can be classified as shown in Figure 1.

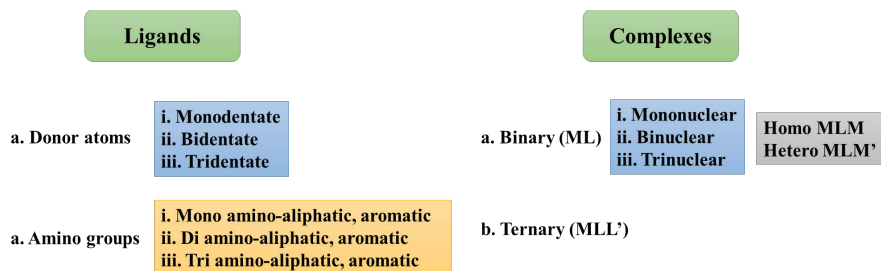


Figure 1. Classification of Schiff bases and metal complexes (Uddin *et al.* 2020)

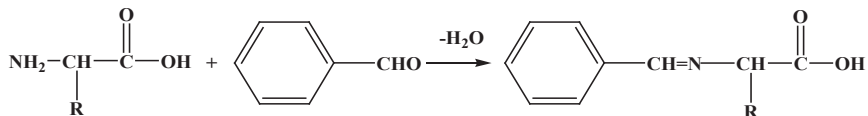
Schiff base-metal complexes

Three methods can be used to synthesize metal complexes of Schiff bases. These methods are the direct interaction of the metal salt with the Schiff base (March, 1972), the condensation of aldehyde, amine and metal salt as a template (Fernández *et al.* 2001), and finally the condensation of aldehyde complexes with amines (Krygowski *et al.* 1997). Metal acetates are the most suitable compounds because they are soluble in alcohol and form weak acid salts in the environment. The most effective of the methods used starts with first synthesizing the ligand and then isolating it. Divalent metal ions are commonly used as metals.

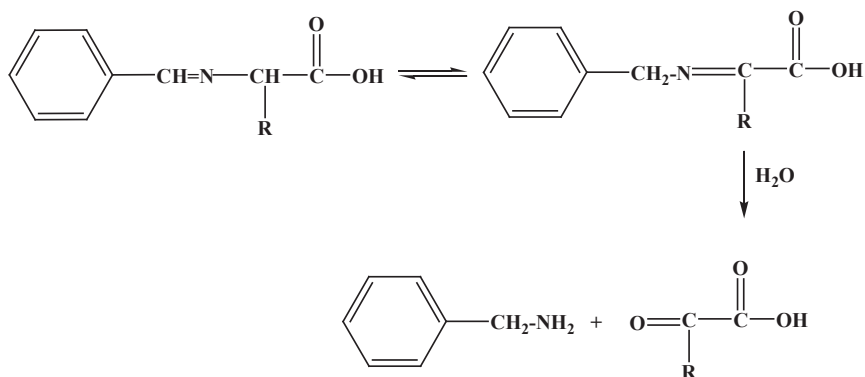
Since the nitrogen atom in the imine bond contains unpaired electrons, it is an electron donor and has a basic character. This atom, which can also be defined as the nitrogen of azomethine, is the primary bonding point for a Schiff base. The azomethine system, in which the nitrogen atom is bonded with a double bond, can also be a coordination site for d-metal ions (Abou-Hussein *et al.* 2014).

Schiff bases are widely used ligands in coordination chemistry. Nitrogen in the imine group has coordinating properties as a donor atom. In addition, the presence of groups such as -OH, -SH, -NH₂ in the ortho position in the benzene ring adjacent to the azomethine group in aromatic Schiff bases and the use of Schiff bases as polydentate ligands have increased their importance in coordination chemistry. Since amino acids contain primary amine groups, they give Schiff base reaction with aldehydes. Since the -NH₂ group in amino acids is activated by the

inductive effect of the $-\text{COOH}$ group, they give Schiff base reaction with aldehydes more easily than other aliphatic primary amines (Asif, 2015). The mechanism of imine formation because of its reaction with benzaldehyde is as follows (Schemes 1 and 2).



Scheme 1. Reaction of an amino acid with benzaldehyde



Scheme 2. Tautomerization reaction of Schiff base

Ligands containing N,N -donor atoms like 1,10-phenanthroline and 2,2'-bipyridine and its derivatives are widely used as ligands in biochemistry studies, especially in inhibition of metalloenzymes (Abebe *et al.* 2018). These types of ligands have a rigid skeleton and excellent ability to coordinate with many metal ions. It exhibits an effective situation in technological applications thanks to strong absorption in the ultraviolet region, its high charge transfer mobility, bright light emission properties. Synthesis of organometallic complexes, biosensors, molecular chemistry, catalysts for oxidative organic synthesis, purification of water, disease diagnosis and treatment, etc. used in a wide variety of fields (Zhang *et al.* 2007, Zhong *et al.* 2008).

Characterization methods

The spectroscopic properties of Schiff bases are of interest because of their biochemical properties as well as their importance in analytical applications. $^1\text{H-NMR}$ studies are for the determination of chemical shift values of imine and bound groups. The peak of the imine

proton is observed as a singlet in the low area and the chemical shift value (δ , ppm) is higher than the bound aromatic groups. FTIR spectral studies uncovered coordination of functional groups of Schiff bases containing OH, NH, CO, HC=N and azomethine nitrogen. Characteristic $\nu(\text{C}=\text{N})$ vibration bands are observed in the FTIR spectra of Schiff bases. In metal complexes, the decrease in electron density on the donor atom by bonding from azomethine nitrogen weakens the double bond and shifts the $\nu(\text{C}=\text{N})$ vibration to a low frequency. In the electronic absorption spectrum of Schiff bases, the absorption peaks of the $\pi \rightarrow \pi^*$ transition of the azomethine or imine group are observed in the ultraviolet region in the range of 200-300 nm. In metal complexes, besides the $\pi \rightarrow \pi^*$ transitions, $\text{L} \rightarrow \text{M}$ or $\text{M} \rightarrow \text{L}$ charge transfer transitions are observed around 400 nm. In transition metals, d-d transitions are observed in the 400-800 nm range. The redox behaviour of the Schiff bases and their complexes is searched by cyclic voltammetry. Thermal stability of Schiff bases and their complexes are investigated by thermogravimetric measurements. X-ray crystallography analysis results provide bond lengths and angles of Schiff bases and their complexes.

Significance of ternary metal complexes

The study of ternary metal complexes has received great importance of late years owing to their wide applications in different fields and their presence in biological environments (Cozzi, 2004). In biological system metal ions form ternary complexes which substantially contain the interaction of the metal ion with two or more different ligands (Marco *et al.* 2006). Ternary metal complexes containing amino acids have importance since they are potential models for enzyme metal ion substrate complexes (Reddy *et al.* 2004).

Recently, ternary metal complexes containing amino acid Schiff base and *N,N*-donor atoms like 2,2'-bipyridine (bpy) (Bandyopadhyay *et al.* 2016, Lu *et al.* 2011, Theetharappan *et al.* 2017, Sasikumar *et al.* 2019, Ebead *et al.* 2016, Osmanković *et al.* 2021), 1,10-phenanthroline (phen) (Lu *et al.* 2011, Li *et al.* 2020, Reddy *et al.* 2004, Zhao *et al.* 2016, Boghaei and Gharagozlou, 2007, Ruman *et al.* 2014, Theetharappan *et al.* 2017, Sasikumar *et al.* 2019, Ebead *et al.* 2016, Osmanković *et al.* 2021), dipyrido[3,2-d:2',3'-f]quinoxaline (dpq) (Lu *et al.* 2011, Reddy *et al.* 2004), dipyrido[3,2-a:2',3'-c]phenazine (dppz) (Lu *et al.* 2011), 5,6-dimethyl-1,10-phenanthroline (dmphen) (Bitu *et al.* 2020, Theetharappan *et al.* 2017) have been reported. Since ternary metal complexes are biologically important, the synthesis and characterization of the ternary metal complexes is significant. In the Table 1 given below,

metal ion, amino acid and *N,N*-donor atoms used in the synthesis of the ternary metal complexes in the literature are given.

Table 1. Schiff bases containing amino acid Schiff base and *N,N*-donor atoms

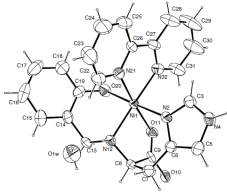
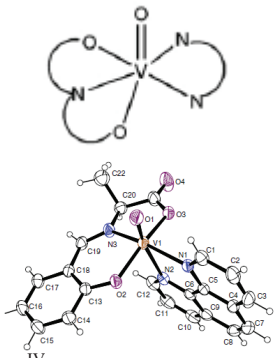
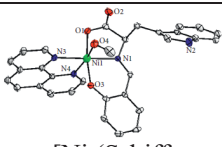
Metal ion	Aldehyde ketone	Amino acids / <i>N,N</i> -donor atom	Structure	Ref
Ni(II)	Salicyl aldehyde	Histidine 2,2'-bipyridine (bpy)	 [Ni(Schiff base)(bpy)]H ₂ O	Bandyopad hay <i>et al.</i> 2006
V(IV)	Salicyl aldehyde	Tyrosine (tyr) Alanine (ala) Asparagine (asn) Lysine (lys) (phen) 1,10-phenanthroline (bpy) 2,2'-bipyridine (dppz) dipyrido[3,2-a:2',3'-c]phenazine (dpq) dipyrido[3,2-d:2',3'-f]quinoxaline	 [V ^{IV} O(Schiff base)(phen)]	Lu <i>et al.</i> 2011
Ni(II)	Salicyl aldehyde <i>o</i> -vanillin 2-hydroxy-1-naphth aldehyde	Tryptophan (trp) (phen) 1,10-phenanthroline	 [Ni (Schiff base)(phen)(CH ₃ OH)]	Li <i>et al.</i> 2020
			 [Ni (Schiff base)(phen)(CH ₃ OH) 2CH ₃ OH]	

Table 1. Continued

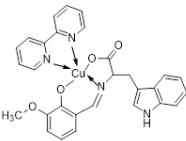
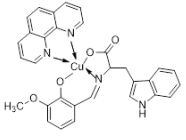
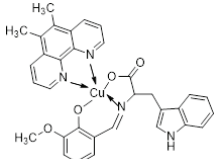
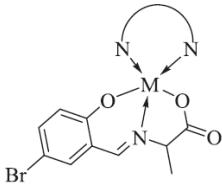
Metal ion	Aldehyde ketone	Amino acids / N,N-donor atom	Structure	Ref
Cu(II)	<i>o</i> -vanillin	Tryptophan (trp) (dmphen) 5,6-dimethyl-1,10-Phenanthroline (phen) 1,10-phenanthroline (bpy) 2,2'-bipyridine	 <p>[Cu(Schiff base)(bpy)]</p>  <p>[Cu(Schiff base)(phen)]</p>  <p>[Cu(Schiff base)(dmphen)]</p>	Theetharappan <i>et al.</i> 2017
Zn(II) Cu(II) Ni(II) Co(II)	5-bromo Salicyl aldehyde	Alanine (ala) (phen) 1,10-phenanthroline (bpy) 2,2'-bipyridine	 <p>[M(Schiff base)(phen/bpy)]</p>	Sasikumar <i>et al.</i> 2019

Table 1. Continued

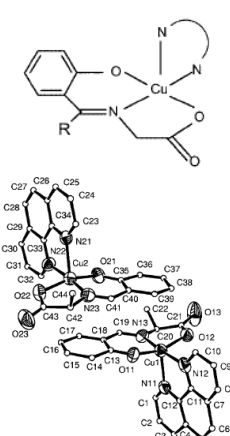
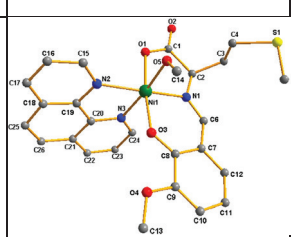
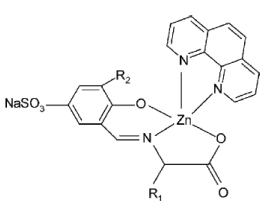
Metal ion	Aldehyde ketone	Amino acids / N,N-donor atom	Structure	Ref
Cu(II)	Salicyl aldehyde	Phenylalanine (phe) Alanine (ala) Glycine (gly) (dpq) dipyrido[3,2-d:2',3'-f]quinoxaline (phen) 1,10-phenanthroline	 <p>[Cu(Schiff base)(phen)]5H₂O</p>	Reddy <i>et al.</i> 2004
Ni(II)	<i>o</i> -vanillin	Methionine (met) (phen) 1,10-phenanthroline	 <p>[Cu(Schiff base)(phen)(CH₃OH)]</p>	Zhao <i>et al.</i> 2016
Zn(II)	Salicyl aldehyde-5-sulfonates	Phenylalanine (phe) Leucine (leu) Valine (val) Alanine (ala) Glycine (gly) (phen) 1,10-phenanthroline	 <p>[Zn(Schiff base)(phen)]</p>	Boghaci and Gharagozlu 2007

Table 1. Continued

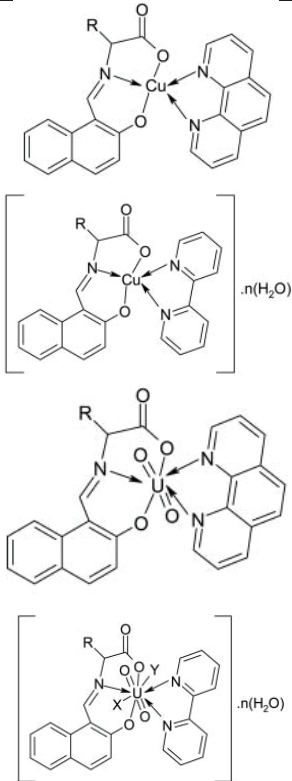
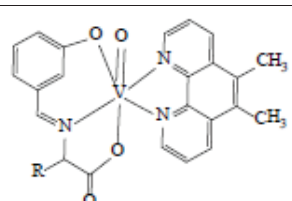
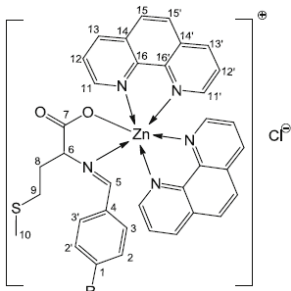
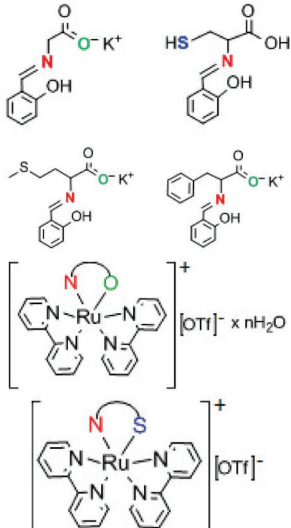
Metal ion	Aldehyde ketone	Amino acids / N,N-donor atom	Structure	Ref
Cu(II) U(II)	2-hydroxy-1-naphth aldehyde	Phenylalanine (phe) Leucine (leu) Valine (val) Alanine (ala) Glycine (gly) (phen) 1,10-phenanthroline (bpy) 2,2'-bipyridine	 <p>The structures show a central metal ion (Cu or U) coordinated to a Schiff base ligand derived from 2-hydroxy-1-naphthaldehyde and an amino acid (R). The Cu(II) complex is shown with 1,10-phenanthroline (phen) and 2,2'-bipyridine (bpy) ligands. The U(II) complex is shown with phen and bpy ligands. The structures are presented as discrete molecules and as complexes with n water molecules, enclosed in brackets with a subscript n(H₂O).</p> <p>$L^1, X = H_2O, n = 1, Y = 0; L^2, X = H_2O, n = 1, Y = 2(CH_3COO); L^3 \text{ and } L^4, X = 0, n = 0, Y = 0; L^5, X = H_2O, n = 1, Y = 2(CH_3COO)$</p>	Ebead <i>et al.</i> 2016
V(IV)	3-hydroxy benz aldehyde	Phenylalanine (phe) Methionine (met) Leucine (leu) Alanine (ala) Glycine (gly) (dmphen) 5,6-dimethyl-1,10-Phenanthroline	 <p>The structure shows a central V(IV) ion coordinated to a Schiff base ligand derived from 3-hydroxybenzaldehyde and an amino acid (R). The complex is also coordinated to a 5,6-dimethyl-1,10-phenanthroline (dmphen) ligand. The structure is shown as a discrete molecule and as a complex with n water molecules, enclosed in brackets with a subscript n(H₂O).</p> <p>[VO(Schiff base)(dmphen)]</p>	Bitu <i>et al.</i> 2020

Table 1. Continued

Metal ion	Aldehyde ketone	Amino acids / N,N-donor atom	Structure	Ref
Cu(II) Co(II) Zn(II)	p-substitute benz aldehyde L1 = NO ₂ L2=OCH ₃	Methionine (met) (phen) 1,10-phenanthroline	 <p>M = Cu(II), Co(II), and Zn(II) Phen = 1,10-phenanthroline</p>	Ruman <i>et al.</i> 2014
Ru(II)	Salicyl aldehyde	Phenylalanine (phe) Methionine (met) Cysteine (cys) Glycine (gly) (bpy) 2,2'-bipyridine		Osmanković <i>et al.</i> 2021

Bandyopadhyay and coworkers have clarified synthesis and characterization of new Schiff base N-(2-hydroxybenzyl)-L-histidine (H₂hb-L-his, H₂L), and its nickel(II) and copper(II) complexes in the absence and presence of N,N-donor atom, 2,2'-bipyridine(bpy). [Ni(H₂hb-L-his)(H₂O)₂], [Cu(H₂hb-L-his)(H₂O)] and [Ni(H₂hb-L-his)(bpy)]H₂O have been characterized by single crystal X-ray diffraction, FTIR, ¹H NMR and CHN analysis methods. According to the X-ray diffraction results, it was determined that [Ni(H₂hb-L-

his,ONNO)(bpy,NN)]H₂O was crystallized in a distorted octahedral geometry (Bandyopadhyay *et al.* 2006).

Lu *et al.*, synthesized a series of oxovanadium complexes - [V^{IV}O(SalAla)(bpy)] (1), (SalAla, salicylidene alanine), [V^{IV}O(SalAla,ONO)(phen,NN)] (2), [V^{IV}O(SalAla,ONO)(dpq,NN)] (3), [V^{IV}O(SalAla,ONO)(dppz,NN)] (4), [V^{IV}O(SalLys,ONO)(dpq,NN)] (5), (SalAla, salicylidene lysine), [V^{IV}O(SalLys,ONO)(dppz,NN)] (6), [V^{IV}O(SalAsp,ONO)(dppz,NN)], (SalAla, salicylidene asparagine), (7), [V^{IV}O(SalTrp,ONO)(dppz,NN)] (8), (SalAla, salicylidene tyrosine), NN: dipyrido [3,2-a:2',3'-c]phenazine (dppz), dipyrido[3,2-d:2',3'-f]quinoxaline (dpq), 1,10-phenanthroline (phen), 2,2'-bipyridine (bpy)-. They have been characterized by single crystal X-ray diffraction, elemental analysis, UV-Visible, FTIR, ESI-MS, EPR, conductivity methods. The structure of [V^{IV}O(SalAla)(phen)] was determined by the single crystal X-ray diffraction method. It was determined that [V^{IV}O(SalAla,ONO)(phen,NN)] was in a distorted octahedral geometry. The Schiff base is coordinated from the imine nitrogen, carboxylate oxygen and phenolate oxygen to the oxovanadium(IV) ion (Lu *et al.* 2011)

Li *et al.*, synthesized three new a distorted octahedral geometries of Ni(II) complexes -[Ni(Trp-sal,ONO)(phen,NN)(CH₃OH)] (1) (Trp-sal, salicylidene tryptophan), [Ni(Trp-*o*-van,ONO) (phen,NN)(CH₃OH)] 2CH₃OH (2) (Trp-*o*-van, *o*-vanillinidene tryptophan), [Ni(Trp-naph,ONO) (phen,NN)(CH₃OH)] (3) (Trp-naph, 2-hydroxy-1-naphthalidene tryptophan), and phen: 1, 10-phenanthroline- and characterized by FTIR, single crystal X-ray diffraction and CHN analysis methods. The Schiff base is coordinated from the imine nitrogen, carboxylate oxygen and phenolate oxygen to the nickel(II) ion (Li *et al.* 2020).

Theetharappan *et al.*, formulated complexes as [Cu(*o*-vanillin-L-tryptophan Schiff base,ONO)(diamine,NN)] (diimine: 5,6-dimethyl -1,10-phenanthroline (dmphen), 1,10-phenanthroline (phen), 2,2'-bipyridine (bpy)) were synthesized and characterized by CHN analysis, UV-Visible, FTIR, ESI-MS, EPR and cyclic voltammetry methods. The researchers determined that the synthesized complexes were in a distorted square pyramid geometry (Theetharappan *et al.* 2017).

Reddy *et al.*, formulated complexes as [Cu(salgly/ala/phe)L] (L: (dpq) dipyrido[3,2-d:2',3'-f]quinoxaline, (phen) 1,10-phenanthroline, salgly, salicylidene glycine, salala, salicylidene alanine, salphe, salicylidene phenylalanine) were synthesized-[Cu(salgly,ONO)(L,NN)] (phen (1), dpq (2)), [Cu(salala,ONO)(L,NN)] (phen (3), dpq (4)), [Cu(salphe,ONO)(L,NN)] (phen (5), dpq (6))- and characterized by single

crystal X-ray diffraction, FTIR and CHN analysis methods. The structure of [Cu(salala,ONO)(phen,NN)] was analysed by the single crystal X-ray diffraction method. The researchers determined that [Cu(salala,ONO)(phen,NN)] was in a distorted square pyramid geometry. The Schiff base is coordinated from the imine nitrogen, carboxylate oxygen and phenolate oxygen to the copper(II) ion (Reddy *et al.* 2004).

Zhao *et al.*, synthesized a new Ni(II) complex - [Ni(*o*-van-met,ONO)(phen,NN) (CH₃OH,O)]- *o*-van-met: *o*-vanillinidene methionine and phen: 1, 10-phenanthroline- and characterized by single crystal X-ray diffraction, FTIR and CHN analysis methods. The structure of [Ni(*o*-van-met,ONO)(phen,NN)(CH₃OH,O)] was determined to be a distorted square pyramid geometry (Zhao *et al.* 2016).

Ebead and coworkers have reported the synthesis and characterization a series of Cu(II) and UO₂(II) complexes, [Cu(L¹)(phen)] (1), [Cu(L²)(phen)] (2), [Cu(L³)(phen)] (3), [Cu(L⁴)(phen)] (4), [Cu(L⁵)(phen)] (5), [Cu(L¹)(bpy)]2H₂O (6), [Cu(L²)(bpy)] (7), [Cu(L³)(bpy)]2H₂O (8), [Cu(L⁴)(bpy)]H₂O (9), [Cu(L⁵)(bpy)]2H₂O (10), [UO₂(L¹)(phen)] (11), [UO₂(L²)(phen)] (12), [UO₂(L³)(phen)] (13), [UO₂(L⁴)(phen)] (14), [UO₂(L⁵)(phen)] (15), [UO₂(L¹)(bpy)(H₂O)]H₂O (16), [UO₂(L²)(bpy)(AcO)₂(H₂O)]H₂O (17), [UO₂(L³)(bpy)] (18), [UO₂(L⁴)(bpy)] (19), [UO₂(L⁵)(bpy)(AcO)₂(H₂O)]H₂O (20), (2-hydroxy-1-naphthaldehyde amino acids Schiff bases, amino acids: glycine L¹; alanine L²; leucine L³; valine L⁴; and phenylalanine L⁵ and phen: 1,10-phenanthroline, bpy: 2,2'-bipyridine). They have been characterized by FTIR, CHN analysis and UV-Visible methods. They suggested that the Schiff bases are coordinated from the imine nitrogen, carboxylate oxygen and phenolate oxygen to the copper(II) and dioxouranium(II) ion (Ebead *et al.* 2016).

Osmankovic *et al.*, formulated complexes as [Ru(bpy)₂(L)]CF₃SO₃ (L: Salicylaldehyde Schiff base, amino acids: glycine (1a); cysteine (1b); methionine (1c); phenylalanine (1d), bpy: 2,2'-bipyridine) were synthesized and characterized by FTIR, ESI-MS, CHN analysis, Ru content and UV-Visible methods. The researchers suggested that [Ru(bpy,NN)₂(L,NO)]CF₃SO₃ was in an octahedral geometry. The Schiff bases 1a, 1b and 1c are coordinated from the imine nitrogen and carboxylate oxygen, while the Schiff base 1d is coordinated from the imine nitrogen and deprotonated -SH group of amino acid moiety to the copper(II) ion (Osmankovic *et al.* 2021).

Bitu *et al.*, synthesized five new a distorted octahedral geometries of oxovanadium(IV) complexes formulated as [VO(L,ONO)(DPhen,NN)] {Dphen: 5,6-dimethyl -1,10-phenanthroline, L: 3-hydroxybenzaldehyde

Schiff base, amino acids: alanine (hb-Ala), phenylalanine (hb-Phe), leucine (hb-Leu), glycine (hb-Gly), methionine (hb-Met)} and characterized by CHN analysis, FTIR, UV-Visible, ESI-MS, magnetic susceptibilities and molar conductance studies. The researchers suggested that the Schiff base is coordinated from the imine nitrogen, carboxylate oxygen and phenolate oxygen while the Dphen is coordinated from two nitrogen atoms to the oxovanadium(IV) ion (Bitu *et al.* 2020).

Boghaei and Gharagozlou have reported the synthesis and characterization a series of ternary Zn(II) complexes $-\text{[Zn(L}^{1-10},\text{ONO)(phen,NN)]}$, $[\text{Zn(L}^4,\text{ONO)(H}_2\text{O,O)}]2\text{H}_2\text{O}$, $[\text{Zn(L}^5,\text{ONO)(H}_2\text{O,O)}]3\text{H}_2\text{O}$, $[\text{Zn(L}^9,\text{ONO)(H}_2\text{O,O)}]\text{H}_2\text{O}$ and $[\text{Zn(L}^{10},\text{ONO)(H}_2\text{O,O)}]\text{H}_2\text{O}$ - (salicylaldehyde-5-sulfonates (sodium salicyl aldehyde-5-sulfonate (L^{1-5}) and sodium 3-methoxy-salicylaldehyde-5-sulfonate (L^{6-10})) amino acids Schiff bases, L^1 (R_2 : H, R_1 : glycine), L^2 (R_2 : H, R_1 : L-phenylalanine), L^3 (R_2 : H, R_1 : L-valine), L^4 (R_2 : H, R_1 : L-alanine), L^5 (R_2 : H, R_1 : L-leucine), L^6 (R_2 : OCH_3 , R_1 : H), L^7 (R_2 : OCH_3 , R_1 : CH_2Ph), L^8 (R_2 : OCH_3 , R_1 : $\text{CH}(\text{CH}_3)_2$), L^9 (R_2 : OCH_3 , R_1 : CH_3), L^{10} (R_2 : OCH_3 , R_1 : L-leucine) and phen: 1,10-phenanthroline). They have been characterized by ^1H NMR and ^{13}C NMR, FTIR, CHN analysis, UV-Visible methods. They suggested that the Schiff bases are coordinated from the imine nitrogen, carboxylate oxygen and phenolate oxygen to the zinc(II) ion (Boghaei and Gharagozlou, 2007).

Sasikumar and coworkers have reported the synthesis and characterization a series of ternary cobalt(II), nickel(II), copper(II) and zinc(II) complexes - $[\text{Co(L,ONO)(phen,NN)}]$ (1), $[\text{Ni(L,ONO)(phen,NN)}]$ (2), $[\text{Cu(L,ONO)(phen,NN)}]$ (3), $[\text{Zn(L,ONO)(phen,NN)}]$ (4), $[\text{Co(L,ONO)(bpy,NN)}]$ (5), $[\text{Ni(L,ONO)(bpy,NN)}]$ (6), $[\text{Cu(L,ONO)(bpy,NN)}]$ (7), $[\text{Zn(L,ONO)(bpy,NN)}]$ (8) - (5-bromo salicylaldehyde amino acid Schiff bases, amino acid: L-alanine, (phen):1,10-phenanthroline and (bpy):2,2'-bipyridyl). Researchers have used different techniques in the characterization of the synthesized complexes like elemental analysis, FTIR, ESI-MS, EPR, UV-Visible, NMR and Powdered X-ray diffractometry. The researchers suggested that the Schiff base is coordinated from the imine nitrogen, carboxylate oxygen and phenolate oxygen while the phen/bpy is coordinated from two nitrogen atoms to the metal(II) ions (Sasikumar *et al.* 2019).

Consequently, this work highlights recently synthesized amino acid Schiff bases and containing *N,N*-donor atoms besides their characterization methods.

REFERENCES

- Abebe, A., Atlabachew, M., Liyew, M., Ferede, E. 2018. Synthesis of organic salts from 1,10-phenanthroline for biological applications, *Cogent Chemistry*, 4(1): 1476077.
- Abou-Hussein, A. A., Linert, W. 2014. Synthesis, spectroscopic, coordination and biological activities of some organometallic complexes derived from thio-Schiff base ligands, *Spectrochimica Acta Part A: Molecular and Biomolecular Spectroscopy*, 117: 763-771.
- Asif, M. 2015. An overview on synthesis and medicinal chemistry potentials of biologically active antimicrobial Schiff's bases and its complexes: a review, *Moroccan Journal of Chemistry*, 3(3): 627-652.
- Bandyopadhyay, S., Mukherjee, G.N., Drew, M.G.B. 2006. Equilibrium studies on mixed ligand complex formation of Co(II), Ni(II), Cu(II) and Zn(II) with N-(2-hydroxybenzyl)-L-histidine (H₂hb-L-his) and typical N,N donor ligands: Crystal structure of [Ni(hb-L-his)(bipyridine)]H₂O complex, *Inorganica Chimica Acta*, 359: 3243-3251.
- Bitu, Md. N. A., Hossain, Md. S., Asraf, Md. A., Hossen, Md. F., Kudrat-E-Zahan, Md. 2020. Synthesis, Characterization and Biological Activity of Oxovanadium(IV) Complexes Containing α -Amino Acid Schiff Bases and 5,6-Dimethyl-1,10-phenanthroline Ligands, *Croatica Chimica Acta*, 93(3): 231-236.
- Boghaei, D. M., Gharagozlou, M. 2007. Spectral characterization of novel ternary zinc(II) complexes containing 1,10-phenanthroline and Schiff bases derived from amino acids and salicylaldehyde-5-sulfonates, *Spectrochimica Acta Part A*, 67: 944-949.
- Cozzi, P. G. 2004. Synthesis, spectral, 3D molecular modeling and antibacterial studies of dibutyltin (IV) Schiff base complexes derived from substituted isatin and amino acids, *Chemical Society Reviews*, 33: 410-421.
- Ebead, Y. H., Salman, H. M. A., Shebany, Y. M., Abdellah, M. A. 2016. Synthesis, Spectroscopic, and Biological Investigations of the Ternary Metal Complexes of Schiff Bases Derived From 2-hydroxy-1-naphthaldehyde and Some Amino Acids, *Synthesis and Reactivity in Inorganic, Metal-Organic, and Nano-Metal Chemistry*, 46: 1819-1828.
- Fernández-G, J. M., del Rio-Portillo, F., Quiroz-García, B., Toscano, R.A., Salcedo, R. 2001. The Structures of Some Orto-Hydroxy Schiff Base Ligands, *Journal of Molecular Structure*, 561: 197-207.

Gasser, G. 2015. Metal complexes and medicine: a successful combination, *Chimia*, 69: 442-446.

İnci, D., Aydın, R., Zorlu, Y. 2021. NOO-type tridentate Schiff base ligand and its one-dimensional Cu(II) coordination polymer: Synthesis, crystal structure, biomacromolecular interactions and radical scavenging activities, *Inorganica Chimica Acta*, 514: 119994.

Krygowski, T. M., Wozniak, K., Anulewicz, R., Pawlak, D., Kolodziejski, W., Grech, E., Szady, A. 1997. Through-Resonance Ionic Hydrogen Bonding in 5-Nitro-Nsalicylideneethylamine, *Journal Physical Chemistry A*, 101: 9399-9404.

Li, Y., Dong, J., Zhao, P., Hu, P., Yang, D., Gao, L., Li, L. 2020. Synthesis of Amino Acid Schiff Base Nickel (II) Complexes as Potential Anticancer Drugs *In Vitro*, *Bioinorganic Chemistry and Applications*, Volume 2020, Article ID 8834859, 15 pages.

Lu, L., Yue, J., Yuan, C., Zhu, M., Han, H., Liu, Z., Guo, M. 2011. Ternary oxovanadium(IV) complexes with amino acid-Schiff base and polypyridyl derivatives: Synthesis, characterization, and protein tyrosine phosphatase 1B inhibition, *Journal of Inorganic Biochemistry*, 105: 1323-1328.

Malakyan, M., Babayan, N., Grigoryan, R., Sarkisyan, N., Tonoyan, V., Tadevosyan, D., Matosyan, V., Aroutiounian, R., Arakelyan, A. 2016. Synthesis, characterization and toxicity studies of pyridinecarboxaldehydes and L-tryptophan derived Schiff bases and corresponding copper (II) complexes, *F1000Res*, 5: 1921.

March, J. 1972. *Advanced Organic Chemistry*, Wiley, NY, USA.

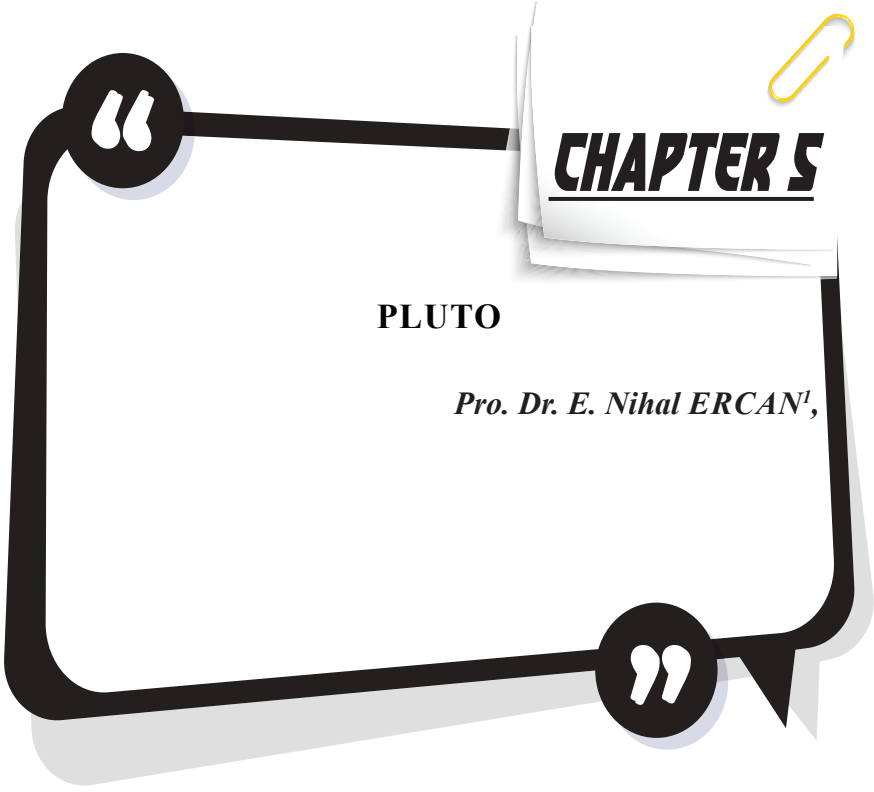
Marco, D., Bombi, V. B., Mass, G. G. 2006. Electrospray mass spectrometry (ESI-MS) in the study of metal-ligand solution equilibria, *Spectrometry Reviews*, 25: 347-379.

Mederos, A., Domínguez, S., Hernández-Molina, R., Sanchiz J. and Brito, F. 1999. Coordinating Ability of Ligands Derived From Phenylenediamines. *Coordination Chemistry Reviews*, 193-195: 857-911.

Osmanković, I., Turkušić, E., Zahirović, A., Kralj, M., Uzelac, L., Kahrović, E. 2021. CT DNA, BSA and Antiproliferative Activity of Ru(II) Bipyridine Complexes Containing Schiff Bases Derived from Amino Acids, *Croatica Chemica Acta*, 94(3): 149-158.

Park, S., Mathur, V. K., Planalp, R. P. 1998. Syntheses, solubilities and oxygen absorption properties of new cobalt(II) Schiff-base complexes, *Polyhedron*, 17(2-3): 325-330.

- Reddy, P. A. N., Nethaji, M., Chakravarty, A. R. 2004. Hydrolytic Cleavage of DNA by Ternary Amino Acid Schiff Base Copper(II) Complexes Having Planar Heterocyclic Ligands, *European Journal of Inorganic Chemistry*, 1440-1446.
- Sasikumar, G., Arulmozhi, S., Ashma, A., Sudha, A., Askar ali, S. J. 2019. Mixed ligand ternary complexes of Co(II), Ni(II), Cu(II) and Zn(II) and their structural characterization, electrochemical, theoretical and biological studies, *Journal of Molecular Structure*, 1187: 108-120.
- Schiff, H. 1864. Mittheilungen aus dem Universitätslaboratorium in Pisa: Eine neue Reihe organischer Basen, *Justus Liebig's Annalen der Chemie*, 131: 118-119.
- Theetharappan, M., Subha, L., Balakrishnan, C., Neelakantan, M. A. 2017. Binding interactions of mixed ligand copper(II) amino acid Schiff base complexes with biological targets: Spectroscopic evaluation and molecular docking, *Applied Organometallic Chemistry*, 31:e3713.
- Uddin, M. N., Ahmed, S. S., Rahatul Alam, S. M. 2020. REVIEW: Biomedical applications of Schiff base metal complexes, *Journal of Coordination Chemistry*, 73(23): 3109-3149.
- Zhang, C., Feng, L., Chen, Z. 2007. Synthesis and photophysical processes of a novel 1,10-phenanthroline-containing *p*-conjugated chromophores and Zn(II) chelated complex, *Spectrochimica Acta Part A*, 66: 1204-1207.
- Zhang, Y. 2017. On Study of New Progress and Application of Coordination Chemistry in Chemistry and Chemical Industry in Recent Years, *IOP Conf. Series: Earth and Environmental Science*, 100: 012020.
- Zhao, P., Wei, Q., Dong, J., Ding, F., Li, J., Li, L. 2016. Synthesis, structure and spectroscopic studies on DNA binding, BSA interaction of a nickel(II) complex containing l-methionine Schiff base and 1,10-phenanthroline, *Journal of Coordination Chemistry*, 69(16): 2437-2453.
- Zhong, C., Huang, H., He, A., Zhang, H. 2008. Synthesis and luminescent properties of novel polymeric metal complexes with bis(1,10-phenanthroline) group, *Dyes and Pigments*, 77: 578-583.



¹ Boğaziçi University, Physics Department

Introduction

We live on a planet that consists of many living things. So far, we have not found any intelligent life other than Earth, so our saying that our world is impressive would not even suffice to describe it. It does not mean that the other planets in our solar system are dull and not attractive. We constantly examine the other planets in our solar system and still find new things; so far, we know a lot of them but not enough. I want to talk about a specific galaxy object, debated for its planetary privileges; Pluto was once known as a planet, nowadays known as a dwarf planet in the Kuiper Belt. [1]

Curiosity under the night sky

Since the beginning of human life, everyone has wondered about the night sky. Under the night sky, people must have wondered what those dots that shine brightly are? Where did they come from? Thanks to scientific studies, we now know that these are stars, and we can examine them better and better each day thanks to our developing technology. Of course, the sky is full of stars. Many of these stars are unbelievably distant from us, such that we use astronomical length measures such as light years. Some of those stars are dead, but we still see them because of how ridiculous our distance from them is.

We also know that not all the bright dots in the sky are stars. There are some planets among them. They are not as far as the stars; these planets belong to our solar system. Since other planets are very distant, we cannot see them as bright. Not all the planets in our solar system are visible to the human eye because they are not close enough to our Sun and don't reflect light that

much. Among all these planets, I want to talk about one in specific. The smallest and furthest “planet” in our solar system: is Pluto.

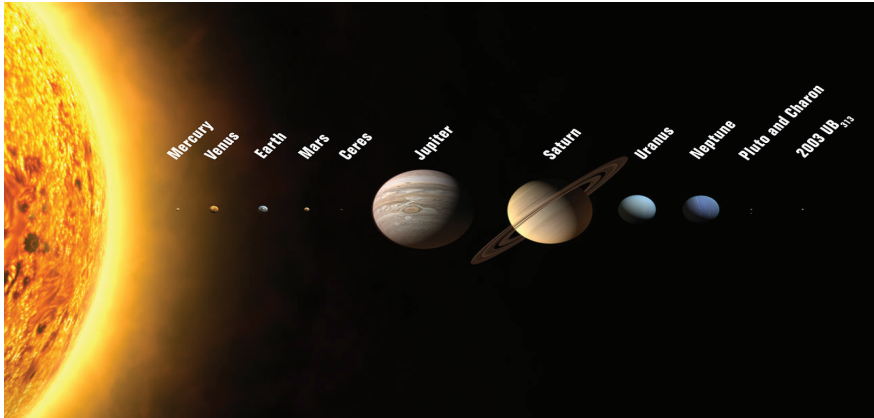


Figure 1: The Solar System.

Pluto is the ninth planet in our solar system and the most distant one from our Sun. It is also a part of the Kuiper Belt, one of our most prominent members. Kuiper Belt is a zone, a ring, beyond Neptune. It consists of hundreds of thousands of objects, or



Figure 2: A colourful landing on Pluto (Animation).NASA

bodies (around one trillion comets), mostly made of ice and rock.[2] Even though I referred to Pluto as a planet, it has been a dwarf planet since 2006. We should start from when Pluto was discovered to understand why it is called a dwarf planet.

Discovery and Early Studies of Pluto

Since the beginning of human history, the first six planets have been known to us because we can see them with the naked eye but not all time. Pluto was discovered just after the discovery of Uranus and Neptune, with the help of telescopes. A scientist named Percival Lowell thought there had to be a planet beyond Neptune, namely Planet X because there were some perturbations of Uranus and Neptune's (orbital) motion. However, he couldn't find the planet; unfortunately, he died before achieving his goal.



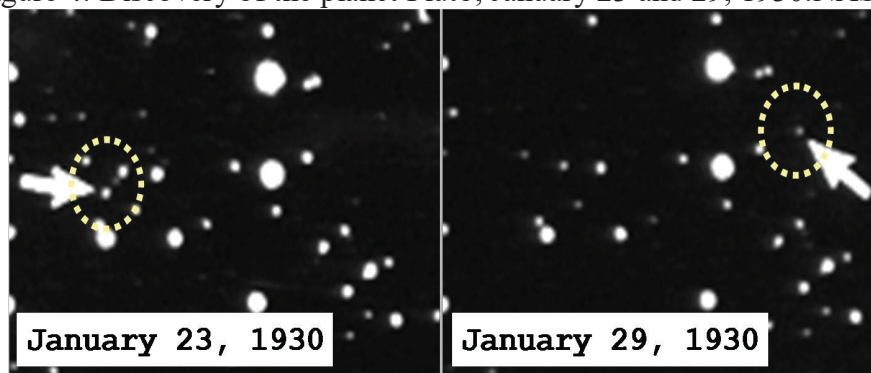
Figure 3: Clyde Tombaugh, in Kansas.NASA

Clyde Tombaugh, who was the observing assistant at that time, was hired to observe this so-called planet X. After looking at the sky for many nights in hopes of finding planet X, he found it on the date February 18 1930 [3]; what he was looking for: a planet, which was named Pluto later on. This observation process took less than a year. Although he found Pluto, it was not the planet X they were expecting because Pluto's mass, or in other words, its gravitational force, was too small for creating perturbations. So even though they didn't aim to find Pluto, they ended up with it.

The name Pluto comes from a god in Roman mythology. God named Pluto is the god of the underworld. The planet Pluto is the outermost planet in our system, and the underworld in these mythologies is also the furthest one from the Earth, hence the name Pluto. Pluto also

has a symbol ♇, which represents its first two letters and initials of Percival Lowell, the person who led to the discovery of Pluto. In 2006, the American Dialect Society decided that the word "plutoed" is the word of the year. "to pluto", someone means "to demote or devalue someone or something".[4]

Figure 4: Discovery of the planet Pluto, January 23 and 29, 1930.NASA



Earlier, famous scientists thought Pluto was Neptune's Moon, which somehow escaped its orbit.[5] They did not just make that up because Triton, the biggest Moon of Neptune, had some similar properties to Pluto. Their sizes are very close, and Triton's period around Neptune is almost equal to Pluto's period of rotation. Scientists believed that Pluto was also a moon of Neptune, and when the two moons encountered, this gave rise to the ejection of Pluto and Triton to have a retrograde orbit which we can still observe. But this theory didn't last long because Pluton was not massive enough to change Triton's trajectory oppositely. After the discovery of Charon (the biggest Moon of Pluto) in 1978, it was no longer possible to assume that Pluto escaped Neptune's orbit and then had a moon of its own.

Everything was great for Pluto since its discovery in 1930; it was a planet, after all! However, Pluto didn't know that people would later see

Pluto as an ordinary object. On August 30 1992, two scientists found an object orbiting beyond Neptune, in a region often called the

Trans-Neptunian region. There were thousands of objects later called Trans-Neptunian Objects (shortly TNOs). Scientists thought that among these TNOs, some could be more massive than Pluto. And in fact, they found one in October of 2003. An object orbiting the Sun was slightly more massive than Pluto, and it even has its moons! They named this object 2003 UB₃₁₃. This discovery made scientists question whether Pluto should be a planet or not.

To specify what a "planet" is, the International Astronomical Union (or IAU) decided to create a commission to get the opinions of professional astronomers and scientists, even historians, writers, and educators. They concluded some meetings. The head of the IAU Planet Definition Committee explained an essential point that they considered while defining a "planet". He said they wanted to avoid information like; distances, magnitudes, and periods. After some debates, the definition took its final form on 2006 August 24. Definition of a planet is A celestial body that,

- 1)It should orbit around the Sun.
- 2)It must have enough mass to achieve hydrostatic equilibrium and, therefore, should have a round shape.
- 3) It should be a neighbourhood of its orbit should be cleared

Here we see that Pluto satisfies the two conditions. However, the 3rd condition is not fulfilled; Pluto has not cleared its orbit. Therefore, Pluto should not be a planet anymore. However, it was not any space object either. IAU also established a new category called "dwarf planets". They are more massive members of their population of things, with close

origins and compositions to each other. They occupy the same neighbourhood as well. As a result, Pluto (also Eris, Makemake, Haumea, and Ceres, the largest object in the asteroid belt) has been called a dwarf planet since then (although the scientific community does not fully accept this).

About two years later, IAU decided to add another type of object for trans-Neptunian dwarf planets that resemble Pluto. These objects are called "plutoids". It was proposed by the IAU committee and accepted worldwide. These objects are celestial bodies orbiting around the Sun, with a semimajor axis greater than Neptune's. Plutoids also have enough mass to create stronger gravity than rigid body forces, achieving a hydrostatic equilibrium shape like planets. Of course, they also do not satisfy the last condition. Their satellites are not called plutoids, even though some are close in mass compared to the plutoids they revolve around. Furthermore, we only know two plutoids, which are Pluto and Eris. It is assumed that there should be more than just two, and maybe it will be discovered in the future.[6]

Properties and Some Observations of Pluto

The Surface

Pluto is very far away from our Sun. It is also tiny in radius (about 2/3 of the Moon). Therefore it has a small surface. This property of Pluto causes low temperatures in the exterior and the atmosphere. Because of this, Pluto's surface plains are mostly made of nitrogen ice, which is about 98%. Some observations also show carbon



Figure 5: Surface of Pluto, with enhanced colours to point out surface differences.NASA

monoxide's absorption and methane's presence in solid form, according to some measurements. [7]

As you can see from the picture, the colour of the surface varies a lot from place to place, brown and dark orange, also white in general. Pluto is one of the most contrastive objects in our Solar System, along with Iapetus (Saturn's Moon).

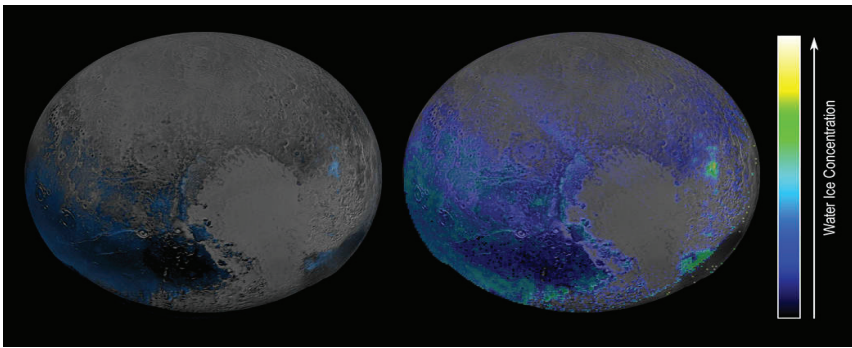


Figure 6 Water ice, NASA

In the early 1990s, scientists discovered ices of water. They have used some new ground-based instrumentations for this discovery. As we can see, the blue regions on the right picture are the parts with water ice.

The surface includes some shapes, specific enough to name them: the Heart (Tombaugh Regio) and the Whale (Cthulhu Macula). [8] The Heart is a relatively bright area mostly made of nitrogen and carbon monoxide. It also does not include any craters, as we can see, which leads to the idea that it is younger than 10



Figure 7: Western lobe of the Heart (Sputnik Planitia), NASA.

million years old. The whale is in a dark area. There is also one called Brass Knuckles, a series of dark spots.

The Interior Structure

We said that Tombaugh Regio (the Heart) does not have craters, so it has to be young. It also suggests that there has to be some geologic activity, so the interior could still be alive, even if very little.

Pluto's density is about twice the water's. This value brings the idea that Pluto is mainly composed of materials like silicate rock and maybe some organic compounds that are denser than water ice. Pluto's interior is believed to have an inner rocky core, surrounded by some water, which is surrounded by water ice.

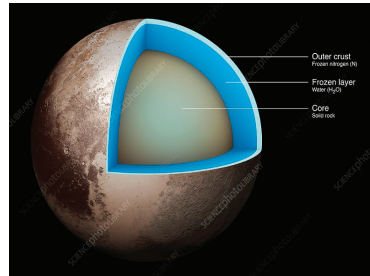


Figure 8: Internal structure of Pluto.NASA

Scientists believe there is a liquid layer because radioactive elements' decay will heat the ices closer to the silicate core. It is possible this heating continues today, and the ocean below the ice slowly gets bigger and bigger.

The Atmosphere of Pluto

Even though the scientists detected methane as ice on the surface in 1976, which gave the idea Pluto could have an atmosphere, they could not observe this for another decade. Pluto's atmosphere was followed in 1988, while Pluto was passing in front of a star concerning Earth. A thin atmosphere was detected due to the light



Figure 9: Haze layer on Pluto, by New Horizons. (NASA)

from the star behind Pluto. [9] Scientists thought that the gases in the atmosphere must be in equilibrium with their ice form on the surface. So, if there were even a tiny change in the temperature, this would result in a significant difference.

About a few years later, Pluto was slightly warmer than usual due to perihelion, and it was a perfect time to study the atmosphere. Scientists calculated the surface pressure, and it was, of course, much lower compared to our surface pressure. The atmosphere might not be detectable during aphelion because of the weak sunlight.

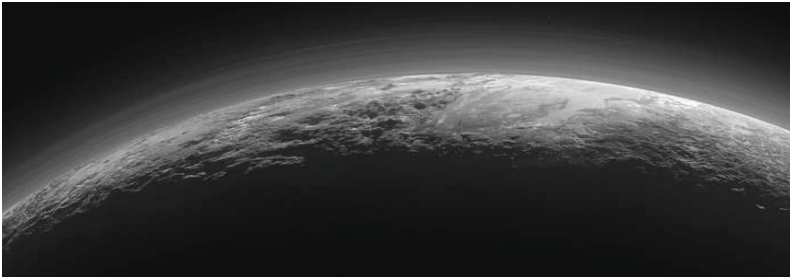


Figure 10: Pluto's atmosphere and surface. NASA

Astronomers found that the primary gas in Pluto's atmosphere is nitrogen, just like in Earth (and Triton, Titan). As expected, there is also some methane, along with very little carbon monoxide and hydrogen cyanide.

Pluto's Moons

Pluto has five moons, also called natural satellites. The largest and the closest one is Charon, which was discovered in 1978. It is relatively big, half the size of Pluto. It does not revolve around Pluto. They revolve



Figure 11: Charon and Pluto NASA

around a common centre of mass outside Pluto because Charon is massive enough compared to Pluto and has achieved hydrostatic equilibrium too. Sometimes Pluto and Charon are referred to as a double system.

Charon's revolution period is precisely equal to Pluto's, called a synchronous orbit. The outcome of this phenomenon is that Charon is visible from only one hemisphere of Pluto. If you imagine you are on the surface of Pluto, you wouldn't see Charon rise or set anytime, and you would only see one face of it, just like Earth and the Moon.

Charon's surface colours are not as varied as Pluton's. It also contains water in the solid form, and it covers most of its surface. Although Pluto has solid methane, Charon seems to have not. Its interior is slightly less dense and made of silicates and organic compounds, and the lower density might be due to having a lower fraction of rock.

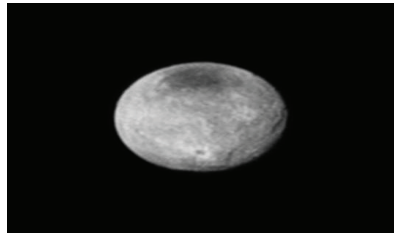


Figure 12: Charon, by New Horizons. NASA

Other than Charon, there are four other moons of Pluto. These are called (from closest to Pluto to furthest) Styx, Nix, Kerberos, and Hydra.

These are all names from mythologies, just like Pluto. These four moons are not just further away from Pluto than Charon is but also

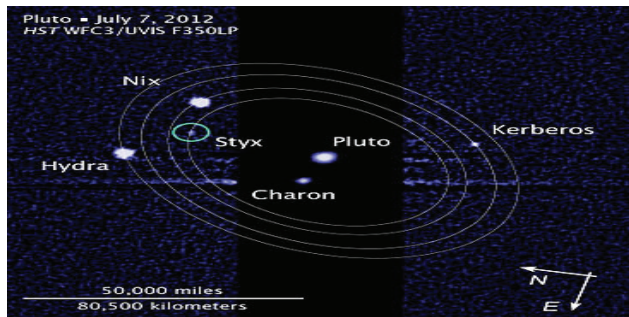


Figure 13: Observed by Hubble Space Telescope, NASA.

less massive. None of them has achieved hydrostatical equilibrium due to their low mass.

Latest Observations about Pluto and Conclusion

Around the time New Horizons flew over Pluto, scientists of New horizons published what they found on Pluto and what was possible there. They said, "Pluto displays a surprisingly wide variety of geological landforms, including those resulting from glaciological and surface-atmosphere interactions as well as impact, tectonic, possible cryovolcanic, and mass-wasting processes." [10]. The possibility that the interior could still be "alive" was an idea that has found other bases later on.

For example, a study in 2017 shows that Tombaugh Regio, or the Heart, which is a plane on the surface of Pluto, is much younger than scientists have guessed. The Heart does not include craters, unlike any other planetary object's surface, which led to the idea that it is possibly more youthful than 10 million years old. But now scientists calculated that it is approximately 200.000 years old.[11]. It is much smaller than scientists expected and therefore surprised them a little. The idea that a portion of the surface is only 200.000 years old supported the idea that there could be tectonic movements even today.

About how Pluto was formed, at first, it was assumed that Pluto was a moon of Neptune and escaped its orbit, but several facts disclaimed this idea. Nowadays, scientists believe Pluto and Charon formed just like the Earth, and the Moon did. It is thought that Pluto and a primitive version of Charon collided. With the collision, most of the scattered pieces started to orbit Pluto, and in time, they formed Charon we know today. This theory could explain why they have common properties like almost equal density and also the reason why Charon is this massive. In

Earth – proto-Moon collision, it is believed that the Moon did not get all the elements in Earth due to its high-temperature origin. It could also explain the case of Pluto and Charon since Charon does not seem to contain methane, Unlike Pluto. [12]

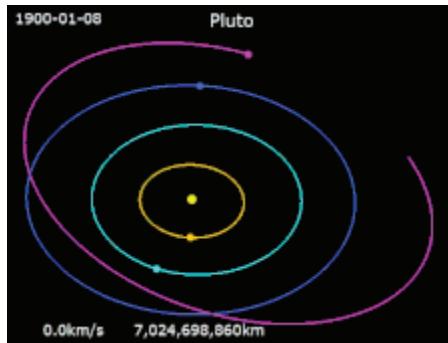


Figure 14: Animation of Pluto's orbit. Wikipedia.

An exciting property of Pluto is its orbit. As we can guess, Pluto requires a lot of time to complete its orbit around the Sun because it is far away from it. It takes approximately 250 years to complete one revolution, which is a very long time compared to Earth. The exciting part, however, is not this. Other planets have almost circular orbits, and they also move in a flat imaginary plane which is called the ecliptic. [13] Pluto, on the other hand, does not share this feature as the rest of them. It is moving in an inclined plane. Also, it has an elliptical orbit, as you can see from the animation. The animation shows Pluto's trajectory from 1900 to 2100, a very long time. You can see the Sun in the middle, then Saturn, Uranus, Neptune, and Pluto in order. This elliptical shape also means that for a short period of Pluto's revolution, Pluto is closer to the Sun than Neptune is. Pluto was closer to the Sun than Neptune between 1979 and 1999.

The biggest argument about Pluto is about what category it is in. Since scientists found other celestial objects that are similar to Pluto, it was argued whether it should stay as a planet or not. I have mentioned that it has been called a dwarf planet since then, with a new term called plutoid. There have been different opinions about it; even now, it is not accepted by all scientists. We know that International Astronomical Union (IAU) has decided on the name dwarf planet. However, the NASA administrator disagrees. In August 2019, in one of his speeches, he said, "You can write that NASA administrator declared Pluto once again." [14]

There are also some other ideas about this, even one that includes our own Moon. This exciting idea (on October 1, 2018) is to change the name of the dwarf planets and the Moon to a "planet". [15] This study claims that some scientists do not follow IAU's call on the "dwarf planet" and have used the name "planet" in their publications. The study also says that clearing the orbit should not be necessary to be a planet, including our Moon and some other moons. As we can see, debates over this topic continue, and they will probably stay the same in the incoming years.

A recent study, published on February 7 2020, suggests that there are icy winds on the surface of Pluto. Most of these atmospheric circulations are happening on Tombaugh Regio, known as the Heart. During the day, the atmosphere and the surface heat up, and this causes some of the ice to vaporize. When it is cold again at night, it returns to the solid form and results in nitrogen winds. Even though the atmosphere is thin, these winds still change the surface. As a result, there are dunes on the surface due to the winds. Note that the main reason for this atmospheric event is the Heart. The scientists said, "If you remove the Heart of Pluto, you won't have the same circulation." [16] They furthermore said Sputnik Planitia, Heart's left lobe, might be necessary to Pluto as much as oceans are to the Earth.

With our conclusion about Pluto, I want to look at the future. Recent studies suggest that in about 5.4 billion years, our Sun will turn into a red giant because of its properties as a star. When all the hydrogen is used, the Sun will collapse onto itself. The core will be denser, and then the Sun will start to grow. As it grows, even though there is a chance the planets' orbits will change, it might "eat" the planets in close range, such as Mercury, Venus, and possibly Earth.[17] As the Sun expands as a red giant, the habitable zone in the Solar System will also change. Pluto will warm up and no longer have an icy surface. We know there is some water ice, which means there will be liquid water. The ocean below the surface will be free from the frozen layer above. There might be no life in the Solar System at that time despite the habitable zone, but Pluto with a new form may still be there

My thanks go to one of my undergraduate students Ali Rıza Özer for his help in helping on the manuscript.

References

- [1] <https://solarsystem.nasa.gov/planets/dwarf-planets/pluto/overview/>
- [2] <https://www.space.com/43-pluto-the-ninth-planet-that-was-a-dwarf.html>
- [3] <https://www.britannica.com/place/Pluto-dwarf-planet/Plutos-moons>
- [4] <https://www.nbcnews.com/id/wbna16529756>
- [5] <https://www.britannica.com/place/Pluto-dwarf-planet/Plutos-moons>
- [6] <https://www.iau.org/news/pressreleases/detail/iau0804/>
- [7] https://www.wikiwand.com/en/Geology_of_Pluto
- [8] https://www.wikiwand.com/en/Geography_of_Pluto
- [9] <https://www.britannica.com/place/Pluto-dwarf-planet/The-atmosphere>
- [10] <https://arxiv.org/abs/1510.07704>
- [11] <https://www.hou.usra.edu/meetings/lpsc2017/pdf/1746.pdf>
- [12] <https://www.britannica.com/place/Pluto-dwarf-planet/Origin-of-Pluto-and-its-moons>
- [13] <https://www.wikiwand.com/en/Ecliptic>
- [14] <https://www.news18.com/news/buzz/nasa-chief-has-declared-pluto-a-planet-once-again-2287607.html>
- [15] <https://www.livescience.com/63716-pluto-earth-moon-are-planets.html>
- [16] <https://www.livescience.com/pluto-heart-powers-icy-winds.html>
- [17] <https://phys.org/news/2016-05-earth-survive-sun-red-giant.html#:~:text=Red%20Giant%20Phase%3A,collapses%20under%20its%20own%20weight.>

Figure 2: The Solar System. Source: <https://www.iau.org/static/archives/images/screen/iau0601a.jpg>

Figure 2: A colourful landing on Pluto(Animation). Source: <https://photojournal.jpl.nasa.gov/thumb/PIA11709.jpg>

Figure 3: Clyde Tombaugh, in Kansas. Source: https://www.kshs.org/portraits/graphics/tombaugh_clyde.jpg

Figure 4: Discovery of the planet Pluto, January 23 and 29, 1930. Source: <https://exploredspace.com/wp-content/uploads/2016/02/fig8-pluto-discovery.jpg>

Figure 5: Surface of Pluto, with enhanced colours to point out surface differences. Source: https://www.nasa.gov/sites/default/files/styles/full_width_feature/public/thumbnails/image/crop_p_color2_enhanced_release_small.png

Figure 6: Water ice. Source: https://www.nasa.gov/sites/default/files/styles/full_width_feature/public/thumbnails/image/nh-global-water-ice.jpg

Figure 7: Western lobe of the Heart (Sputnik Planitia) ,NASA. Source: https://www.nasa.gov/sites/default/files/styles/full_width/public/thumbnails/image/nh-pluto_heart.jpg.png?itok=iLtBi-8l

Figure 8: Internal structure of Pluto. Source: https://media.sciencephoto.com/image/c0269672/800wm/C0269672-Structure_of_Pluto_illustration.jpg

Figure 9: Haze layer on Pluto, by New Horizons. (NASA). Source: https://www.nasa.gov/sites/default/files/styles/full_width_feature/public/thumbnails/image/01142016_color_haze_layers_no-scale.png

Figure 10: Pluto's atmosphere and surface. NASA. Source: https://www.nasa.gov/sites/default/files/styles/full_width/public/thumbnails/image/nh-apluto-wide-9-17-15-final_0.png?itok=KgDuBFqu

Figure 11: Charon and Pluto. Wikipedia. Source: https://upload.wikimedia.org/wikipedia/commons/2/2f/Pluto-Charon_system-new.gif

Figure 12: Charon, by New Horizons. NASA. Source: https://www.nasa.gov/sites/default/files/thumbnails/image/nh-charon_150709_0.png

Figure 13: Observed by Hubble Space Telescope, Wikipedia. Source: https://upload.wikimedia.org/wikipedia/commons/thumb/1/1a/Pluto_moon_P5_discovery_with_moons%27_orbits.jpg/1024px-Pluto_moon_P5_discovery_with_moons%27_orbits.jpg

Figure 14: Animation of Pluto's orbit. Wikipedia. Source: https://upload.wikimedia.org/wikipedia/commons/a/af/Animation_of_Pluto_orbit.gif



CHAPTER 6

**A STUDY ON EXTENSION OF MADDOX'S
SPACE AND ITS CERTAIN MATRIX
TRANSFORMATIONS**

Fadime GÖKÇE¹,

¹ Assoc. Prof. Dr. Fadime GÖKÇE, Pamukkale University, Faculty of Science,
Denizli, Turkey Email:fgokce@pau.edu.tr Orcid No: 0000-0003-1819-3317

1. INTRODUCTION

One of the most basic concepts of mathematics is the notions of series (or sequences). The study about the notion of convergence of the series goes back to very old times. In the absence of the concept of convergence, which we now know well, mathematicians arrived at some contradictory results about the sum of the series by performing random operations, and they could not resolve these contradictions for a long time. A number of the existing contradictions have came up with a solution with the help of Gauss's binomial theorem, which explains the expression $(1+x)^n$ where $n \in \mathbb{N}$. Cauchy, who has studies on this subject, has developed a new perspective by formulating the definition of convergence of the sequence (or series). Thus, the concepts of convergence and divergence of the sequence (series) emerged. Although this definition given by Cauchy removed many uncertainties at that time, it caused the following problem to arise: Could the non-convergent series have a sum? The answer to this question is given by expanding the concept of convergence. So, the summability theory was born. For example, taking $x = -1$ in the following formula

$$1 + x + x^2 + \dots = \frac{1}{1-x} \quad (|x| < 1),$$

Euler has obtained the following equality

$$1 - 1 + 1 - 1 + \dots = \frac{1}{2}.$$

This is essentially wrong in terms of the concept of Cauchy convergent, because the series to the left of the equation is not convergent. However, the transformation sequence obtained via the 1st order Cesàro mean of the sequence (s_n) , the transformation sequence of partial sums of the sequence (x_n) , is

$$t_n = \frac{1}{n+1} \sum_{k=0}^n s_k = \frac{1}{2} + \frac{1}{4(n+1)} [1 + (-1)^n]$$

and also the transformation sequence (t_n) converges to $1/2$. Therefore, the sum of the above divergent series is calculated as $1/2$ with this method. This example have a great importance as it shows that divergent series can be summable.

After all of these processes, nowadays, the summability theory has an important role in applied mathematics, engineering sciences, and analysis essentially in functional analysis, approximation theory, calculus, quantum mechanics, probability theory, Fourier analysis. One of the main subjects in the summability theory is the theory of sequence spaces that concerns with the generalization of the notion of convergence for series and sequences. In this context, the main purpose of the theory is to assign a limit value for divergent series or sequences by using a transformation which is given by the most general linear mappings of

infinite matrices. The reason why matrices are used for a general linear operator is that a linear operator from a sequence space to another one can be given by an infinite matrix. In this regard, the literature in the field of summability theory continues to develop not only on the generation of sequence spaces through the matrix domain of a particular matrices such as Hölder, Euler, Cesàro, Hausdorff, Nörlund and weighted mean matrices and on the investigation of their topological, algebraic structures and matrix transformations but also on examinations about new series spaces derived by several absolute summability methods from a different perspective (for instance, Gökçe & Sarigöl,2020a; Gökçe & Sarigöl, 2020b; Gökçe & Hazar, 2019; Gökçe & Sarigöl,2018a; Gökçe & Sarigöl, 2018b; Mohapatra & Sarigöl, 2017; Ilkhan, 2020). In a recent study (Gökçe & Hazar, 2019), the space $|A_f^\theta|_k$ has been introduced and studied. In the present study, we have introduced a new series space

$$|A_f^\theta|(\mu) = \left\{ x \in \omega : \sum_{n=0}^{\infty} \theta_n^{\mu_n-1} \left| \hat{a}_n \sum_{v=0}^n a_v x_v \right|^{\mu_n} < \infty \right\}$$

which is reduced to a lot of sequence spaces such as $|A_f^\theta|_k, l(\mu), |\bar{N}_p^\theta|(\mu)$ with special selections and examined in terms of algebraic and topological properties such as basis, duals, isomorphism and also, obtained the necessary and sufficient conditions for the matrix U belongs to the matrix classes $(|A_f^\theta|(\mu), |B_f^\psi|(\lambda)), (|A_f^\theta|(\mu), \Gamma)$, where $\Gamma = \{c, c_0, l_\infty\}$.

Firstly, we recall some known concepts. Any vector subspace of ω , the set of all complex (or real) sequences, is called a sequence space. In this respect, c, c_0, l_∞ are examples of sequence spaces which represent the sets of all convergent, null and bounded sequences. Besides, c_s, b_s stand for the spaces of all convergent, bounded series, respectively.

Let $X, Y \subset \omega, U = (u_{nv})$ be an arbitrary infinite matrix of complex components. If the series

$$U_n(x) = \sum_{v=0}^{\infty} u_{nv} x_v$$

converges for all $n \in \mathbb{N} = \{0, 1, 2, \dots\}$, then, U -transform of the sequence $x = (x_v)$ is denoted by $U(x) = (U_n(x))$. Also, it is said that U identifies a matrix transformation from the space X into the space Y , and denoted by $U \in (X, Y)$ or $U: X \rightarrow Y$ if $U(x) = (U_n(x)) \in Y$ for every $x \in X$.

A matrix T is called a triangle if $t_{nv} = 0$ for $v > n$ and otherwise $t_{nv} \neq 0$ for all n, v .

The concepts of domain of an infinite matrix U in X and the multiplier space of X and Y are, respectively, identified by

$$X_U = \{x = (x_n) \in \omega : U(x) \in X\} \quad (1)$$

$$S(X, Y) = \{t = (t_n) \in \omega : xt = (x_n t_n) \in Y \text{ for all } x \in X\}.$$

According to the notation of multiplier space, the α, β and γ duals of X are described as

$$X^\alpha = S(X, l) = \{t = (t_k) \in \omega : xt = (x_k t_k) \in l, \text{ for all } x = (x_k) \in X\},$$

$$X^\beta = S(X, c_s) = \{t = (t_k) \in \omega : xt = (x_k t_k) \in c_s, \text{ for all } x = (x_k) \in X\},$$

$$X^\gamma = S(X, b_s) = \{t = (t_k) \in \omega : xt = (x_k t_k) \in b_s, \text{ for all } x = (x_k) \in X\}.$$

Let X be a topological vector space that is a linear space compatible with a topology which makes both operations of the vector space continuous, over \mathbb{R} . If, for all $a \in \mathbb{R}$ and $x \in X$,

- There exists a subadditive function $f: X \rightarrow \mathbb{R}$ such that $f(0) = 0, f(x) = f(-x)$
- Scalar multiplication is continuous that is, $|a_n - a| \rightarrow 0, f(x_n - x) \rightarrow 0$ imply $f(a_n x_n - ax) \rightarrow 0$ as $n \rightarrow \infty$,

then, X is called a paranormed space.

Let take any subspace $X \subset \omega$. If it is a Frechet space with continuous coordinates $R_n: X \rightarrow \mathbb{C}$, where $R_n(x) = x_n$ for all $x \in X, n \in \mathbb{N}$, then X is called an FK -space. On the other hand, an FK -space whose metric is given by a norm is said to be a BK -space. These concepts have very important place in summability theory for instance, matrix transformations between FK -spaces (or BK -spaces) are continuous. It is said that an FK -space X including the set of all finite sequences have AK property if

$$\lim_{j \rightarrow \infty} x^{[j]} = \lim_{j \rightarrow \infty} \sum_{v=0}^j x_v e^{(v)} = x,$$

for each sequence $x \in X$. Here, $e^{(v)}$ is a sequence whose terms given by

$$e_{nv}^{(v)} = \begin{cases} 1, & n = v \\ 0, & n \neq v \end{cases}$$

for $v \geq 0$. For an example to these concepts, it can be presented the Maddox's space

$$l(\mu) = \left\{ x = (x_n) : \sum_{n=0}^{\infty} |x_n|^{\mu_n} < \infty \right\}.$$

This space is an *FK*-space with *AK* property with the following paranorm

$$f(x) = \left(\sum_{n=0}^{\infty} |x_n|^{\mu_n} \right)^{1/M}$$

where $M = \max \{ 1, \sup_n \mu_n \}$. The paranorm is the natural paranorm of the Maddox's space. On the other hand, in the case of $\mu_n \geq 1$ for all n , this space is a *BK*- space with the following norm

$$\|x\| = \inf \left\{ \xi > 0 : \sum_{n=0}^{\infty} |x_n/\xi|^{\mu_n} \leq 1 \right\},$$

(Maddox, 1969,1968,1967).

Throughout this paper, we assume that (θ_n) and (ψ_n) are arbitrary sequences of positive numbers, $\mu = (\mu_n)$ and $\lambda = (\lambda_n)$ are bounded sequences of positive real numbers, $0 < \inf \mu_n \leq H < \infty, 0 < \inf \lambda_n \leq K < \infty$ and μ_n^* is the conjugate of μ_n such that $1/\mu_n + 1/\mu_n^* = 1$ for $\mu_n > 0, 1/\mu_n^* = 0$ for $\mu_n = 1$.

Let consider an infinite series $\sum a_v$ with the sequence of n th partial sum $s = (s_n)$, and let $\theta = (\theta_n)$ be any sequence of positive real numbers, $\mu = (\mu_n)$ be a bounded sequence of positive real numbers. If

$$\sum_{n=1}^{\infty} \theta_n^{\mu_n-1} |U_n(s) - U_{n-1}(s)|^{\mu_n} < \infty,$$

the series $\sum a_v$ is said to be summable $|U, \theta_n|(\mu)$ (Gökçe & Sarıgöl, 2018b). It should be pointed out that the summability $|U, \theta_n|(\mu)$ includes several well-known summability methods for special cases of the matrix U and the sequences θ, μ . For instance, if we chose the Euler, Nörlund, Cesàro matrices instead of U , the summability method $|U, \theta_n|(\mu)$ is reduced to the summabilities $|E^r, \theta_n|(\mu), |N, p_n, \theta_n|(\mu), |C, \alpha, \beta|(\mu)$ (with $\theta_n = n$ for all n) (Gökçe & Sarıgöl, 2020b, 2018a, 2019), respectively, and again if we chose the weighted mean matrix instead of U , the summability method $|U, \theta_n|(\mu)$ is reduced to the summability

$|\bar{N}, p_n, \theta_n|(\mu)$ studied by Gökçe and Sarıgöl (2018). Here, the weighted mean matrix is given by

$$a_{nj} = \begin{cases} p_j/P_n, & 0 \leq j \leq n \\ 0, & j > n \end{cases}$$

where (p_n) is a positive sequence with $P_n = p_0 + p_1 + \dots + p_n \rightarrow \infty$ as $n \rightarrow \infty$, ($P_{-1} = p_{-1} = 0$). The space $|\bar{N}_p^\theta|(\mu)$ which is the set all of series summable by $|\bar{N}, p_n, \theta_n|(\mu)$ can be present as

$$|\bar{N}_p^\theta|(\mu) = \left\{ x = (x_\nu) \in \omega : \sum_{n=1}^{\infty} \theta_n^{\mu_{n-1}} \left| \frac{p_n}{P_n P_{n-1}} \sum_{\nu=1}^n P_{\nu-1} x_\nu \right|^{\mu_n} < \infty \right\}$$

Now, using factorable matrix, we introduce a new space

$$|A_f^\theta|(\mu) = \left\{ x = (x_\nu) \in \omega : \sum_{n=0}^{\infty} \theta_n^{\mu_{n-1}} \left| \hat{a}_n \sum_{\nu=0}^n a_\nu x_\nu \right|^{\mu_n} < \infty \right\}$$

which is the extension of the space $|\bar{N}_p^\theta|(\mu)$. Here, by a factorable matrix, we mean that the lower triangular whose entries given by

$$a_{n\nu} = \begin{cases} \hat{a}_n a_\nu, & 0 \leq \nu \leq n \\ 0, & \nu > n \end{cases} \tag{2}$$

where (\hat{a}_n) and (a_n) are any sequences of real numbers.

According to notation of domain, it can be easily seen that $|A_f^\theta|(\mu) = (l(\mu))_{T_A^{(\mu)}}$, where the matrix $T_A^{(\mu)} = (t_{n\nu}^{(\mu)})$ defined by

$$t_{n\nu}^{(n)} = \begin{cases} \theta_n^{1/\mu_n^*} \hat{a}_n a_\nu, & 0 \leq \nu \leq n \\ 0, & \nu > n. \end{cases} \tag{3}$$

So, with this equality, the connection between Maddox’s space $l(\mu)$ and the space $|A_f^\theta|(\mu)$ is established.

Besides, since each triangle matrix has a unique inverse (Wilansky, 1984), the triangle matrix $T_A^{(\mu)}$ has the inverse stated by $S_A^{(\mu)}$ whose terms is given by

$$s_{n\nu}^{(\mu)} = \begin{cases} \frac{-1}{\theta_{n-1}^{1/\mu_{n-1}^*} a_n \hat{a}_{n-1}}, & \nu = n - 1 \\ \frac{1}{\theta_n^{1/\mu_n^*} a_n \hat{a}_n}, & \nu = n \\ 0, & \nu \neq n - 1, n. \end{cases} \tag{4}$$

Before the main theorems, we remind certain lemmas which have important role in their proofs:

Lemma 1.1 (Grosse-Erdmann,1993) Let $\mu = (\mu_v)$, $\lambda = (\lambda_v)$ be arbitrary bounded sequences of strictly positive numbers.

(i) If $\mu_v > 1$ for all v , then, $U \in (l(\mu), l)$ iff there exists an integer $K > 1$ such that

$$\sup \left\{ \sum_{v=0}^{\infty} \left| \sum_{n \in B} u_{nv} K^{-1} \right|^{\mu_v^*} : B \subset \mathbb{N} \text{ finite} \right\} < \infty. \tag{5}$$

(ii) If $\mu_v \leq 1$ and $\lambda_v \geq 1$ for all $v \in \mathbb{N}$ then $U \in (l(\mu), l(\lambda))$ iff there exists some K such that

$$\sup_v \sum_{n=0}^{\infty} |u_{nv} K^{-1/\mu_v}|^{\lambda_n} < \infty.$$

(iii) If $\mu_v \leq 1$ for all v , then,

$$U \in (l(\mu), c) \Leftrightarrow (a) \lim_{n \rightarrow \infty} u_{nv} \text{ exists for each } v,$$

$$(b) \sup_{n,v} |u_{nv}|^{\mu_v} < \infty$$

$$U \in (l(\mu), c_0) \Leftrightarrow (c) \lim_{n \rightarrow \infty} u_{nv} = 0 \text{ for each } v, \quad (b) \text{ holds}$$

$$U \in (l(\mu), l_{\infty}) \Leftrightarrow (b) \text{ holds.}$$

(iv) If $\mu_v > 1$ for all v , then,

$$U \in (l(\mu), c)$$

$\Leftrightarrow (a')$ $\lim_{n \rightarrow \infty} u_{nv}$ exists for each v , (b') there exists a number $K > 1$ such that

$$\sup_n \sum_{v=0}^{\infty} |u_{nv} M^{-1}|^{\mu_v^*} < \infty,$$

$U \in (l(\mu), c_0) \Leftrightarrow (c')$ $\lim_{n \rightarrow \infty} u_{nv} = 0$ for each v , (b') holds

$$U \in (l(\mu), c_0) \Leftrightarrow (b') \text{ holds.}$$

Note that the condition (5) has a rather difficulties in applications. Lemma 1.2 produces a condition which is equivalent to (5) and also more practical in most cases. So, we will prefer following lemma in the proofs of our main theorems.

Lemma 1.2 (Sarigöl, 2013) Let $U = (u_{nv})$ be an infinite matrix with complex components, (μ_n) be a bounded sequence of positive numbers. If $W_\mu [U] < \infty$ or $L_\mu [U] < \infty$, then

$$(2c)^{-2}W_\mu [U] \leq L_\mu [U] \leq W_\mu [U],$$

where $c = \max\{1, 2^{H-1}\}, H = \sup_v \mu_v$.

$$W_\mu [U] = \sum_{v=0}^{\infty} \left(\sum_{n=0}^{\infty} |u_{nv}| \right)^{\mu_v}$$

and

$$L_\mu [U] = \sup \left\{ \sum_{v=0}^{\infty} \left| \sum_{n \in B} u_{nv} \right|^{\mu_v} : B \subset \mathbb{N} \text{ finite} \right\}.$$

Lemma 1.3. (Malkowsky & Rakocevic, 2000) Let R be a triangle. Then, for $X, Y \subset \omega, U \in (X, Y_R)$ iff $B = RU \in (X, Y)$.

Lemma 1.4. (Malkowsky & Rakocevic, 2007) Assume that X is an FK -space with AK property, R is a triangle, S is its inverse and Y is any subset of ω . Then, we have $U \in (X_R, Y)$ iff $\tilde{U} \in (X, Y)$ and $V^{(n)} \in (X, c)$ for all n , where

$$\tilde{u}_{nv} = \sum_{j=v}^{\infty} u_{nj} s_{jv}, n, v = 0, 1, \dots$$

$$v_{mv}^{(n)} = \begin{cases} \sum_{j=v}^m u_{nj} s_{jv}, & 0 \leq v \leq m \\ 0, & v > m. \end{cases}$$

Proposition 1.5. (Malkowsky & Rakocevic, 2007) Let (X, d) be a linear metric sequence space and $(b^{(n)})$ is a basis of it. Then, the sequence $(S(b^{(n)}))$ is basis of $Y = X_R$ with the metric d_R defined by $d_R(y, \tilde{y}) = d(R(y), R(\tilde{y}))$ for all $y, \tilde{y} \in Y$.

Lemma 1.6. (Wilansky, 1984) Let X and Y be BK -spaces, and U be an arbitrary infinite matrix of complex components. If U is a matrix

transformation from the space X into Y , that is, $U \in (X, Y)$, then it is a bounded linear operator.

2. THE SPACE $|A_f^\theta|(\mu)$

In this section, we begin to investigate certain algebraic and topological properties of the mentioned space.

Theorem 2.1

(a) The set $|A_f^\theta|(\mu)$ becomes a linear space with the coordinate-wise addition and scalar multiplication. Moreover, this space is an FK -space under the following paranorm

$$\|x\|_{|A_f^\theta|(\mu)} = \|T_A^{(\mu)}(x)\|_{l(\mu)} = \left(\sum_{n=0}^{\infty} |x_n|^{\mu_n}\right)^{\frac{1}{M}} \tag{6}$$

where $M = \max\{1, \sup_n \mu_n\}$.

(b) If $\mu_n = k$ for all $n \in \mathbb{N}$, the space $|A_f^\theta|(\mu)$ is a BK -spaces with the following norm

$$\|x\|_{|A_f^\theta|(\mu)} = \|T_A^{(k)}(x)\|_k.$$

Proof. The first part of the proof is a standard verification, so it is left to reader. Since the matrix $T_A^{(\mu)}$ is a triangle matrix, $|A_f^\theta|(\mu) = (l(\mu))_{T_A^{(\mu)}}$ and $l(\mu)$ is an FK -space, then it is written that $|A_f^\theta|(\mu)$ is also an FK -space from Wilansky's Theorem 4.3.2 (1984). This completes the proof.

The second part of the theorem can also be proved in similar method.

Theorem 2.2 The space $|A_f^\theta|(\mu)$ has a Schauder basis.

Proof. Let $y = T_A^{(k)}(x)$ for each $x \in |A_f^\theta|(\mu)$. It is known that the sequence $(e^{(n)})$ is the Schauder base of the Maddox's space $l(\mu)$. So, considering (6), it is written that

$$\left\|y - \sum_{v=0}^n y_v e^{(v)}\right\|_{l(\mu)} = \left\|x - \sum_{v=0}^n x_v S_A^{(\mu)}(e^{(v)})\right\|_{|A_f^\theta|(\mu)} \rightarrow 0 \text{ as } (n \rightarrow \infty)$$

which means that the sequence $S_A^{(\mu)}(e^{(v)})$ is the Schauder basis of the space $|A_f^\theta|(\mu)$.

Considering the Theorem 2.1-2.2, it can be said that the absolute series space $|A_f^\theta|(\mu)$ is a separable space because it is a linear metric space with a Schauder basis.

Theorem 2.3. There exists a linearly isomorphism between the space $|A_f^\theta|(\mu)$ and the Maddox's space $l(\mu)$.i.e., $|A_f^\theta|(\mu) \cong l(\mu)$.

Proof. To prove the theorem, it should be shown that there exists a linear bijection between $|A_f^\theta|(\mu)$ and $l(\mu)$. Let take into account the transformation $T_A^{(\mu)}: |A_f^\theta|(\mu) \rightarrow l(\mu)$ such that

$$y = T_A^{(\mu)}(x) = \left(\theta_n^{1/\mu_n^*} \hat{a}_n \sum_{v=0}^n a_v x_v \right) \text{ for all } x \in |A_f^\theta|(\mu).$$

Since the matrix corresponding the transformation $y = T_A^{(\mu)}(x)$ given by (3) is triangle, it is clear that the transformation $T_A^{(\mu)}$ is a linear bijection. Also,

$$\|x\|_{|A_f^\theta|(\mu)} = \|T_A^{(\mu)}(x)\|_{l(\mu)}$$

that is, the paranorm is preserved. Thus, the $|A_f^\theta|(\mu)$ is linearly isomorphic to the Maddox's space $l(\mu)$.

We describe the following sets:

$$D_1 = \left\{ z = (z_v) \in \omega : \exists K > 1, \sum_{v=0}^{\infty} \frac{K^{-1/\mu_v^*}}{\theta_v} \left(\left| \frac{z_v}{a_v \hat{a}_v} \right| + \left| \frac{z_{v+1}}{a_{v+1} \hat{a}_v} \right| \right)^{\mu_v^*} < \infty \right\},$$

$$D_2 = \left\{ z = (z_v) \in \omega : \exists K > 1: \sup_v \left\{ \left(\frac{\theta_v^{-1/\mu_v^*}}{K^{1/\mu_v} |\hat{a}_v|} \right) \left(\left| \frac{z_v}{a_v} \right| + \left| \frac{z_{v+1}}{a_{v+1}} \right| \right) \right\} < \infty \right\},$$

$$D_3 = \left\{ z = (z_v) \in \omega : \exists K > 1: \sup_n \left(\sum_{v=0}^{n-1} \frac{K^{-1/\mu_v^*}}{\theta_v} \left| \frac{1}{\hat{a}_v} \Delta \left(\frac{z_v}{a_v} \right) \right|^{\mu_v^*} + \frac{K^{-1/\mu_n^*}}{\theta_n} \left| \frac{z_n}{\hat{a}_n a_n} \right|^{\mu_n^*} \right) < \infty \right\},$$

$$D_4 = \left\{ z = (z_v) \in \omega : \sup_v \left(\left| \frac{\theta_v^{-1/\mu_v^*}}{\hat{a}_v} \Delta \left(\frac{z_v}{a_v} \right) \right|^{\mu_v} + \left| \frac{\theta_v^{-1/\mu_v^*} z_v}{\hat{a}_v a_v} \right|^{\mu_v} \right) < \infty \right\},$$

where $\Delta z_n = z_n - z_{n+1}$.

Theorem 2.4. If $\mu_v > 1$ for all v , then

$$\{|A_f^\theta|(\mu)\}^\alpha = D_1, \{|A_f^\theta|(\mu)\}^\beta = \{|A_f^\theta|(\mu)\}^\gamma = D_3$$

and if $\mu_v \leq 1$ for all v , then,

$$\{|A_f^\theta|(\mu)\}^\alpha = D_2, \{|A_f^\theta|(\mu)\}^\beta = \{|A_f^\theta|(\mu)\}^\gamma = D_4$$

Proof. By the definition of the β dual, $z \in \{|A_f^\theta|(\mu)\}^\beta$ if and only if $(z_n x_n) \in c_s$ for all $x \in |A_f^\theta|(\mu)$. It follows from (4) that

$$\begin{aligned} \sum_{z=0}^m z_v x_v &= \sum_{v=0}^m \frac{z_v}{a_v} \left(\frac{y_v}{\theta_v^{1/\mu_v^*} \hat{a}_v} - \frac{y_{v-1}}{\theta_{v-1}^{1/\mu_{v-1}^*} \hat{a}_{v-1}} \right) \\ &= \frac{z_m y_m}{a_m \theta_m^{1/\mu_m^*} \hat{a}_m} + \sum_{v=0}^{m-1} \frac{1}{\theta_v^{1/\mu_v^*} \hat{a}_v} \left(\frac{z_v}{a_v} - \frac{z_{v+1}}{a_{v+1}} \right) y_v \\ &= \sum_{v=0}^m h_{mv} y_v \end{aligned}$$

where $y_n = \theta_n^{1/\mu_n^*} \hat{a}_n \sum_{v=0}^n a_v x_v$ for $n \geq 0$ and

$$h_{mv} = \begin{cases} \frac{1}{\theta_v^{1/\mu_v^*} \hat{a}_v} \left(\frac{z_v}{a_v} - \frac{z_{v+1}}{a_{v+1}} \right), & 0 \leq v \leq m-1 \\ \frac{z_m}{a_m \theta_m^{1/\mu_m^*} \hat{a}_m}, & v = m \\ 0, & v > m \end{cases} \tag{7}$$

and so we get that $z \in \{|A_f^\theta|(\mu)\}^\beta$ iff $H \in (l(\mu), c)$. Using Lemma 1.1, it is immediately obtained that $z \in \{|A_f^\theta|(\mu)\}^\beta$ equals to $z \in D_3$ for $\mu_v > 1$ and $z \in D_4$ for $\mu_v \leq 1$ for all n , which concludes the part of proof.

The proof of other part can be proved in similar way, so it is left to reader.

3. MATRIX TRANSFORMATIONS

In this section, we give the characterizations of the matrix classes $(|A_f^\theta|(\mu), |B_f^\psi|(\lambda)), (|A_f^\theta|(\mu), \Gamma)$, where $\Gamma = \{c, c_0, l_\infty\}$.

Theorem 3.1 Assume that A, B are any factorable matrices, $U = (u_{nv})$ is arbitrary infinite matrix of complex components, (μ_n) and (λ_n) are any bounded sequences of positive numbers satisfying $\mu_n \leq 1$ and $\lambda_n \geq 1$ for all $n \in \mathbb{N}$. Then, $U \in \left(|A_f^\theta|(\mu), |B_f^\psi|(\lambda) \right)$ iff there exists an integer $K > 1$ such that, for $n = 0, 1, \dots$,

$$\sup_v \left(\left| \frac{\theta_v^{-1/\mu_v^*}}{\hat{a}_v} \Delta \left(\frac{u_{nv}}{a_v} \right) \right|^{\mu_v} + \left| \frac{\theta_v^{-1/\mu_v^*} u_{nv}}{\hat{a}_v a_v} \right|^{\mu_v} \right) < \infty \tag{8}$$

and

$$\sup_v \sum_{n=0}^{\infty} \left| K^{-1/\mu_v} \frac{\psi_n^{1/\lambda_n^*} \hat{b}_n}{\theta_v^{1/\mu_v^*} \hat{a}_v} \sum_{j=0}^n b_j \Delta \left(\frac{u_{jv}}{a_v} \right) \right|^{\lambda_n} < \infty \tag{9}$$

Besides, if $U \in \left(|A_f^\theta|(\mu), |B_f^\psi|(\lambda) \right)$, then U determines a bounded linear operator.

Proof. Let that $\mu_n \leq 1$ and $\lambda_n \geq 1$ for all $n \in \mathbb{N}$. Since $|A_f^\theta|(\mu) = (l(\mu))_{T_A(\mu)}$, considering Lemma 1.4, it can be written that $U \in \left(|A_f^\theta|(\mu), |B_f^\psi|(\lambda) \right)$ iff $\tilde{U} \in \left(l(\mu), |B_f^\psi|(\lambda) \right)$ and $V^{(n)} \in (l(\mu), c)$, where the matrices \tilde{U} and $V^{(n)}$ are defined by

$$\begin{aligned} \tilde{u}_{nv} &= \frac{1}{\theta_v^{1/\mu_v^*} \hat{a}_v} \Delta \left(\frac{u_{nv}}{a_v} \right) \\ v_{mv}^{(n)} &= \begin{cases} \frac{1}{\theta_v^{1/\mu_v^*} \hat{a}_v} \Delta \left(\frac{u_{nv}}{a_v} \right), & 0 \leq v \leq m-1 \\ \frac{u_{nv}}{a_v \theta_v^{1/\mu_v^*} \hat{a}_v}, & v = m \\ 0, & v > m. \end{cases} \end{aligned}$$

If we apply Lemma 1.1 to the matrix $V^{(n)}$, we obtain the condition (8). Moreover, since $|B_f^\psi|(\lambda) = (l(\lambda))_{T_B(\lambda)}$, $\tilde{U} \in \left(l(\mu), |B_f^\psi|(\lambda) \right)$ equals to $T_B^{(\lambda)} \circ \tilde{U}(x) \in l(\lambda)$ whenever $x \in l(\mu)$, i.e, $T_B^{(\lambda)} \circ \tilde{U} \in (l(\mu), l(\lambda))$. So, the condition (9) holds.

Besides of this, since $|A_f^\theta|(\mu)$ and $|B_f^\psi|(\lambda)$ are FK-spaces, U determines a bounded operator by Theorem 4.2.8 of Wilansky (1984). Hence, the proof is completed.

Theorem 3.2 Let A, B be any factorable matrices, $U = (u_{nv})$ be arbitrary infinite matrix of complex components. If (μ_n) is any bounded sequence of positive numbers satisfying $\mu_n > 1$ for all $n \in \mathbb{N}$, then $U \in (|A_f^\theta|(\mu), |B_f^\psi|)$ iff there exists an integer $K > 1$ such that, for $n \in \mathbb{N}$,

$$\sup_m \left(\sum_{v=0}^{m-1} \frac{K^{-1/\mu_v^*}}{\theta_v} \left| \frac{1}{\hat{a}_v} \Delta \left(\frac{u_{nv}}{a_v} \right) \right|^{\mu_v^*} + \frac{K^{-1/\mu_m^*}}{\theta_m} \left| \frac{u_{nm}}{\hat{a}_m a_m} \right|^{\mu_m^*} \right) < \infty \tag{10}$$

and

$$\sum_{v=0}^{\infty} \left(\sum_{n=0}^{\infty} \left| K^{-1} \frac{\hat{b}_n}{\theta_v^{1/\mu_v^*} \hat{a}_v} \sum_{j=0}^n b_j \Delta \left(\frac{u_{jv}}{a_v} \right) \right|^{\mu_v^*} \right) < \infty. \tag{11}$$

Also, if $U \in (|A_f^\theta|(\mu), |B_f^\psi|)$, then U determines a bounded linear operator.

Proof. Let $\mu_n > 1$ for all $n \in \mathbb{N}$. It is obvious from Lemma 1.4 that $U \in (|A_f^\theta|(\mu), |B_f^\psi|)$ if and only if $\tilde{U} \in (l(\mu), |B_f^\psi|)$ and $V^{(n)} \in (l(\mu), c)$ where the matrices \tilde{U} and $V^{(n)}$ are defined as above theorem with $\lambda_n = 1$ for all n . Applying Lemma 1.1 to the matrix $V^{(n)}$, the condition (10) is immediately obtained. Further, since $|B_f^\psi| = (l)_{T_B^{(\lambda)}}$, $\tilde{U} \in (l(\mu), |B_f^\psi|)$ equals to $T_B^{(\lambda)} \circ \tilde{U} \in (l(\mu), l)$. So, with together Lemma 1.1, we get the last condition (11).

If it is pointed out that the spaces $|A_f^\theta|(\mu)$ and $|B_f^\psi|$ are FK -spaces, the second part of Theorem is obtained as a result of Theorem 4.2.8 of Wilansky.

Theorem 3.3. Let $U = (u_{nv})$ be any infinite matrix of complex components, A be any factorable matrix, $\mu = (\mu_n)$ be a bounded sequence of positive numbers satisfying $\mu_n \leq 1$ for all n . Then, for $n = 0, 1, \dots$,

(a) $U \in (|A_f^\theta|(\mu), c)$ if and only if

$$\sup_v \left(\left| \frac{\theta_v^{-1/\mu_v^*}}{\hat{a}_v} \Delta \left(\frac{u_{nv}}{a_v} \right) \right|^{\mu_v} + \left| \frac{\theta_v^{-1/\mu_v^*} u_{nv}}{\hat{a}_v a_v} \right|^{\mu_v} \right) < \infty \tag{12}$$

$$\lim_{n \rightarrow \infty} \frac{1}{\theta_v^{1/\mu_v^*} \hat{a}_v} \Delta \left(\frac{u_{nv}}{a_v} \right) \text{ exists for each } v, \tag{13}$$

and

$$\sup_{n,v} \left| \frac{1}{\theta_v^{1/\mu_v^*} \hat{a}_v} \Delta \left(\frac{u_{nv}}{a_v} \right) \right|^{\mu_v} < \infty. \tag{14}$$

(b) $U \in (|A_f^\theta|(\mu), c_0)$ if and only if (12), (14) hold and

$$\lim_{n \rightarrow \infty} \frac{1}{\theta_v^{1/\mu_v^*} \hat{a}_v} \Delta \left(\frac{u_{nv}}{a_v} \right) = 0 \text{ for each } v, \tag{15}$$

(c) $U \in (|A_f^\theta|(\mu), l_\infty)$ if and only if (12), (14) hold.

Proof. Since the remaining part can be proved similar way, we just prove (a) to avoid repetition.

(a) Let $\mu_n \leq 1$ for all n . Note that $|A_f^\theta|(\mu) = (l(\mu))_{T_A^{(\mu)}}$. By

Lemma 1.4, it is said that $U \in$

$(|A_f^\theta|(\mu), c)$ iff $\tilde{U} \in (l(\mu), c)$ and $V^{(n)} \in (l(\mu), c)$, where these matrices described as in Theorem 3.1. Now, if we apply Lemma 1.1 to the matrices \tilde{U} and $V^{(n)}$, it follows that $\tilde{U} \in (l(\mu), c)$ if and only if the conditions (13) and (14) hold and also $V^{(n)} \in (l(\mu), c)$ if and only if the condition (12) holds which concludes the proof of (a).

Theorem 3.4. Assume that A is a factorable matrix, $U = (u_{nv})$ is any infinite matrix of complex components. If $\mu = (\mu_n)$ is a bounded sequence of positive numbers satisfying $\mu_n > 1$ for all $n \in \mathbb{N}$. Then,

(a) The necessary and sufficient conditions for $U \in$

$$\begin{aligned} & (|A_f^\theta|(\mu), c) \text{ are} \\ \sup_m \left(\sum_{v=0}^{m-1} \frac{K^{-1/\mu_v^*}}{\theta_v} \left| \frac{1}{\hat{a}_v} \Delta \left(\frac{u_{nv}}{a_v} \right) \right|^{\mu_v^*} + \frac{K^{-1/\mu_m^*}}{\theta_m} \left| \frac{u_{nm}}{\hat{a}_m a_m} \right|^{\mu_m^*} \right) < \infty, \exists K > 1, \end{aligned} \tag{16}$$

$$\lim_{n \rightarrow \infty} \frac{1}{\theta_v^{1/\mu_v^*} \hat{a}_v} \Delta \left(\frac{u_{nv}}{a_v} \right) \text{ exists for each } v, \tag{17}$$

and

$$\sup_n \sum_{v=0}^{\infty} \left| \frac{1}{\theta_v^{1/\mu_v^*} \hat{a}_v} \Delta \left(\frac{u_{nv}}{a_v} \right) K^{-1} \right|^{\mu_v^*} < \infty, \exists K > 1, \tag{18}$$

for $n = 0, 1, \dots$

(b) $U \in (|A_f^\theta|(\mu), c_0)$ if and only if (16), (18) hold and

$$\lim_{n \rightarrow \infty} \frac{1}{\theta_v^{1/\mu_v^*} \hat{a}_v} \Delta \left(\frac{u_{nv}}{a_v} \right) = 0 \text{ for each } v, \tag{19}$$

(c) $U \in (|A_f^\theta|(\mu), l_\infty)$ if and only if (16), (18) hold.

Proof. The theorem can be proved in similar method with Theorem 3.3, so it is left to reader.

Theorem 3.5. Let A be a factorable matrix, $U = (u_{nv})$ be any infinite matrix of complex components and $\Gamma = \{c, c_0, l_\infty\}$. If $U \in (|A_f^\theta|(\mu), \Gamma)$, then U defines a bounded linear operator.

Proof. Because of matrix transformations between FK -spaces are continuous, it can be immediately seen that the matrix operators between the spaces c, c_0, l_∞ which are BK -spaces, i.e, normed FK -spaces, and $|A_f^\theta|(\mu)$ are bounded linear operators.

4. APPLICATIONS

Our main theorems include the characterizations of certain well known matrix classes and also other new classes. In this section, with special selections, we obtain some of them. First, let take the identity matrix I instead of the matrix U . Then, it is immediately seen that the characterizations of the matrix classes lead to the comparisons of these summability methods. We express these results in Corollary 1 and Corollary 2.

Corollary 4.1. Let (μ_n) and (λ_n) be any bounded sequences of positive numbers satisfying $\mu_n \leq 1$ and $\lambda_n \geq 1$ for all $n \in \mathbb{N}$. Then $|A_f^\theta|(\mu) \subset |B_f^\psi|(\lambda)$ iff there exists an integer $K > 1$ such that

$$\sup_v \left\{ \left| K^{-1/\mu_v} \frac{\psi_v^{1/\lambda_n} \hat{b}_v b_v}{\theta_v^{1/\mu_v^*} \hat{a}_v a_v} \right|^{\lambda_v} + \sum_{n=v+1}^{\infty} \left| K^{-1/\mu_v} \frac{\psi_n^{1/\lambda_n} \hat{b}_n}{\theta_v^{1/\mu_v^*} \hat{a}_v} \Delta \left(\frac{b_v}{a_v} \right) \right|^{\lambda_n} \right\} < \infty, n = 0, 1, \dots$$

Proof. Let us take unit matrix I instead of U in Theorem 3.1. Then, the condition (8) holds directly, and also the condition (9) gives us the above condition.

Corollary 4.2. Let (μ_n) be arbitrary bounded sequence of positive numbers satisfying $\mu_n > 1$ for all $n \in \mathbb{N}$. Then, $|A_f^\theta|(\mu) \subset |B_f^\psi|(\lambda)$ iff there exists an integer $K > 1$ such that

$$\sum_{v=0}^{\infty} \left(\left| K^{-1} \frac{\hat{b}_v b_v}{\theta_v^{1/\mu_v^*} \hat{a}_v a_v} \right| + \sum_{n=v+1}^{\infty} \left| K^{-1} \frac{\hat{b}_n}{\theta_v^{1/\mu_v^*} \hat{a}_v} \Delta \left(\frac{b_v}{a_v} \right) \right| \right)^{\mu_v^*} < \infty, \text{ for } n = 0, 1, \dots$$

If we take $\hat{a}_n = \frac{p_n}{P_n P_{n-1}}$, $a_n = P_{n-1}$, then the space $|A_f^\theta|(\mu)$ reduces to the space $|\bar{N}_p^\theta|(\mu)$ studied by Gökçe and Sarıgöl (2018). So, the following results are obtained:

Corollary 4.3 Let $U = (u_{nv})$ be an infinite matrix of complex component, $\mu = (\mu_n)$ be arbitrary bounded sequence of positive numbers satisfying $\mu_n > 1$ for all $n \in \mathbb{N}$. Then $U \in (|\bar{N}_p^\theta|(\mu), |\bar{N}_q|)$ iff there exists some integer $K > 1$ such that, for $n = 0, 1, \dots$,

$$\sup_m \left| \frac{K^{-1} P_m u_{nm}}{\theta_m^{1/\mu_m^*} p_m} \right|^{\mu_m^*} < \infty,$$

$$\sum_{v=0}^{\infty} \left| K^{-1} \frac{P_v}{\theta_v^{1/\mu_v^*} p_v} \left(u_{nv} - \frac{P_{v-1}}{P_v} u_{n,v+1} \right) \right|^{\mu_v^*} < \infty,$$

$$\sum_{v=0}^{\infty} \left(\frac{K^{-1} P_v}{\theta_v^{1/\mu_v^*} p_v} \sum_{n=1}^{\infty} \frac{q_n}{Q_n Q_{n-1}} \left| \sum_{j=1}^n Q_{j-1} \left(u_{jv} - \frac{P_{v-1}}{P_v} u_{j,v+1} \right) \right| \right)^{\mu_v^*} < \infty.$$

Corollary 4.4 Let $U = (u_{nv})$ be an infinite matrix of complex components. If $\mu = (\mu_n)$ and $\lambda = (\lambda_n)$ are any bounded sequences of positive numbers and $\mu_n \leq 1$ and $\lambda_n \geq 1$ for all n , then, $U \in (|\bar{N}_p^\theta|(\mu), |\bar{N}_q^\psi|(\lambda))$ iff there exists an integer $K > 1$ such that, for $n = 0, 1, \dots$,

$$\sup_v \left| \frac{P_v}{\theta_v^{1/\mu_v^*} p_v} \left(u_{nv} - \frac{P_{v-1}}{P_v} u_{n,v+1} \right) \right|^{\mu_v} < \infty$$

$$\sup_m \left| \frac{P_m u_{nm}}{\theta_m^{1/\mu_m^*} p_m} \right| < \infty,$$

and

$$\sup_v \sum_{n=1}^{\infty} \left| \frac{\psi_n^{1/\lambda_n^*} q_n K^{-1/\mu_n} P_v}{Q_n Q_{n-1} \theta_v^{1/\mu_n^*} p_v} \sum_{j=1}^n Q_{j-1} \left(u_{nv} - \frac{P_{v-1}}{P_v} u_{n,v+1} \right) \right|^{\lambda_n} < \infty.$$

If we take $\mu_n = k, \lambda_n = 1$ (and $\lambda_n = k, \mu_n = 1$) for all n in addition to the above selections, we get the following results given by Sarigöl (2011a):

Corollary 4.5. Let $U = (u_{nv})$ be a triangle. The necessary and sufficient condition for $U \in \left(|\bar{N}_p^\theta|_k, |\bar{N}_q| \right)$ is

$$\sum_{v=1}^{\infty} \frac{1}{\theta_v p_v^{k^*}} \left\{ \sum_{n=v}^{\infty} \frac{q_n}{Q_n Q_{n-1}} \left| \sum_{m=v}^n Q_{m-1} (P_v u_{mv} - P_{v-1} u_{m,v+1}) \right| \right\}^{k^*} < \infty.$$

Corollary 4.6. Let $U = (u_{nv})$ be a triangle. The necessary and sufficient conditions for $U \in \left(|\bar{N}_p|, |\bar{N}_q^\theta|_k \right)$ are

$$\begin{aligned} \frac{P_v q_v}{Q_v p_v} u_{vv} &= o\left(\theta_v^{\frac{1}{k}-1}\right), \\ \sum_{n=v+1}^{\infty} \left| \theta_n^{1/k^*} \frac{q_n}{Q_n Q_{n-1}} \sum_{m=v+1}^n Q_{m-1} u_{m,v+1} \right|^k &= o(1), v \rightarrow \infty, \\ \sum_{n=v+1}^{\infty} \left| \theta_n^{1/k^*} \frac{q_n}{Q_n Q_{n-1}} \sum_{m=v}^n Q_{m-1} (u_{mv} - u_{m,v+1}) \right|^k &= o\left(\left(\frac{p_v}{P_v}\right)^k\right). \end{aligned}$$

Finally, we conclude this section with the result of Sarigöl (2011b) which is also a good example giving the connection between absolute summability factors and special matrix transformation:

Corollary 4.7 Let $(a_n), (b_n), (A_n), (B_n)$ be sequences of positive numbers connected by

$$Y_n^* = \hat{a}_n \sum_{v=1}^n a_{v-1} x_v, X_n^* = \hat{b}_n \sum_{v=1}^n b_{v-1} \varepsilon_v x_v$$

where (ε_v) is a sequence of complex numbers and $k \geq 1$. Then, $\sum_{n=1}^{\infty} |Y_n^*| < \infty \Rightarrow \sum_{n=1}^{\infty} |X_n^*|^k < \infty$

if and only if

$$\left| \frac{\hat{b}_v b_v \varepsilon_v}{\hat{a}_v a_v} \right| = o(1) \tag{20}$$

and

$$\left| \frac{1}{\hat{a}_v} \Delta \left(\frac{b_v \varepsilon_v}{a_v} \right) \right| \left(\sum_{n=v+1}^{\infty} \hat{b}_n^k \right)^{1/k} = O(1). \quad (21)$$

Proof . Take $\mu_n = 1, \lambda_n = k, \psi_n = 1$ and U as diagonal matrix with $c_{vv} = \varepsilon_v$ in Theorem 3.1. Then, $x \in |A_f^\theta|(\mu)$ iff $\sum_{n=1}^{\infty} |Y_n^*| < \infty$ and $\varepsilon x \in |B_f^\psi|(\lambda)$ iff $\sum_{n=1}^{\infty} |X_n^*|^k < \infty$. Further, (8) is automatically satisfied and the condition (9) reduces to

$$\sup_v \sum_{n=0}^{\infty} \left| \frac{\hat{b}_n}{\hat{a}_v} \sum_{r=v}^n b_r \left(\frac{u_{rv}}{a_v} - \frac{u_{r,v+1}}{a_{v+1}} \right) \right|^k < \infty,$$

and, it is clear that the last condition is equivalent (20) and (21). So, the proof is completed.

5. REFERENCES

- GÖKÇE, F., SARIGÖL, M.A. (2020a), Series spaces derived from absolute Fibonacci summability and matrix transformations, *Bollettino dell'Unione Matematica Italiana*, 13, 29-38.
- GÖKÇE, F., SARIGÖL, M.A. (2020b), On absolute Euler spaces and related matrix operators, *Proceedings of the National Academy of Sciences, India. Section A. Physical Sciences*, 90 (5), 769-775.
- GÖKÇE, F., GÜLEÇ, G. C. H. (2019), Compact and matrix operators on the space $|A_f^\theta|_k$, *Tbilisi Mathematical Journal*, 12(4), 1-13.
- GÖKÇE, F., SARIGÖL, M.A. (2019), Extension of Maddox's space $l(\mu)$ with Nörlund means, *Asian-European Journal of Mathematics*, 12(06), 2040005.
- GÖKÇE, F., SARIGÖL, M.A. (2018a), Generalization of the space $l(p)$ derived by absolute Euler summability and matrix operators. *Journal of Inequalities and Applications*, 2018, 133.
- GÖKÇE, F., SARIGÖL, M.A. (2018b), A new series space $|\bar{N}_p^\theta|(\mu)$ and matrix transformations with applications, *Kuwait Journal of Science*, 45(4), 1-8.
- GROSSE-ERDMANN, K.G. (1993), Matrix transformations between the sequence spaces of Maddox, *Journal of Mathematical Analysis and Applications*, 180, 223-238
- MADDOX, I. J. (1969), Some properties of paranormed sequence Spaces, *Journal of the London Mathematical Society. Second Series*, 316-322.
- MADDOX, I. J. (1968), Paranormed sequence spaces generated by infinite matrices, *Mathematical Proceedings of the Cambridge Philosophical Society*, 64, 335-340.
- MADDOX, I. J. (1967), Spaces of strongly summable sequences, *The Quarterly Journal of Mathematics*, 18, 345-355.
- MALKOWSKY, E., RAKOCEVIĆ, V. (2007), On matrix domains of triangles, *Applied Mathematics and Computation*, 189(2), 1146-1163.
- E MALKOWSKY, E., RAKOCEVIĆ, V. (2000), An introduction into the theory of sequence space and measures of noncompactness, *Zbornik radova (Beogr)*, 17, 143-234.
- MOHAPATRA, R. N., SARIGÖL, M.A. (2017), On matrix operators on the series space $|\bar{N}_p^\theta|_k$, *Ukrainian Mathematical Journal*, 69 (11), 1524-1533.

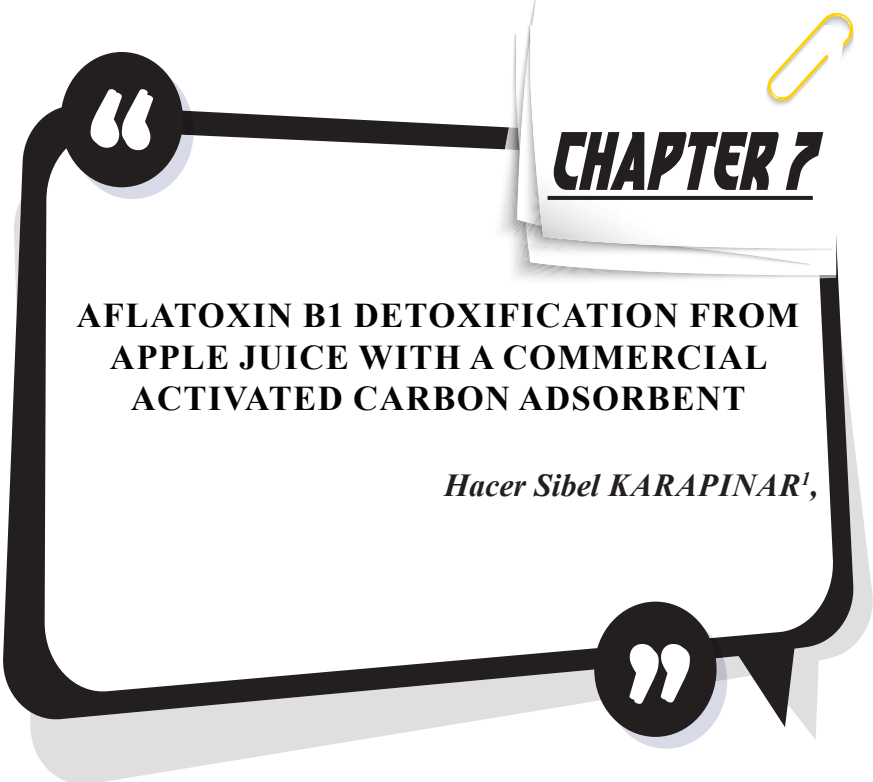
İLKHAN, M. (2020), Matrix Domain of a Regular Matrix Derived by Euler Totient Function in the Spaces c_0 and c . *Mediterranean Journal of Mathematics*, 17 (1), 1-21.

SARIGÖL, M.A. (2013), An inequality for matrix operators and its applications. *Journal of Classical Analysis*, 2, 145-150

SARIGÖL, M.A. (2011a), Matrix transformations on fields of absolute weighted mean summability, *Studia Scientiarum Mathematicarum Hungarica*, 48(3), 331-341.

SARIGÖL, M.A. (2011b), Characterization of general summability factors and applications, *Computers & Mathematics with Applications*, 62, 2665-2670.

WILANSKY, A. (1984), Summability Through Functional Analysis, Mathematics Studies, 85. North Holland, Amsterdam



CHAPTER 7

AFLATOXIN B1 DETOXIFICATION FROM APPLE JUICE WITH A COMMERCIAL ACTIVATED CARBON ADSORBENT

Hacer Sibel KARAPINAR¹,

¹ Lecturer Dr. Hacer Sibel KARAPINAR

Scientific and Technological Research & Application Center, Karamanoglu Mehmetbey University, 70200, Karaman, Turkey

Orcid ID; 0000-0002-0123-3901, E-mail:sibelkarapinar@kmu.edu.tr

1. INTRODUCTION

Since the existence of chemical pollutants in the food shackle is one of the most important basic health-threatening, public anxiety about food safety has increased significantly all over the world in the last decade (Pérez-Ortega et al., 2017). The secondary metabolites known as aflatoxins are produced by a number of fungal species, particularly *Aspergillus flavus*, *Aspergillus paraciticus*, and *Aspergillus nominous* (Novas and Cabral, 2002). *Aspergillus* toxins are commonly found in pears, apples, grapes, dried fruits, cereals, peanuts, spices, juice or milk, feed for animals and other food products (González-Jartín et al., 2019). Acute high exposure to Aflatoxin B1 (AFB1), the most toxic of the aflatoxins, can cause serious disease and death (Pascari et al., 2018). For the International Agency for Research on Cancer (IARC), AFB1 (Figure 1) is a group 1 carcinogen. Additionally, AFs are immunosuppressive, genotoxic, and teratogenic (IARC, 1982). This toxic metabolite develops when suitable conditions are not created during the harvesting, processing, transportation, and storage of food products. In more than 100 nations now, limit levels for AFB1 less than 20 $\mu\text{g kg}^{-1}$ have been established for diverse foods (Bhat and Reddy, 2017; Xue et al., 2019). Different cleaning methods were used during the pretreatment of the food samples to remove, minimize matrix influence, and concentrate AFB1. Some of the techniques employed include immunoaffinity columns (IACs), liquid-liquid extraction (LLE), and solid-phase extraction (SPE) (Pakshir et al., 2020; Pallares et al., 2017; Ye et al., 2019; Yang et al., 2020). Once a food product has become contaminated with mycotoxins, the compounds can be reduced or eliminated through the physical removal of the contaminated source substance, the inclusion of chemical binding agents or modifiers, or enzymatic therapies (Taheur et al., 2019). Since the European Union does not permit the chemical detoxification of food, new methods are required to improve food from a toxicological standpoint (EC No. 1881-2006). Therefore, nanotechnology can offer a new approach to detoxification with wide applications in food treatment. Various practices have been improved in the food area, including increasing food safety by allowing the detection of contaminants and promoting the bioavailability of certain compounds (He and Hwang, 2016). Also, very few studies have been done using nanomaterials for the elimination of natural toxins from food (Abd-Elsalam et al., 2017, Magro et al., 2016). Among some practices improved to reduce mycotoxins from aqueous solutions, chitosan-coated Fe_3O_4 particles, graphene oxide changed with chitosan materials, and magnetic carbon nanocomposites were used (Abbasi Pirouz et al., 2018, Luo et al., 2017, Zahoor and Ali Khan, 2016, Magro et al., 2016). Activated carbon has a very wide surface area, which makes it capable of adsorbing a lot of pollutants

(Bazana et al., 2019). According to reports, activated carbon has a significant capacity to absorb pollutants (Zahoor and Khan, 2016, Wongtangtintan et al., 2016). Activated carbon is an environmentally friendly, readily available, and low-cost adsorbent. In addition, activated carbons are porous materials with fast and strong adsorption capacity (Bilardi et al., 2020). The commonly used IAC cleaning method is complex, expensive, and time-consuming. The purpose of this study is to determine the performance of commercial activated carbon material for the detoxification of aflatoxin B1 from apple juice.

2. MATERIAL AND METHODS

2.1. Appliances and chemicals used

Acetonitrile ($\geq 99.9\%$, HPLC-grade), methanol ($\geq 99.9\%$, HPLC-grade), water (HPLC-grade), potassium bromide, and nitric acid (65.0-67.0%) were bought from Merck (Germany). Commercial powder activated carbon (extra pure) and the AFB1 (1000 ng ml^{-1}) standard solution was ensured from Sigma-Aldrich (USA) and solutions were protected in the fridge at $-16 \text{ }^\circ\text{C}$ and the dark. Working standards were diluted with methanol and prepared daily before the calibration curve was created. Vicam (AflaTest®, USA) supplied the immunoaffinity columns. All glassware was cleaned with $0.5 \text{ mol l}^{-1} \text{ HNO}_3$ and carefully rinsed with water before use. Aflatoxin B1 analyzes were performed on a high performance liquid chromatography (HPLC, USA) system.

2.2. System conditions

Analyzes were performed using an Agilent 1260 Infinity Quaternary Pump, a fluorescence detector (FLD, Agilent 1260), and the Agilent 1260 Infinity HPLC system. C18-ODS2 (250 mm- $5\mu\text{m}$ -4.6 mm, Waters, USA) column was used for the separation and quantitative analysis of aflatoxin components. Each sample with an injection volume of $150 \mu\text{l}$. The FLD detector was fixed at 360 nm excitation and 440 nm emission to get better spectra. The mobile phase was prepared as $100 \text{ mg l}^{-1} \text{ KBr}$ and $120 \mu\text{l l}^{-1} \text{ 65\% HNO}_3$, methanol: acetonitrile (60:40, v/v/v) in water. The flow rate was set at 1.1 ml min^{-1} at room temperature ($22 \text{ }^\circ\text{C}$). AFB1 post-column aflatoxin derivatization was performed using Cobra-Cell embedded in the HPLC system. The peak retention time for AFB1 was 23.269 minutes.

2.3. Preparation of Examples for Analysis

Aflatoxin extraction was performed as described in our previous work (Karapınar and Bilgiç, 2022). In this method, apple juice samples

were purchased from the market in closed packages. 25 ml of AFB1-free apple juice samples were taken, and 100 ml of water/methanol (30:70, v/v) was joined and mixed thoroughly for 5 minutes. The mixture was filtered through filter paper and then 15 ml of the filtrate was diluted to 30 ml with distilled water. The AFB1 standard (100 ng ml^{-1}) was added to the extract (Figure 2). 5 ml of the extract was placed in a polypropylene centrifuge tube. Commercial activated carbon adsorbent was added to the tube, vortexed for 10 seconds, and then shaken gently on the platform shaker for 20 minutes. The mixture was centrifuged (5000 rpm) for 5 minutes and the supernatant was taken from the tube and aflatoxin B1 was defined by HPLC-FLD. All samples were filtered through a $0.22 \mu\text{m}$ PTFE membrane filter and stored at $+4 \text{ }^\circ\text{C}$ in glass-amber bottles.

2.4. Method validation

For the applicability of the method, certain concentrations of AF working standards were added to AFB1-free apple juice samples and HPLC-column derivatization-FLD analysis was performed (Figure 2). To analyze the linearity, four injection matrix-matched calibrations (with five different doses) from the AFB1 standard in the concentration range of $0.25\text{-}10 \text{ ng ml}^{-1}$ were used and the correlation coefficient (R^2) of the linear regression equation was calculated. With a signal-to-noise ratio (S/N) of 3 and 10, the lowest detectable concentrations were determined as LOD (limit of detection) and LOQ (limit of quantification), respectively. LOD value of 0.18 ng ml^{-1} and LOQ value of 0.56 ng ml^{-1} were determined for AFB1. Relative standard deviations (RSD %) were calculated by adding aflatoxin B1 standard at a concentration of 2.0 ng ml^{-1} to the blank sample and determining the method reproducibility within days ($n=5$) and between days ($n=5$) (Table 1).

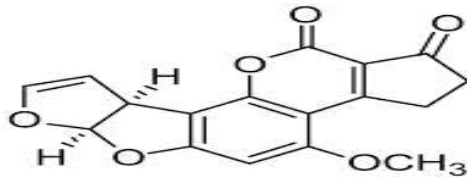


Figure 1. Chemical structure of AFB1

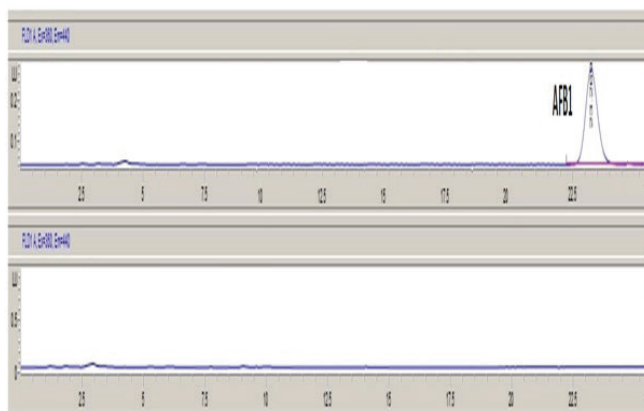


Figure 2. Chromatogram of 100 ng ml^{-1} for AFB1 extracted spiked apple juice and blank apple juice sample, respectively

Table 1. Linear range and equation, R^2 value, LODs, LOQs, method precision of AFB1 in apple juice

AF	Linear Range (ng ml^{-1})	Linear Equation	R^2	LOD (ng ml^{-1})	LOQ (ng ml^{-1})	RSD (%)	
						Intra-day (n= 8)	Inter-days (n=8)
AFB1	0.25 - 10.0	$y = 0.0298 + 8.6431x$	0.9994	0.18	0.56	0.4	6.7

3. RESULTS AND DISCUSSION

The quantity of adsorbent coupled to the sample solution has an impact on the number of active sites on the adsorbent and how fine it interacts with the target analytes (Karapınar and Balıkçioğlu, 2022). The effects of adsorbent amount, vortex time, and pH on the adsorption of commercial activated carbon and AFB1 from apple juice samples were investigated.

During aflatoxin extraction from apple juice samples, 1.0 mg, 2.0 mg, 4.0 mg, 8.0 mg, 12 mg, and 14 mg adsorbent amounts were tested and changes were determined. AFB1 recovery increased from 51.5% to 96.7% when the quantity of adsorbent was increased from 1.0 mg to 4.0 mg, and recoveries did not change notably when higher than 4.0 mg of commercial activated carbon was used (Figure 3). The large surface area of activated carbon facilitates the adsorption and π - π electrostatic

attraction of aflatoxins resulting from strong interaction with furan and coumarin rings (Yu et al., 2018).

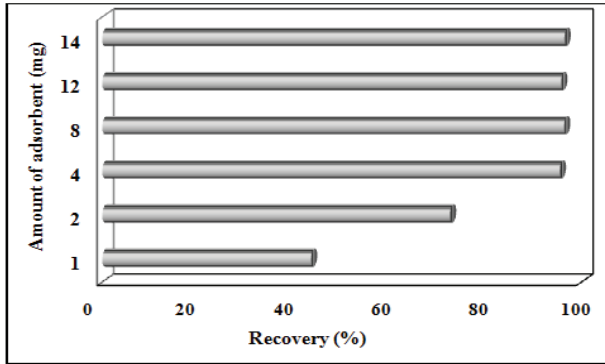


Figure 3. The amount of adsorbent from the parameters affecting the extraction efficiency

One of the parameters affecting the extraction efficiency is the pH of the solution. The effect of the pH of the solution on the recovery was investigated in the pH range of 3-8 (Figure 4). At high acidic or alkaline pH levels of AFB1, lower recovery efficiency may occur due to the degradation of its molecular structure. During the production of commercial activated carbon, the oxygen-containing functional groups on its surface are usually reduced. For this reason, changing the pH of the activated carbon is generally expected not to affect the surface charge (Mahpishanian and Sereshti, 2016).

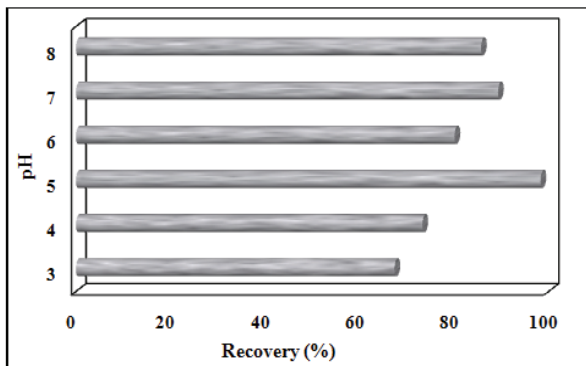


Figure 4. The pH from the parameters affecting the extraction efficiency

Mass transfer from the aqueous phase to the extraction phase can be effectively accelerated using vortexing (Amoli-Diva et al., 2015). In

order to ascertain the impact of vortex time on aflatoxin B1 recovery, it was extracted with 4.0 mg of commercial activated carbon while shaking for 1 to 10 minutes. Six minutes of vortex time was found to be sufficient for good adsorption-extraction efficiency (Figure 5). There was no significant difference in extraction yield between the sixth and tenth minutes. It is thought that the short vortex time may be due to the very low internal diffusion resistance of the adsorbent in the sample solution, the excellent dispersion of the adsorbent, or the high surface-to-volume ratio of the adsorbent (Khodadadi et al., 2018).

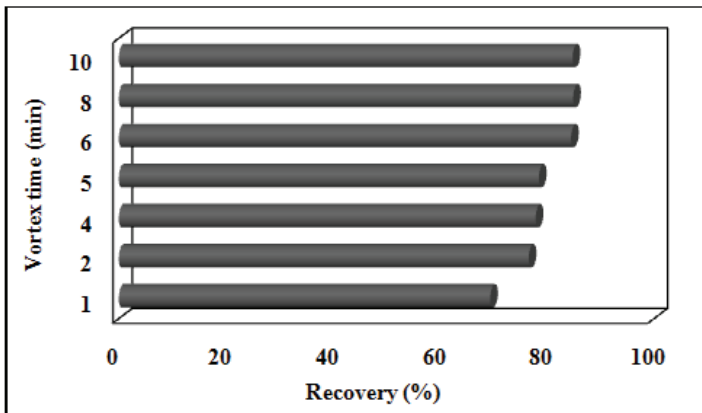


Figure 5. The vortex time affecting the extraction yield

As a result, the highest recovery was obtained from the commercial activated carbon adsorbent and AFB1 adsorption adsorbent quantity of 4.0 mg, vortex time of 6 minutes, and pH 5 from apple juice samples. The method applied with commercial activated carbon can be considered as an important alternative to the traditional method due to its high extraction efficiency, easy application and environmental friendliness.

In addition, the immunoaffinity column method, which is frequently used, was applied to apple juice samples with aflatoxin added. For immunoaffinity column cleansing, 15 ml of extract was mixed with 60 ml of phosphate-buffered saline (PBS). AflaTest® IAC was used at 1-2 drops per second to filter the mixture. After washing the column twice with 15 ml of PBS, it was rinsed with 1.5 ml of methanol. The eluate was collected in a vial and diluted with HPLC-grade water (1.5 ml) (Karami-Osboo and Maham, 2018). According to the immunoaffinity column procedure performed by adding AFB1 to the blank samples that were confirmed to be free of aflatoxin, it was determined that the extraction approach applied with commercial activated carbon was more successful and higher recovery efficiency (%) was calculated (Table 2).

Table 2. Results of IAC and proposed commercial activated carbon-SPE procedures in apple juice sample

AF	Spike (ng ml ⁻¹)	Recovery ± RSD (%)	
		IAC	AC-SPE
AFB1	2.0	94.5 ± 4.1	95.8 ± 2.1

4. CONCLUSION

Commercial activated carbon was used as a sorbent for the extraction method. The pH (3–8), vortex time (1–10) and the amount of adsorbent (1–14 mg) were investigated for the adsorption of activated carbon used to adsorb the aflatoxins in the samples. The highest aflatoxin B1 recovery was obtained at 4.0 mg of activated carbon adsorbent, vortex time of 6 minutes, and pH 5. Aflatoxin removal with commercial activated carbon is a promising, simple, and easy method, and it has been determined to be applicable in ready-made fruit juices. It has been determined that commercial activated carbon has a significant potential to remove aflatoxin B1 from fruit juices due to its large surface area, which increases the capacity to bind aflatoxin species. Applicability of this easy method will increase the production, quality, and safety of fruit juice on an industrial scale in the near future for the removal of aflatoxins.

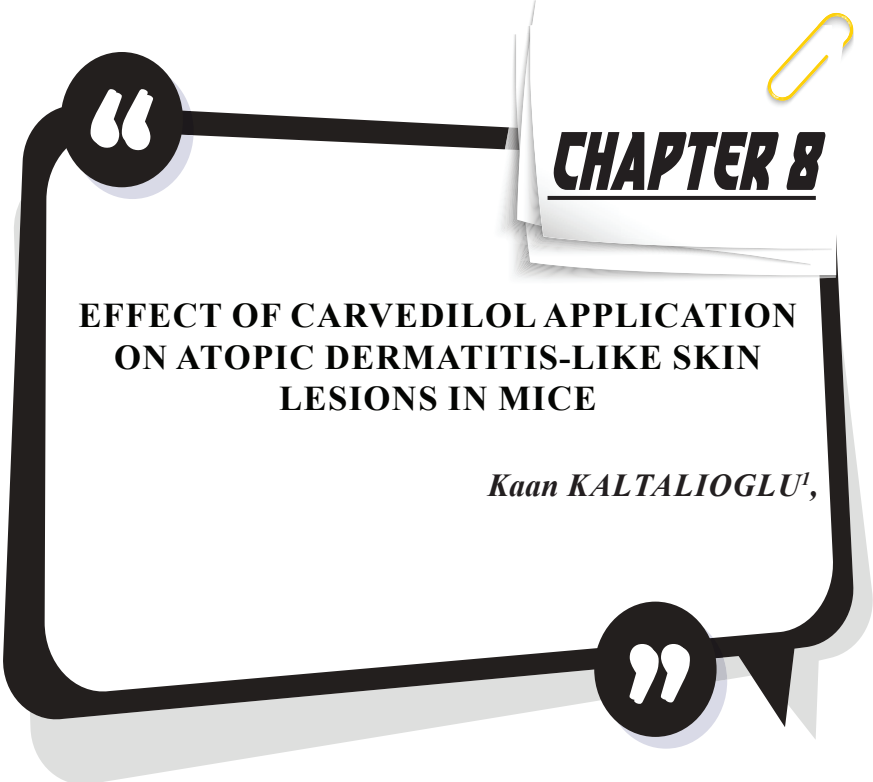
5. REFERENCES

- Abbasi Pirouz, A., Abedi Karjiban, R., Abu Bakar, F., & Selamat, J. (2018). A novel adsorbent magnetic graphene oxide modified with chitosan for the simultaneous reduction of mycotoxins. *Toxins*, 10(9), 361.
- Abd-Elsalam, K. A., Hashim, A. F., Alghuthaymi, M. A., & Said-Galiev, E. (2017). Nanobiotechnological strategies for toxigenic fungi and mycotoxin control. In *Food preservation* (pp. 337-364). Academic Press.
- Amoli-Diva, M., Taherimaslak, Z., Allahyari, M., Pourghazi, K., & Manafi, M. H. (2015). Application of dispersive liquid–liquid microextraction coupled with vortex-assisted hydrophobic magnetic nanoparticles based solid-phase extraction for determination of aflatoxin M1 in milk samples by sensitive micelle enhanced spectrofluorimetry. *Talanta*, 134, 98-104.
- Bazana, S. L., Shimabuku-Biadola, Q. L., Arakawa, F. S., Gomes, R. G., Cossich, E. S., & Bergamasco, R. (2019). Modified activated carbon with silver–copper mixed oxides nanoparticles for removal of heavy metals from water. *International journal of Environmental Science and Technology*, 16(11), 6727-6734.
- Bhat, R., & Reddy, K. R. N. (2017). Challenges and issues concerning mycotoxins contamination in oil seeds and their edible oils: Updates from last decade. *Food Chemistry*, 215, 425-437.
- Bilardi, S., Calabrò, P. S., Greco, R., & Moraci, N. (2020). Removal of heavy metals from landfill leachate using zero valent iron and granular activated carbon. *Environmental technology*, 41(4), 498-510.
- EC No. 1881/2006. (2006). Commission Regulation (EC) No. 1881/2006 of 19 December 2006 setting maximum levels for certain contaminants in foodstuffs. *Official Journal of the European Union*, L 364, p. 14–17.
- González-Jartín, J. M., de Castro Alves, L., Alfonso, A., Piñeiro, Y., Vilar, S. Y., Gomez, M. G., ... & Botana, L. M. (2019). Detoxification agents based on magnetic nanostructured particles as a novel strategy for mycotoxin mitigation in food. *Food chemistry*, 294, 60-66.
- He, X., & Hwang, H.M. (2016). Nanotechnology in food science: Functionality, applicability, and safety assessment. *Journal of food and drug analysis*, 24(4), 671-681.
- International Agency for Research on Cancer. (1982). Evaluation of the carcinogenic risk of chemicals to humans. *Chemicals, industrial processes and industries associated with cancer in humans* (No. Suppl. 4).

- Karami-Osboo, R., & Maham, M. (2018). Pre-concentration and extraction of aflatoxins from rice using air-assisted dispersive liquid-liquid microextraction. *Food analytical methods*, 11(10), 2816-2821.
- Karapınar, H. S., & Balıkcıoğlu, A. (2022). Boron-doped activated carbon nanocomposite as a selective adsorbent for rapid extraction of aflatoxins in nut samples. *Journal of Food Composition and Analysis*, 104680.
- Karapınar, H. S., & Bilgiç, A. (2022). A new magnetic Fe₃O₄@ SiO₂@ TiO₂-APTMS-CPA adsorbent for simple, fast and effective extraction of aflatoxins from some nuts. *Journal of Food Composition and Analysis*, 105, 104261.
- Khodadadi, M., Malekpour, A., & Mehrgardi, M. A. (2018). Aptamer functionalized magnetic nanoparticles for effective extraction of ultratrace amounts of aflatoxin M1 prior its determination by HPLC. *Journal of Chromatography A*, 1564, 85-93.
- Luo, Y., Zhou, Z., & Yue, T. (2017). Synthesis and characterization of nontoxic chitosan-coated Fe₃O₄ particles for patulin adsorption in a juice-pH simulation aqueous. *Food Chemistry*, 221, 317-323.
- Mahpishanian, S., & Sereshti, H. (2016). Three-dimensional graphene aerogel-supported iron oxide nanoparticles as an efficient adsorbent for magnetic solid phase extraction of organophosphorus pesticide residues in fruit juices followed by gas chromatographic determination. *Journal of Chromatography A*, 1443, 43-53.
- Novas, M. V., & Cabral, D. (2002). Association of mycotoxin and sclerotia production with compatibility groups in *Aspergillus flavus* from peanut in Argentina. *Plant Disease*, 86(3), 215-219.
- Pakshir, K., Mirshekari, Z., Nouraei, H., Zareshahabadi, Z., Zomorodian, K., Khodadadi, H., & Hadaeagh, A. (2020). Mycotoxins detection and fungal contamination in black and green tea by HPLC-based method. *Journal of toxicology*, 2020.
- Pallares, N., Font, G., Manes, J., & Ferrer, E. (2017). Multimycotoxin LC-MS/MS analysis in tea beverages after dispersive liquid-liquid microextraction (DLLME). *Journal of agricultural and food chemistry*, 65(47), 10282-10289.
- Pascari, X., Ramos, A. J., Marín, S., & Sanchís, V. (2018). Mycotoxins and beer. Impact of beer production process on mycotoxin contamination. A review. *Food Research International*, 103, 121-129.
- Pérez-Ortega, P., Lara-Ortega, F. J., Gilbert-López, B., Moreno-González, D., García-Reyes, J. F., & Molina-Díaz, A. (2017). Screening of over 600 pesticides, veterinary drugs, food-packaging contaminants, mycotoxins, and other chemicals in food by ultra-high performance liquid

chromatography quadrupole time-of-flight mass spectrometry (UHPLC-QTOFMS). *Food Analytical Methods*, 10(5), 1216-1244.

- Magro, M., Moritz, D. E., Bonaiuto, E., Baratella, D., Terzo, M., Jakubec, P., ... & Vianello, F. (2016). Citrinin mycotoxin recognition and removal by naked magnetic nanoparticles. *Food Chemistry*, 203, 505-512.
- Wongtangtintan, S., Neeratanaphan, L., Ruchuwarak, P., Suksangawong, S., Tengjaroenkul, U., Sukon, P., & Tengjaroenkul, B. (2016). Comparative study of aflatoxin B1 adsorption by Thai bentonite and commercial toxin binders at different temperatures in vitro. *Livestock Research for Rural Development*, 28(4), 2016.
- Xue, Z., Zhang, Y., Yu, W., Zhang, J., Wang, J., Wan, F., ... & Kou, X. (2019). Recent advances in aflatoxin B1 detection based on nanotechnology and nanomaterials-A review. *Analytica chimica acta*, 1069, 1-27.
- Yang, Y., Li, G., Wu, D., Liu, J., Li, X., Luo, P., ... & Wu, Y. (2020). Recent advances on toxicity and determination methods of mycotoxins in foodstuffs. *Trends in food science & Technology*, 96, 233-252.
- Ye, Z., Cui, P., Wang, Y., Yan, H., Wang, X., Han, S., & Zhou, Y. (2019). Simultaneous determination of four aflatoxins in dark tea by multifunctional purification column and immunoaffinity column coupled to liquid chromatography tandem mass spectrometry. *Journal of agricultural and food chemistry*, 67(41), 11481-11488.
- Yu, L., Ma, F., Ding, X., Wang, H., & Li, P. (2018). Silica/graphene oxide nanocomposites: Potential adsorbents for solid phase extraction of trace aflatoxins in cereal crops coupled with high performance liquid chromatography. *Food chemistry*, 245, 1018-1024.
- Zahoor, M., & Ali Khan, F. (2016). Aflatoxin B1 detoxification by magnetic carbon nanostructures prepared from maize straw. *Desalination and water treatment*, 57(25), 11893-11903.
- Taheur, F. B., Kouidhi, B., Al Qurashi, Y. M. A., Salah-Abbès, J. B., & Chaieb, K. (2019). Biotechnology of mycotoxins detoxification using microorganisms and enzymes. *Toxicon*, 160, 12-22.



CHAPTER 8

EFFECT OF CARVEDILOL APPLICATION ON ATOPIC DERMATITIS-LIKE SKIN LESIONS IN MICE

Kaan KALTALIOGLU¹,

¹ Corresponding Author: *Dr. Kaan Kaltalioglu Vocational School of Espiye, Giresun University, 28600, Giresun, Turkey
e-mail: kaan.kaltalioglu@gmail.com
Kaan Kaltalioglu: ORCID ID: 0000-0002-4995-2657

INTRODUCTION

Atopic dermatitis (AD) is an irritating inflammatory skin condition that affects 11-30% of children and 2-10% of adults (Bieber, 2010; Shaw, Currie, Koudelka, & Simpson, 2011). It is one of the most common types of eczema characterized by itch, rash and dryness in the skin. It is caused by the abnormalities in the immunological and inflammatory responses (Guo, Wang, Li, Yang, & Wang, 2018; Ikezawa et al., 2010). Additionally, it is believed that this is linked to abnormalities in skin genes that are essential for barrier function and elasticity (Jin, He, Oyoshi, & Geha, 2009).

The etiology of AD is complex. Early theories of etiology ascribed AD mostly to cutaneous inflammation at lesion sites, but subsequent research has shown that it is caused by keratinocyte differentiation abnormalities and high immune responses (Gao et al., 2004; Roesner, Werfel, & Heratizadeh, 2016; Schmid-Grendelmeier & Ballmer-Weber, 2010). AD is distinguished by over IgE synthesis, peripheral blood eosinophilia, activation of mast cell, and an elevation in Th2 and Th1 cytokines (Neis et al., 2006; Wierenga et al., 1991). AD is a serious skin disease that places a significant burden on patients' quality of life, as well as their health outcomes (Senra & Wollenberg, 2014). The most efficient therapy method for enhancing the overall life quality for patients with AD is to reduce the amount of scratching that is caused by related itching. As a result, there is a significant requirement for the investigation of innovative and successful treatments for AD (Niebuhr & Werfel, 2010; Park, Lee, Lee, & Kim, 2013).

Carvedilol is a third generation non-selective beta-adrenergic and α_1 -receptor antagonist with proven clinical efficacy in heart failure (HF) and myocardial infarction therapy (MI) (Dargie, 2001; Poole-Wilson et al., 2003). The efficacy of carvedilol has also been shown in conditions such as stroke, renal failure, and diabetes mellitus (Ongun Özdemir & Ertaş, 2005). Unlike other beta-antagonists, carvedilol almost fully inhibits the enhanced sympathetic activity (Packer, 1998). Moreover, carvedilol suppresses presynaptic β_2 stimulation and does not raise myocardial β_1 receptor density as do β_1 -selective blockers (Bristow et al., 1986; Gilbert et al., 1996).

In case reports, it has been reported that daily administration of 6.25 mg of Carvedilol is good for red scrotum syndrome and red vulva syndrome characterized by hyperalgesia (increased sensitivity to pain) and burning sensation (Hajj & Ayoub, 2018; Merhi, Ayoub, & Mrad,

2017). While no serious side effects were observed as a result of the application of carvedilol, which was continued for approximately 1 month, it was reported that the patient's complaints ceased and they were satisfied in the observations of the patients after 2,4 and 6 months. In addition, it has been reported in various studies that carvedilol has antioxidant, antiproliferative, antihypertensive and antiinflammatory activity (Book, 2002; Feuerstein, Yue, Ma, & Ruffolo, 1998; Saeidnia & Abdollahi, 2013).

Therefore, in this study, its purpose was to examine the curvative effects of carvedilol application, which was selected due to the studies mentioned in the atopic dermatitis-like model to be created with 2,4-dinitrochlorobenzene (DNCB) in swiss albino mice. For this, the scratching behaviors were examined. IgE levels, which are important markers in AD, were determined in serum samples.

MATERIALS AND METHODS

Reagents

All of the chemicals were obtained from either Sigma-Aldrich (USA) or Merck KGaA (Germany).

Animals

Gazi University's Local Animal Experimentation Ethics Committee authorized the experimental protocol (G.Ü.ET-18.098). For the purpose of the study, male Swiss albino mice (n=18) weighing 25–30 g were used. These mice were individually kept in clean cages under standard conditions, and they were fed water and a standard rodent food. Animals will be divided into 3 groups as control, DNCB and DNCB+CARVEDILOL (Table 1).

Table 1. Group specifications

Groups	Specifications
Control	Healthy animals, in order to compare the values of the other groups, a control group was performed in which only acetone: olive oil (4:1) mixture was applied (n=6).

DNCB	Only DNCB-induced animals, DNCB was used to create AD-like lesions (n=6).
DNCB+CARVEDILOL	DNCB and Carvedilol administrated animals, after DNCB induction, 3 mg/kg carvedilol was applied (n=6).

DNCB-induced AD-like Skin Lesion Model and treatment

The AD-like model was created with topical application of 2,4-dinitrochlorobenzene (DNCB) as described previously (Yu et al., 2017). The dorsal skin of the animal was shaved, and then 1% DNCB (in acetone:olive oil = 4:1) was treated to it for the purpose of sensitization on days 1 and 3. The same process will be repeated with 0.2% DNCB, once every 3 days for 12 days. Six days later, 3 mg/kg of carvedilol daily was applied to the dorsal region of the animal until day 12 in DNCB+CARVEDILOL group.

Examination of scratching behavior

Following the conclusion of all treatments, scratching was reported. The animals were put in cages and given 15 minutes to adapt. The scratching activities were recorded for the next 10 minutes, and this procedure was repeated six times (total 60 min). This investigation characterized scratching activity as movements of the hind paws. While movements with the hind paws were documented on the nose, ear and dorsal skin, licking of the abdomen and dorsum during grooming was not. All evaluations were conducted blindly (Yu et al., 2017).

Determination of IgE levels

The IgE level was tested using an ELISA kit (Abcam, UK) as recommended by the manufacturer.

Statistical Analysis

All of the data were analyzed using two-tailed paired and unpaired Student's t tests. The mean and standard deviation were also presented for each set of data. When p value was less than 0.05, it was decided that there was a statistically significant difference between the groups.

RESULTS

Effect of carvedilol on scratching behavior

The scratching behavior was examined based on the quantity of relevant activities seen, such as ear, nose, and dorsal scratching with hind paws. In the DNCB-induced group, scratching behavior was observed average 11 times per 10-minute period (Figure 1). This value is significant when compared with the control group ($p < 0.05$). In the DNCB+CARVEDILOL group, scratching behavior was observed average 9 times per 10-minute period (Figure 1). Although a decrease was founded in the DNCB+CARVEDILOL group compared to the DNCB group, this decrease was not found to be statistically ($p > 0.05$) (Figure 1).

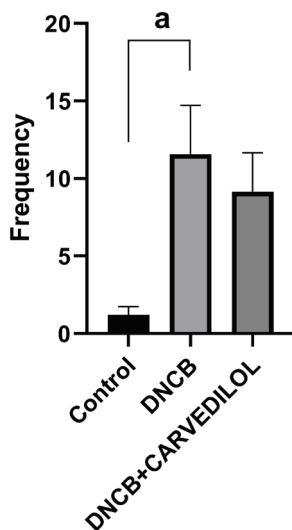


Figure 1. The effects of carvedilol on scratching behavior in control and DNCB-induced mice. Frequency was given in 10 minutes. a $p < 0.05$ as compared to the control group

Effect of carvedilol on IgE level

The IgE level significantly increased in the DNCB group as compared to the the control group ($p < 0.05$) (Table 2). IgE levels in serum were elevated after repeated DNCB induction. As shown in Figure 2, no significant change was determined in the DNCB+CARVEDILOL group as compared to the DNCB group ($p > 0.05$).

Table 2. The effects of carvedilol on IgE levels in control and DNCB-induced mice. a $p < 0.05$ as compared to the control group

	IgE (ng/mL)
Control (n=6)	3.21 ± 0.53
DNCB (n=6)	12.25 ± 2.52^a
DNCB+Carvedilol (n=6)	10.10 ± 3.27

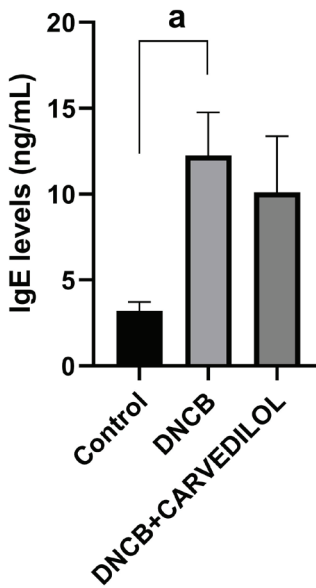


Figure 2. Serum IgE levels in Swiss albino mice. a $p < 0.05$ as compared to the control group

DISCUSSION

AD is a rare inflammatory skin condition that may be chronic or recurrent. It has a general negative impact on health by impairing the life quality of patients with AD (Yu et al., 2017). Generally, it is identified by erythematous plaques, pruritic, and papules. Although it is known that AD develops owing to skin barrier abnormalities, abnormal immunological activation and genetic susceptibility, the mechanism underlying its pathogenesis is not clearly understood (Choi et al., 2021; Weidinger & Novak, 2016). Steroid application remains the treatment of choice for AD. But, this application is accompanied with adverse effects, including as red burning skin, cataracts, atrophy, growth retardation, and acne (Arkwright et al., 2013; Leung & Bieber, 2003). Because of this, a significant amount of effort is being put into the investigation of possible treatments for AD using animal models (Kitamura, Takata, Aizawa, Watanabe, & Wada, 2018). Carvedilol is a nonselective β -blocker that also has various bioactivities (El-Shitany & El-Desoky, 2016; Hameed, Aydin, & Başaran, 2016). In our study, it was aimed to examine the therapeutic effects of carvedilol in the atopic dermatitis-like model to be created with 2,4-dinitrochlorobenzene (DNCB).

Induction with DNCB is a well-studied model for constructing an AD-like model and is preferred because of its reproducibility (Fujii, Takeuchi, Sakuma, Sengoku, & Takakura, 2009; Yang et al., 2011). In our study, scratching behaviors and serum IgE levels were found to be statistically higher in the DNCB group compared to the control group ($p < 0.05$). Likewise, it has been indicated that serum IgE levels are increased in AD (Matsuda, 1997). These findings showed that the DNCB-induced AD-like skin lesion model was an effective animal model.

In the scratching behavior test, it was determined that carvedilol application reduced scratching compared to the DNCB group, but this situation was not statistically significant ($p > 0.05$). Wang et al. (2014) determined that carvedilol application (5 mg/kg) showed a strong anti-inflammatory activity by decreasing pro-inflammatory cytokines and increasing anti-inflammatory cytokines in myocarditis-induced mice model. Moreover, Yuan et al. (2004) reported that carvedilol application (20 mg/kg) not only suppresses inflammatory cytokines but also shows antioxidant properties. The lack of statistical significance in the activity of carvedilol in our study may be due to the low dose selected in our study, when taken into account in other studies.

IgE is an antibody found in the blood (Sutton, Davies, Bax, & Karagiannis, 2019). Testing for IgE sensitization is now the most important part of the diagnostic assessment process in cases where allergies are suspected (Ansotegui et al., 2020). Elevated serum IgE levels is rarely found in patients with AD (Biedermann, Skabytska, Kaesler, & Volz, 2015; Brunner et al., 2017). In this study, carvedilol application not statistically decreased DNCB-induced IgE level ($p>0.05$). This data is also supported by the result obtained from the scratch behavior test.

CONCLUSION

In conclusion, the current study demonstrated that carvedilol application not suppressed AD-like skin lesions in DNCB-induced mice, did not show therapeutic effect against AD-like skin lesions. This may be due to the used dose. The obtained results should be supported by different doses and methods.

REFERENCES

- Ansotegui, I. J., Melioli, G., Canonica, G. W., Caraballo, L., Villa, E., Ebisawa, M., ... Zuberbier, T. (2020). IgE allergy diagnostics and other relevant tests in allergy, a World Allergy Organization position paper. *World Allergy Organization Journal*, 13(2), 100080. <https://doi.org/10.1016/j.waojou.2019.100080>
- Arkwright, P. D., Motala, C., Subramanian, H., Spergel, J., Schneider, L. C., & Wollenberg, A. (2013). Management of Difficult-to-Treat Atopic Dermatitis. *The Journal of Allergy and Clinical Immunology: In Practice*, 1(2), 142–151. <https://doi.org/10.1016/j.jaip.2012.09.002>
- Bieber, T. (2010). Atopic Dermatitis. *Annals of Dermatology*, 22(2), 125. <https://doi.org/10.5021/ad.2010.22.2.125>
- Biedermann, T., Skabytska, Y., Kaesler, S., & Volz, T. (2015). Regulation of T Cell Immunity in Atopic Dermatitis by Microbes: The Yin and Yang of Cutaneous Inflammation. *Frontiers in Immunology*, 6. <https://doi.org/10.3389/fimmu.2015.00353>
- Book, W. M. (2002). Carvedilol: a nonselective beta blocking agent with antioxidant properties. *Congestive Heart Failure (Greenwich, Conn.)*, 8(3), 173–177, 190. <https://doi.org/10.1111/j.1527-5299.2002.00718.x>
- Bristow, M. R., Ginsburg, R., Umans, V., Fowler, M., Minobe, W., Rasmussen, R., ... Jamieson, S. (1986). Beta 1- and beta 2-adrenergic-receptor subpopulations in nonfailing and failing human ventricular myocardium: coupling of both receptor subtypes to muscle contraction and selective beta 1-receptor down-regulation in heart failure. *Circulation Research*, 59(3), 297–309. <https://doi.org/10.1161/01.res.59.3.297>
- Brunner, P. M., Silverberg, J. I., Guttman-Yassky, E., Paller, A. S., Kabashima, K., Amagai, M., ... Taieb, A. (2017). Increasing Comorbidities Suggest that Atopic Dermatitis Is a Systemic Disorder. *Journal of Investigative Dermatology*, 137(1), 18–25. <https://doi.org/10.1016/j.jid.2016.08.022>
- Choi, J., Sutaria, N., Roh, Y. S., Bordeaux, Z., Alphonse, M. P., Kwatra, S. G., & Kwatra, M. M. (2021). Translational Relevance of Mouse Models of Atopic Dermatitis. *Journal of Clinical Medicine*, 10(4), 613. <https://doi.org/10.3390/jcm10040613>
- Dargie, H. J. (2001). Effect of carvedilol on outcome after myocardial infarction in patients with left-ventricular dysfunction: the CAPRICORN randomised trial. *Lancet (London, England)*, 357(9266), 1385–1390. [https://doi.org/10.1016/s0140-6736\(00\)04560-8](https://doi.org/10.1016/s0140-6736(00)04560-8)

- El-Shitany, N. A., & El-Desoky, K. (2016). Protective Effects of Carvedilol and Vitamin C against Azithromycin-Induced Cardiotoxicity in Rats via Decreasing ROS, IL1- β , and TNF- α Production and Inhibiting NF- κ B and Caspase-3 Expression. *Oxidative Medicine and Cellular Longevity*, 2016, 1–13. <https://doi.org/10.1155/2016/1874762>
- Feuerstein, G., Yue, T. L., Ma, X., & Ruffolo, R. R. (1998). Novel mechanisms in the treatment of heart failure: inhibition of oxygen radicals and apoptosis by carvedilol. *Progress in Cardiovascular Diseases*, 41(1 Suppl 1), 17–24. [https://doi.org/10.1016/s0033-0620\(98\)80027-3](https://doi.org/10.1016/s0033-0620(98)80027-3)
- Fujii, Y., Takeuchi, H., Sakuma, S., Sengoku, T., & Takakura, S. (2009). Characterization of a 2,4-Dinitrochlorobenzene-Induced Chronic Dermatitis Model in Rats. *Skin Pharmacology and Physiology*, 22(5), 240–247. <https://doi.org/10.1159/000235551>
- Gao, X. K., Nakamura, N., Fuseda, K., Tanaka, H., Inagaki, N., & Nagai, H. (2004). Establishment of Allergic Dermatitis in NC/Nga Mice as a Model for Severe Atopic Dermatitis. *Biological and Pharmaceutical Bulletin*, 27(9), 1376–1381. <https://doi.org/10.1248/bpb.27.1376>
- Gilbert, E. M., Abraham, W. T., Olsen, S., Hattler, B., White, M., Mealy, P., ... Bristow, M. R. (1996). Comparative hemodynamic, left ventricular functional, and antiadrenergic effects of chronic treatment with metoprolol versus carvedilol in the failing heart. *Circulation*, 94(11), 2817–2825. <https://doi.org/10.1161/01.cir.94.11.2817>
- Guo, J. Z., Wang, W. H., Li, L. F., Yang, S. M., & Wang, J. (2018). The role of metallothionein in a dinitrofluorobenzene-induced atopic dermatitis-like murine model. *Scientific Reports*, 8(1), 2–10. <https://doi.org/10.1038/s41598-018-29410-w>
- Hajj, C., & Ayoub, N. (2018). Carvedilol for Treatment of Red Vulva Syndrome. *JAMA Dermatology*, 154(6), 731. <https://doi.org/10.1001/jamadermatol.2018.0246>
- Hameed, H., Aydin, S., & Başaran, N. (2016). Sinapic acid: Is it safe for humans? *Fabad Journal of Pharmaceutical Sciences*, 41(1), 39–49.
- Ikezawa, Z., Komori, J., Ikezawa, Y., Inoue, Y., Kirino, M., Katsuyama, M., & Aihara, M. (2010). A Role of Staphyococcus aureus, Interleukin-18, Nerve Growth Factor and Semaphorin 3A, an Axon Guidance Molecule, in Pathogenesis and Treatment of Atopic Dermatitis. *Allergy, Asthma and Immunology Research*, 2(4), 235. <https://doi.org/10.4168/aaair.2010.2.4.235>
- Jin, H., He, R., Oyoshi, M., & Geha, R. S. (2009). Animal models of atopic

- dermatitis. *The Journal of Investigative Dermatology*, 129(1), 31–40. <https://doi.org/10.1038/jid.2008.106>
- Kitamura, A., Takata, R., Aizawa, S., Watanabe, H., & Wada, T. (2018). A murine model of atopic dermatitis can be generated by painting the dorsal skin with hapten twice 14 days apart. *Scientific Reports*, 8(1), 1–9. <https://doi.org/10.1038/s41598-018-24363-6>
- Leung, D. Y., & Bieber, T. (2003). Atopic dermatitis. *The Lancet*, 361(9352), 151–160. [https://doi.org/10.1016/S0140-6736\(03\)12193-9](https://doi.org/10.1016/S0140-6736(03)12193-9)
- Matsuda, H. (1997). Development of atopic dermatitis-like skin lesion with IgE hyperproduction in NC/Nga mice. *International Immunology*, 9(3), 461–466. <https://doi.org/10.1093/intimm/9.3.461>
- Merhi, R., Ayoub, N., & Mrad, M. Carvedilol for the treatment of red scrotum syndrome, 3 JAAD Case Reports 464–466 (2017). Elsevier Inc. <https://doi.org/10.1016/j.jcdr.2017.06.021>
- Neis, M., Peters, B., Dreuw, A., Wenzel, J., Bieber, T., Mauch, C., ... Merk, H. (2006). Enhanced expression levels of IL-31 correlate with IL-4 and IL-13 in atopic and allergic contact dermatitis. *Journal of Allergy and Clinical Immunology*, 118(4), 930–937. <https://doi.org/10.1016/j.jaci.2006.07.015>
- Niebuhr, M., & Werfel, T. (2010). Innate immunity, allergy and atopic dermatitis. *Current Opinion in Allergy & Clinical Immunology*, 10(5), 463–468. <https://doi.org/10.1097/ACI.0b013e32833e3163>
- Ongun Özdemir, A., & Ertas, F. (2005). Karvedilol : Klinik Kullanımı. *Dahili Tıp Bilimleri Dergisi*, 12(4), 183–189.
- Packer, M. (1998). β -adrenergic blockade in chronic heart failure: Principles, progress, and practice. *Progress in Cardiovascular Diseases*, 41(1), 39–52. [https://doi.org/10.1016/S0033-0620\(98\)80030-3](https://doi.org/10.1016/S0033-0620(98)80030-3)
- Park, S. J., Lee, Y. H., Lee, K. H., & Kim, T. J. (2013). Effect of eriodictyol on the development of atopic dermatitis-like lesions in ICR mice. *Biological and Pharmaceutical Bulletin*, 36(8), 1375–1379. <https://doi.org/10.1248/bpb.b13-00296>
- Poole-Wilson, P. A., Swedberg, K., Cleland, J. G. F., Di Lenarda, A., Hanrath, P., Komajda, M., ... Carvedilol Or Metoprolol European Trial Investigators. (2003). Comparison of carvedilol and metoprolol on clinical outcomes in patients with chronic heart failure in the Carvedilol Or Metoprolol European Trial (COMET): randomised controlled trial. *Lancet (London, England)*, 362(9377), 7–13. [https://doi.org/10.1016/S0140-6736\(03\)13800-7](https://doi.org/10.1016/S0140-6736(03)13800-7)

- Roesner, L. M., Werfel, T., & Heratizadeh, A. (2016). The adaptive immune system in atopic dermatitis and implications on therapy. *Expert Review of Clinical Immunology*, 12(7), 787–796. <https://doi.org/10.1586/1744666X.2016.1165093>
- Saeidnia, S., & Abdollahi, M. (2013). Toxicological and pharmacological concerns on oxidative stress and related diseases. *Toxicology and Applied Pharmacology*, 273(3), 442–455. <https://doi.org/10.1016/j.taap.2013.09.031>
- Schmid-Grendelmeier, P., & Ballmer-Weber, B. K. (2010). Neurodermitis. *Therapeutische Umschau*, 67(4), 175–185. <https://doi.org/10.1024/0040-5930/a000031>
- Senra, M. S., & Wollenberg, A. (2014). Psychodermatological aspects of atopic dermatitis. *British Journal of Dermatology*, 170, 38–43. <https://doi.org/10.1111/bjd.13084>
- Shaw, T. E., Currie, G. P., Koudelka, C. W., & Simpson, E. L. (2011). Eczema Prevalence in the United States: Data from the 2003 National Survey of Children's Health. *Journal of Investigative Dermatology*, 131(1), 67–73. <https://doi.org/10.1038/jid.2010.251>
- Sutton, B., Davies, A., Bax, H., & Karagiannis, S. (2019). IgE Antibodies: From Structure to Function and Clinical Translation. *Antibodies*, 8(1), 19. <https://doi.org/10.3390/antib8010019>
- Wang, D., Chen, Y., Jiang, J., Zhou, A., Pan, L., Chen, Q., ... Chen, C. (2014). Carvedilol has stronger anti-inflammation and anti-virus effects than metoprolol in murine model with coxsackievirus B3-induced viral myocarditis. *Gene*, 547(2), 195–201. <https://doi.org/10.1016/j.gene.2014.06.003>
- Weidinger, S., & Novak, N. (2016). Atopic dermatitis. *The Lancet*, 387(10023), 1109–1122. [https://doi.org/10.1016/S0140-6736\(15\)00149-X](https://doi.org/10.1016/S0140-6736(15)00149-X)
- Wierenga, E. A., Snoek, M., Jansen, H. M., Bos, J. D., van Lier, R. A., & Kapsenberg, M. L. (1991). Human atopen-specific types 1 and 2 T helper cell clones. *Journal of Immunology (Baltimore, Md. : 1950)*, 147(9), 2942–2949. Retrieved from <http://www.ncbi.nlm.nih.gov/pubmed/1680923>
- Yang, G., Lee, K., Lee, M.-H., Kim, S.-H., Ham, I.-H., & Choi, H.-Y. (2011). Inhibitory effects of Chelidonium majus extract on atopic dermatitis-like skin lesions in NC/Nga mice. *Journal of Ethnopharmacology*, 138(2), 398–403. <https://doi.org/10.1016/j.jep.2011.09.028>
- Yu, H., Li, H., Li, Y., Li, M., & Chen, G. (2017). Effect of isoliquiritigenin for

the treatment of atopic dermatitis-like skin lesions in mice. *Archives of Dermatological Research*, 309(10), 805–813.
<https://doi.org/10.1007/s00403-017-1787-3>

Yuan, Z., Shioji, K., Kihara, Y., Takenaka, H., Onozawa, Y., & Kishimoto, C. (2004). Cardioprotective effects of carvedilol on acute autoimmune myocarditis: anti-inflammatory effects associated with antioxidant property. *American Journal of Physiology-Heart and Circulatory Physiology*, 286(1), H83–H90.
<https://doi.org/10.1152/ajpheart.00536.2003>



CHAPTER 9

ESTIMATION OF BASIC ASTROPHYSICAL PARAMETERS AND ORBITAL PERIOD ANALYSIS OF SEMI-DETACHED BINARY VX LAC

Dr. Muhammed Faruk YILDIRIM¹,

¹ Çanakkale Onsekiz Mart University, Astrophysics Research Center and Ulupınar Observatory, 17020, Çanakkale, Turkey. mf.yildirim@hotmail.com

Çanakkale Onsekiz Mart University, Department of Electricity and Energy, Çan Vocational School, 17400, Çanakkale, Turkey. mf.yildirim@hotmail.com

ORCID Code: (0000-0003-2382-7011)

1. INTRODUCTION

Studies in the field of astrophysics can achieve more sensitive results with developing technology and increasing sensitive satellite data (TESS, KEPLER, etc.). One of the most important fields for stellar astrophysics studies is binary star studies and this field creates a very important application laboratory environment for those working in stellar astrophysics. Binary stars are systems that are interconnected by gravitational force. These systems consist of two components that orbit around their common center of mass according to Kepler's laws. Eclipsing binary stars are formed when the two components eclipsing each other over time according to the observer's line of sight. Semi-detached systems (also known as Classical Algol) are usually in the class of eclipsing binary with one component filled the Roche lobe and the other the Roche lobe not filled. They were classified as semi-detached types in the classification made by Kopal (1959) according to Roche geometry. The evolved component is less mass and is in the subgiant or giant state, while the other component is more mass and located in the main sequence. If there is a mass transfer from the second component to the unevolved first component, which is the main sequence star, the first component may become more massive. Due to such situations, semi-detached binaries are among the most interesting species for researchers. In this paper, light curve (LC) analysis of the VX Lac semi-detached system was made and the basic astrophysical parameters were determined. In addition, the orbital period analysis for VX Lac was conducted and interpreted in detail.

VX Lac (TIC 128785705, Gaia EDR3 1905008284306000128, SAO 72615, TYC 3214-1295-1) is a semi-detached eclipsing binary star system with an orbital period of about 1 day. The spectral type of VX Lac, whose orbital period is about one day, was first expressed as F0 by Cannon (1934). Later, the spectral type of the VX Lac was cataloged as F0 + K4 IV by Svechnikov & Kuznetsova (1990). There is no spectral study in the literature of the system. The period change study of the VX Lac classical algol system was done by Zaslavskii et al. (2008). Zaslavskii et al. (2008) reported both an upward parabola and a sinusoidal change in their period analysis study for the system. They obtained the period of sinusoidal variation as about 68 years. In addition, the sinusoidal-like change is explained by the presence of a possible third component and it is said that the minimum mass of the third body will be $0.4 M_{\odot}$. In the same study, the reason for the parabolic change was explained as mass exchange from the less mass body to the more mass one. The LC analysis of VX Lac (light curve is taken from the SuperWASP data archive) and orbital period analysis were done by Zaslavskii (2016). In the study by Zaslavskii (2016), the temperatures of the components of VX Lac were determined ($T_1=7228$ K, $T_2=4486$ (36) K). In the same study, it was

reported that the period of the VX Lac increased and a sinusoidal change was also detected, and the period of the sinusoidal change was calculated as 49 years.

2. DATA INFORMATION

The LC of the VX Lac variable system was observed by the TESS (Transiting Exoplanet Survey Telescope; Ricker et al., 2015) satellite and archived by MAST (Mikulski Archive for Space Telescopes, <https://archive.stsci.edu>). Photometric observations of TESS for VX Lac started in September 2019 with an exposure time of 1800 sec. and observations were made for about a month. The sequence number of the observation is 16 and it was made as the HLSP mission. And also the observation data of VX Lac was released in February 2021. In this paper, the LC from MAST was converted to normalized flux for the VX Lac system. In addition, the LC for the VX Lac was taken from the SuperWASP (Super Wide Angle Search for Planets; Butters et al., 2010) database and converted to normalized flux. The most important parameter to investigate the orbital period variation is the eclipse times, and therefore, eclipse times were acquired from the LC in this paper.

Table 1. Eclipse times and errors calculated using TESS and SuperWASP data for VX Lac.

Eclipse Times (HJD+2400000)	Errors	Type (I/II)	Mission
53192.5806	0.0009	I	SuperWASP
53200.6366	0.0008	II	SuperWASP
53243.6159	0.0012	II	SuperWASP
53248.4548	0.0002	I	SuperWASP
54006.5127	0.0029	II	SuperWASP
54303.6177	0.0002	I	SuperWASP
54402.4726	0.0001	I	SuperWASP
54409.4589	0.0019	II	SuperWASP
58739.1577	0.0059	I	TESS
58739.6971	0.0047	II	TESS
58746.6792	0.0065	I	TESS
58747.2179	0.0019	II	TESS
58752.5909	0.0011	II	TESS
58753.1285	0.0073	I	TESS
58760.6499	0.0062	I	TESS
58761.1877	0.0051	II	TESS

Eight eclipse times were obtained for the VX Lac system from the LC converted to normalized flux from the SuperWASP database and

listed with their errors in Table 1. Since the studies in the literature are generally in HJD, the data from TESS was converted from BJD to HJD in this study as well. Eight eclipse times were calculated using the TESS data of the VX Lac system and are given in Table 1 along with their errors. The eclipse times were acquired using the least squares technique.

3. PHOTOMETRIC ANALYSIS METHOD

3.1. LIGHT CURVE ANALYSIS

The LC solution of the VX Lac variable system was made using the Wilson-Devinney (Wilson and Devinney (WD), 1971) technique, which is generally used in the literature. The Wilson & Devinney technique consists of two main parts, “Light Curve (LC)” and “Differential Correction (DC)”. While searching for a solution in this method, it is first necessary to determine the temperature of the first body (T_1) and the mass ratio (q) of the VX Lac ($q=M_2/M_1$). Usually in solutions, the temperature of the first body is taken as the rate obtained from the spectral data and the solutions are made according to this constant value. In this study, the temperature value of the first component for VX Lac was determined as 7161 K given by Eker et al (2020) according to the F0 spectral type estimated by Svechnikov & Kuznetsova (1990). Since the q value of the VX Lac system can be acquired precisely with spectral data, if it can be determined, the spectral mass ratio can be used as a starting parameter in light curve solutions. However, in systems where the q value is not certain, the photometric q search way can be used. Q search was performed for the VX Lac system and the mass ratio was determined (see Figure 1). The LC solution for any system is directly related to the nature of the system to be studied. MODs defined in the WD method impose restrictions on the solution of light curves of systems with different physical and geometric properties. MOD2 was selected for the VX Lac system and the parameters and errors determined as a result of the LC analysis are given in Table 2. The compatibility of the theoretical fit and observational data acquired as a result of the LC analysis for the VX Lac system is given in Figure 2.

Table 2. The LC analysis results of the VX Lac, its errors and comparison with the results obtained in the literature.

Parameters	This Study	Zasche (2016)
i (deg)	87.39 (26)	86.84 (25)
T_1 (K)	7161	7228
T_2 (K)	4736 (38)	4486 (36)
Ω_1	3.769 (35)	4.589 (19)
Ω_2	3.175 (28)	5.021 (18)
q	0.487 (21)	-
L_1/L_1+L_2	0.900 (4)	-
L_2/L_1+L_2	0.100 (5)	-
a (R_\odot)	5.95 (3)	-
$g_1=g_2$	0.32	-
$A_1=A_2$	0.5	-
<i>Roche-lobe filling factor (%)</i>	76-90	-

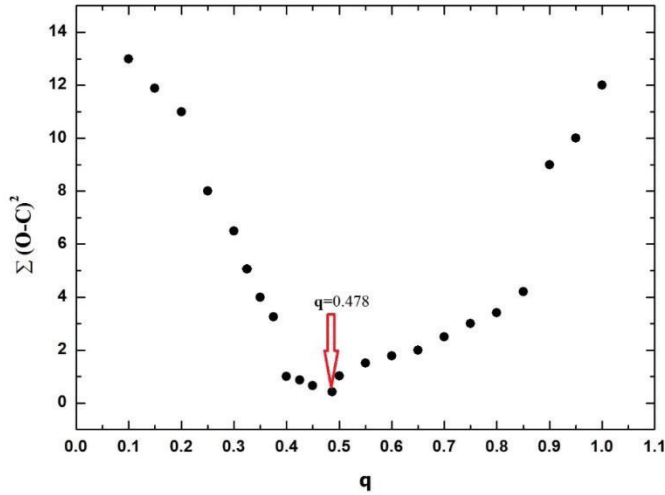


Figure 1. Q-search for the VX Lac semi-detached system.

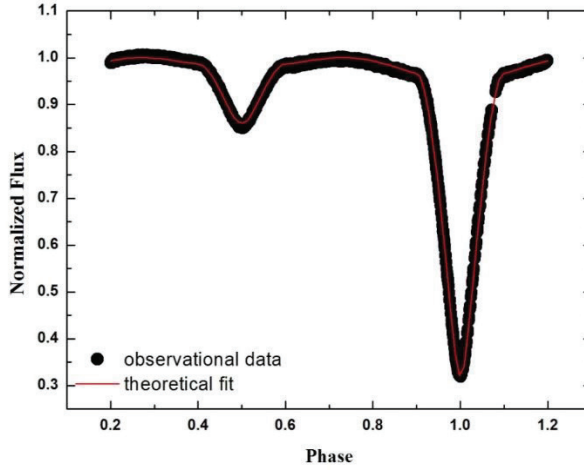


Figure 2. The compatibility of the theoretical (red continuous line) and observational data (black dots) of the VX Lac eclipsing system.

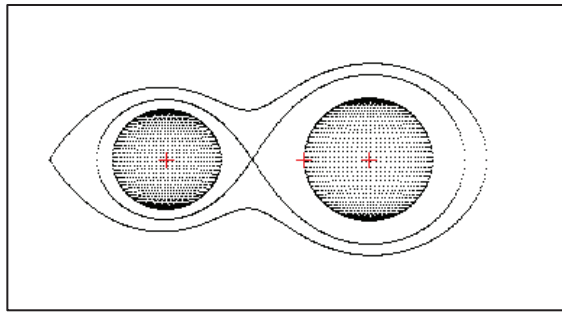


Figure 3. Roche lobe geometry of the VX Lac variable system at 0.75 phases.

3.2. ORBITAL PERIOD ANALYSIS

One of the most easily determined parameters in eclipsing binary stars is the orbital period (hereafter OP will be used instead of ‘the orbital period’). Successive eclipses in the LCs allow us to calculate OP. In addition, if there is a variation in OP with the sensitively determined minima times, it can also be revealed. Some physical events that occur in a binary system may cause OP of the system to change. For example; light time effect (LITE) due to a third object in the system, apsidal motion in the system, magnetic activity of the cold component, mass loss from the system or mass transfer between components. The mechanisms that really cause OP change of the system are the mass loss from the system and the mass exchange between the components or the mechanisms originating from magnetic activity. OP change seen due to other mechanisms does not indicate the true period change. In this study,

the O–C (Obs.–Calc.) way, which is well known in the literature, was preferred for orbital period change. The increasing parabola in the O–C graphs means the increasing of OP, which can be explained by the mass exchange from the less mass object to the more mass object (expected for classical Algols). If there is a change in decreasing parabola shape, the period is decreasing, and this can be explained by mass exchange from the more mass object to the less mass, or by some form of mass loss from the system. Increasing parabolic variation was determined in the analysis for semi-detached system VX Lac. Assuming that mass transfer or loss may be the cause of OP variation, conservative and non-conservative mass exchange mechanisms were taken into account in this study and this situation was formulated by Erdem & Öztürk (2014) and given in equation 1.

$$\frac{\dot{P}}{P} = \left\{ 2 \left\{ \frac{R_A}{a} \right\}^2 \frac{M_1 + M_2}{M_1 M_2} - \frac{2}{M_1 + M_2} \right\} \dot{M} + \frac{3(M_1 - M_2)}{M_1 M_2} \dot{M}_1 \tag{1}$$

R_A , is known as the Alfen radius and its upper limit is 10 times the radius of the losing star (Tout and Hall 1991). In Equation 1, M_1 and M_2 are the first and second component masses, respectively, \dot{M}_1 ; mass transferred to the first component, \dot{M} ; the mass lost by the system and a is the distance between the two components.

The parameters obtained as a result of the orbital period change for VX lac are given in Table 3. In addition, the graphs obtained due to the O–C analysis are given in Fig. 3 and Fig. 4. The causes of sinusoidal change in the figures may be possible components due to the LITE or may be due to magnetic activity. The sinusoidal changes, which are frequently seen in the O–C graphs of eclipsing binaries, are also seen in semi-detached systems. If this is a recurrent change, the LITE often caused by a third component around the system can be cited as its source. The LITE effect is formulated by Equation 2 given by Irwin (1959).

$$\Delta t = \frac{a_{12} \sin i'}{c} \left\{ \frac{1 - e'^2}{1 + e' \cos v'} \sin(v' + w') + e' \cos w' \right\} \tag{2}$$

The terms in equation 2 can be defined below.

Δt : is the time delay due to the possible third object.

$a_{12} \sin i'$: the semi-major axis.

i' : inclination.

e' : eccentricity.

v' : true anomaly.

w' : the longitude ratio of the periastron of the third-body orbit.

In some studies in the literature, it has been suggested that the cause for the periodic variation could be due to LITE (e.g. Yildirim, 2020, 2022).

Table 3. Parameters, errors and comparison of VX Lac obtained as a result of O–C analysis with the results obtained in the literature.

Parameters	This Study	Zasche (2016)
T_0 (HJD+2400000)	42026.3854 (13)	40908.9074 (12)
P_{orb} (day)	1.0744974 (1)	1.07449709 (14)
Q (day)	$1.4 (1) \times 10^{-10}$	-
dP/dt (day/year)	9.5×10^{-8}	-
$dM/dt_{cons.}$ (M_{\odot} /year)	4.6×10^{-8}	-
$dM/dt_{non\ cons.}$ (M_{\odot} /year)	4.9×10^{-8}	-
e_3	0.19 (4)	0.239
ω_3 (deg)	65 (14)	-
A_3 (day)	0.014 (3)	0.0144
P_3 (year)	47 (1)	49.3
$f(m_3)$ (M_{\odot})	0.0062 (2)	-
m_3 (M_{\odot}) (for $i=90$)	0.35	-
e_4	0.07 (2)	-
ω_4 (deg)	85 (21)	-
A_4 (day)	0.0022 (4)	-
P_4 (year)	11 (1)	-
$f(m_4)$ (M_{\odot})	0.00046 (1)	-
m_4 (M_{\odot}) (for $i=90$)	0.15	-

If cyclical changes are visible on the O–C graph, the magnetic cycling of the cold component can shown as the cause. One of the accepted explanations for this was tried to be explained by Applegate (1992). Variations of O–C owing to the magnetic cycling are cyclical and may be represented by the equation 3.

$$Min I = T_0 + E x P + A_{mod} \sin \left[\frac{2\pi}{P_{mod}} (E - T_s) \right] \quad (3)$$

The terms in equation 3 can be defined as follows (In Equation 3, T_0 , E , and P represent the light elements.)

T_0 : the initial minimum time.

P : the orbital period.

E : the epoch number.

A_{mod} : the amplitude.

P_{mod} : the period.

T_s : minimum moment of the periodic variation.

According to the Applegate model, the such period changes value should be approximately $\Delta P / P \approx 10^{-5}$. As a result of the analysis for the VX Lac system, two cyclical changes were detected. Therefore, the parameters obtained by making Applegate (1992) calculations for both cyclical changes are listed in Table 4.

Table 4. Some parameters for the Applegate model for VX Lac system.

Parameters	First Sinüsoidal	Second Sinüsoidal
P_{mod} (year)	47	11
$\Delta P/P$	5.1×10^{-6}	3.4×10^{-6}
ΔJ (erg s ⁻¹)	1.5×10^{48}	9.8×10^{47}
$\Delta \Omega/\Omega$	0.006	0.004
ΔE (erg)	1.2×10^{42}	5.4×10^{41}
I_s (g cm ²)	3.6×10^{54}	3.6×10^{54}
$\Delta L/L_1$	0.083	0.16
B (kG)	9	16
ΔQ_1	3.2×10^{50}	2.1×10^{50}
ΔQ_2	1.55×10^{50}	1.1×10^{50}

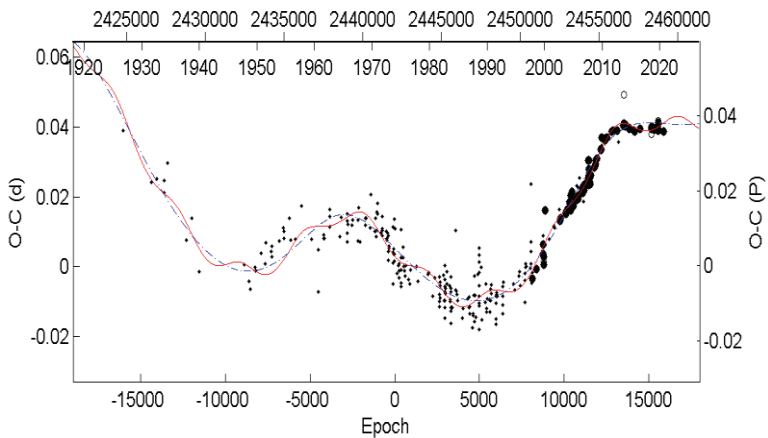


Figure 3. Representation of VX Lac system with O-C graph and theoretical curves. The dashed blue lines represent the third component. And the solid red line is the theoretical fit of the fourth body.

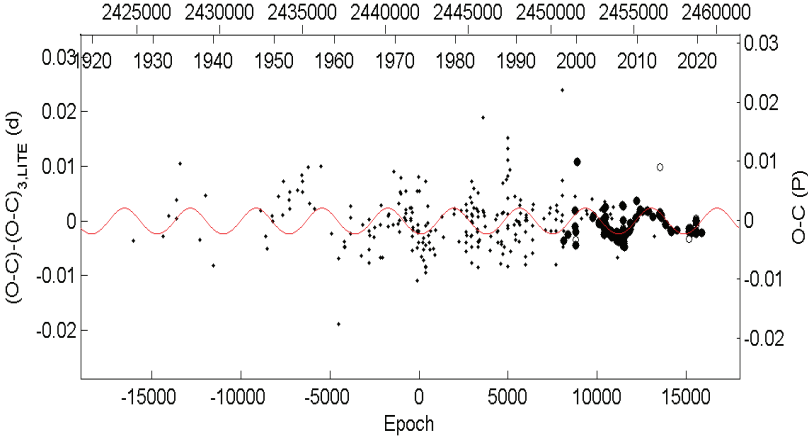


Figure 4. Fourth body theoretical fit for the VX Lac system. The red continuous line represents the theoretical fit of the fourth body.

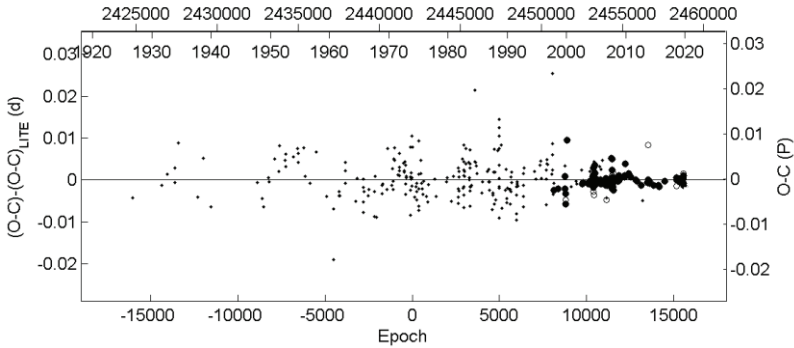


Figure 5. For VX Lac, residuals from the compatibility between the observational data and the theoretical data are seen.

4. RESULTS AND DISCUSSIONS

Because there is no spectral study of VX Lac in the literature, it will be very significant to determine its absolute parameters, so in this study the basic astrophysical parameters are estimated (see Table 5). If the first object of the VX Lac is taken as a normal main sequence star, it should have a mass of $1.64 M_{\odot}$. The error value for the first component is taken as 10% of the mass of the object. So, the absolute parameters of the VX Lac can be calculated by using the mass ratio $q=0.487 \pm 0.021$ obtained in consequence of photometric analysis. While calculating the absolute parameters, the values for the Sun from Pecaut & Mamajek (2013) were used ($T_{eff} = 5771.8 (0.7) \text{ K}$, $g = 27423.2 (7.9) \text{ cm.s}^{-2}$, $M_{bol} = 4.7554 \pm$

0.0004 mag). The estimated masses and radii for the components of VX Lac were obtained as $M_1=1.64 M_\odot$, $M_2=0.80 M_\odot$ and $R_1=1.84 R_\odot$, $R_2=1.54 R_\odot$ respectively. The masses and radii calculated in this study support the values estimated by Svechnikov & Kuznetsova (1990) and Budding et al. (2004). In addition, the luminosity calculated for the components ($L_1=7.85 L_\odot$, $L_2=1.05 L_\odot$) also support the study of Budding et al. (2004). The bolometric correction (BC) values of the components of the VX Lac whose photometric analysis was performed were taken from the study by Eker et al. (2020), taking into account the temperatures and luminosity classes of the components. The estimated basic astrophysical parameters for the components are given in Table 5. In consequence of photometric analysis, the distance determined for VX Lac is 432 (31) pc, which is very close to the distance value given by Gaia Collaboration (2022) ($d_{\text{Gaia-DR3}}=439$ (8)).

Table 5. Estimated basic astrophysical parameters for the VX Lac eclipsing system and comparison with the studies in the literature.

Parameters	This Study	Svechnikov & Kuznetsova (1990)	Budding et al. (2004)
$M_1 (M_\odot)$	1.64 (16)	1.45	1.48
$M_2 (M_\odot)$	0.80 (5)	0.47	1.07
$R_1 (R_\odot)$	1.84 (7)	1.60	1.70
$R_2 (R_\odot)$	1.54 (6)	1.50	1.26
$\log g_1$ (cgs)	4.12 (5)	-	-
$\log g_2$ (cgs)	3.97 (8)	-	-
$M_{bol,1}$ (mag)	2.50 (13)	-	-
$M_{bol,2}$ (mag)	4.68 (20)	-	-
$L_1 (L_\odot)$	7.85 (12)	-	6.60
$L_2 (L_\odot)$	1.05 (18)	-	2.16
$d_{\text{photometri}}$ (pc)	432 (31)	-	-
$d_{\text{Gaia-DR3}}$ (pc)	439 (8)	-	-

For the orbital period analysis of the semi-detached VX Lac system in this study, 392 eclipse times were taken from the literature. In addition, a total of 408 data with sixteen eclipse times obtained from SuperWASP (8 eclipse times) and TESS (8 eclipse times) data were used. In the O–C graph, if the variation is in the parabolic form, the period is either decreasing or increasing. The positivity of the coefficient (Q) of the parabola demonstrates that the period has increased, and its negativity

indicates that it has decreased. The increase in the period can be expressed by the mass exchange from the less mass to the more mass. In the O–C diagram for VX Lac, a parabolic change with increasing period is observed, which is consistent with previous analysis studies. Along with this change, there are also two different sinusoidal changes. Sinusoidal changes have assumed to be the LITE caused by possible third and fourth bodies (Light Time Effect=LITE) and some orbital parameters of the third and fourth bodies are obtained by using equation (2) in the solution (see Table 3). Parabola calculation and LITE terms given in the third part of the study were applied with the least squares way.

The minimum values of possible third and fourth body masses were calculated as $M_3=0.35 M_\odot$ and $M_4=0.15 M_\odot$, respectively. The period of the third body, which makes orbital motion with a common mass center with the binary, was calculated as $P_3=47$ years, and OP of the fourth object was calculated as $P_4=11$ years. The parameters found through the period analysis are presented in Table 3. In the analysis made using approximately 100 years of data, the amount of OP increase in the semi-detached VX Lac system was calculated as 9.5×10^{-8} days/year. Increase of orbital period, assuming conservative mass exchange from the less massive one to the more massive one. The mass exchange value between the components is calculated as $dM/dt=4.6 \times 10^{-8} M_\odot/\text{year}$, in this case the total mass of the system does not change. With the assumption of nonconservative mass, this rate was determined as $4.6 \times 10^{-8} M_\odot/\text{year}$, this is slightly above the conservative mass exchange ratio.

The second cyclical change in the VX Lac has obtained for the first time in this paper. The cause of second cyclical change may also be magnetic activity. Therefore, the Applegate (1992) model was applied and the obtained parameters are listed in Table 4. If one looks at Table 4, it is close to the values suggested by Applegate (1992). In particular, the second cyclical change being 11 years was close to the year value similar to the spot cycle on the Sun (between 8 and 11 years for the Sun).

The location of the VX Lac system, whose basic astrophysical parameters such as mass and radius are estimated, on the $\log M$ – $\log R$ diagram provides us with information about the evolution of the system. Therefore, the RW Cet, BO Gem, DG Lac and SW Oph systems, together with the VX Lac, are positioned on the $\log M$ – $\log R$ diagram (see, Figure 6). Mass and radius values of RW Cet, BO Gem, DG Lac and SW Oph systems are taken from Budding et al. (2004). Evolutionary pathways and ZAMS (zero age main sequence) and TAMS (terminal age main sequence) lines were generated for single stars and Solar chemical abundance models given by Bressan et al (2012) ($Z [\text{Fe}/\text{H}] = 0.014$ for metallicity). When Figure 6 is examined, it is seen that the first bodies of the systems are in the main sequence, while the second bodies are in the sub-giant or giant position. The positions of the bodies of the systems in

the $\log M$ – $\log R$ diagram show that they have the characteristics of semi-detached systems.

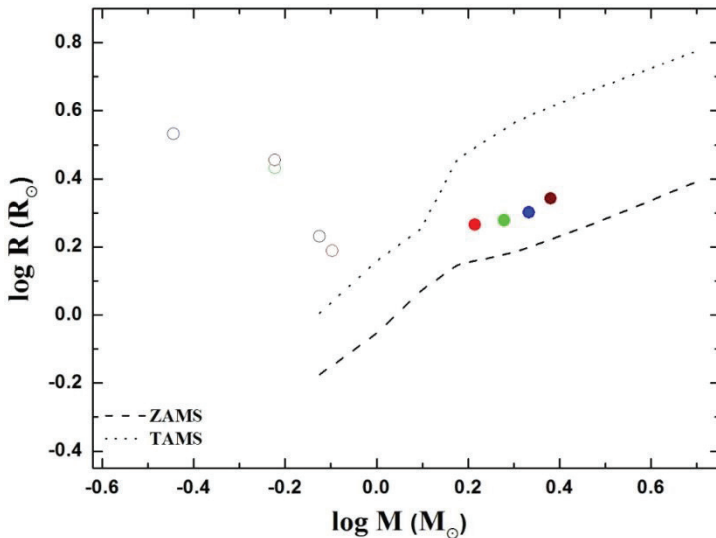


Figure 6. The $\log M$ – $\log R$ graphs represent of the components of VX Lac (red), RW Cet (black), BO Gem (blue), DG Lac (green) and SW Oph (brown). The first bodies of the systems are demonstrated as filled circles and the second bodies as hollow circles.

Future spectral studies for the VX Lac semi-detached system will be very important as the mass ratio and spectral type of the VX Lac can be obtained more precisely. With the calculating of the q , the mass and radius etc. values of the system will be calculated more precisely. In this study, possible third and fourth components can be also determined in the spectral observations for the causes of sinusoidal change determined in the O–C analysis. It will also be important to make observations of magnetic activity for the VX Lac system. Continuation of photometric observations and determination of new eclipse times will be remarkable in terms of orbital period analysis.

5. ACKNOWLEDGMENT

In this paper, data archives of O–C Gateway (Paschke & Brat, 2006), Atlas O–C (Kreiner, 2004), Simbad (<http://simbad.u-strasbg.fr/simbad/>), TESS, MAST (<https://archive.stsci.edu>) and Gaia–DR3 (<https://www.cosmos.esa.int/web/gaia/dr3>) were used. And so, we thank these working teams.

6. REFERENCES

- Applegate, J.H., 1992. A Mechanism for Orbital Period Modulation in Close Binaries. *Astrophysical Journal*, 385, 621.
- Bressan, A., Marigo, P., Girardi, L., Salasnich, B., Dal C.C., Rubele, S., Nanni, A., 2012. PARSEC: stellar tracks and isochrones with the PAdova and TRieste Stellar Evolution Code. *Monthly Notices of the Royal Astronomical Society*, 427, 1, 127-145.
- Budding, E., Erdem, A., Çiçek, C., Bulut, I., Soyduğan, F., Soyduğan, E., Bakış, V., Demircan, O., 2004. Catalogue of Algol type binary stars. *Astronomy and Astrophysics*, 417, 263-268.
- Butters, O.W., West, R.G., Anderson, D.R., Collier, C.A., Clarkson, W.I., Enoch, B., Haswell, C.A., Hellier, C., Horne, K., Joshi, Y., Kane, S.R., Lister, T.A., Maxted, P.F.L., Parley, N., Pollacco, D., Smalley, B., Street, R.A., Todd, I., Wheatley, P.J., Wilson, D.M., 2010. The first WASP public data release. *Astronomy and Astrophysics*, 520, L10, 4.
- Cannon, A. J., 1934. Spectra of Ninety-four Variable Stars. *Harvard College Observatory Bulletin*, 897, 12-12.
- Eker, Z., Soyduğan, F., Bilir, S., Bakış, V., Aliçavuş, F., Özer, S., Aslan, G., Alpsoy, M., Köse, Y., 2020. Empirical bolometric correction coefficients for nearby main-sequence stars in the Gaia era. *Monthly Notices of the Royal Astronomical Society*, 496, 3, 3887-3905.
- Erdem, A., Öztürk, O., 2014. Non-conservative mass transfers in Algols. *Monthly Notices of the Royal Astronomical Society*, 441, 2, 1166-1176.
- Gaia Collaboration, 2022. VizieR Online Data Catalog: Gaia DR3 Part 1. Main source (Gaia Collaboration, 2022). VizieR On-line Data Catalog: I/355. Originally published in: *Astron. Astrophys.*, in prep. (2022)
- Irwin, J.B. 1959. Standard light-time curves. *Astronomical Journal*, 64, 149-155.
- Kopal, Z., 1959. The classification of close binary systems. *Annales d'Astrophysique*, 18, 379.
- Kreiner, J. M., 2004. Up-to-Date Linear Elements of Eclipsing Binaries. *Acta Astronomica*, 54, 207-210.
- Paschke, A. Brat, L., 2006. O-C Gateway, a Collection of Minima Timings. *Open European Journal on Variable Stars*, 23, 13-15.
- Pecaut, M.J., Mamajek, E.E., 2013. Intrinsic Colors, Temperatures, and Bolometric Corrections of Pre-main-sequence Stars. *The Astrophysical Journal Supplement*, 208, 1, 9.
- Ricker, G. R., Winn J. N., Vanderspek R., Latham, D.W., Bakos, Gaspar A., Bean, J.L., Berta-Thompson, Z.K., Brown, Timothy M., Buchhave, L., Butler, N.R., Butler, R.P., Chaplin, W.J., Charbonneau, D., Christensen-Dalsgaard, J., Clampin, M., Deming, D., Doty, J., De Lee, N., Dressing, C., Dunham, E.W., 2015. Transiting Exoplanet Survey Satellite (TESS).

Journal of Astronomical Telescopes, Instruments, and Systems, 1.

- Svechnikov M. A. & Kuznetsova E. F., 1990. Izd-vo Uralskogo Universiteta, Sverdlovsk.
- Tout, C.A., Hall, D.S., 1991. Wind driven mass transfer in interacting binary systems. *Monthly Notices of the Royal Astronomical Society*, 253, 9-18.
- Wilson, R.E., Devinney, E.J., 1971. Realization of accurate close-binary light curves: Application to MR cygni. *The Astrophysical Journal*, 166, 605-619.
- Yıldırım, M.F., 2020. Orbital period behaviour of three semi-detached binaries: AI Cru, V1898 Cyg and Z Vul. *Bitlis Eren University Journal of Science and Technology*, 10, 2, 49-53.
- Yıldırım, M.F., 2022. Photometric Investigation of Contact Binary DY Cet Based on TESS Data. *Research in Astronomy and Astrophysics*, 22, 5, 8.
- Zasche, P., 2016. First analysis of eight Algol-type binaries: EI Aur, XY Dra, BP Dra, DD Her, VX Lac, WX Lib, RZ Lyn, and TY Tri. *New Astronomy*, 42, 1-9.
- Zasche, P., Liakos, A., Wolf, M. and Niarchos, P., 2008. Period Changes in Six SemiDetached Algol-Type Binaries. *New Astronomy*, 13 (6), 405-413.



CHAPTER 10

λ -STATISTICAL CONVERGENCE OF FRACTIONAL DIFFERENCE SEQUENCES ON NEUTROSOPHIC NORMED SPACES

*Dr. Öğr. Üyesi Nazmiye GONUL BILGIN¹,
Gurel BOZMA²*

1 Zonguldak Bulent Ecevit University, 0000-0001-6300-6889

2 Gurel BOZMA, Zonguldak Governorate, 0000-0002-0916-5894

Introduction

Since sequence convergence is very necessary in basic mathematical theory, many different kinds of convergence concepts have been tried to be carried over into summability, approximation theory, and probability theory. The concept of difference sequence space was defined by Kizmaz. These sequence spaces is modification by Et and Colak in 1995. Long before this work Fast, introduced statistical convergence briefly in 1951, and then Schoenberg examined statistical convergence in detail with the help of summation method in 1959. The concept of statistical convergence is worked under different name. (Mursaleen, 2000), introduced the λ statistical convergence and Hazarika and Savas carried these concept on n -normed spaces in 2013. λ -statistically convergent difference sequences using fuzzy numbers is studied in (Altinok et al, 2012).

Some important definitions and features of neutrophic set theory will now be given, which are necessary for the development of this work. Now, let's recall λ_v -statistically convergent.

Let $\lambda = (\lambda_v)$ be a non-decreasing, $\lambda_1 = 1$, $\lambda_{v+1} \leq \lambda_v + 1$ such that $\lim_{v \rightarrow \infty} \lambda_v = \infty$. Also, let $\mathcal{J}_v = [v + 1 - \lambda_v, v]$ and $t_v(x) = \frac{1}{\lambda_v} \sum_{r \in \mathcal{J}_v} x_r$. In this case, (x_v) is named λ - statistically convergent to ℓ if for all $\varepsilon > 0$,

$$\lim_{v \rightarrow \infty} \frac{1}{\lambda_v} |\{r \in \mathcal{J}_v: |x_v - \ell| \geq \varepsilon\}| = 0. \quad (1)$$

In this situation, it is denoted by $x_v \rightarrow \ell(st)_\lambda$.

On the other hand let's examine the general structure of sequence spaces obtained with the help of the fractional difference operator, which is one of the areas where statistical convergence is applied. Let, $\Gamma(u)$ demonstrate the Euler Gamma function where u is real number and $u \notin \{0, -1, -2, \dots\}$. Here the notations in (Kadak and Baliarsingh, 2015) and (Ercan, 2018) will be used. Then a generalization of fractional difference operator is given in (Baliarsingh and Dutta, 2015) as

$$\Delta^u(x_v) = \sum_{j=0}^{\infty} (-1)^j \frac{\Gamma(u+1)}{j! \Gamma(u-j+1)} x_{j+v}. \quad (2)$$

After then, Δ^u - statistical convergence and graded state of this concept is defined in (Ercan, 2018) and (Mursaleen and Baliarsingh, 2022), respectively.

The concepts of fuzzy, intuitionistic fuzzy and neutrosophic sets has revolutionized many areas such as mathematics, science, engineering, medicine. This concepts is given by (Zadeh,1965), (Atanassov,1986) and (Smarandache,1999). The second of these theories deals with an imprecise and uncertain situation by corresponding degree of membership and degree of non-membership to particular object. Neutrosophic logic is a powerful tool for modeling instability and uncertainty in a variety of problems that arise in science and engineering. It has very important and facilitating applications in many fields.

The neutrosophic set is investigated by (Smarandache,1999) and he determined the Neutrosophic set using degree of truth, inaccuracy and uncertainty. Neutrosophic normed spaces is given in (Kirisci and Simsek, 2020) and is examined statistical convergence this spaces. In (Kisi, 2021) lacunary statistical convergent in NNS is studied. Many studies have been done with different types of convergence in this space. e.g(Gonul Bilgin,2022).

The concept of convergence in the NNS space is defined as follows. (Kirisci and Simsek, 2020), (Khan et. al, 2021).

Let \mathcal{U} be a neutrosophic normed space (NNS), $\beta > 0$. For (x_v) in \mathcal{U} , let $0 < \varepsilon < 1$. So, the sequence (x_v) is called convergence to ℓ if there exists $k \in \mathbb{N}$, such that $G(x_v - \ell, \beta) > 1 - \varepsilon, B(x_v - \ell, \beta) < \varepsilon, Y(x_v - \ell, \beta) < \varepsilon$. That is $\lim_{v \rightarrow \infty} G(x_v - \ell, \beta) = 1, \lim_{v \rightarrow \infty} B(x_v - \ell, \beta) = 0, \lim_{v \rightarrow \infty} Y(x_v - \ell, \beta) = 0$. Then, the sequence (x_v) is named a convergent sequence in \mathcal{U} . The convergent in NNS is showed by $N - \lim x_v = \ell$.

Many investigations have been made with different types of convergence in different spaces.e.g(Gonul Bilgin and Bozma, 2021)

Now let's recall the definition of statistical convergence is given in (Kirisci and Simsek, 2020). Take a NNS \mathcal{U} . A sequence (x_k) is named statistical convergence, if there exist ℓ so that the set

$$T_\varepsilon = \{k \leq n: G(x_k - \ell, \beta) \leq 1 - \varepsilon \text{ or } B(x_k - \ell, \beta) \geq \varepsilon, Y(x_k - \ell, \beta) \geq \varepsilon\}$$

has natural density is zero, for every $\varepsilon > 0$ and $\beta > 0$. That is $d(T_\varepsilon) = 0$ or equivalently,

$$\lim_{n \rightarrow \infty} \frac{1}{n} |\{k \leq n: G(x_k - \ell, \beta) \leq 1 - \varepsilon \text{ or } B(x_k - \ell, \beta) \geq \varepsilon, Y(x_k - \ell, \beta) \geq \varepsilon\}| = 0.$$

Then, we show $st - \lim x_k = \ell(N)$ or $x_k \rightarrow \ell(st(N))$. The set of statistical convergence segences in NN will be denoted by $St(N)$.

Based on these studies, the concepts of Δ_λ^u – statistical convergence and the concept of $(\Delta_\lambda^{u,p})$ –Cesaro summable, for fractional difference

sequences will be introduced in our work. Also, the concept of $(\Delta_\lambda^u)^\alpha$ -statistically convergent is given and important coverage relations are given. It is accepted throughout the article that (2) is a convergent series and the number of terms in the sum symbol changes up to u .

2. Matherial and Methods

Now, Δ_λ^u – statistical convergence, $(\Delta_\lambda^{u,p})$ –Cesaro summable for fractional difference sequences will be introduced in Neutrosophic normed spaces. The connection between these concepts will be defined.

Definition 2.1 Let $\lambda = (\lambda_v)$ be a non-decreasing, $\lambda_1 = 1$, $\lambda_{v+1} \leq \lambda_v + 1$ such that $\lim_{v \rightarrow \infty} \lambda_v = \infty$, $J_v = [v + 1 - \lambda_v, v]$ and also u be a convenient fraction. In this case, if there is a ℓ number such that

$$\lim_{v \rightarrow \infty} \frac{1}{\lambda_v} |\{t \in J_v : |\Delta_\lambda^u(x_v) - \ell| \geq \varepsilon\}|$$

for every $\varepsilon > 0$, $x = (x_v)$ sequence is called Δ_λ^u - statistically convergent and the set of Δ_λ^u - statistically convergent sequences is denoted by $S(\Delta_\lambda^u)$. As a result, $x \rightarrow \ell \left((st)_{\Delta_\lambda^u} \right)$ can be written.

Theorem 2.1 $x = (x_k), z = (z_k)$ be sequences of real numbers.

i) If $S(\Delta_\lambda^u) - \lim x_k = \check{x}$ and α belongs to real numbers, then $S(\Delta_\lambda^u) - \lim \alpha x_k = \alpha \check{x}$.

ii) If $S(\Delta_\lambda^u) - \lim x_k = \check{x}$, $S(\Delta_\lambda^u) - \lim z_k = \check{z}$, then $S(\Delta_\lambda^u) - \lim(x_k + z_k) = \check{x} + \check{z}$.

Proof.

i) If $\alpha = 0$, it is seen easily. Let assume $\alpha \neq 0$, then we have desired result from

$$\frac{1}{\lambda_v} |\{k \leq n : |\Delta_\lambda^u \alpha x_k - \alpha \check{x}| \geq \varepsilon\}| \leq \frac{1}{\lambda_v} \left| \left\{ k \leq n : |\Delta_\lambda^u x_k - \check{x}| \geq \frac{\varepsilon}{|\alpha|} \right\} \right|.$$

ii) It is seen from following inequality;

$$\begin{aligned} \frac{1}{\lambda_v} |\{k \leq n : |\Delta_\lambda^u(x_k + z_k) - (\check{x} + \check{z})| \geq \varepsilon\}| &\leq \frac{1}{\lambda_v} \left| \left\{ k \leq n : |\Delta_\lambda^u x_k - \check{x}| \geq \frac{\varepsilon}{2} \right\} \right| \\ + \frac{1}{\lambda_v} \left| \left\{ k \leq n : |\Delta_\lambda^u z_k - \check{z}| \geq \frac{\varepsilon}{2} \right\} \right|. \end{aligned}$$

Definition2.2 Let $\lambda = (\lambda_v)$ be sequence as given in Definition 2.1 and let u be a convenient fraction. Then, if there is a $v^\circ = v^\circ(\varepsilon)$ number such that for every $\varepsilon > 0$

$$\lim_{v \rightarrow \infty} \frac{1}{\lambda_v} |\{t \in \mathcal{J}_v : |\Delta_\lambda^u(x_v) - \Delta_\lambda^u(x_{v^\circ})| \geq \varepsilon\}| = 0,$$

the sequence $x = (x_v)$ is called the Δ_v^α - statistical Cauchy sequence.

Theorem2.2 If the sequence $x = (x_v)$ is Δ_λ^u - statistically convergent, then the sequence $x = (x_v)$ is the Δ_λ^u - statistical Cauchy sequence.

Proof.

Suppose $x = (x_v) \in S(\Delta_\lambda^u)$ and $\varepsilon > 0$. In this case, for almost all v

$$|\Delta_\lambda^u(x_v) - \ell| < \frac{\varepsilon}{2}.$$

For a selected number v° ,

$$|\Delta_\lambda^u(x_{v^\circ}) - \ell| < \frac{\varepsilon}{2}$$

can be written. From here it becomes

$$|\Delta_\lambda^u(x_v) - \Delta_\lambda^u(x_{v^\circ})| < |\Delta_\lambda^u(x_v) - \ell| + |\Delta_\lambda^u(x_{v^\circ}) - \ell| < \varepsilon.$$

Thus x is a Δ_λ^u -statistical Cauchy sequence.

Definition 2.3 Let $p > 0$. (x_v) is called to be strongly $(\Delta_\lambda^{u,p})$ -Cesaro summable, if there is a $\ell \in \mathbb{R}$ such that

$$\lim_{v \rightarrow \infty} \frac{1}{\lambda_v} \sum_{j=1}^v |\Delta_\lambda^u x_v - \ell|^p = 0.$$

Then, (x_v) is strongly $(\Delta_\lambda^{u,p})$ -Cesaro summable to ℓ . The set of these sequences is shown with $L(\Delta_\lambda^{u,p})$. If $\ell = 0$, then this spaces is shown with $\omega(\Delta_\lambda^{u,p})$.

Definition 2.4 Let $\lambda = (\lambda_v)$ be a sequences with the properties given in Definition 2.1, $\mathcal{J}_v = [v + 1 - \lambda_v, v]$ and u be a convenient fraction. For $0 < \alpha \leq 1$ let $\lambda_v^\alpha = (\lambda_1^\alpha, \lambda_2^\alpha, \dots, \lambda_v^\alpha, \dots)$. Then, if there is a ℓ number such that

$$\lim_{v \rightarrow \infty} \frac{1}{\lambda_v^\alpha} |\{t \in \mathcal{J}_v : |\Delta_\lambda^u(x_v) - \ell| \geq \varepsilon\}|$$

for every $\varepsilon > 0$, $x = (x_v)$ sequence is called $(\Delta_\lambda^u)^\alpha$ - statistically convergent to ℓ and the set of $(\Delta_\lambda^u)^\alpha$ - statistically convergent sequences is denoted by $S((\Delta_\lambda^u)^\alpha)$. As a result, $x \rightarrow \ell \left((st)_{\Delta_\lambda^u} \right)$ can be written.

Clearly, for all $0 < \alpha \leq 1$, $(\Delta_\lambda^u)^\alpha$ - statistically convergent is well defined, however for $\alpha > 1$ this property does not always have to be true.

In the lemma below, a density comparison will be made for the type of convergence we defined using the density concept of a well-known set in the literature.

Lemma 2.1 Let $\mathcal{J}_v = [v + 1 - \lambda_v, v]$, u be a convenient fraction and $\aleph \subseteq \mathbb{N}$. If for all $0 < \alpha \leq \varrho \leq 1$, then

$$(\delta_\lambda^u)^\varrho(\aleph) \leq (\delta_\lambda^u)^\alpha(\aleph).$$

Proof.

Let $0 < \alpha \leq \varrho \leq 1$ and $\lambda_v^\alpha \leq \lambda_v^\varrho$. In this case, $\frac{1}{\lambda_v^\varrho} \leq \frac{1}{\lambda_v^\alpha}$. Hence,

$$\frac{1}{\lambda_v^\varrho} |\{t \in \mathcal{J}_v : |\Delta_\lambda^u(x_v) - \ell| \geq \varepsilon\}| \leq \frac{1}{\lambda_v^\alpha} |\{t \in \mathcal{J}_v : |\Delta_\lambda^u(x_v) - \ell| \geq \varepsilon\}|.$$

So,

$$(\delta_\lambda^u)^\varrho(\aleph) \leq (\delta_\lambda^u)^\alpha(\aleph).$$

Lemma 2.2 Let $\lambda = (\lambda_v)$ be a sequences with the properties given in Definition 2.1, $\mathcal{J}_v = [v + 1 - \lambda_v, v]$ and u be a convenient fraction. For $0 < \alpha \leq 1$, if (x_v) is Δ_λ^u - statistically convergent then these sequence is $(\Delta_\lambda^u)^\alpha$ - statistically convergent.

Proof.

The proof is easily obtained from the definition.

Definition 2.5 Let $\lambda = (\lambda_v)$ be sequence as given in Definition 2.1 and let u be a convenient fraction. Then, if there is a $v^\circ = v^\circ(\varepsilon)$ number such that for every $\varepsilon > 0$

$$\lim_{v \rightarrow \infty} \frac{1}{\lambda_v^\alpha} |\{t \in \mathcal{J}_v : |(\Delta_\lambda^u)^\alpha(x_v) - (\Delta_\lambda^u)^\alpha(x_{v^\circ})| \geq \varepsilon\}| = 0,$$

the sequence $x = (x_v)$ is called the $(\Delta_\lambda^u)^\alpha$ - statistical Cauchy sequence.

Proposition 2.1 Let $\lambda = (\lambda_v)$ be a sequences with the properties given in Definition 2.1, $\mathcal{J}_v = [v + 1 - \lambda_v, v]$ and u be a convenient fraction. For $0 < \alpha \leq 1$, if $\liminf_v \frac{\lambda_v}{v} > 0$ then $S(\Delta^u) \subset S(\Delta_\lambda^u)$.

Proof.

Let $\liminf_v \frac{\lambda_v}{v} > 0$ and (x_v) is Δ^u - statistical convergent sequences. Then,

$$\begin{aligned} \frac{1}{v} |\{t \leq v: |\Delta^u(x_v) - \ell| \geq \varepsilon\}| &\geq \frac{1}{v} |\{t \in \mathcal{J}_v: |\Delta^u(x_v) - \ell| \geq \varepsilon\}| \\ &= \frac{\lambda_v}{v} \frac{1}{\lambda_v} |\{t \in \mathcal{J}_v: |\Delta^u(x_v) - \ell| \geq \varepsilon\}|. \end{aligned}$$

So, (x_v) is (Δ_λ^u) - statistical convergent sequences. Then, $S(\Delta^u) \subset S(\Delta_\lambda^u)$.

Definition 2.6 Let $p > 0$. (x_v) is called to be strongly $(\Delta_\lambda^{u,p})^\alpha$ -Cesaro summable, if there is a $\ell \in \mathbb{R}$ such that

$$\lim_{v \rightarrow \infty} \frac{1}{\lambda_v^\alpha} \sum_{j=1}^v |\Delta_\lambda^u x_v - \ell|^p = 0.$$

Then, (x_v) is strongly $(\Delta_\lambda^{u,p})^\alpha$ -Cesaro summable to ℓ . The set of these sequences is shown with $L((\Delta_\lambda^{u,p})^\alpha)$. If $\ell = 0$, then this spaces is shown with $\omega((\Delta_\lambda^{u,p})^\alpha)$.

Theorem2.3 Let $0 < \inf P_v \leq P_v \leq \sup P_v < \infty$ and u be a convenient fraction. In this case $L((\Delta_\lambda^{u,p})) \subset S(\Delta_\lambda^u)$.

Proof.

Let $(x_v) \in L((\Delta_\lambda^{u,p}))$, $t \in \mathcal{J}_v$. In this case,

$$\begin{aligned} \frac{1}{\lambda_v} \sum_{t \in \mathcal{J}_v} |\Delta_\lambda^u(x_t) - \ell|^{P_v} &\geq \frac{1}{\lambda_v} \sum_{\substack{|\Delta_\lambda^u(x_t) - \ell| \geq \varepsilon \\ t \in \mathcal{J}_v}} |\Delta^\alpha(x_t) - \ell|^{P_v} \\ &\geq \frac{1}{\lambda_v} \sum_{\substack{|\Delta_\lambda^u(x_t) - \ell| \geq \varepsilon \\ t \in \mathcal{J}_v}} \varepsilon^{\inf P_v} \\ &\geq \frac{1}{\lambda_v} |\{t \in \mathcal{J}_v: |\Delta^\alpha(x_t) - \ell| \geq \varepsilon\}| \varepsilon^{\inf P_v}. \end{aligned}$$

For $v \rightarrow \infty$, we get

$$\begin{aligned} \lim_{v \rightarrow \infty} \frac{1}{\lambda_v} |\{t \in \mathcal{J}_v: |\Delta_\lambda^u(x_t) - \ell| \geq \varepsilon\}| \\ \leq \frac{1}{\varepsilon^{\inf P_v}} \left(\lim_{v \rightarrow \infty} \frac{1}{\lambda_v} \sum_{t \in \mathcal{J}_v} |\Delta_\lambda^u(x_t) - \ell|^{P_v} \right) = 0, \end{aligned}$$

so, $x \in S(\Delta_\lambda^u)$ then, $L((\Delta_\lambda^{u,p})) \subset S(\Delta_\lambda^u)$.

Theorem2.4 Let $0 < p < \infty$. If $x = (x_v)$ is strongly $(\Delta_\lambda^{u,p})$ -Cesaro summable to ℓ , then it is (Δ_λ^u) -statistically convergent to ℓ .

Proof. For any sequence $x = (x_v)$ and $\varepsilon > 0$,

$$\begin{aligned} \sum_{v=1}^m |\Delta_\lambda^u x_v - \ell|^p &= \sum_{\substack{v=1 \\ |x_v - \ell| \geq \varepsilon}}^m |\Delta_\lambda^u x_v - \ell|^p + \sum_{\substack{v=1 \\ |x_v - \ell| < \varepsilon}}^m |\Delta_\lambda^u x_v - \ell|^p \\ &\geq \sum_{v=1}^m |\Delta_\lambda^u x_v - \ell|^p \end{aligned}$$

$$\geq |\{k \leq n: |\Delta^u x_v - \ell| \geq \varepsilon\}| \varepsilon^p$$

and so

$$\frac{1}{\lambda_v} \sum_{v=1}^m |\Delta_\lambda^u x_v - \ell|^p \geq \frac{1}{\lambda_v} |\{k \leq n: |\Delta_\lambda^u x_v - \ell| \geq \varepsilon\}| \varepsilon^p.$$

Therefore, if $x = (x_v)$ is $(\Delta_\lambda^{u,p})$ -Cesaro summable to ℓ , then, this sequence is (Δ_λ^u) -statistically convergent to ℓ .

3. Main Results

Now, the concept of (Δ_λ^u) -statistical convergence in Neutrosophic normed spaces will be defined and important properties of convergence in these spaces will be introduced.

Definition3.1 Let $(X, \mu^T, \gamma^F, \eta^I, \boxtimes, \otimes)$ be a Neutrosophic normed spaces and let $\lambda = (\lambda_v)$ be sequence as given in Definition 2.1 and let u be a convenient fraction. $x = (x_v)$ is called (Δ_λ^u) -statistical convergence according to neutrosophic normed where for every $\varepsilon > 0$ and $\mathfrak{h} > 0$, there exist a ℓ :

$$\delta_\lambda^u \{k: \mu^T(\Delta_\lambda^u x_v - \ell, \mathfrak{h}) \leq 1 - \varepsilon \text{ or } \eta^I(\Delta_\lambda^u x_v - \ell, \mathfrak{h}) \geq \varepsilon, \gamma^F(\Delta_\lambda^u x_v - \ell, \mathfrak{h}) \geq \varepsilon\} = 0.$$

Equivalent to this information, we will say that

$$\lim_v \frac{|\{k \in \mathcal{I}_v: \mu^T(\Delta_\lambda^u x_v - \ell, \mathfrak{h}) \leq 1 - \varepsilon \text{ or } \eta^I(\Delta_\lambda^u x_v - \ell, \mathfrak{h}) \geq \varepsilon, \gamma^F(\Delta_\lambda^u x_v - \ell, \mathfrak{h}) \geq \varepsilon\}|}{\lambda_v} = 0,$$

is also (Δ_λ^u) -statistical convergence according to neutrosophic normed. In this case, we use $st_{\Delta_\lambda^u}^{\mathcal{N}} - \lim x = \ell$. The set of all this sequences will demonstrated with $St_{\Delta_\lambda^u}^{\mathcal{N}}$.

Lemma 3.1 Let $(X, \mu^T, \gamma^F, \eta^I, \boxtimes, \otimes)$ be a Neutrosophic normed spaces, $\lambda = (\lambda_v)$ be sequence as given in Definition 2.1 and let u be a convenient fraction. Let $x = (x_v)$ is (Δ_λ^u) -statistical convergence according to neutrosophic normed where for every $\varepsilon > 0$ and $\mathfrak{b} > 0$, then the next situations are equivalent in $(X, \mu_T, \nu_F, \eta_I, \odot, \otimes)$:

$$\begin{aligned}
 & \text{i. } st_{\Delta_\lambda^u}^{\mathcal{N}} - \lim x = \ell, \\
 & \text{ii. } \lim_v \frac{|\{k \in \mathcal{J}_v: \mu^T(\Delta_\lambda^u x_v - \ell, \mathfrak{b}) > 1 - \varepsilon \text{ or } \eta^I(\Delta_\lambda^u x_v - \ell, \mathfrak{b}) \leq \varepsilon, \gamma^F(\Delta_\lambda^u x_v - \ell, \mathfrak{b}) \leq \varepsilon\}|}{\lambda_v} \\
 & = 0, \\
 & \text{iii. } \lim_v \frac{|\{k \in \mathcal{J}_v: \mu^T(\Delta_\lambda^u x_v - \ell, \mathfrak{b}) \leq 1 - \varepsilon\}|}{\lambda_v} \\
 & = 0, \lim_v \frac{|\{k \in \mathcal{J}_v: \eta^I(\Delta_\lambda^u x_v - \ell, \mathfrak{b}) \geq 1 - \varepsilon\}|}{\lambda_v} = 0, \\
 & \lim_v \frac{|\{k \in \mathcal{J}_v: \gamma^F(\Delta_\lambda^u x_v - \ell, \mathfrak{b}) \geq 1 - \varepsilon\}|}{\lambda_v} = 0, \\
 & \text{iv. } \lim_v \frac{|\{k \in \mathcal{J}_v: \mu^T(\Delta_\lambda^u x_v - \ell, \mathfrak{b}) > 1 - \varepsilon\}|}{\lambda_v} \\
 & = 0, \lim_v \frac{|\{k \in \mathcal{J}_v: \eta^I(\Delta_\lambda^u x_v - \ell, \mathfrak{b}) \leq 1 - \varepsilon\}|}{\lambda_v} = 0, \\
 & \lim_v \frac{|\{k \in \mathcal{J}_v: \gamma^F(\Delta_\lambda^u x_v - \ell, \mathfrak{b}) \leq 1 - \varepsilon\}|}{\lambda_v} = 0,
 \end{aligned}$$

The proof is easily obtained from Definition3.1.

Theorem 3.1 Let $(X, \mu^T, \gamma^F, \eta^I, \boxtimes, \otimes)$ be a NNS. If, $x = (x_v)$ is (Δ_λ^u) -statistical convergence, then this limit is unique.

Proof Let $st_{\Delta_\lambda^u}^{\mathcal{N}} - \lim x = \ell_1$ and $st_{\Delta_\lambda^u}^{\mathcal{N}} - \lim x = \ell_2$ such that $\ell_1 \neq \ell_2$. For given $\varepsilon > 0$ and $\mathfrak{b} > 0$,

$(1 - \varepsilon) \boxtimes (1 - \varepsilon) > 1 - \mathfrak{F}$ and $\varepsilon \otimes \varepsilon < \mathfrak{F}$. For any $\mathfrak{b} > 0$ is defined the next sets:

$$\begin{aligned} \mathfrak{I}_{\mu^T}(\varepsilon, \mathfrak{b}) &= \{k \in \mathcal{J}_v: \mu^T(\Delta_\lambda^u x_v - \ell_1, \mathfrak{b}) \leq 1 - \varepsilon\}, \mathfrak{I}_{\bar{\mu}^T}(\varepsilon, \mathfrak{b}) \\ &= \{k \in \mathcal{J}_v: \bar{\mu}^T(\Delta_\lambda^u x_v - \ell_2, \mathfrak{b}) \leq 1 - \varepsilon\} \end{aligned}$$

$$\begin{aligned} \mathfrak{I}_{\eta^i}(\varepsilon, \mathfrak{b}) &= \{k \in \mathcal{J}_v: \eta^i(\Delta_\lambda^u x_v - \ell_1, \mathfrak{b}) \leq 1 - \varepsilon\}, & \mathfrak{I}_{\bar{\eta}^i}(\varepsilon, \mathfrak{b}) &= \{k \in \\ \mathcal{J}_v: \bar{\eta}^i(\Delta_\lambda^u x_v - \ell_2, \mathfrak{b}) \leq 1 - \varepsilon\} \end{aligned}$$

and

$$\begin{aligned} \mathfrak{I}_{\gamma^f}(\varepsilon, \mathfrak{b}) &= \{k \in \mathcal{J}_v: \gamma^f(\Delta_\lambda^u x_v - \ell_1, \mathfrak{b}) \leq 1 - \varepsilon\}, \mathfrak{I}_{\bar{\gamma}^f}(\varepsilon, \mathfrak{b}) \\ &= \{k \in \mathcal{J}_v: \bar{\gamma}^f(\Delta_\lambda^u x_v - \ell_2, \mathfrak{b}) \leq 1 - \varepsilon\} \end{aligned}$$

Using $st_{\Delta_\lambda^u}^{\mathcal{N}} - \lim x = \ell_1$ and Lemma3.1, for each $\mathfrak{b} > 0$,

$$\delta_\lambda^u \left(\mathfrak{I}_{\mu^T}(\varepsilon, \mathfrak{b}) \right) = \delta_\lambda^u \left(\mathfrak{I}_{\eta^i}(\varepsilon, \mathfrak{b}) \right) = \delta_\lambda^u \left(\mathfrak{I}_{\gamma^f}(\varepsilon, \mathfrak{b}) \right) = 0$$

can be written. Also, with the help of $st_{\Delta_\lambda^u}^{\mathcal{N}} - \lim x = \ell_2$ for each $\mathfrak{b} > 0$

is obtained. Now;

$$\begin{aligned} \mathfrak{I}(\varepsilon, \mathfrak{b}) \\ = \left(\left(\mathfrak{I}_{\mu^T}(\varepsilon, \mathfrak{b}) \right) \cup \left(\mathfrak{I}_{\bar{\mu}^T}(\varepsilon, \mathfrak{b}) \right) \right) \cap \left(\left(\mathfrak{I}_{\eta^i}(\varepsilon, \mathfrak{b}) \right) \cup \left(\mathfrak{I}_{\bar{\eta}^i}(\varepsilon, \mathfrak{b}) \right) \right) \cap \left(\left(\mathfrak{I}_{\gamma^f}(\varepsilon, \mathfrak{b}) \right) \cup \left(\mathfrak{I}_{\bar{\gamma}^f}(\varepsilon, \mathfrak{b}) \right) \right) \end{aligned}$$

is defined. Then, $\delta_\lambda^u \left(\mathfrak{I}(\varepsilon, \mathfrak{b}) \right) = 0$, $\delta_\lambda^u \left(\mathbb{N} / \mathfrak{I}(\varepsilon, \mathfrak{b}) \right) = 1$, can be written. So; three possible situations is written, if $k \in \left(\mathbb{N} / \mathfrak{I}(\varepsilon, \mathfrak{b}) \right)$ is taken;

- i.) $k \in \left(\mathbb{N} / \left(\left(\mathfrak{I}_{\mu^T}(\varepsilon, \mathfrak{b}) \right) \cup \left(\mathfrak{I}_{\bar{\mu}^T}(\varepsilon, \mathfrak{b}) \right) \right) \right)$,
- ii.) $k \in \left(\mathbb{N} / \left(\left(\mathfrak{I}_{\eta^i}(\varepsilon, \mathfrak{b}) \right) \cup \left(\mathfrak{I}_{\bar{\eta}^i}(\varepsilon, \mathfrak{b}) \right) \right) \right)$ and
- iii.) $k \in \left(\mathbb{N} / \left(\left(\mathfrak{I}_{\gamma^f}(\varepsilon, \mathfrak{b}) \right) \cup \left(\mathfrak{I}_{\bar{\gamma}^f}(\varepsilon, \mathfrak{b}) \right) \right) \right)$

From i.) $\mu^T(\ell_1 - \ell_2, \mathfrak{b}) \geq \mu^T \left(\Delta_\lambda^u x_v - \ell_1, \frac{\mathfrak{b}}{2} \right) \boxtimes \mu^T \left(\Delta_\lambda^u x_v - \ell_2, \frac{\mathfrak{b}}{2} \right) > (1 - \varepsilon) \boxtimes (1 - \varepsilon) > 1 - \mathfrak{F}$.

is obtained. Then for all $\mathfrak{b} > 0$, and $\varepsilon > 0$ is arbitrary, $\mu^T(\ell_1 - \ell_2, \mathfrak{b}) = 1$. So, $\ell_1 = \ell_2$.

Now considering ii.) and so using $k \in \left(\mathbb{N} / \left(\left(\mathfrak{I}_{\eta^i}(\varepsilon, \mathfrak{b}) \right) \cup \left(\mathfrak{I}_{\check{\eta}^i}(\varepsilon, \mathfrak{b}) \right) \right) \right)$,

$$\eta^i(\ell_1 - \ell_2, \mathfrak{b}) \geq \eta^i \left(\Delta_\lambda^u x_v - \ell_1, \frac{\mathfrak{b}}{2} \right) \otimes \eta^i \left(\Delta_\lambda^u x_v - \ell_2, \frac{\mathfrak{b}}{2} \right) < \varepsilon \otimes \varepsilon < \mathfrak{F}$$

is getting. So, for $\varepsilon > 0$ is arbitrary, $\eta^i(\ell_1 - \ell_2, \mathfrak{b}) = 0$ Then, $\ell_1 = \ell_2$. Furthermore, using iii.) since

$$k \in \left(\mathbb{N} / \left(\left(\mathfrak{I}_{\gamma^f}(\varepsilon, \mathfrak{b}) \right) \cup \left(\mathfrak{I}_{\check{\gamma}^f}(\varepsilon, \mathfrak{b}) \right) \right) \right)$$

$$\gamma^f(\ell_1 - \ell_2, \mathfrak{b}) \geq \gamma^f \left(\Delta_\lambda^u x_v - \ell_1, \frac{\mathfrak{b}}{2} \right) \otimes \gamma^f \left(\Delta_\lambda^u x_v - \ell_2, \frac{\mathfrak{b}}{2} \right) < \varepsilon \otimes \varepsilon < \mathfrak{F}$$

can be written. Then, for $\varepsilon > 0$ is arbitrary, $\gamma^f(\ell_1 - \ell_2, \mathfrak{b}) = 0$. So, $\ell_1 = \ell_2$.

Since all cases are taken into account, $\ell_1 = \ell_2$.

Proposition 3.1 Let $st_{\Delta_\lambda^u}^{\mathcal{N}} - \lim x = \ell_1$, $st_{\Delta_\lambda^u}^{\mathcal{N}} - \lim x = \ell_2$. In this case,

i) $st_{\Delta_\lambda^u}^{\mathcal{N}} - \lim(x_v + \check{x}_v) = \ell_1 + \ell_2,$

ii) $st_{\Delta_\lambda^u}^{\mathcal{N}} - \lim \check{c}(x_v) = \check{c}\ell_1,$

iii) $st_{\Delta_\lambda^u}^{\mathcal{N}} - \lim(x_v \check{x}_v) = \ell_1 \ell_2.$

Definition 3.2 Let $(X, \mu^T, \gamma^f, \eta^i, \boxtimes, \otimes)$ be a Neutrosophic normed spaces, $\lambda = (\lambda_v)$ be sequence as given in Definition 2.1 and let u be a convenient fraction. Let $x = (x_v)$ is a sequences in neutrosophic normed where for every $\varepsilon > 0$ and $\mathfrak{b} > 0$, if there exists \check{r} such that for all $\varepsilon > 0$ and $\mathfrak{b} > 0$,

$$\delta_\lambda^u \{k: \mu^T(\Delta_\lambda^u x_v - \ell, \mathfrak{b}) \leq 1 - \varepsilon \text{ or } \eta^i(\Delta_\lambda^u x_v - \ell, \mathfrak{b}) \geq \varepsilon, \gamma^f(\Delta_\lambda^u x_v - \ell, \mathfrak{b}) \geq \varepsilon\} = 0.$$

then $x = (x_v)$ is called (Δ_λ^u) -statistical Cauchy sequences on $(X, \mu^T, \gamma^f, \eta^i, \boxtimes, \otimes)$.

Now, similar to the proof in literature , the relationship between (Δ_λ^u) –statistical convergence of sequences and being Cauchy sequences will also be given in the following lemmas.

Lemma 3.2 On $(X, \mu^T, \gamma^F, \eta^I, \boxtimes, \otimes)$ if $x = (x_v)$ is (Δ_λ^u) –statistical convergence then this sequences is (Δ_λ^u) –statistical Cauchy sequences.

Proof Let $x = (x_v)$ is (Δ_λ^u) –statistical convergence sequences on $(X, \mu^T, \gamma^F, \eta^I, \boxtimes, \otimes)$ then for given $\varepsilon > 0$ and choosing $\mathfrak{b} > 0$ such that $(1 - \varepsilon) \boxtimes (1 - \varepsilon) > 1 - \mathfrak{F}$ and $\varepsilon \otimes \varepsilon < \mathfrak{F}$. For any $\mathfrak{b} > 0$, it can be written. Let

$$\delta_\lambda^u(\mathcal{G}_1) = \delta_\lambda^u\{k \in \mathcal{J}_v: \mu^T(\Delta_\lambda^u x_v - \ell, \mathfrak{b}) \leq 1 - \varepsilon \text{ or } \eta^I(\Delta_\lambda^u x_v - \ell, \mathfrak{b}) \geq \varepsilon, \gamma^F(\Delta_\lambda^u x_v - \ell, \mathfrak{b}) \geq \varepsilon\} = 0,$$

$$\delta_\lambda^u(\mathcal{G}_2) = \delta_\lambda^u\{k \in \mathcal{J}_v: \mu^T(\Delta_\lambda^u x_v - \ell, \mathfrak{b}) > 1 - \varepsilon \text{ or } \eta^I(\Delta_\lambda^u x_v - \ell, \mathfrak{b}) < \varepsilon, \gamma^F(\Delta_\lambda^u x_v - \ell, \mathfrak{b}) < \varepsilon\} = 1.$$

Let $d \in \mathcal{G}_2$ then $\mu^T(\Delta_\lambda^u x_v - \ell, \frac{\mathfrak{b}}{2}) > 1 - \varepsilon$ and $\eta^I(\Delta_\lambda^u x_v - \ell, \frac{\mathfrak{b}}{2}) < \varepsilon$, $\gamma^F(\Delta_\lambda^u x_v - \ell, \frac{\mathfrak{b}}{2}) < \varepsilon$

Let $\mathfrak{G} = \{k \in \mathcal{J}_v: \mu^T(\Delta_\lambda^u x_v - \ell, \mathfrak{b}) \leq 1 - \mathfrak{F} \text{ or } \eta^I(\Delta_\lambda^u x_v - \ell, \mathfrak{b}) \geq \mathfrak{F}, \gamma^F(\Delta_\lambda^u x_v - \ell, \mathfrak{b}) \geq \mathfrak{F}\}$

It is desired to show that $\mathfrak{G} \subset \mathcal{G}_1$, so $d \in (\mathfrak{G}/\mathcal{G}_1)$. Then

$$\begin{aligned} \mu^T(\Delta_\lambda^u x_v - \ell, \mathfrak{b}) &\leq 1 - \mathfrak{F} \text{ or } \mu^T(\Delta_\lambda^u x_v - \ell, \frac{\mathfrak{b}}{2}) \\ &> 1 - \mathfrak{F}, \mu^T(\Delta_\lambda^u x_v - \ell, \frac{\mathfrak{b}}{2}) > 1 - \mathfrak{F} \end{aligned}$$

Here, $\mu^T(\Delta_\lambda^u x_v - \ell, \frac{\mathfrak{b}}{2}) > 1 - \mathfrak{F}$. On the other hands,

$$\begin{aligned} 1 - \mathfrak{F} &\geq \mu^T(\Delta_\lambda^u x_d - \Delta_\lambda^u x_v, \mathfrak{b}) \geq \mu^T(\Delta_\lambda^u x_d - \ell, \frac{\mathfrak{b}}{2}) \boxtimes \mu^T(\Delta_\lambda^u x_v - \ell, \frac{\mathfrak{b}}{2}) \\ &> (1 - \varepsilon) \boxtimes (1 - \varepsilon) > 1 - \mathfrak{F}. \end{aligned}$$

But it is not possible.

On the other hands,

$$\eta^I(\Delta_\lambda^u x_v - \ell, \mathfrak{b}) \geq \varepsilon \text{ and } \eta^I(\Delta_\lambda^u x_v - \ell, \frac{\mathfrak{b}}{2}) < \varepsilon,$$

with a similar technique, $\eta^I(\Delta_\lambda^u x_d - \ell, \frac{\mathfrak{b}}{2}) < \varepsilon$ So,

$$\mathfrak{F} \leq \eta^I(\Delta_\lambda^u x_d - \Delta_\lambda^u x_v, \mathfrak{b}) \leq \eta^I(\Delta_\lambda^u x_d - \ell, \frac{\mathfrak{b}}{2}) \otimes \eta^I(\Delta_\lambda^u x_v - \ell, \frac{\mathfrak{b}}{2}) < \varepsilon \otimes \varepsilon < \mathfrak{F}.$$

But this is not possible. Again in the same way,

$$\gamma^f(\Delta_\lambda^u x_v - \ell, \mathfrak{b}) \geq \varepsilon \text{ and } \gamma^f\left(\Delta_\lambda^u x_v - \ell, \frac{\mathfrak{b}}{2}\right) < \varepsilon,$$

with a similar technique, $\gamma^f\left(\Delta_\lambda^u x_d - \ell, \frac{\mathfrak{b}}{2}\right) < \varepsilon$ So,

$$\mathbb{F} \leq \gamma^f(\Delta_\lambda^u x_d - \Delta_\lambda^u x_v, \mathfrak{b}) \leq \gamma^f\left(\Delta_\lambda^u x_d - \ell, \frac{\mathfrak{b}}{2}\right) \otimes \gamma^f\left(\Delta_\lambda^u x_v - \ell, \frac{\mathfrak{b}}{2}\right) < \varepsilon \otimes \varepsilon < \mathbb{F}.$$

It is not possible. Hence, $\mathfrak{G} \subset \mathfrak{G}_1$. So, $\delta_\lambda^u(\mathfrak{G}) = 0$. Then, $x = (x_v)$ is (Δ_λ^u) –statistical Cauchy sequences in Neutrosophic normed spaces.

Definition 12 $(X, \mu^T, \gamma^f, \eta^i, \boxtimes, \otimes)$ is named (Δ_λ^u) -statistical complete, if all (Δ_λ^u) -statistical Cauchy sequences is (Δ_λ^u) -statistical convergent.

Definition 14 Let $(X, \mu^T, \gamma^f, \eta^i, \boxtimes, \otimes)$ be a Neutrosophic normed spaces. $x = (x_v)$ is called (Δ_λ^u) -statistical bounded, if there exists some $\mathfrak{b} > 0$ such that

$$\delta_\lambda^u\{k: \mu^T(\Delta_\lambda^u x_v - \ell, \mathfrak{b}) > 1 - \varepsilon \text{ or } \eta^i(\Delta_\lambda^u x_v - \ell, \mathfrak{b}) < \varepsilon, \gamma^f(\Delta_\lambda^u x_v - \ell, \mathfrak{b}) < \varepsilon\} = 0,$$

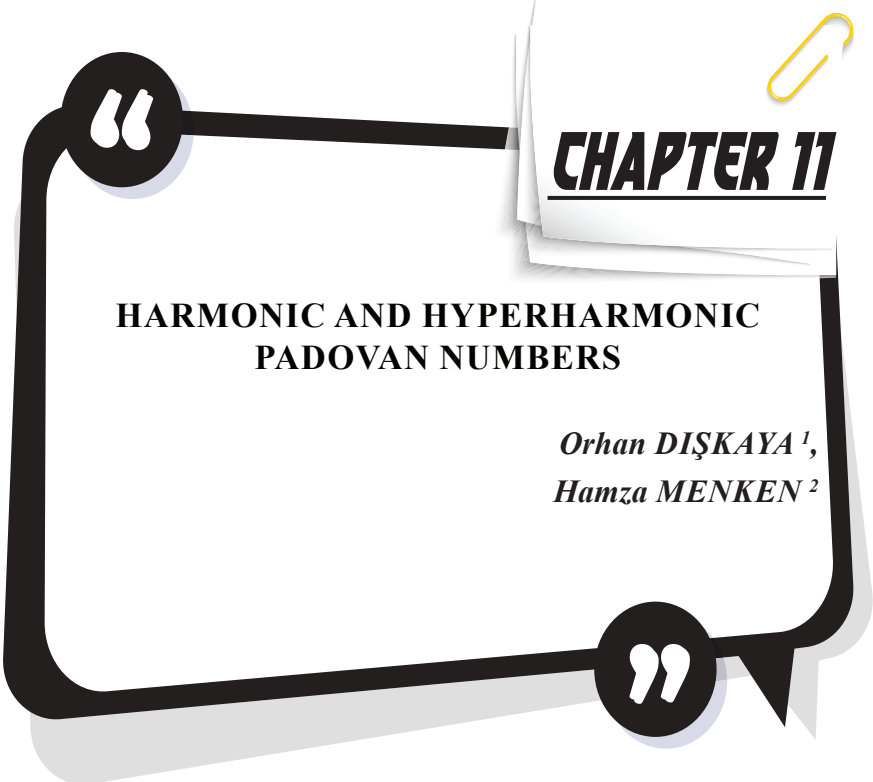
4. Conclusion

In this paper, we have defined Δ_λ^u – statistical convergence and $(\Delta_\lambda^{u,p})$ –Cesaro summable, for fractional difference sequences. Also, Δ_λ^u – statistical convergence with respect to neutrosophic norm is introduced and some fundamental properties are examined. Then, important coverage relations are given for the concept of $(\Delta_\lambda^u)^\alpha$ -statistically convergent.

References

- [1] Et, M. and Çolak, R., 1995. On some generalized difference sequence spaces, *Soochow J. Math.*, 21, 377- 386.
- [2] Kızmaz, H., 1981. On certain sequence spaces, *Canad. Math. Bull.*, 24, 169-176.
- [3] Schoenberg I. J., The integrability of certain functions and related summability methods. *Amer. Math. Monthly* 66, 361–375 (1959).
- [4] Fast H., Sur la convergence statistique. *Colloq. Math.* 2, 241–244 (1951).
- [5] M. Mursaleen, λ -statistical convergence, *Math. Slovaca*, 50(1)(2000),111-115.
- [6] Altinok, H., Çolak, R., & Altin, Y. (2012). On the class of λ -statistically convergent difference sequences of fuzzy numbers. *Soft Computing*, 16(6), 1029-1034.
- [7] Atanassov, K. (1986). Intuitionistic Fuzzy Sets. *Fuzzy Sets and Systems*. 20, 87-96.
- [8] Et, M., Altinok, H., and Altin, Y. (2004). On Some Generalized Sequence Spaces. *Applied Mathematics and Computation*. 154(1), 167-173.
- [9] Fast, H. (1951). Sur la convergence statistique. *Colloq. Math.* 2, 241-244.
- [10] Fridy, J.A. and Orhan, C. (1993). Lacunary Statistical Convergence. *Pacific J. Math.*160, 43-51.
- [11] Gonul, N. (2013). Lacunary A-Convergence. *Karaelmas Journal of Science and Engineering*. 3(1), 17-20.
- [12] Gonul Bilgin, N. and Bozma, G. (2020). On Fuzzy n-Normed Spaces Lacunary Statistical Convergence of Order α . *i-Manager's Journal on Mathematics*. 9(2), 1-9.
- [13] Gonul Bilgin, N. (2022). Hibrid Δ -Statistical Convergence For Neutrosophic Normed Space. *Journal Of Mathematics*, 2022.
- [15] Bilgin, N. G. (2022). Nötrosifik Normlu Uzaylarda Rough İstatistiksel Yakınsaklık. *Euroasia Journal Of Mathematics, Engineering, Natural & Medical Sciences*, 9(21), 47_55-47_55.
- [16] Gonul Bilgin, N. and Bozma, G. (2021). Fibonacci Lacunary Statistical Convergence of Order Ψ in IFNLS. *Int. J. Adv. Appl. Math. and Mech.* 8(4), 28-36.
- [17] Karakus, S. Demirci, K. and Duman, O. (2008). Statistical Convergence On Intuitionistic Fuzzy Normed Spaces. *Chaos Solitons Fractals*. 35, 763-769
- [18] Khan, V. A., Khan, M. D. and Ahmad, M. (2021). Some New Type of Lacunary Statistically Convergent Sequences In Neutrosophic Normed Space. *Neutrosophic Sets and Systems*. 42, 239-252.

- [19] Khan, V. A., Fatima, H., Khana, M. D. and Ahamd, A. (2021). Spaces of Neutrosophic λ -statistical Convergence Sequences and Their Properties. *Journal Math. Comp.Science.* 23, 1-9.
- [20] Kirisci, M. and Simsek, N. (2020). Neutrosophic Normed Spaces and Statistical Convergence. *The Journal of Analysis.* 28 1059-1073.
- [21] Smarandache, F.A. (1999). Unifying Field in Logics: Neutrosophic Logic. In Philosophy. American Research Press.
- [22] Steinhaus, H. (1951). Sur la Convergence Ordinaire et la Convergence Asymptotique. *Colloq. Math.* 2, 73-74.
- [23] Zadeh, L. (1965). Fuzzy Sets, *Inform. and Control.* 8, 338-353.



CHAPTER 11

HARMONIC AND HYPERHARMONIC PADOVAN NUMBERS

*Orhan DIŞKAYA*¹,
*Hamza MENKEN*²

1 Ress.Asst., Department of Mathematica, Faculty of Science, Mersin University, Mersin, Turkey. Orcid: 0000-0001-5698-7834

2 Prof. Dr., Department of Mathematica, Faculty of Science, Mersin University, Mersin, Turkey. Orcid: 0000-0003-1194-3162 *Author for correspondence; e-mail address: orhandiskaya@mersin.edu.tr

1. INTRODUCTION

The harmonic and hyperharmonic Fibonacci numbers introduced and studied by Tuğlu at ell. [1]. They had some combinatorial identities, and the spectral and Euclidean norms of circulant matrices involving harmonic and hyperharmonic Fibonacci numbers obtained by Tuğlu and Kızılateş [2,3].

The present work deals with the harmonic and hyperharmonic Padovan numbers. First, a summary of the definitions and some properties of harmonic and hyperharmonic numbers is presented. Following that, the definitions of the hyper-Padovan numbers, harmonic Padovan numbers, and hyperharmonic Padovan numbers are given, along with some of their identities. Finally, different sums and properties that include harmonic Padovan numbers are derived by applying the rules of the difference operator method.

2. MATERIALS AND METHODS

Definition 2.1 Let $n \in \mathbb{N}$. The n th harmonic number H_n is defined by

$$H_n = \sum_{k=1}^n \frac{1}{k} \quad (1)$$

where $H_0 = 0$. The n th harmonic number H_n can be written as

$$H_n = \frac{\left[\begin{matrix} n+1 \\ 2 \end{matrix} \right]}{n!} \quad (2)$$

where $\left[\begin{matrix} n \\ k \end{matrix} \right]$ is the first-kind Stirling number, which counts the permutations of n components produced by k disjoint cycles by Graham et al. [4].

There are many studies in the literature on the harmonic numbers (see, Savio et al. [5], Spiess [6], Benjamin et al. [7], Cheon and El-Mikkawy [8], Dil and Mező [9], Sofo and Srivastava [10], Choi [11] Sun [12], Boyadzhiev [13], Chu [14], Wu and Chen [15]). The following are some of the harmonic number rules discovered in these studies by Graham et al. [4].

- i. $\sum_{k=1}^{n-1} H_k = nH_n - n,$
- ii. $\sum_{k=1}^{n-1} \binom{k}{m} H_k = \binom{n}{m+1} \left(H_n - \frac{1}{m+1} \right), \quad m \in \mathbb{N}^+,$

- iii. $\sum_{k=1}^{n-1} kH_k = \frac{n^2}{2} \left(H_n - \frac{1}{2} \right), \quad n^2 = n(n-1),$
- iv. $\sum_{k=0}^n \binom{n}{k} H_k = 2^n \left(H_n - \sum_{k=1}^n \frac{1}{k2^k} \right),$
- v. $\sum_{k=0}^n \binom{n}{k} (-1)^k H_k = -\frac{1}{n}.$

Conway and Guy [16] defined hyperharmonic numbers, one of the generalizations of harmonic numbers, as follows.

Definition 2.2 For $n, r \in \mathbb{N}^+$, r th order n th ordinary hiperharmonic number is defined by

$$H_n^{(r)} = \sum_{k=1}^n H_k^{(r-1)} \tag{3}$$

with $H_n^{(0)} = \frac{1}{n}$ and $H_n^{(1)} = H_n$ by Conway and Guy [16].

Benjamin et al. [17], for $0 \leq m \leq r - 1$, we have

$$H_n^{(r)} = \sum_{k=1}^n \binom{n+r-k-1}{r-1} \frac{1}{k}, \tag{4}$$

and

$$H_n^{(r)} = \sum_{k=1}^n \binom{n+r-m-k-1}{r-m-1} H_k^{(m)} \tag{5}$$

Graham et al. [4], some Difference Operator Methods:

1. The finite difference 3peratör for any function $\mu(x)$ is defined as

$$\Delta\mu(x) = \mu(x+1) - \mu(x).$$

2. For $m \in \mathbb{N}$, the decreasing power m of x is of the form

$$x^m = x(x-1)(x-2)\dots(x-n+1).$$

3. Operator difference operator, the equation $\Delta x^m = mx^{m-1}$ is true.
4. The inverse of the Δ operator is \sum , and if $\Delta\mu(x) = \psi(x)$ is

$$\sum_a^b \psi(x) \delta_x = \sum_{x=a}^{b-1} \psi(x) = \mu(b) - \mu(a). \tag{6}$$

In addition, the inverse difference operator \sum provides the following properties:

$$\sum x^m \delta_x = \begin{cases} \frac{x^{m+1}}{m+1}, & m \neq -1 \\ H_x, & m = -1 \end{cases} \tag{7}$$

and

$$\sum_a^b u(x) \Delta v(x) \delta_x = u(x)v(x) \Big|_a^b - \sum_a^b v(x+1) \Delta u(x) \delta_x. \tag{8}$$

5. Tuğlu and Kızılateş [2,3] let us now give an example where we will use the feature (8). If $u(k) = H_k$ and $\Delta v(k) = 1$ are selected in the expression (8), it becomes $\Delta u(k) = \frac{1}{k+1}$ and $v(k) = k$. Thus,

$$\sum_0^n H_k \delta_k = kH_k \Big|_0^n - \sum_0^n \delta_k$$

is obtained. If the (6) feature is used, we get

$$\sum_{k=0}^{n-1} H_k = nH_n - n.$$

3. RESULTS AND DISCUSSION

In this part, the hyper Padovan and harmonic Padovan numbers are defined. In addition, some theorems and identities have been obtained.

Definition 3.1 For $r \in \mathbb{N}^+$, hyper-Padovan numbers are defined by

$$P_n^{(r)} = \sum_{k=0}^n P_k^{(r-1)} \tag{9}$$

with $P_n^{(0)} = P_n$, $P_0^{(r)} = 1$.

Table 1. Some Hyper-Padovan numbers

n	0	1	2	3	4	5	6	7	8
$P_n^{(0)}$	1	1	1	2	2	3	4	5	7

$P_n^{(1)}$	1	2	3	5	7	10	14	19	26
$P_n^{(2)}$	1	3	6	11	18	28	32	51	77
$P_n^{(3)}$	1	4	10	21	39	67	99	150	227

Definition 3.2 Let P_n be the n th Padovan number. The n th harmonic Padovan number \mathfrak{R}_n is defined by

$$\mathfrak{R}_n = \sum_{k=0}^n \frac{1}{P_k}, \quad n \geq 0. \tag{10}$$

Table 2. Some Harmonik-Padovan numbers

n	0	1	2	3	4	5	6	7	8
\mathfrak{R}_n	1	2	3	$\frac{7}{2}$	4	$\frac{13}{3}$	$\frac{55}{12}$	$\frac{287}{60}$	$\frac{2069}{420}$

Theorem 3.3 Let \mathfrak{R}_n be the n th harmonic Padovan number. Then we have

$$\sum_{k=0}^{n-1} \mathfrak{R}_k = n\mathfrak{R}_n - \sum_{k=0}^{n-1} \frac{k+1}{P_{k+1}}, \quad n \geq 0 \tag{11}$$

Proof. In the equality (8). If we choose as $u(k) = \mathfrak{R}_k$ and $\Delta v(k) = 1$.

We have $\Delta u(k) = \frac{1}{P_{k+1}}$, $v(k) = k$ and

$$\sum_0^n \mathfrak{R}_k \delta_k = k\mathfrak{R}_k \Big|_0^n - \sum_0^n \frac{k+1}{P_{k+1}} \delta_k$$

Using the equality (6), we obtain

$$\sum_{k=0}^{n-1} \mathfrak{R}_k = n\mathfrak{R}_n - \sum_{k=0}^{n-1} \frac{k+1}{P_{k+1}}.$$

Theorem 3.4 Let \mathfrak{R}_n be the n th harmonik Padovan number. Then we have

$$\sum_{k=0}^{n-1} \mathfrak{R}_k^2 = n\mathfrak{R}_n^2 - \sum_{k=0}^{n-1} \frac{k+1}{P_{k+1}} \left(2\mathfrak{R}_k + \frac{1}{\mathfrak{R}_{k+1}} \right), \quad n \geq 0 \tag{12}$$

Proof. In the equality (8). If we choose as $u(k) = \mathfrak{R}_k^2$ and $\Delta v(k) = 1$.

We have $\Delta u(k) = \frac{1}{P_{k+1}} \left(2\mathfrak{R}_k + \frac{1}{P_{k+1}} \right)$, $v(k) = k$ and

$$\sum_0^n \mathfrak{R}_k^2 \delta_k = k\mathfrak{R}_k^2 \Big|_0^n - \sum_0^n \frac{k+1}{P_{k+1}} \left(2\mathfrak{R}_k + \frac{1}{P_{k+1}} \right) \delta_k$$

Using the equality (6), we obtain

$$\sum_{k=0}^{n-1} \mathfrak{R}_k^2 = n\mathfrak{R}_n^2 - \sum_{k=0}^{n-1} \frac{k+1}{P_{k+1}} \left(2\mathfrak{R}_k + \frac{1}{P_{k+1}} \right).$$

Theorem 3.5 Let \mathfrak{R}_n be the n th harmonic Padovan number and m be a nonzero natural number. Then we have

$$\sum_{k=0}^{n-1} \binom{k}{m} \mathfrak{R}_k = \binom{n}{m+1} \mathfrak{R}_n - \sum_{k=0}^{n-1} \binom{k+1}{m+1} \frac{1}{P_{k+1}}, \quad n \geq 0 \tag{13}$$

Proof. If we choose as $u(k) = \mathfrak{R}_k$ ve $\Delta v(k) = \binom{k}{m}$. We have

$\Delta u(k) = \frac{1}{P_{k+1}}$ and $v(k) = \binom{k}{m+1}$. Here, using the equality (6) and (8),

we obtain

$$\sum_0^n \binom{k}{m} \mathfrak{R}_k \delta_k = \binom{k}{m+1} \mathfrak{R}_k \Big|_0^n - \sum_0^n \binom{k+1}{m+1} \frac{1}{P_{k+1}} \delta_k,$$

$$\sum_{k=0}^{n-1} \binom{k}{m} \mathfrak{R}_k = \binom{n}{m+1} \mathfrak{R}_n - \sum_{k=0}^{n-1} \binom{k+1}{m+1} \frac{1}{P_{k+1}}.$$

Theorem 3.6 Let \mathfrak{R}_n be the n th harmonic Padovan number and m be a nonzero natural number. Then we have

$$\sum_{k=0}^{n-1} k^m \mathfrak{R}_k = \frac{n^{m+1}}{m+1} \mathfrak{R}_n - \sum_{k=0}^{n-1} \frac{(k+1)^{m+1}}{m+1} \frac{1}{P_{k+1}}, \quad n \geq 0. \tag{14}$$

Proof. In (8) getting $u(k) = \mathfrak{R}_k$ and $\Delta v(k) = k^m$. We have

$\Delta u(k) = \frac{1}{P_{k+1}}$, $v(k) = \frac{(k+1)^{m+1}}{m+1}$ and

$$\sum_{k=0}^{n-1} k^m \mathfrak{R}_k = \frac{n^{m+1}}{m+1} \mathfrak{R}_n - \sum_{k=0}^{n-1} \frac{(k+1)^{m+1}}{m+1} \frac{1}{P_{k+1}}.$$

In (14), if we choose $m = 0$, then we get (11). If we choose $m = 1$ in (14), we have a special case of (13).

Proposition 3.7 Let $\{\mathfrak{R}_n\}_{n \geq 0}$ be the n th harmonic Padovan numbers. Then we have

$$\sum_{k=0}^{n-1} k^2 \mathfrak{R}_k = \frac{n^2(2n-1)}{6} \mathfrak{R}_n - \frac{1}{6} \sum_{k=0}^{n-1} \frac{(k+1)^2(2k+1)}{P_{k+1}}.$$

Proof. In (14), if $m = 2$ and $m = 1$ are accepted respectively, we get

$$\sum_{k=0}^{n-1} k^2 \mathfrak{R}_k = \frac{n^2(2n-1)}{6} \mathfrak{R}_n - \frac{1}{6} \sum_{k=0}^{n-1} \frac{(k+1)^2(2k+1)}{P_{k+1}}.$$

Now we will give the relation between harmonic numbers and harmonic Padovan numbers in the following theorem.

Theorem 3.8 H_n and \mathfrak{R}_n be the n th harmonic numbers and the n th harmonic Padovan numbers, respectively. Then we have

$$\sum_{k=0}^{n-1} \frac{\mathfrak{R}_k}{k+1} = H_n \mathfrak{R}_n - \sum_{k=0}^{n-1} \frac{H_{k+1}}{P_{k+1}} \tag{15}$$

Proof. In (8). If we choose as $u(k) = \mathfrak{R}_k^2$ and $\Delta v(k) = \frac{1}{k+1}$. We have

$$\Delta u(k) = \frac{1}{P_{k+1}}, \quad v(k) = H_k \text{ and}$$

$$\sum_0^n \frac{\mathfrak{R}_k}{k+1} \delta_k = H_n \mathfrak{R}_k \Big|_0^n - \sum_0^n \frac{H_{k+1}}{P_{k+1}} \delta_k$$

Using the equality (6), we obtain

$$\sum_{k=0}^{n-1} \frac{\mathfrak{R}_k}{k+1} = H_n \mathfrak{R}_n - \sum_{k=0}^{n-1} \frac{H_{k+1}}{P_{k+1}}.$$

Proposition 3.9 The following identity is holds:

$$\sum_{k=0}^{n-1} \frac{\mathfrak{R}_k}{k+1} = \frac{\begin{bmatrix} n+1 \\ 2 \end{bmatrix}}{n!} \mathfrak{R}_n - \sum_{k=0}^{n-1} \frac{\begin{bmatrix} k+2 \\ 2 \end{bmatrix}}{(k+1)! P_{k+1}}.$$

between the Stirling number of the first kind and the n th harmonic Padovan numbers $\{\mathfrak{R}_n\}_{n \geq 0}$.

Proof. In (15), if $H_n = \frac{\binom{n+1}{2}}{n!}$ is taken, the above identity is obtained.

The summing formula that gives the relationship between the Padovan number and the harmonic Padovan number is given in the following theorem.

Theorem 3.10 Let $\{\mathfrak{R}_n\}_{n \geq 0}$ be the n th harmonic Padovan numbers. Then we have

$$\sum_{k=0}^{n-1} P_{k-4} \mathfrak{R}_k = P_n \mathfrak{R}_n - n$$

Proof. In (8). If we choose as $u(k) = \mathfrak{R}_k$ and $\Delta v(k) = P_{k-4}$. We have

$$\Delta u(k) = \frac{1}{P_{k+1}}, \quad v(k) = P_k.$$

Thus, we obtain

$$\begin{aligned} \sum_0^n P_{k-4} \mathfrak{R}_k \delta_k &= P_k \mathfrak{R}_k \Big|_0^n - \sum_0^n \frac{P_{k+1}}{P_{k+1}} \delta_k, \\ \sum_{k=0}^{n-1} P_{k-4} \mathfrak{R}_k &= P_n \mathfrak{R}_n - n. \end{aligned}$$

In this section, a connection similar to the connection between harmonic and hyperharmonic numbers will be established between harmonic Padovan numbers and hyperharmonic Padovan numbers. Then, various identities related to hyperharmonic Padovan numbers will be obtained.

Definition 3.11 Let $\{\mathfrak{R}_n\}_{n \geq 0}$ be the n th harmonic Padovan numbers.

For $r \in \mathbb{N}^+$, the n th hyperharmonic Padovan numbers $\mathfrak{R}_n^{(r)}$ are defined by

$$\mathfrak{R}_n^{(r)} = \sum_{k=0}^n \mathfrak{R}_k^{(r-1)} \tag{16}$$

where $\mathfrak{R}_n^{(0)} = \frac{1}{P_n}$, $\mathfrak{R}_0 = 1$ and $\mathfrak{R}_0^{(k)} = 1$ for $k \geq 0$.

Table 3. Some hyperharmonic Padovan numbers

n	0	1	2	3	4	5	6	7	8
$\mathfrak{R}_n^{(1)}$	1	2	3	$\frac{7}{2}$	4	$\frac{13}{3}$	$\frac{55}{12}$	$\frac{287}{60}$	$\frac{2069}{420}$
$\mathfrak{R}_n^{(2)}$	1	3	6	$\frac{19}{2}$	$\frac{27}{2}$	$\frac{107}{6}$	$\frac{269}{12}$	$\frac{1632}{60}$	$\frac{13493}{420}$
$\mathfrak{R}_n^{(3)}$	1	4	10	$\frac{39}{2}$	33	$\frac{305}{6}$	$\frac{879}{12}$	$\frac{6027}{60}$	$\frac{55682}{420}$

Let us now give the recurrence relation, which we will use in the proof of the various identities of the hyperharmonic Padovan numbers.

Proposition 3.12 For $n, r \in \mathbb{N}^+$, the hyperharmonic Padovan numbers have recurrence relation by

$$\mathfrak{R}_n^{(r)} = \mathfrak{R}_{n-1}^{(r)} + \mathfrak{R}_n^{(r-1)}. \tag{17}$$

Proof. Using (16), we get

$$\begin{aligned} \mathfrak{R}_n^{(r)} &= \sum_{k=0}^n \mathfrak{R}_k^{(r-1)} \\ &= \sum_{k=0}^{n-1} \mathfrak{R}_k^{(r-1)} + \mathfrak{R}_n^{(r-1)} = \mathfrak{R}_{n-1}^{(r)} + \mathfrak{R}_n^{(r-1)} \end{aligned}$$

We may prove the following theorem for hyperharmonic Padovan numbers, which is comparable to the condition given by (4) of hyperharmonic numbers.

Theorem 3.13 For $1 \leq i, j \leq n$, we have

$$\mathfrak{R}_{n-i+1}^{(j)} = \sum_{k=i}^n \binom{n-k+j-1}{j-1} \frac{1}{P_{k-i+1}}. \tag{18}$$

Proof. We begin by recalling the definition of the hyperharmonic Padovan numbers $\mathfrak{R}_n^{(j)}$. If we use this definition in (16) $j-1$ times, we get

$$\mathfrak{R}_{n-i+1}^{(j)} = \sum_{k_j=0}^{n-i+1} \sum_{k_{j-1}=0}^{k_j} \dots \sum_{k_1=0}^{k_2} \frac{1}{P_{k_1}}.$$

We use induction on n to obtain

$$\sum_{k_j=0}^{n-i+1} \sum_{k_{j-1}=0}^{k_j} \dots \sum_{k_1=0}^{k_2} \frac{1}{P_{k_1}} = \sum_{k=i}^n \binom{n-k+j-1}{j-1} \frac{1}{P_{k-i+1}}$$

Obviously, it is true for $n = 1$. Suppose it is true for some $n > 1$, then using the induction, we obtain

$$\begin{aligned}
 \sum_{k_j=0}^{n-i+2} \sum_{k_{j-1}=0}^{k_j} \dots \sum_{k_1=0}^{k_2} \frac{1}{P_{k_1}} &= \sum_{k_j=0}^{n-i+1} \sum_{k_{j-1}=0}^{k_j} \dots \sum_{k_1=0}^{k_2} \frac{1}{P_{k_1}} + \sum_{k_{j-1}=0}^{n-i+2} \sum_{k_{j-2}=0}^{k_{j-1}} \dots \sum_{k_1=0}^{k_2} \frac{1}{P_{k_1}} \\
 &= \sum_{k_j=0}^{n-i+1} \sum_{k_{j-1}=0}^{k_j} \dots \sum_{k_1=0}^{k_2} \frac{1}{P_{k_1}} + \sum_{k_{j-1}=0}^{n-i+1} \sum_{k_{j-2}=0}^{k_{j-1}} \dots \sum_{k_1=0}^{k_2} \frac{1}{P_{k_1}} + \sum_{k_{j-2}=0}^{n-i+2} \sum_{k_{j-3}=0}^{k_{j-2}} \dots \sum_{k_1=0}^{k_2} \frac{1}{P_{k_1}} \\
 &= \sum_{k_j=0}^{n-i+1} \sum_{k_{j-1}=0}^{k_j} \dots \sum_{k_1=0}^{k_2} \frac{1}{P_{k_1}} + \sum_{k_{j-1}=0}^{n-i+1} \sum_{k_{j-2}=0}^{k_{j-1}} \dots \sum_{k_1=0}^{k_2} \frac{1}{P_{k_1}} + \sum_{k_2=0}^{n-i+1} \sum_{k_1=0}^{k_2} \frac{1}{P_{k_1}} + \sum_{k_1=0}^{n-i+2} \frac{1}{P_{k_1}} \\
 &= \sum_{k_j=0}^{n-i+1} \sum_{k_{j-1}=0}^{k_j} \dots \sum_{k_1=0}^{k_2} \frac{1}{P_{k_1}} + \sum_{k_{j-1}=0}^{n-i+1} \sum_{k_{j-2}=0}^{k_{j-1}} \dots \sum_{k_1=0}^{k_2} \frac{1}{P_{k_1}} + \sum_{k_2=0}^{n-i+1} \sum_{k_1=0}^{k_2} \frac{1}{P_{k_1}} + \sum_{k_1=0}^{n-i+1} \frac{1}{P_{k_1}} + \frac{1}{P_{n-i+2}}
 \end{aligned}$$

If the sum property of the binomial coefficients is used, we have

$$\begin{aligned}
 \sum_{k_j=0}^{n-i+2} \sum_{k_{j-1}=0}^{k_j} \dots \sum_{k_1=0}^{k_2} \frac{1}{P_{k_1}} &= \sum_{k=i}^n \frac{1}{P_{k-i+1}} \left[\binom{n-k+j-1}{j-1} + \binom{n-k+j-2}{j-2} + \dots + \binom{n-k}{0} \right] + \frac{1}{P_{n-i+2}} \\
 &= \sum_{k=i}^n \frac{1}{P_{k-i+1}} \binom{n-k+j}{j-1} + \frac{1}{P_{n-i+2}} \\
 &= \sum_{k=i}^{n+1} \binom{n-k+j}{j-1} \frac{1}{P_{k-i+1}}
 \end{aligned}$$

Proposition 3.14 The following identity is holds:

$$\mathfrak{R}_n^{(r)} = \sum_{k=1}^n \binom{n-k+r-1}{r-1} \frac{1}{P_k} \tag{19}$$

Proof. In (18). If we choose as $i = 1$ and $j = r$, (19) is obtained.

Proposition 3.15 The following identity is holds:

$$\sum_{k=1}^n \frac{k}{P_k} = (n+1)\mathfrak{R}_n - \mathfrak{R}_n^{(2)}$$

Proof. In (19). If we choose $r = 2$, we get

$$\begin{aligned}
 \mathfrak{R}_n^{(2)} &= \sum_{k=1}^n (n-k+1) \frac{1}{P_k} \\
 &= n \sum_{k=1}^n \frac{1}{P_k} - \sum_{k=1}^n \frac{k}{P_k} + \sum_{k=1}^n \frac{1}{P_k} \\
 &= (n+1)\mathfrak{R}_n - \mathfrak{R}_n^{(2)}
 \end{aligned}$$

Theorem 3.16 For $0 \leq m \leq r-1$, we have

$$\mathfrak{R}_n^{(r)} = \sum_{t=1}^n \binom{n+r-m-t-1}{r-m-1} \mathfrak{R}_t^{(m)}$$

Proof. We prove this by induction on n . Obviously, it is true for $n = 1$. Suppose it is true for some $n > 1$, identity in (17). Then using the induction, we obtain

$$\begin{aligned}
 \mathfrak{R}_{n+1}^{(r)} &= \mathfrak{R}_{n+1}^{(r-2)} + \mathfrak{R}_n^{(r-1)} + \mathfrak{R}_n^{(r)} \\
 &= \mathfrak{R}_{n+1}^{(r-3)} + \mathfrak{R}_n^{(r-2)} + \mathfrak{R}_n^{(r-1)} + \mathfrak{R}_n^{(r)} \\
 &\quad \vdots \\
 &= \mathfrak{R}_{n+1}^{(m)} + \mathfrak{R}_n^{(m+1)} + \mathfrak{R}_n^{(m+2)} + \dots + \mathfrak{R}_n^{(r-2)} + \mathfrak{R}_n^{(r-1)} + \mathfrak{R}_n^{(r)} \\
 &= \mathfrak{R}_{n+1}^{(m)} + \sum_{k=1}^n \left[\binom{n-k}{0} + \binom{n-k+1}{1} + \dots + \binom{n-k+r-m-1}{r-m-1} \right] \mathfrak{R}_k^{(m)} \\
 &= \mathfrak{R}_{n+1}^{(m)} + \sum_{k=1}^n \binom{n-k+r-m}{r-m-1} \mathfrak{R}_k^{(m)} \\
 &= \sum_{k=1}^{n+1} \binom{n-k+r-m}{r-m-1} \mathfrak{R}_k^{(m)}
 \end{aligned}$$

REFERENCES

- [1] Tuglu N., Kızılateş C. and Kesim S., *Adv. Difference Equ.*, 2015; **(1)**: 1-12. DOI: 10.1186/s13662-015-0635-z.
- [2] Tuglu N. and Kızılateş C., *J. Inequal. Appl.*, 2015; **2015(1)**: 1-11. DOI: 10.1186/s13660-015-0778-1.
- [3] Tuglu N. and Kızılateş C., *Gazi University Journal of Science*, 2015; **28(3)**: 497-501.
- [4] Graham R., Knuth D. and Patashnik K., *Concrete Mathematics*, Addison-Wesley, 1989.
- [5] Savio D. Y., Lamagna E. A. and Liu S. M., *Summation of harmonic numbers*. In *Computers and Mathematics*, Springer, New York, 1989.
- [6] Spiess J., *Math. Comp.*, 1990; **55(192)**: 839-863. DOI: 10.1090/S0025-5718-1990-1023769-6.
- [7] Benjamin A. T., Preston G. O. and Quinn J. J., *Mathematics Magazine*, 2002; **75(2)**: 95-103. DOI: 10.1080/0025570X.2002.11953110.
- [8] Cheon G. S. and El-Mikkawy M. E. A., *J. Number Theory*, 2008; **128(2)**:413-425. DOI: 10.1016/j.jnt.2007.08.011.
- [9] Dil, A. and Mezö I., *Appl. Math. Comput.*, 2008; **206(2)**: 942-951. DOI: 10.1016/j.amc.2008.10.013.
- [10] Sofo A. and Srivastava H. M., *Ramanujan J.*, 2011; **25(1)**: 93-113. DOI: 10.1007/s11139-010-9228-3.
- [11] Choi J., *Appl. Math. Comput.*, 2011; **218(3)**: 734-740. DOI: 10.1016/j.amc.2011.01.062.
- [12] Sun Z. W., *Proc. Amer. Math. Soc.*, 2012; **140(2)**: 415-428. DOI: 10.1090/S0002-9939-2011-10925-0.
- [13] Boyadzhiev K. N., *J. Integer Seq.*, 2012; **15(1)**: 1-11.
- [14] Chu W., *Filomat*, 2012; **26(1)**: 143-152.
- [15] Wu B. L. and Chen Y. G., *J. Number Theory*, 2017; **175**: 66-86. DOI: 10.1016/j.jnt.2016.11.027.
- [16] Conway J. H. and Guy R. K., *The Book of Numbers*, Springer, New York, 1996.
- [17] Benjamin A. T., Gaebler D. and Gaebler, R., *Integers*, 2003; **3**: 1–9.



CHAPTER 12

REMOVAL OF MALACHITE GREEN FROM WASTEWATER

*Oya AYDIN URUCU¹,
Emrah ÇAKMAKÇI*

Dyestuffs are compounds that have a wide range of uses in our daily life. They are used in many applications from textiles to inks, from plastics to coatings, from the paper industry to leather, from the construction industry to foods, from medical and biochemical processes to analytical methods. However, some of these dyes show toxic properties. For this reason, especially toxic dyestuffs should be disposed of or removed without mixing with the environment.

The natural dyestuffs were used until the fabrication of a dye called mauveine, which was produced for the first time in 1856 by William Henry Perkin. After the manufacturing of mauveine, industry gradually started to give way to synthetic dyestuffs, and it is known that approximately 1000000 synthetic dyestuffs have been synthesized today [1]. These dyestuffs, which reach an annual production volume of 700000 tons, bring environmental pollution and pose a great threat to human and environmental health [1, 2].

Malachite green (MG) is a water-soluble, green crystalline powder in the cationic (basic) dyestuff class. It is also one of the triphenylmethane group dyestuffs and is known by names such as aniline green, diamond green B, Victoria green B, and basic green 4. Malachite green is mostly found in the form of chloride or oxalate salt. The chemical structure of MG is given below.

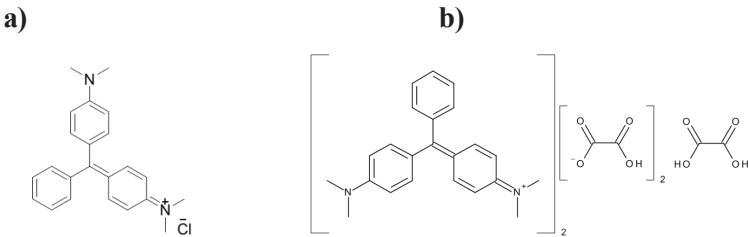


Figure 1. Chemical structure of MG: a) MG chloride and b) MG oxalat

MG is synthesized by the condensation of dimethylaniline with benzaldehyde and subsequent oxidation (**Figure 2**):

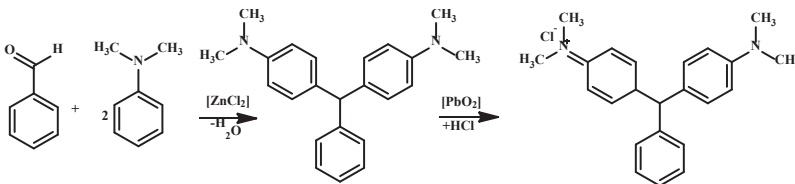


Figure 2. Synthesis of MG

The usage areas of MG are listed below [1, 3, 4]. It is most commonly used as a biocide in the aquaculture industry to combat bacterial and fungal infections in fish.

Common uses of MG:

- For dyeing silk, wool, leather, cotton and paper,
- Antiparasitic, antibacterial and antifungal drug in aquaculture and commercial fish hatchery industry,
- Fungicide for humans,
- Medical disinfectant, food additive, food colouring agent,
- Dye for microscopic analysis of cells and culture samples,
- Used as a pH indicator [1, 3, 4].

Although widely used, MG molecule is highly toxic to humans and shows carcinogenic, genotoxic and mutagenic effects [5]. It also damages the nervous system, kidneys, liver, heart, reduces fertility, and causes lesions on the skin, eyes, lungs, and bones [1].

For this reason, leaving this paint to soil or water sources creates serious problems for the environment and human health. Although its use has been restricted and even banned in various countries in recent years, it is still used in various products.

Because of these toxic effects, MG must be removed from aqueous environments. Many methods have been developed for chemical (Fenton reagents, ozonization, photocatalysis), biological and physical (Coagulation-Flocculation, membrane filtration, adsorption) removal [6]. Among these, the most widely used method is adsorption processes that provide physical removal.

Chemical methods

Fenton reagent

Fenton's reagent is widely used for the removal of MG. It is a cost-effective reagent that reacts easily with organic compounds and does not produce toxic compounds during oxidation.

Fenton reaction is one of the most effective methods for removing organic pollutants that are oxidatively decomposed by hydroxyl radicals formed from H_2O_2 , in which Fe^{2+} is used as a catalyst. The efficiency of the Fenton process depends on the pH of the reaction medium, along with the H_2O_2 and Fe^{2+} concentrations. [7,8,9].

Ozonation

Ozonation is one of the methods that gives the best results in the degradation of dyes [10]. In oxidation with ozone, the chromophoric system is destroyed and reactive dyes are bleached. Reaction mechanisms of ozonolytic degradation, it has been determined that both direct molecular ozone attack and free radical mechanism work simultaneously during the reaction processes [11]. Ozone's high oxidation potential (2.07 V) allows it to degrade most organic compounds.

In order to produce non-hazardous waste during ozonation, the required amount of ozone can be estimated according to the chemical structure of the dye [1]. Many methods have been developed for the removal of malachite green with this method [10, 12, 13].

Electrochemical methods- Photocatalysis

Highly efficient, clean, environmentally friendly and recyclable electrochemical methods have attracted great interest in MG removal.

Photocatalysis

One of the most important features of semiconductor photocatalysis, which is one of the most successful methods for wastewater treatment, is that it removes all pollutants from wastewater. In 1972, Fujishima and Honda determined the photocatalytic splitting of water into oxygen and hydrogen using TiO_2 . Afterwards, this method has become a promising approach, especially to remove organic pollutants from the environment [14]. In recent years, many important and interesting studies have been carried out on the creation of new photocatalytic materials. Electron hole pairs are produced when light is shined on a semiconductor used in semiconductor photocatalysis. The photocatalytic degradation process usually uses a visible light radiation source rather than an ultraviolet radiation source. The ultraviolet radiation source contains very little of the solar radiation, while the visible light radiation source contains more than 40%. As a result, photodegradation with visible light is preferable to photodegradation with UV energy. An ideal photocatalyst has a favorable band gap, large surface area, and low cost [15].

Metal oxide semiconductors such as ZnO and TiO_2 are used as promising photocatalyst materials in the degradation of organic pollutants due to their low toxicity, high chemical stability, and high oxidation capacity. A large number of photocatalyst materials have been produced for bleaching malachite green with this method [15, 16, 17].

Ultrasonic electrochemistry is the use of ultrasonic waves to support the oxidation process. Ultrasonic wave has three main effects. The first and most important effect is cavitation. This effect is the negative pressure in the liquid when the ultrasonic wave comes into contact with

the liquid. The dissolved gas in the liquid is supersaturated, the gas overflows with the ultrasonic wave and small bubbles are formed. When the bubbles burst, the surrounding liquid quickly enters, creating instantaneous high temperature and pressure. The second effect is the thermal effect and occurs due to the increase in temperature of the liquid molecules after the absorption of ultrasonic energy. The third effect of ultrasound is its chemical effect, which can accelerate the reactions by making a positive effect on some chemical reactions [18].

With the combined use of ultrasound and electrochemistry, methods can be developed that are cost-effective, environmentally friendly and produce little secondary pollution. This common method was also used for the removal of MG [18].

Biological Methods

While the biological degradation of wastewater is cost-effective and environmentally friendly, the most important disadvantage is that biological bacteria can easily be poisoned and lose its decomposition effect. Various enzymes produced by fungi and bacteria, such as phenol oxidases, laccase, lignin, and azoreductases, have the potential to degrade dyes.

Environmentally friendly biological treatment methods have been developed to minimize the lethal effect of MG on the environment and to dispose of its wastes safely [19, 20, 21].

Physical methods

Coagulation-Flocculation

Fe and Al salts or polymeric materials are generally used to remove dyestuffs from water by coagulation. Once these chemicals are added to the suspension, they cause the stable colloidal particles to precipitate or aggregate. The method is highly effective and widely used. The most important disadvantage is the high metallic content in the resulting sludge. In recent years, these chemical coagulants have started to be replaced by natural coagulants in order to avoid the disadvantages caused by chemicals.

Natural coagulants prevent toxic sludge formation, are renewable and have less negative impact on the pH of the water. Natural coagulants prevent toxic sludge formation, are renewable and have less negative impact on the pH of the water [22, 23].

Membrane filtration

Membrane filtration method is one of the most promising techniques to remove MG from wastewater because it is easy to use, provides high efficiency and requires low energy consumption. Especially in recent

years, one-dimensional natural cellulose nanofibers (CNFs) with high surface-to-volume ratio, suitable structure stability and biocompatibility, metal-organic frameworks (MOFs), which are defined as crystal coordination polymers with periodic porous structure, have been used for this purpose [24, 25].

Adsorption

For this purpose, many adsorbent materials have been studied in the literature. However, their adsorption capacity generally varies. Materials with high adsorption are either relatively expensive or have difficult multi-step preparation conditions. Although some nanoparticles such as zinc oxide have been reported to be very effective, the fact that nanoparticles themselves are controversial in terms of human and environmental health limits their use.

In the review published by Tewari et al. in 2018, a ranking was given for the first 20 of MG adsorbents according to their adsorbing capacity. In this study, the capacities of adsorbents ranged from 0.71 to 4983 mg/g in a total of 183 studies for MG. At the same time, it has been determined that nanocomposites are extremely effective. However, the main problem here is the difficulty in the synthesis of these materials in general. For example, the highest capacity adsorbent reported in the literature is ZnO/ZnFe₂O₄ with 5000 mg/g MG holding capacity. The synthesis of this nanomaterial is two-stage, and the first stage requires heating at 200°C for 12 hours, and the second stage requires heating at 500°C for two hours [26]. Similar problems exist for studies involving other nanomaterials. In addition, there is not enough information about the effects of nanomaterials on human and environmental health.

Granular hydrogels were synthesized using chitosan (a natural polymer), acrylic acid, itaconic acid, methylenebisacrylamide (crosslinker) and attapulgit (a kind of clay) for MG adsorption [27]. While these hydrogels reach an adsorption capacity of 1750 mg/g in about 60 minutes at 30°C, they reach a high capacity of 2433 mg/g (after 5 hours) under optimum conditions. Therefore, it has reached the best result after nanomaterials/nanocomposites among the studies done so far. Studies containing hydrogel used in MG adsorption are summarized in the literature (Table 1).

Table 1. Hydrogels used in MG removal

Hydrogel	(q,mg/g)	Conditions*	References
Chitosan-Acrylic acid-itaconic acid-attapulgit granule hydrogels	2433	30°C, 5 h, pH=8-11	27
Gelatin-acrylic acid-acrylamide-attapulgit	1370	30°C, 2 h, pH=3-10	28

hydrogels			
Carrageenan-acrylic acid/TiO ₂ -NH ₂ hydrogels	833.33	30°C, 3-6 h, pH=7	29
Xanthan-Fe ₃ O ₄ nanoparticles-acrylic acid-acrylamide hydrogels	497.15	25°C, 24h, pH=6.5	30
Co-Cu nanoparticles-acrylic acid-acrylamide hydrogels	238.09	Room temperature, 2 h	31
Chitin-epichlorohydrin hydrogel	33.58	30°C, 25h, pH=7	32
Acrylamide-maleic acid hydrogel	19.45	25°C, 1 h	33
Poly(vinyl alcohol)-acrylic acid-acrylamide hydrogel	-	pH=9	34
Gum ghatti-acrylic acid-acrylamide hydrogel	-	-	35
Alginate/polyaspartate hydrogels	350	25°C	36
Imidazole modified acrylate-containing photocured hydrogels	714.28	25°C, 220 min	37

When these hydrogels are examined, it is seen that the adsorption of MG includes groups such as acid, amine and carbonyl that can hydrogen bond with MG (or provide adhesion by electrostatic interactions). In the second highest study given in this table, it was found that imidazole groups as well as these groups contributed to the adsorption of MY by π - π stacking [38].

References

1. Raval, N. P., Shah, P. U., & Shah, N. K. (2017). Malachite green “a cationic dye” and its removal from aqueous solution by adsorption. *Applied Water Science*, 7(7), 3407-3445.
2. Zhang, F., Wei, Z., Zhang, W., & Cui, H. (2017). Effective adsorption of malachite green using magnetic barium phosphate composite from aqueous solution. *Spectrochimica Acta Part A: Molecular and Biomolecular Spectroscopy*, 182, 116-122.
3. Tanyol, M. (2017). Malahit yeşili içeren atıksuların fenton oksidasyon prosesi ile renk gideriminde işletme parametrelerinin optimizasyonu. *Fırat Üniversitesi Mühendislik Bilimleri Dergisi*, 29(1), 183-191.
4. https://tr.wikipedia.org/wiki/Malahit_ye%C5%9Fili
5. Rahman, I. A., Saad, B., Shaidan, S., & Rizal, E. S. (2005). Adsorption characteristics of malachite green on activated carbon derived from rice husks produced by chemical–thermal process. *Bioresource technology*, 96(14), 1578-1583.
6. Tewari, K., Singhal, G., & Arya, R. K. (2018). Adsorption removal of malachite green dye from aqueous solution. *Reviews in Chemical Engineering*, 34(3), 427-453.
7. Hameed, B. H., & Lee, T. W. (2009). Degradation of malachite green in aqueous solution by Fenton process. *Journal of hazardous materials*, 164(2-3), 468-472.
8. Fuentealba, D., Venegas, C., Morales, M., & Waissbluth, O. (2016). Comparing Photo-Fenton Degradation of Malachite Green Using Fe II and Fe III Salts Under UVA Light Irradiation. *Journal of the Brazilian Chemical Society*, 27, 341-348.
9. Hu, Y., Li, Y., He, J., Liu, T., Zhang, K., Huang, X., ... & Liu, J. (2018). EDTA-Fe (III) Fenton-like oxidation for the degradation of malachite green. *Journal of environmental management*, 226, 256-263.
10. Kusvuran, E., Gulnaz, O., Samil, A., & Yildirim, Ö. (2011). Decolorization of malachite green, decolorization kinetics and stoichiometry of ozone-malachite green and removal of antibacterial activity with ozonation processes. *Journal of hazardous materials*, 186(1), 133-143.
11. Wang, C., Yediler, A., Lienert, D., Wang, Z., & Kettrup, A. (2003). Ozonation of an azo dye CI Remazol Black 5 and toxicological assessment of its oxidation products. *Chemosphere*, 52(7), 1225-1232.
12. Parvarideh, R., Aghapour, A. A., Jafari, S. J., Karimzadeh, S., & Khorsandi, H. (2019). A comparison of single and catalytic ozonation for decolorization of malachite green. *Desalination and Water Treatment*, 152, 411-418.

13. Mirila, D. C., Pirvan, M. Ş., Platon, N., Georgescu, A. M., Zichil, V., & Nistor, I. D. (2018). Total Mineralization of Malachite Green Dye by Advanced Oxidation Processes. *Acta Chem. Iasi*, 26, 263-280.
14. Pelaez, M., Nolan, N.T., Pillai, S.C., Seery, M.K., Falaras, P., Kontos, A.G., Dunlop, P.S.M., Hamilton, J.W.J., Byrne, J.A., O'Shea, K., Entezari, M.H., & Dionysiou, D.D. (2012). A review on the visible light active titanium dioxide photocatalysts for environmental applications. *Applied Catalysis B: Environmental*, 125, 331-349.
<https://doi.org/10.1016/j.apcatb.2012.05.036>
15. Jasrotia, R., Verma, A., Verma, R., Godara, S. K., Ahmed, J., Mehtab, A., ... & Kalia, S. (2022). Photocatalytic degradation of malachite green pollutant using novel dysprosium modified Zn–Mg photocatalysts for wastewater remediation. *Ceramics International*.
16. Liu, Y., Ohko, Y., Zhang, R., Yang, Y., & Zhang, Z. (2010). Degradation of malachite green on Pd/WO₃ photocatalysts under simulated solar light. *Journal of Hazardous Materials*, 184(1-3), 386-391.
17. Chen, C. C., Lu, C. S., Chung, Y. C., & Jan, J. L. (2007). UV light induced photodegradation of malachite green on TiO₂ nanoparticles. *Journal of hazardous materials*, 141(3), 520-528.
18. Ren, Q., Kong, C., Chen, Z., Zhou, J., Li, W., Li, D., ... & Lu, Y. (2021). Ultrasonic assisted electrochemical degradation of malachite green in wastewater. *Microchemical Journal*, 164, 106059.
19. Santal, A. R., Rani, R., Kumar, A., Sharma, J. K., & Singh, N. P. (2022). Biodegradation and detoxification of textile dyes using a novel bacterium *Bacillus* sp. AS2 for sustainable environmental cleanup. *Biocatalysis and Biotransformation*, 1-15.
20. Vijayalakshmi, S. R., & Muthukumar, K. (2014). Biodegradation of malachite green by *Ochrobactrum* sp. *World Journal of Microbiology and Biotechnology*, 30(2), 429-437.
21. Du, L. N., Zhao, M., Li, G., Xu, F. C., Chen, W. H., & Zhao, Y. H. (2013). Biodegradation of malachite green by *Micrococcus* sp. strain BD15: biodegradation pathway and enzyme analysis. *International Biodeterioration & Biodegradation*, 78, 108-116.
22. Igwegbe, C. A., Ighalo, J. O., Onukwuli, O. D., Obiora-Okafo, I. A., & Anastopoulos, I. (2021). Coagulation-flocculation of aquaculture wastewater using green coagulant from *Garcinia kola* seeds: Parametric studies, kinetic modelling and cost analysis. *Sustainability*, 13(16), 9177.
23. Hamoud, H. I., Fingueneisel, G., & Azambre, B. (2017). Removal of binary dyes mixtures with opposite and similar charges by adsorption, coagulation/flocculation and catalytic oxidation in the presence of CeO₂/H₂O₂ Fenton-like system. *Journal of environmental management*, 195, 195-207.

24. Zhang, W., Yang, K., Han, X., Cai, H., Lu, W., Yuan, Y., ... & Gao, F. (2022). Metal-organic frameworks decorated pomelo peel cellulose nanofibers membranes for high performance dye rejection. *Colloids and Surfaces A: Physicochemical and Engineering Aspects*, 649, 129393.
25. Arabkhani, P., & Asfaram, A. (2020). Development of a novel three-dimensional magnetic polymer aerogel as an efficient adsorbent for malachite green removal. *Journal of Hazardous Materials*, 384, 121394.
26. Liu, J., Zeng, M., & Yu, R. (2016). Surfactant-free synthesis of octahedral ZnO/ZnFe₂O₄ heterostructure with ultrahigh and selective adsorption capacity of malachite green. *Scientific reports*, 6(1), 1-10.
27. Zheng, Y., Zhu, Y., & Wang, A. (2014). Highly efficient and selective adsorption of malachite green onto granular composite hydrogel. *Chemical Engineering Journal*, 257, 66-73.
28. Zheng, Y., Zhu, Y., Wang, F., & Wang, A. (2015). Gelatin-grafted granular composite hydrogel for selective removal of malachite green. *Water, Air, & Soil Pollution*, 226(10), 1-12.
29. Pourjavadi, A., Doulabi, M., & Doroudian, M. (2014). Adsorption characteristics of malachite green dye onto novel kappa-carrageenan-g-polyacrylic acid/TiO₂-NH₂ hydrogel nanocomposite. *Journal of the Iranian Chemical Society*, 11(4), 1057-1065.
30. Mittal, H., Parashar, V., Mishra, S. B., & Mishra, A. K. (2014). Fe₃O₄ MNPs and gum xanthan based hydrogels nanocomposites for the efficient capture of malachite green from aqueous solution. *Chemical Engineering Journal*, 255, 471-482.
31. Naseer, F., Ajmal, M., Bibi, F., Farooqi, Z. H., & Siddiq, M. (2018). Copper and cobalt nanoparticles containing poly (acrylic acid-co-acrylamide) hydrogel composites for rapid reduction of 4-nitrophenol and fast removal of malachite green from aqueous medium. *Polymer Composites*, 39(9), 3187-3198.
32. Tang, H., Zhou, W., & Zhang, L. (2012). Adsorption isotherms and kinetics studies of malachite green on chitin hydrogels. *Journal of hazardous materials*, 209, 218-225.
33. Jasim, L. S., Radhy, N. D., & Jamel, H. O. (2018). Synthesis and characterization of poly (Acryl Amide-Maleic Acid) hydrogel: adsorption kinetics of a malachite green from aqueous solutions. *Eurasian Journal of Analytical Chemistry*, 13(1b), em74.
34. Dey, S., Kirti, N. S., & Kuila, S. B. (2018). Studies on the Removal of Dye Using Filled Polymeric FIPN Hydrogel. *adsorption*, 10, 11.
35. Mittal, H., Maity, A., & Ray, S. S. (2015). Gum ghatti and poly (acrylamide-co-acrylic acid) based biodegradable hydrogel-evaluation of the flocculation and adsorption properties. *Polymer Degradation and Stability*, 120, 42-52.

36. Jeon, Y. S., Lei, J., & Kim, J. H. (2008). Dye adsorption characteristics of alginate/polyaspartate hydrogels. *Journal of Industrial and Engineering Chemistry*, 14(6), 726-731.
37. Urucu, O. A., Aracier, E. D., & Çakmakçı, E. (2019). Allylimidazole containing OSTE based photocured materials for selective and efficient removal of gold from aqueous media. *Microchemical Journal*, 146, 997-1003.
38. Lin, K. Y. A., & Chang, H. A. (2015). Ultra-high adsorption capacity of zeolitic imidazole framework-67 (ZIF-67) for removal of malachite green from water. *Chemosphere*, 139, 624-631.



CHAPTER 13

AN OVERVIEW OF PRISMATIC EYEGLASSES

*Assoc. Prof. Dr. Tuba ÖZDEMİR ÖGE ¹,
Asst. Prof. Dr. Mecit ÖGE ²*

¹ Bartın University, Vocational School of Health Services, Bartın, Turkey, 74100,
E-mail: tozdemir@bartin.edu.tr, ORCID ID, <https://orcid.org/0000-0001-6690-7199>

² Bartın University, Faculty of Engineering, Architecture and Design, Department of
Mechanical Engineering, Kutlubey-Yazıcılar Campus, 74100 Bartın, Turkey; E-mail:
mecitoge@bartin.edu.tr, ORCID ID, <https://orcid.org/0000-0001-5243-0828>.

Prisms

Prismatic lenses are triangular-shaped prisms. The prism has no focusing power. As the light is refracted in the prism, it always deviates towards the base. The thick part of the prismatic lens forms the base of the prism (BASE), and the thin part forms the top of the prism (APEX). In the use of prismatic glasses in strabismus, the top of the prism is placed in the same direction as the shift in the eye (Özer, 2006). The diopter power of spherical lenses (SPH), diopter (D), and axis (AKS) directions of cylindrical (CYL) lenses, contact lens diopter, as well as the prism base direction and prism diopter of prismatic lenses are determined with the lensometer.

Prismatic lenses are generally used in cases where the eye muscles cannot function to obtain binocular vision. Prismatic lenses are also sometimes used in conditions such as Nystagmus, Dyslexia, Autism and Down's Syndrome (Optisyeninesi, 2022). As shown in Figure 1, strabismus can be classified according to its direction as inward strabismus (esotropia), outward strabismus (exotropia), upward strabismus (hypertropia) and downward strabismus (hypotropia) (Gezer, 2012).

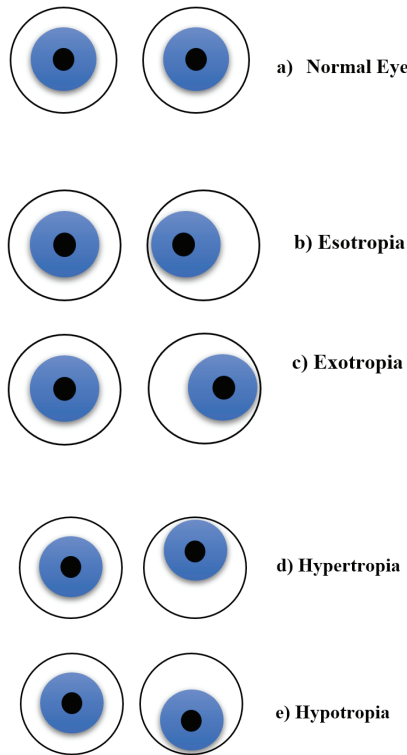


Figure 1. Normal eye and types of strabismus

Therapeutical prisms can be classified as classical glass prisms, and Fresnel prisms (Şahlı and İdil 2020).

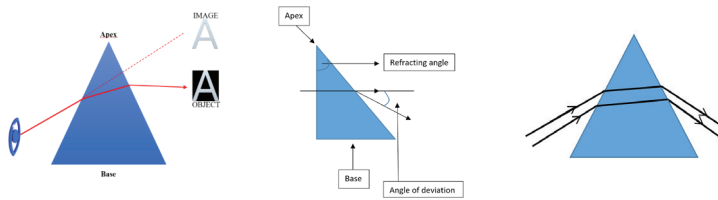


Figure 2. A prism and rays travelling through the prism

Apex, base, refracting angle, angle of deviation, and refracting power are prism terminology as shown in Figure 2. An eye looking through a prism sees the image of the object it is looking at as displaced (shifted) towards the top of the prism. Prismatic effect is measured by prism diopter. Prism dioptre and centrad are the unit of a prism. 1 prism diopter (*Equation 1*) is called prismatic effect that deflects light 1 cm from its original direction at a distance of 1 meter (Figure 3).

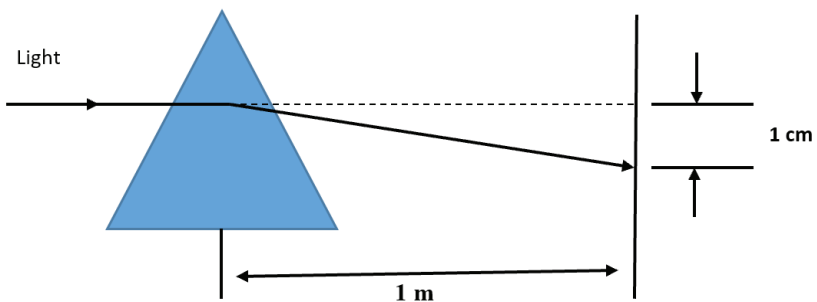


Figure 3. A prism deviating a ray of light

$$\text{Prism Diopter} = \frac{\text{Deviation (cm)}}{\text{Distance (m)}} \quad \text{Deviation produced by a prism} \quad (1)$$

Ophthalmic lenses are prism systems when viewed in cross-section. To avoid an undesired prism effect, it should be ensured that the user looks from the optical center. If the eye looks from the optical center of the lens, the prismatic effect does not occur (there is no prismatic effect in the optical center), the image is perceived in its real (actual) place, the image does not change is not displaced (Aksak and Küçüker 2005).

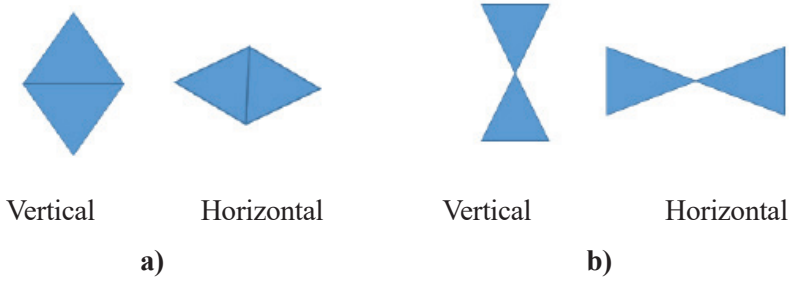


Figure 4. a) Plus and b) Minus lenses

Convex lenses are base-to-base prism systems (Figure 4a). For this reason, rays coming parallel to the convex lens from infinity (optical axis) converge at a focal point after passing through the lens. They show convergent properties, that is, they collect light. Due to their production as an apex-to-apex prism system, in concave lenses (Figure 4b), incident rays coming from infinity parallel to the optical axis diverge from each other as they refract. Hence, concave lenses show divergent characteristic.

Prism Base Direction

Base is the reference point or prism. The direction of the prism's base should be shown in the prescription. If the base direction is outward, it is called base out (BO), if the direction is inward, it is called base in (BI), if the direction is upward, it is called base up (BU) and if the direction is downward, it is called base down (BD). Accordingly, prism directions are shown in the prescription as "BASE IN", "BASE OUT", "BASE UP" and "BASE DOWN". Prism directions can also be provided in cross directions. For the use of prismatic lenses in cross directions, a 360° chart is used (Figure 5). For prisms with vertical directions, the direction of the "BASE UP" prism is represented with 90° in the chart for both eyes. Likewise, the direction of the "BASE DOWN" prism is represented with 270° in the chart for both eyes. For horizontal prisms, the direction of "BASE IN" prism is represented with 0° and that of the "BASE OUT" prism is represented with 180° for the right eye, whereas they are respectively represented with 180° and 0° for the left eye (Figure 5). Prism notation is used to give information about the magnitude or amount of the prism as well as the direction of its base. The base of the prism is indicated by the Greek Delta symbol Δ . The direction of the prism base is provided in degrees or through a combination of DOWNS, UPS, INs and OUTs. Base directions were given in Figure 6.

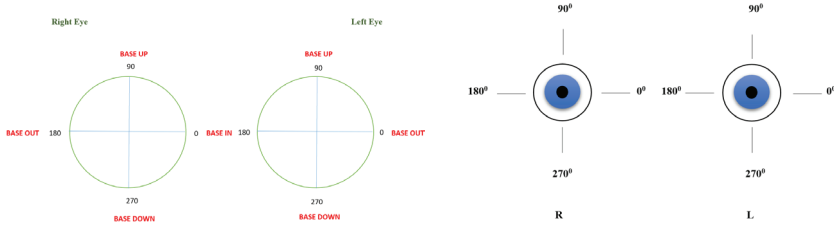


Figure 5. 360° chart

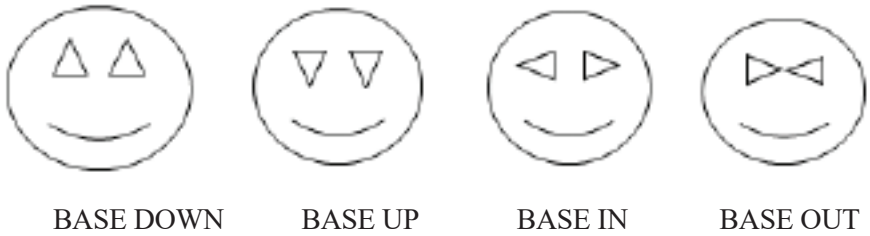


Figure 6. Base directions

Figure 7.a shows the illustration of a patient (6 ΔD base out or 6 ΔD base 180°) with 6 ΔD inward shift on right eye. Figure 7.b shows the illustration of a patient (6 ΔD base in or 6 ΔD base 0°) with 6 ΔD outward shift on right eye. Figure 7.c shows the illustration of a patient (6 ΔD base out or 6 ΔD base 0°) with 6 ΔD inward shift on left eye. Figure 7.d shows the illustration of a patient (6 ΔD base in or 6 ΔD base 180°) with 6 ΔD outward shift on left eye. Figure 7.e shows the illustration of a patient (6 ΔD base down or 6 ΔD base 270°) with 6 ΔD upward shift on right eye. Figure 7.f shows the illustration of a patient (6 ΔD base up or 6 ΔD base 90°) with 6 ΔD downward shift on right eye. Figure 7.g shows the illustration of a patient (6 ΔD base down or 6 ΔD base 270°) with 6 ΔD upward shift on left eye. Figure 7.h shows the illustration of a patient (6 ΔD base up or 6 ΔD base 90°) with 6 ΔD downward shift on left eye.

	<p>a) 6 ΔD base out or 6 ΔD base 180°</p>
	<p>b) 6 ΔD base in or 6 ΔD base 0°</p>

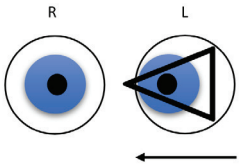
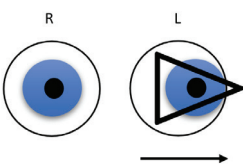
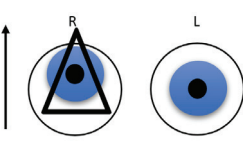
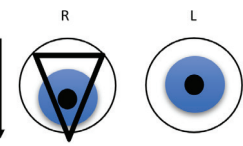
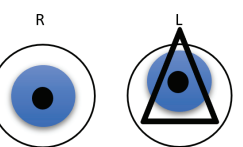
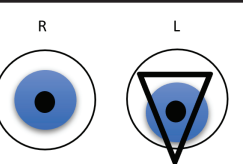
	c) 6 ΔD base out or 6 ΔD base 0°
	d) 6 ΔD base in or 6 ΔD base 180°
	e) 6 ΔD base down or 6 ΔD base 270°
	f) 6 ΔD base up or 6 ΔD base 90°
	g) 6 ΔD base down or 6 ΔD base 270°
	h) 6 ΔD base up or 6 ΔD base 90°

Figure 7. Prism orientations

As the prism power moves away from the optical center, the dioptric power of the lens increases in direct proportion to the distance from the center. This relationship is known as Prentice's law (*Equation 2*). The prism power in diopters of the prism at any point on the lens surface is equal to the power of the lens in diopters multiplied by its distance from the optical center in cm (Ünlüçerçi, 2016).

$$\Delta (\text{Prism diopter}) = h (\text{cm}) \cdot D (\text{diopter}) \quad (2)$$

Δ Prism is prism diopter (prismatic effect), D is the diopter power of the lens, h is the distance of the point, prismatic effect of which is in question, to the optical center (cm).

In cases where a single eye contains both horizontal and vertical prisms, vertical and horizontal notations accompanied with the magnitude of prismatic diopter can be used to evaluate the compound prism's base direction for the respective eye. The prism arising from such vertical and horizontal prism at the same time is referred to as the "Resultant prism" (Figure 8). Other notations involve the use of an angle notation to directly indicate the prism's base direction.

The resultant prism arising from vertical and horizontal prisms can be calculated by using the below Equation 3:

$$R = \sqrt{V^2 + H^2} \tag{3}$$

where H denotes the horizontal prism, and V denotes the vertical prism, and R denotes the resultant prism. The prism's base direction can be found using the below Equation 4:

$$\tan\theta = \frac{V}{H} \tag{4}$$

In this case, the prism's base direction is either θ or $180 - \theta$ (Brooks, 1992).

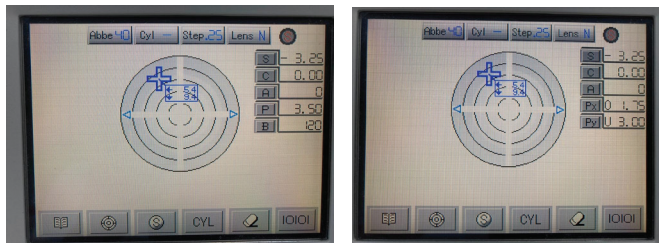


Figure 8. Resultant prism notation with prism amount and base direction



Figure 9. Focimeter measurement of prismatic eyeglasses.

During the use of focimeters to measure prism, the rings system within the optical device is used to measure the prismatic diopter of prismatic lenses. Each ring represents the magnitude of one prism diopter, and the scale is used to determine the direction of the prism base (Figure 9) (Aksak and Küçükler 2005).

Canceling (Subtraction) and Compounding (Addition) Prismatic Effect

In binocular vision the total prism effect arising from both eyes may be cancelled (subtraction) or compound (addition) depending on the direction of the prism prescribed by the doctor for each eye. As shown in Figure 10,

the canceling effect is observed in BI+BO, BU+BU and BD+BD situations, whereas the prismatic effect is compound or added in BI+BI, BO+BO and BU+BD situations.

	<p>1 ΔD BO (R) 1 ΔD BO (L)</p>	<p>Addition Total prism= 2 ΔD</p>
	<p>1 ΔD BO (R) 1 ΔD BI (L)</p>	<p>Subtraction Total prism= 0 ΔD</p>
	<p>1 ΔD BI (R) 1 ΔD BI (L)</p>	<p>Addition Total prism= 2 ΔD</p>
	<p>1 ΔD BI (R) 1 ΔD BO (L)</p>	<p>Subtraction Total prism= 0 ΔD</p>
	<p>1 ΔD BD (R) 1 ΔD BD (L)</p>	<p>Subtraction Total prism= 0 ΔD</p>
	<p>1 ΔD BU (R) 1 ΔD BD (L)</p>	<p>Addition Total prism= 2 ΔD</p>

Figure 10. Combinations of BU, BD, BI and BO situations for different eyes that result in cancelling and compounding prismatic effect.

Splitting Prism

Splitting prism refers to the process of balancing or distributing a prism that is prescribed by the doctor between both eyes to avoid an imbalance in terms of lens thickness and weight between the two lenses. The process can be carried out by a professional dispenser as long as the doctor is consulted. By this process, in addition to avoiding weight and thickness imbalance between two lenses, chromatic aberration can be also reduced. When splitting prescribed prism between the two eyes, the prism is generally evenly distributed in accordance with the compounding and cancelling prismatic effect rules which were mentioned previously (Bhootra, 2009). As illustrated in Figure 11, placing a 6Δ BD prism on the right eye results in the same effect with placing a 3Δ BU prism on the left eye and a 3Δ BD prism on the right eye since the compound effect of these prisms is 6Δ BD according to the compounding prismatic effect rule. This way the weight and thickness of a 6Δ prismatic lens can be evenly distributed between both lenses (McCleary, 2018).

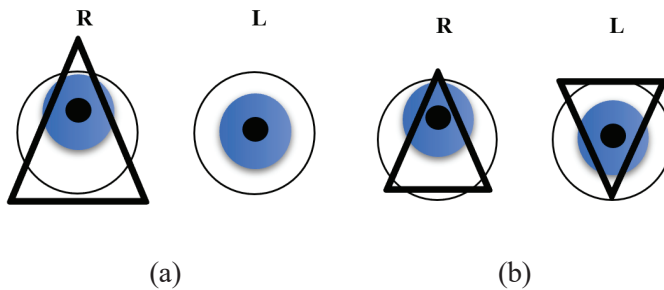


Figure 11. a) Right eye with 6Δ BD prism, b) Right eye with 3Δ BD and left eye with 3Δ BU prism

Conclusion

The basics and terminology of prism in the fields of ophthalmology and opticianry were explained on examples in this study. The measurement of prism diopter and base directions were shown on focimeter. Also, the types of prism notations were briefly explained. The subjects of splitting prisms, addition and subtraction of prisms; the types of strabismus and its compensation by use of prisms were also explained. This work has been introduced with a view to contribute to the works on prismatic eyeglasses and provide the readers with brief and concise information on this subject.

References

- Acun Gezer., Binoküler Görme ve Şaşılık., Klinik Gelişim., 2012; 25: 40-49.
- Ahmet Özer., Prism and Prismatic Effects of Lenses., Türkiye Klinikleri J Ophthalmol 2006, 15.
- Aksak, E., Küçüker, T. 2005. “Gözlükçülük”. Tüm Optik ve Optometrik Meslekler Birliği Derneği. Baskı: Esen Ofset Matbaacılık San. ve Tic. A.Ş.
- Bhootra A.K. (2009). Ophthalmic Lenses. Jaypee Brothers Medical Publishers (P) Ltd. New Delhi.
- Brooks, C.W. (1992) Understanding Lens Surfacing, Oxford: Butterworth-Heinemann.
- Esra ŞAHLI., Aysun İDİL., Current Use of Prisms in Ophthalmology, Türkiye Klinikleri J Ophthalmol. 2020;29(2):158-68.
- McCleary D.S. (2018). The Optician Training Manual (2nd Edition): Simple Steps to Becoming a Great Optician, Santa Rosa Publishing.
- Prismatic eyeglasses, <https://optisyeninsesi.com/prizmatik-camlar-nedir-ve-ne-amacla-kullanilir-1/> Accessed: 08.10.2022
- Ünlüçerçi., N. C., Optisyenler için Görme Optiği ve Görme Kusurlarının Düzeltmesi, Nobel Tıp Kitabevleri, 2016.



CHAPTER 14

CAUSALITY ANALYSIS IN STATISTICAL AND ECONOMETRIC MODELS: INVESTIGATING CAUSALITY RELATIONSHIP BETWEEN TURKEY'S PRIMARY ENERGY USE AND GROSS DOMESTIC PRODUCT BY GRANGER CAUSALITY TEST

Neslihan İYİT^{1}, Harun YONAR², Aynur YONAR³*

1 ** The theory part of this study is a part of Harun Yonar's Ph.D. Thesis entitled "*Investigation of economic growth and risk assessments of countries with generalized linear models*" supervised by Assist.Prof.Dr.Neslihan İyit in Statistics Department, Graduate School of Natural Sciences, Selçuk University.

Assoc.Prof.Dr., Statistics Department, Faculty of Science, Selcuk University, Konya, Turkey

*Corresponding Author: Email: niyit@selcuk.edu.tr

ORCID ID: 0000-0002-5727-6441

2 Assist.Prof.Dr., Biostatistics Department, Veterinary Faculty, Selcuk University, Konya, Turkey

ORCID ID: 0000-0003-1574-3993

3 Assist.Prof.Dr., Statistics Department, Faculty of Science, Selcuk University, Konya, Turkey

ORCID ID: 0000-0003-1681-9398

In studies in the field of statistics and econometrics, it is very important to determine the “causality” relationships between the dependent and explanatory variables to be included in the statistical or econometric model. Thus, in determining the model that best fits the data structure, to reveal how the variables behave with each other; it is extremely important to determine the relationships between these variables and to obtain valid statistical inferences from the constructed model.

Although the “correlation coefficient”, which is frequently used in the determination of the statistical relationships between the variables, is very useful to see the movements of the variables in terms of direction and behavior, but not sufficient. Kendall (1961) stated that it would not be correct to evaluate the “correlation” as a cause-effect relationship between the variables. No matter how strong a statistical relationship is, the concept of “causality” should also be examined (Gujarati, 1999). On the other hand, while “causality analysis” tests can give a cause-effect relationship between the variables; they cannot give information about the severity of the relationship.

“Granger causality test” proposed by Granger (1969) is frequently used in the causality studies in econometric models. Then Toda and Yamamoto (1995) suggested causality analysis when the constraint brought by the stationarity condition in the Granger test was removed and based on the “Vector Autoregression (VAR) model”.

The main purpose of this book chapter is to construct the theory of the “Granger causality test” used in the causality analysis in detail and to show its important usage in econometric data analysis empirically. For this purpose, an extended literature review was conducted on the “Granger causality test” and the “causality analysis” in econometric data analysis, and then the main findings in the literature are given as follows;

Ahmad and Kwan (1991) used the “Granger causality test” to investigate the relationship between exports and national income with a consistent data set for 47 developing countries in the African continent.

Ahmad and Harnhirun (1996) examined the causality relationship between exports and economic growth for the five member countries of the Association of Southeast Asian Nations (ASEAN), Indonesia, Malaysia, Philippines, Singapore and Thailand, using the “Granger causality test”. They found that the expansion in exports for these countries did not cause economic growth.

Ahmad (2001) made an evaluation of important econometric studies in the literature that estimated the causality relationship between

exports and economic growth and found that there is no causal relationship between exports and economic growth in both developed and developing countries.

Soytas and Sari (2003) examined the causality relationship between energy consumption and gross domestic product (GDP) for G-7 countries. They found bi-directional causality relationship among these variables for Argentina, from GDP to energy consumption for Italy and Korea, and from energy consumption to GDP for Turkey, France, Germany and Japan.

Narayan and Smyth (2005) examined the relationship between electricity consumption, employment and real income in Australia within the framework of cointegration and causality analyses. They concluded that electricity consumption, employment and real income are combined and that long-term employment and real income are the cause of electricity consumption by “Granger's causality test”. In the short run, they showed that there is a weak unidirectional “Granger causality relationship” from income to electricity consumption and from income to employment.

Shirazi and Manap (2005) investigated the causal and dynamic relationships between exports, imports and GDP for countries in South Asia, India, Pakistan, Bangladesh, Nepal and Sri Lanka. To check for causality aspects between these variables, they used the “Granger causality test” based on the method of Toda and Yamamoto (1995). They showed that there was long-run equilibrium between the three variables for all the countries studied, except Sri Lanka.

Narayan and Prasad (2008) examined the causality relationship between electricity consumption and real GDP for 30 OECD countries. They found an inverse causality relationship between GDP and electricity consumption in Australia, Iceland, Italy, Slovak Republic, Czech Republic, Korea, Portugal and England. In short, they found that electricity consumption protection policies will negatively affect the GDP in these countries.

Payne (2010) examined the literature on the causality relationship between energy consumption and economic growth. It is observed that there is no clear consensus between energy consumption and economic growth for a particular country or group of countries.

Yonar and İyit (2018) investigated in modeling causality relationships between various economic indicators and electricity consumption of the countries belonging to different income levels.

After giving an extended overview to the literature about causality analysis by “Granger causality test”, some basic concepts used in the causality analysis are defined as follows;

➤ **Stationarity**

The concept of “stationarity”, which expresses a statistical equilibrium, refers to a stochastic process in which the mean and variance of the series do not change over the period of time studied, and the common variance between the two periods examined depends only on the distance between these two periods. (Işığışık, 1994; Gujarati, 1999).

If the series Y_t corresponding to a stochastic process having these properties;

$$\text{i. Mean : } E[Y_t] = \mu_Y \quad (1)$$

$$\text{ii. Variance : } Var[Y_t] = \sigma_Y^2 \quad (2)$$

$$\text{iii. Covariance : } Cov[Y_t, Y_{t+k}] = \gamma_k \quad k \neq 0 \quad (3)$$

then the form of “stationarity structure” is called “weak stationarity”. Here μ_Y , σ_Y^2 and γ_k are fixed for $\forall t$ and also γ_k is the covariance between Y_t and Y_{t+k} values with k period difference (Farnum ve Stanton, 1989; Gujarati, 1999; Sevüktekin and Nargeleşkenler, 2007).

In addition to the weak stationarity properties of the Y_t series, if the distribution of the series does not change over time, there will be “strong stationarity” (Akgül, 2003; Sevüktekin and Nargeleşkenler, 2007).

There are a number of methods developed for the determination of “stationarity”. These are; graphical analysis, autocorrelation analysis (correlogram) and unit root tests. Quite commonly used unit root tests for the determination of stationarity are Dickey and Fuller (1979) test, Augmented Dickey-Fuller (ADF) test, Phillips and Perron (1988) unit root test, and etc. (Sevüktekin and Nargeleşkenler, 2007; Çil, 2015).

After the determination of the stationarity situation, non-stationary series can be made stationary by using different transformation techniques

such as taking the difference, taking the logarithm, and recovering from the trend effect (Işığışok, 1994).

➤ **Dickey-Fuller Test and Augmented Dickey-Fuller Test**

The Dickey-Fuller (DF) unit root test, developed by Dickey and Fuller (1979), is a widely used unit root test in time series stationarity tests. The Dickey-Fuller model is a sequential regression model that includes a lagged variable of the series;

$$\Delta Y_t = (\rho - 1)\Delta Y_{t-1} + u_t \quad (4)$$

by taking the difference of the autoregressive model $AR(1)$. Here $\delta = (\rho - 1)$, hypotheses can be set up as follows;

$$\begin{aligned} H_0 &= \delta \geq 0 \text{ (There is a unit root)} \\ H_1 &= \delta < 0 \text{ (There is no unit root)} \end{aligned} \quad (5)$$

If the absolute value of the DF statistic is less than the absolute value of the Mac Kinnon critical value after the difference, it is decided that it is unit root and the series is not stationary (Kutlar, 2005; Tari, 2010).

The unit root test, known as Augmented Dickey Fuller (ADF) test in the literature, is a p^{th} degree autoregressive model of $AR(1)$ and is based on autocorrelation between error terms. The ADF test is extended by including one or more lagged values of the primary differences of the dependent variable enough to prevent the error terms from being sequentially dependent. Here, the information criteria for the selection of the appropriate p delay value are used. The model equation for the ADF test is given as follows;

$$\Delta Y_t = \beta_0 + \beta_1 t + \delta Y_{t-1} + \sum_{i=1}^m \alpha_i \Delta Y_{t-i} + \varepsilon_t \quad (6)$$

The hypotheses and evaluation criteria of the ADF test can be made in the same way as in DF test (Tari, 2010).

➤ **Vector Autoregression (VAR) Model**

The *VAR* model developed by Sims (1980) gives the opportunity to evaluate all the variables in a system integrity. In the *VAR* model, the lagged value of each variable and the lagged values of the other variables are located to the right of a multi-equation system (Gujarati, 1999; Kutlar, 2005; Tari, 2010; Yerdelen and Tatoğlu, 2017). The *VAR* model having two variables and p lag can be given as follows;

$$Y_t = \alpha_{10} + \sum_{i=1}^p \alpha_{11i} Y_{t-i} + \sum_{i=1}^p \alpha_{12i} X_{t-i} + u_{1t} \quad (7)$$

$$X_t = \alpha_{20} + \sum_{i=1}^p \alpha_{21i} Y_{t-i} + \sum_{i=1}^p \alpha_{22i} X_{t-i} + u_{2t} \quad (8)$$

Here, α_{i0} is the fixed term; α_{ijk} is the parameter belonging to the k^{th} lag of j^{th} variable in the i^{th} equation (Gujarati, 1999).

The determination of the optimal lag length is made using the log-likelihood ratio or using information criteria. In the literature, many criteria are used to determine the lag length, especially Akaike (AIC) and Schwarz (SIC) information criteria are the most preferred ones (Bhatti ve Al-Shanfari, 2017).

➤ Cointegration

The misspecification problem in regression occurs in modeling long-term relationships in non-stationary time series. Differentiation operations performed to ensure stability eliminate the fluctuations in the series, causing the permanent shocks to which the data was exposed in the past to disappear and the long-term equilibrium relationship hidden in the data cannot be determined correctly (Tari, 2010).

The cointegration analysis developed by Engle-Granger (1987) is a powerful approach that can test the relationship between two time series without requiring the stationarity condition. Cointegration means that even if each of the series of economic variables is not stationary separately, the linear combination of these series can be stationary. In other words, if two non-stationary series are integrated (stationary at the same order) after taking the difference separately, the stationarity of the error term of these

series indicates that the series are cointegrated and there is a long-term equilibrium relationship between them (Engle and Granger, 1987; Gujarati, 1999; Kutlar, 2005). On the other hand, in the stationary series, these series are cointegrated, since the equilibrium relationship is provided in the long run.

➤ **Granger and Toda-Yamamoto Causality Tests**

Granger (1969) and Toda-Yamamoto (1995) causality tests are the most used tests in causality analysis in the literature. The superiority of the Toda-Yamamoto causality test over the Granger causality test is that while the Granger causality test can only be performed for stationary variables, the Toda-Yamamoto causality test does not require a stationary condition.

➤ **Granger Causality Test**

The first definition of the concept of causality in statistics and economics literature was given by the famous mathematician Wiener (1956), but it is known as the Granger causality test in the literature, since Granger (1969) provided the greatest methodological contribution to the concept of causality (Gujarati, 1999).

Granger causality test is a method used to reveal a cause-effect relationship between two stationary series and to determine the direction of this causality relationship. Since economic variables are generally not stationary, before starting the causality analysis, the variables should be adjusted for trend and seasonal effects and should be stabilized (Işığışık, 1994).

X and Y are two stationary variables, using the lagged values of these two variables, the equations for the Granger causality test are given as follows;

$$Y_t = \sum_{i=1}^m \alpha_i Y_{t-i} + \sum_{i=1}^m \beta_i X_{t-i} + u_{1t} \quad (9)$$

$$X_t = \sum_{i=1}^m \gamma_i X_{t-i} + \sum_{i=1}^m \delta_i Y_{t-i} + u_{2t} \quad (10)$$

Here, α_i , β_i , γ_i and δ_i are coefficients of the lagged variables, m is the lag length for all variables, u_{1t} and u_{2t} are the uncorrelated random errors (Granger, 1969; Gujarati, 1999).

In the evaluation of the Granger causality test for two variables, the stationarity of the series is checked before starting the test. If the series are not stationary, the stationarity of the error term is investigated by testing the cointegration relationships using the Engle and Granger (1987) cointegration test (Tari, 2010).

Let X_t and Y_t be two stationary series. Hypotheses used for causality testing from X_t to Y_t from these series can be set up as follows.

$$\begin{aligned} H_0 : \beta_i = 0 ; i = 1, 2, \dots, m \text{ for } \forall i \\ H_1 : \beta_i \neq 0 ; i = 1, 2, \dots, m \text{ for } \exists i \end{aligned} \quad (11)$$

In the hypothesis test given by Eq. (11), if the tested null hypothesis cannot be rejected, at least one $\beta_i = 0$ means that the Y_{t-1}, \dots, Y_{t-m} lagged variables do not have a place in the relationship and therefore there is no causality relationship from X_t to Y_t . In the hypothesis test given by Eq. (11), the rejection of the tested null hypothesis indicates that there is a causality relationship from X_t to Y_t . The test statistics used in the testing of the hypotheses given by Eq. (11) is as follows;

$$F = \frac{(RSS_R - RSS_{UR}) / m}{RSS_{UR} / (n - k)} \quad (12)$$

Here, m is the number of lagged variables not included in the model, n is the sample size, k is the number of parameters estimated in the unconstrained model, RSS_R is the sum of the squares of the error terms of the constrained model, RSS_{UR} is the sum of the squares of the error terms of the unconstrained model (Gujarati, 1999).

F -test statistic value calculated from Eq.(12) is compared with the F -table value determined by the degrees of freedom as m and $(n - k)$

according to the α significance level. If $F_{test\ statistic} > F_{tablevalue}$ then the null hypothesis H_0 can be rejected and concluded that there is a causality relationship from X_t to Y_t . If $F_{test\ statistic} < F_{tablevalue}$ then the null hypothesis H_0 cannot be rejected and concluded that there is no causality relationship from X_t to Y_t .

Thus, after having knowledge for the causality relationship from X_t to Y_t , the causality relationship from Y_t to X_t is tested. At this stage, the hypotheses built on the d_i coefficient given by Eq. (10) are as follows (Tari, 2010);

$$\begin{aligned} H_0 : \delta_i &= 0; \quad i = 1, 2, \dots, m \quad \text{for } \forall i \\ H_1 : \delta_i &\neq 0; \quad i = 1, 2, \dots, m \quad \text{for } \exists i \end{aligned} \tag{13}$$

After estimating the β_i and d_i parameters of the hypotheses given by Eq. (1) and Eq. (13) using the Least Squares (LS) method, the possible results are given as follows (Işığınçok, 1994; Tari, 2010);

- i.** If b_i is statistically significant then it can be said that the X_t series is the (Granger) cause of the Y_t series. In this case, there is a one-way causality relationship from X_t to Y_t ($X_t \rightarrow Y_t$).
- ii.** If δ_i is statistically significant then it can be said that Y_t series is the (Granger) cause of the X_t series. In this case, there is a one-way causality relationship from Y_t to X_t ($Y_t \rightarrow X_t$).
- iii.** If β_i and δ_i are both statistically significant, there is a bi-directional causality relationship ($X_t \leftrightarrow Y_t$).
- iv.** If β_i and δ_i are both statistically insignificant, it means that the two series are not the cause of each other and these two series are said to be independent of each other.

Granger (1969) causality test is widely used in the literature, but it also receives some criticism. These can be given as follows (Işığınçok, 1994);

- i. It can be listed as the fact that the causality direction is affected as a result of the test being overly sensitive to the lag length,
- ii. The test can only be applied to stationary series,
and
- iii. The real relationship cannot be revealed as a result of long-term loss of information in the series to which the stationarization process is applied.

➤ Toda-Yamamoto Generalized Causality Test

In the method developed by Toda and Yamamoto (1995), the restriction imposed by the “stationarity” condition in the Granger test is removed and the causality analysis based on the “VAR system” can be examined.

The biggest advantage of this method; It can be used in non-stationary situations or in situations where stationarity can be achieved at different levels. In this test, only the cases of integration of the series are taken into account, without stationarization, loss of information and without the need for co-integration analysis (Toda and Yamamoto, 1995).

The Toda-Yamamoto generalized causality test consists of two stages. In the first stage, the appropriate lag length (k) is determined for the VAR model. In the second stage, the maximum lag length of the model is obtained by adding the lag length determined for the model as much as the integration degree of the series with the highest integration degree (d_{\max}) among the series used. In the Toda-Yamamoto test, the significance of the model parameters is tested using a Modified Wald (MWALD) test statistic with a chi-square (χ^2) distribution (Shan and Tian, 1998; Awokuse and Yang, 2003).

By adding the VAR model delay length (d_{\max}) to the X_t and Y_t series, the equations for the Toda-Yamamoto generalized causality test are given as follows;

$$Y_t = \lambda_{10} + \sum_{i=1}^{k+d_{\max}} \varphi_{1i} Y_{t-i} + \sum_{i=1}^{k+d_{\max}} \alpha_{1i} X_{t-i} + u_{1t} \quad (14)$$

$$X_t = \lambda_{20} + \sum_{i=1}^{k+d_{\max}} \gamma_{2i} X_{t-i} + \sum_{i=1}^{k+d_{\max}} \vartheta_{2i} Y_{t-i} + u_{2t} \quad (15)$$

where k is the optimal lag length in the predicted VAR model, d_{max} is the maximum integration degree of the model and the VAR model to be established is obtained with adding the lag-length $(k + d_{max})$. The hypotheses established for the Toda-Yamamoto generalized causality analysis of the VAR model in Eq. (14) are given as follows;

$$\begin{aligned} H_0 : \alpha_{1i} &= 0; \quad i = 1, 2, \dots, k + d_{max} \quad \text{for } \forall i \\ H_1 : \alpha_{1i} &\neq 0; \quad i = 1, 2, \dots, k + d_{max} \quad \text{for } \exists i \end{aligned} \tag{16}$$

If the null hypothesis (H_0) in Eq.(16) is rejected, then it can be concluded that “The X_t series is the Toda-Yamamoto cause of the Y_t series”.

The hypotheses established for the Toda-Yamamoto generalized causality analysis of the VAR model in Eq. (15) are given as follows;

$$\begin{aligned} H_0 : J_{2i} &= 0; \quad i = 1, 2, \dots, k + d_{max} \\ H_1 : J_{2i} &\neq 0; \quad i = 1, 2, \dots, k + d_{max} \end{aligned} \tag{17}$$

If the null hypothesis (H_0) in Eq.(17) is rejected, then it can be concluded that “The Y_t series is the Toda-Yamamoto cause of the X_t series” (Toda and Yamamoto, 1995).

➤ **Investigating Granger Causality Relationship Between Energy Use and Gross Domestic Product by Granger Causality Test**

In the application part of this book chapter, it will be examined whether one time series can be used to predict another with the Granger Causality test. The data set consists of Turkey's Gross Domestic Product (GDP (current US\$)) and primary energy use (kg of oil equivalent per capita) values between 1960 and 2015 taken from World Development Indicators taking place in WorldBank (2018). All statistical analyzes including “Granger causality test” and checking “stationarity” condition are done using R programme “lmtest” (Zeileis and Hothorn, 2002) and “tseries” libraries. The dataset used in this study carried out by taking the logarithm of the series. Before checking stationarity condition using “Augmented Dickey-Fuller test (Banerjee et al. (1993), Said and Dickey (1984)), the graphs of the variables behaviour in the data set are given in Figure1 and Figure 2.

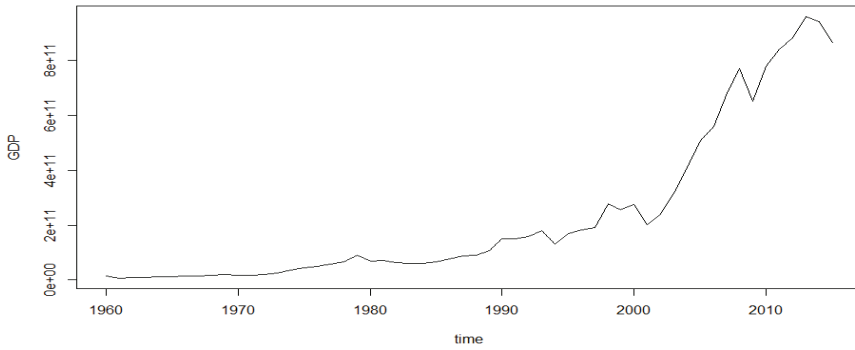


Figure 1. Time series graph of GDP values for Turkey between 1960 and 2015

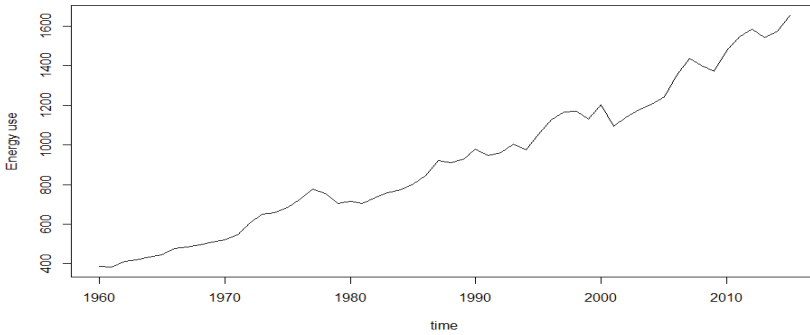


Figure 2. Time series graphs of primary energy use values for Turkey between 1960 and 2015

Before investigating the causality relationship between Turkey's GDP (current US\$) and primary energy use (kg of oil equivalent per capita) by Granger causality test, stationarity analyzes using “Augmented Dickey-Fuller test” are carried out for these two series, and the results are given in Table 1.

Table 1. Augmented Dickey-Fuller test results for Turkey's GDP and primary energy usage values

Augmented Dickey-Fuller Test

```
data: df`Energy use`
Dickey-Fuller = -2.7189, Lag order = 3, p-value = 0.2847
alternative hypothesis: stationary
```

Augmented Dickey-Fuller Test

```
data: df$GDP
Dickey-Fuller = -3.4676, Lag order = 3, p-value = 0.05431
alternative hypothesis: stationary
```

According to Augmented Dickey-Fuller Test results given in Table 1, both series of Turkey's GDP and primary energy use are not stationary ($p > 0.05$). Differentiation is performed to ensure stationarity, and first-order differentiation is performed for both time series of the variables. Augmented Dickey-Fuller Test results of these series are given in Table 2.

Table 2. Augmented Dickey-Fuller test results of the series for Turkey's GDP and primary energy use with first-order differentiation

Augmented Dickey-Fuller Test

```
data: df_GDP
Dickey-Fuller = -4.2426, Lag order = 3, p-value = 0.01
alternative hypothesis: stationary
```

Augmented Dickey-Fuller Test

```
data: df_Energy
Dickey-Fuller = -3.7078, Lag order = 3, p-value = 0.03225
alternative hypothesis: stationary
```

It is determined that by the first-order differentiation for Turkey's GDP and primary energy use series, the stability condition is provided according to the Augmented Dickey-Fuller test results after the acquisition process ($p < 0.05$).

Using the first-order differentiated series of Turkey's GDP and primary energy use, it is determined whether Turkey's primary energy use is the Granger cause of Turkey's GDP or not, and then whether Turkey's GDP is the Granger cause of Turkey's primary energy use are examined. The results for both of these Granger causality relationships between these variables investigation are given in Table 3.

Table 3. Granger causality test results for Turkey's GDP and primary energy use variables

```

Granger causality test
Model 1: df_GDP ~ Lags(df_GDP, 1:3) + Lags(df_Energy, 1:3)
Model 2: df_GDP ~ Lags(df_GDP, 1:3)
  Res.Df Df    F Pr(>F)
1      45
2      48 -3 3.042 0.03844 *
---
Signif. codes:  0 '***' 0.001 '**' 0.01 '*' 0.05 '.' 0.1 ' ' 1
Granger causality test

Model 1: df_Energy ~ Lags(df_Energy, 1:3) + Lags(df_GDP, 1:3)
Model 2: df_Energy ~ Lags(df_Energy, 1:3)
  Res.Df Df    F Pr(>F)
1      45
2      48 -3 0.9796 0.4108

```

It is examined whether Turkey's primary energy use is the Granger cause of Turkey's GDP. When the test statistic is examined, the F -test statistic value is 3.042 and p-value is $p=0.03844 < 0.05$; Then the null hypothesis H_0 that the Turkey's primary energy use is not the Granger cause of Turkey's GDP seems to be rejected. And then it is concluded that the Turkey's primary energy use is not the Granger cause of Turkey's GDP according to the Granger causality test.

In the examination of whether Turkey's GDP is the Granger cause of Turkey's primary energy use, the F -test statistic is 0.9796 and p-value is $p=0.4108 > 0.05$; then it is concluded that the Turkey's GDP is not the Granger cause of Turkey's primary energy use according to the Granger causality test.

References

- 1) Wiener, N. (1956), The theory of prediction, *Modern mathematics for engineers*.
- 2) Kendall, M. G. (1961), The advanced theory of statistics: Inference and relationship, Charles Griffin.
- 3) Granger, C. W. (1969), Investigating causal relations by econometric models and cross-spectral methods, *Econometrica: Journal of the Econometric Society*, 424-438.
- 4) Dickey, D. A. and Fuller, W. A. (1979), Distribution of the estimators for autoregressive time series with a unit root, *Journal of the American statistical association*, 74 (366a), 427-431.
- 5) Sims, C. A. (1980), Macroeconomics and reality, *Econometrica: Journal of the Econometric Society*, 1-48.
- 6) Said, S. E. and Dickey, D. A. (1984), Testing for Unit Roots in Autoregressive-Moving Average Models of Unknown Order. *Biometrika* 71, 599-607.
- 7) Engle, R. F. and Granger, C. W. (1987), Co-integration and error correction: representation, estimation, and testing, *Econometrica: journal of the Econometric Society*, 251-276.
- 8) Phillips, P. C. and Perron, P. (1988), Testing for a unit root in time series regression, *Biometrika*, 75 (2), 335-346.
- 9) Farnum, N. R. and Stanton, L. W. (1989), Quantitative forecasting methods, Pws Pub Co.
- 10) Ahmad, J. and Kwan, A. C. (1991), Causality between exports and economic growth: empirical evidence from Africa, *Economics Letters*, 37 (3), 243-248.
- 11) Banerjee, J. J. Dolado, J. Galbraith, W. and Hendry, D. F. (1993), Cointegration, Error Correction, and the Econometric Analysis of Non-Stationary Data, Oxford University Press, Oxford.
- 12) Işığçok, E. (1994), Zaman serilerinde nedensellik çözümlemesi: Türkiye'de para arzı ve enflasyon üzerine ampirik bir araştırma, Uludağ Üniversitesi Basımevi.
- 13) Toda, H. Y. and Yamamoto, T. (1995), Statistical inference in vector autoregressions with possibly integrated processes, *Journal of econometrics*, 66 (1-2), 225-250.
- 14) Ahmad, J. and Harnhirun, S. (1996), Cointegration and causality between exports and economic growth: evidence from the ASEAN countries, *The Canadian Journal of Economics/Revue canadienne d'Economie*, 29, S413-S416.
- 15) Shan, J. and Tian, G. G. (1998), Causality between exports and economic growth: the empirical evidence from Shanghai, *Australian Economic Papers*, 37 (2), 195-202.
- 16) Gujarati, D. N. (1999), Temel Ekonometri (Çev. Ümit Şenesen, Gülay Günlük Şenesen), *Birinci Basım, İstanbul: Literatür Yayınları*.
- 17) Ahmad, J. (2001), Causality between exports and economic growth: what do the econometric studies tell us?, *Pacific Economic Review*, 6 (1), 147-167.
- 18) Zeileis, A. and Hothorn, T. (2002), Diagnostic Checking in Regression Relationships. *R News* 2(3), 7-10. URL <https://CRAN.R-project.org/doc/Rnews/>

- 19) Akgül, I. (2003), Zaman Serilerinin Analizi ve ARIMA modelleri, Der Yayınevi.
- 20) Awokuse, T. O. and Yang, J. (2003), The informational role of commodity prices in formulating monetary policy: a reexamination, *Economics Letters*, 79 (2), 219-224.
- 21) Soytaş, U. and Sari, R. (2003), Energy consumption and GDP: causality relationship in G-7 countries and emerging markets, *Energy economics*, 25 (1), 33-37.
- 22) Kutlar, A. (2005), Uygulamalı Ekonometri, Nobel Kitabevi.
- 23) Narayan, P. K. and Smyth, R. (2005), Electricity consumption, employment and real income in Australia evidence from multivariate Granger causality tests, *Energy policy*, 33 (9), 1109-1116.
- 24) Shirazi, N. S. and Manap, T. A. A. (2005), Export-led growth hypothesis: Further econometric evidence from South Asia, *The Developing Economies*, 43 (4), 472-488.
- 25) Sevüktekin, M. and Nargeleçekenler, M. (2007), Ekonometrik zaman serileri analizi: EViews uygulamalı, Nobel Yayın Dağıtım.
- 26) Narayan, P. K. and Prasad, A. (2008), Electricity consumption–real GDP causality nexus: Evidence from a bootstrapped causality test for 30 OECD countries, *Energy Policy*, 36 (2), 910-918.
- 27) Payne, J. E., 2010, Survey of the international evidence on the causal relationship between energy consumption and growth, *Journal of Economic Studies*, 37 (1), 53-95.
- 28) Tari, R. (2010), Ekonometri, *Umuttepe Yayınları, Kocaeli*.
- 29) Çil Yavuz, N. (2015), Finansal Ekonometri, Baskı, Der Yayınları, İstanbul.
- 30) Bhatti, M. I. and Al-Shanfari, H. (2017), Econometric analysis of model selection and model testing, Routledge.
- 31) Yerdelen Tatoğlu, F. (2017), Panel Zaman Serileri Analizi, *Beta Basım Yayın Dağıtım AŞ, İstanbul*.
- 32) Yonar, H. and İyit, N. (2018), Modeling The Causality Relationships Between Gdp/Gni and Electricity Consumption According to Income Levels of Countries By Generalized Estimating Equations, *Selcuk University Social Sciences Institute Journal* (39), 191-200.
- 33) WorldBank, 2018, World Development Indicators [online], <https://www.worldbank.org/>
- 34) R Core Team (2021), R: A language and environment for statistical computing. R Foundation for Statistical Computing, Vienna, Austria. URL <https://www.R-project.org/>.
- 35) Trapletti, A. and Hornik, K. (2022), tseries: Time Series Analysis and Computational Finance. R package version 0.10-52.